

Analytical Modelling of Fines Migration in Porous Media

Yulong Yang, B.Sc. (Hons), M.Sc.

A thesis submitted for the degree of
Doctor of Philosophy (Ph.D.)

Australian School of Petroleum
Faculty of Engineering, Computer & Mathematical Sciences
The University of Adelaide



July 2016

To

my wife, Yang

*who has been a constant source of support and encouragement during the challenges
of my study and life,*

and my mum and dad, who have always loved me unconditionally.

I am truly thankful for having you in my life.

Table of Contents

Abstract	iii
Declaration	vi
Acknowledgment	vii
Thesis by Publication	ix
1 Contextual Statement	1
1.1 Thesis structure.....	5
1.2 How the publications are related to the thesis	8
1.3 References	13
2 Literature Review	15
2.1 Introduction	15
2.2 Fines migration in natural reservoirs	16
2.3 Governing equations.....	18
2.3.1 <i>Traditional kinetics model</i>	19
2.3.2 <i>Mechanisms of fines detachment</i>	20
2.3.3 <i>The maximum retention function</i>	27
2.3.4 <i>Release delay effect of attached particles</i>	39
2.4 Analytical solutions for constant filtration and formation damage coefficient	40
2.5 Summary.....	47
2.6 References	48
3 Analytical modelling of fines migration in porous media	53
3.1 Slow migration of mobilised fines during flow in reservoir rocks: Laboratory study	54
3.2 Slow migration of detached fine particles over rock surface in porous media	65
3.3 Fines mobilisation by low-salinity water injection: 3-point-pressure tests.....	117
3.4 Fines migration in aquifers and oilfields: laboratory and mathematical modelling	131

4	Mathematical modelling of fines migration in geothermal reservoirs.....	210
5	Laboratory-based mathematical modelling of graded proppant injection in CBM reservoirs	224
6	Deep bed and cake filtration of two-size particle suspension in porous media.....	243
7	Conclusions.....	256

Abstract

Hereby I present a PhD thesis by publications. Altogether, the thesis includes: a) five journal papers, b) one book chapter, and one c) SPE conference paper. Five journal papers have already been published. The journal publication list includes high-impact-factor academic journals: *International Journal of Coal Geology*, *Geothermics*, *Journal of Natural Gas Science and Engineering*. The list also includes *Journal of Petroleum Science and Engineering*, which is a major academic journal in petroleum industry. I have also submitted one book chapter to be edited by Springer. Besides, the content of this thesis is published in six full-volume SPE technical papers of Society of Petroleum Engineering.

The thesis presents *new analytical models for fines migration in porous media*. The novelty of this work is the new governing equation system accounting for two effects during fines migration in rocks: slow drift of mobilised fines along rock surface, and the delayed release of fine particles (non-equilibrium effect).

Migration of fine particles in natural reservoirs is one of the main causes for formation damage in oil and gas fields. Numerous laboratory observations show that permeability stabilisation time is much longer than one pore volume injected. However, the existing mathematical models for fines migration, which are widely used in petroleum reservoir simulation, cannot predict the long-term stabilisation phenomenon.

The new analytical solutions derived in this thesis successfully model the physical mechanisms of the permeability stabilisation delay and match well with laboratory data. Long permeability stabilisation period during coreflood tests exhibiting fines migration is explained by slow fines rolling and sliding, and also by

the diffusive delay in particle mobilisation. The analytical models have been derived for both slow fines migration and delayed mobilisation. Laboratory coreflood tests to observe the effects of flow velocity and salinity on fines migration and consequent permeability decline have been carried out, with the measurements of breakthrough fines concentration and pressure drop along the whole core and its sections. Matching of the experimental data, along with the analysis of the tuned coefficients shows that the slow-particle model exhibits higher accuracy of matching and more typical strained-concentration dependency of the tuning parameters than the delay-release model. The effect of temperature on fines migration is analysed systematically, which can be applied to geothermal reservoir conditions.

In this thesis, a new analytical solution is derived for the simultaneous processes of deep bed filtration and cake build-up during injection of two-sized particles. Formation of low permeable external filter cake during drilling and water injection has been intensively studied in the literature. The external cake may significantly reduce the well index. There are no existing mathematical models accounting for simultaneous particle filtration through external cake and in the core. The proposed model in this work fills the gap. Two scenarios of cake formation are identified, corresponding to the high and low fractions of small particles injected, respectively. Laboratory coreflooding tests with injection of two-sized particles have been performed, from which the rate and pressure drop data are collected. The data treatment shows excellent agreement between the measured pressure drop history and the modelled result.

The derived mathematical models and their analytical solutions in this thesis are applicable to the prediction of the extent of formation damage and the well behaviour in different types of reservoirs, including oil/gas, geothermal and coal bed methane

reservoirs. Also, these models can be applied to numerous environmental and chemical engineering processes, including the disposal of industrial wastes into aquifers, propagation of contaminants and pollutants in vadose zone, and industrial water treatment.

Declaration

I certify that this work contains no material which has been accepted for the award of any other degree or diploma in my name, in any university or other tertiary institution and, to the best of my knowledge and belief, contains no material previously published or written by another person, except where due reference has been made in the text. In addition, I certify that no part of this work will, in the future, be used in a submission in my name, for any other degree or diploma in any university or other tertiary institution without the prior approval of the University of Adelaide and where applicable, any partner institution responsible for the joint-award of this degree. I give consent to this copy of my thesis when deposited in the University Library, being made available for loan and photocopying, subject to the provisions of the Copyright Act 1968. The author acknowledges that copyright of published works contained within this thesis resides with the copyright holder(s) of those works.

I also give permission for the digital version of my thesis to be made available on the web, via the University's digital research repository, the Library Search and also through web search engines, unless permission has been granted by the University to restrict access for a period of time.

Yulong Yang

15/07/2016

Acknowledgment

I would never be able to finish my dissertation without the enthusiastic guidance of my supervisors, kind help from colleagues, and endless support from my family.

Firstly, I would like to express my sincere gratitude to my supervisor, Professor Pavel Bedrikovetsky, who truly brought me into the sanctuary of science and taught me how to think as a scientist. He explained me the basic mathematics and physics with unfailing patience. His never-to-be-forgotten charming when deriving equations on the board showed me the magic of mathematics, which highly inspired my interests and encouraged me to continue pursuing the truth of science in my future career. Without his expertise and support I would not have been able to complete my PhD thesis and have such fruitful four years.

Very special thanks to Dr Themis Carageorgos for the strong support, detailed review and earnest help. She is always like a mother to me and let me feel the warmth of home. Her comforting words always encourage me to move on.

I would also like to express my very great appreciation to my co-supervisor Dr Zhenjiang You, for spending so much time in discussing with me and helping me solve problems. He kept on steering me to the right direction during the past four years, which truly accelerated my research progress. I have been so fortunate to have him as a mentor.

Sincere thanks are also extended towards Dr Alex Badalyan for his professional technical assistance and meticulous editing for my work.

The constructive criticism and excellent advice of Dr Fernando Siqueira and Dr Abbas Zeinijahromi have been invaluable on both academic and personal level, for which I am extremely grateful. Their quick but deep thinking always impress me.

A big thank you to all of the fantastic people I have been incredibly lucky to work and collaborate with, Professor Pacelli Zitha (Delft University of Technology), Professor Alexandre Vaz, Rebeca Sacramento and Maria Oliveira (North Fluminense State University), Dr Alireza Keshavarz, Dr Azim Kalantariasl and Dr Sara Borazjani (The University of Adelaide). Thank them all for inspiration, mentoring, motivation and detailed review of my work.

Last but not least, I would like to thank my family for all their love and encouragement. To my parents, you are the first community that encouraged me to find my passion and show belief in me. And most of all to my loving, supportive, encouraging and beautiful wife, Yang, without you this would not have been possible. Thank you!

Thesis by Publication

Published Journal Papers

Yang, Y., Siqueira, F. D., Vaz, A., You, Z. and Bedrikovetsky, P., 2016. Slow migration of detached fine particles over rock surface in porous media. *Journal of Natural Gas Science and Engineering*, 34: 1159-1173.

You, Z., **Yang, Y.**, Badalyan, A., Bedrikovetsky, P. and Hand, M., 2016. Mathematical modelling of fines migration in geothermal reservoirs. *Geothermics*, 59: 123-133.

Keshavarz, A., **Yang, Y.**, Badalyan, A., Johnson, R. and Bedrikovetsky, P., 2014. Laboratory-based mathematical modelling of graded proppant injection in CBM reservoirs. *International Journal of Coal Geology*, 136: 1-16.

Sacramento, R.N., **Yang, Y.**, You, Z., Waldmann, A., Martins, A.L., Vaz, A.S., Zitha, P.L. and Bedrikovetsky, P., 2015. Deep bed and cake filtration of two-size particle suspension in porous media. *Journal of Petroleum Science and Engineering*, 126: 201-210.

Oliveira, M. A., Vaz, A. S., Siqueira, F. D., **Yang, Y.**, You, Z. and Bedrikovetsky, P., 2014. Slow migration of mobilised fines during flow in reservoir rocks: Laboratory study. *Journal of Petroleum Science and Engineering*, 122, 534-541.

Submitted Book Chapter

Yang, Y., Siqueira, F. D., Vaz, A., Badalyan, A., You, Z., Zeinijahromi, A., Carageorgos T., Bedrikovetsky, P., 2016. Fines migration in aquifers and oilfields: laboratory and mathematical modelling, Springer.

International full-volume conference papers

Yang, Y., You, Z., Siqueira, F. D., Vaz, A., Bedrikovetsky, P., 2016. Modelling of slow fines migration and formation damage during rate alteration. SPE-182320-MS.

SPE Asia Pacific Oil & Gas Conference and Exhibition, 25-27 October, Perth, Australia.

Yang, Y., You, Z., Siqueira, F. D., Vaz, A., Bedrikovetsky, P., 2016. A New Phenomenon of Slow Fines Migration in Oil and Gas Fields (Laboratory and Mathematical Modelling). SPE-179027-MS. SPE International Conference and Exhibition on Formation Damage Control, 24-26 February, Lafayette, Louisiana, USA.

Bhattacharya, S. S., Paitaridis, J., Pedler, A., Badalyan, A., **Yang, Y.**, Carageorgos, T., Lemon, N., Bedrikovetsky, P., 2016. Fines Mobilisation by Low-Salinity Water Injection: 3-Point-Pressure Tests. SPE-178947-MS. SPE International Conference and Exhibition on Formation Damage Control, 24-26 February, Lafayette, Louisiana, USA.

A. Badalyan, Z. You, **Yang, Y.**, T. Carageorgos, U. Schacht, P. Bedrikovetsky, M. Hand, 2015. New Laboratory Method to Assess Formation Damage in Geothermal Wells. SPE-174199-MS. SPE European Formation Damage Conference held in Budapest, Hungary, 3-5 June.

Yang, Y., Sacramento, R. N., You, Z., Leibson, A., Waldmann, A. T. A., Zitha, P. L., Bedrikovetsky, P. G. 2014. External Cake Built of Bi-sized Particles in Well Injectivity and Drilling. SPE 169276. In SPE Latin America and Caribbean Petroleum Engineering Conference.

Siqueira, F. D., **Yang, Y.**, Vaz, A. S., You, Z., Bedrikovetsky, P. G., 2014. Prediction of Productivity Decline in Oil and Gas Wells Due to Fines Migration: Laboratory and Mathematical Modelling. SPE-171475-MS. SPE Asia Pacific Oil & Gas Conference and Exhibition, 14-16 October, Adelaide,

Z. You, A. Badalyan, **Yang, Y.**, P. Bedrikovetsky, M. Hand, C. Matthews, 2015. Modelling of productivity decline in geothermal reservoirs due to fines migration-induced formation damage. World Geothermal Congress, 19-25 April, Melbourne, Australia.

1 Contextual Statement

Significance of the PhD project Natural reservoir fines, their mobilization, migration and straining is one of the main causes for well productivity damage in petroleum reservoirs. Fine particles detachment from grains and pore walls in the natural reservoir rocks followed by their migration and straining, may yield significant permeability decline (Fig. 1). This phenomenon has been widely reported since the 1950s, and is currently an intensive research topic worldwide (Monaghan et al., 1959; Hewitt, 1963; Mungan, 1965; Sharma and Yortos, 1987; Khilar and Fogler, 1987, 1998; Valdya and Fogler, 1992; Byrne et al., 2009, 2014; Civan, 2014; Bai et al., 2015; Guo et al., 2015; Han et al., 2015). Another reason for well impairment is extremely low permeable external filter cake (Ding et al., 2004; Wagner et al., 2006; Quintero et al., 2007). The cake is usually formed during drilling, waterflooding with low-quality water and produced water re-injection into reservoir. The external filter cake usually causes substantial reduction in well injectivity and productivity indexes. The phenomenon of skin factor due to low-permeable external filter cake has also been intensively studied since 1930s (Ruth et al., 1933; Abrams, 1977; Van Oort et al., 1993; Tien et al. 1997; Ghalambor and Economides, 2002; Parn-anurak and Engler, 2005; Ding et al., 2006; Civan, 2007; Dalmazzone et al., 2007; Ding et al., 2008; Alotaibi et al., 2009; Salimi et al., 2009; Lohne et al., 2010; Karimi et al., 2011; Tien, 2012).

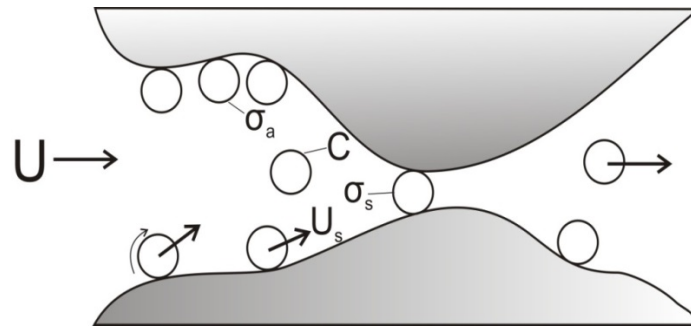


Fig. 1 Sketch of fines detachment, migration, and straining with consequent permeability decline

Derivation of new mathematical models and their field applications is based on the results of adjustment of the models by the laboratory study data. Successful mathematical modelling in order to describe particular experimental and field phenomena, can highly improve the understanding of physical mechanisms. This understanding is an essential part of the advanced technology development. Analytical modelling provides fast calculations, clear structure of flow phenomena, straightforward interpretation of laboratory data, and visual representation of oil/gas/water recovery mechanisms. However, due to the limitations of the classical models, the long-term stabilisation and the multi-stage behaviour of impedance curve during deep bed filtration of released fines and of the injected particles cannot be reliably predicted. Therefore, derivation of new mathematical models for fines migration in rocks and the analytical solutions is a significant challenge, not only in petroleum industry, but also in other fields involving fluid flow in porous media.

State of the art According to the data from fines migration tests (clean water injection) (Fig. 2), rock permeability stabilises after a high number of pore volumes injected. However, the classical filtration theory says that it takes a flight time along the overall core for a mobilised particle to appear at the end of the core. Each fine particle transported by the carrier fluid, is either strained inside the core or appears at the effluent after one pore volume injection. According to Fig. 2, permeability

stabilisation times are significantly higher than one pore volume injected (PVI). This phenomenon is explained by slow motion of particles along the rock surface: the mobilised particles move along the rock with velocity U_s , which is much smaller than the carrier fluid velocity U . When combined with the DLVO theory, the new proposed model allows analysing the impedance behaviour under variant flow rates, salinities and temperatures.

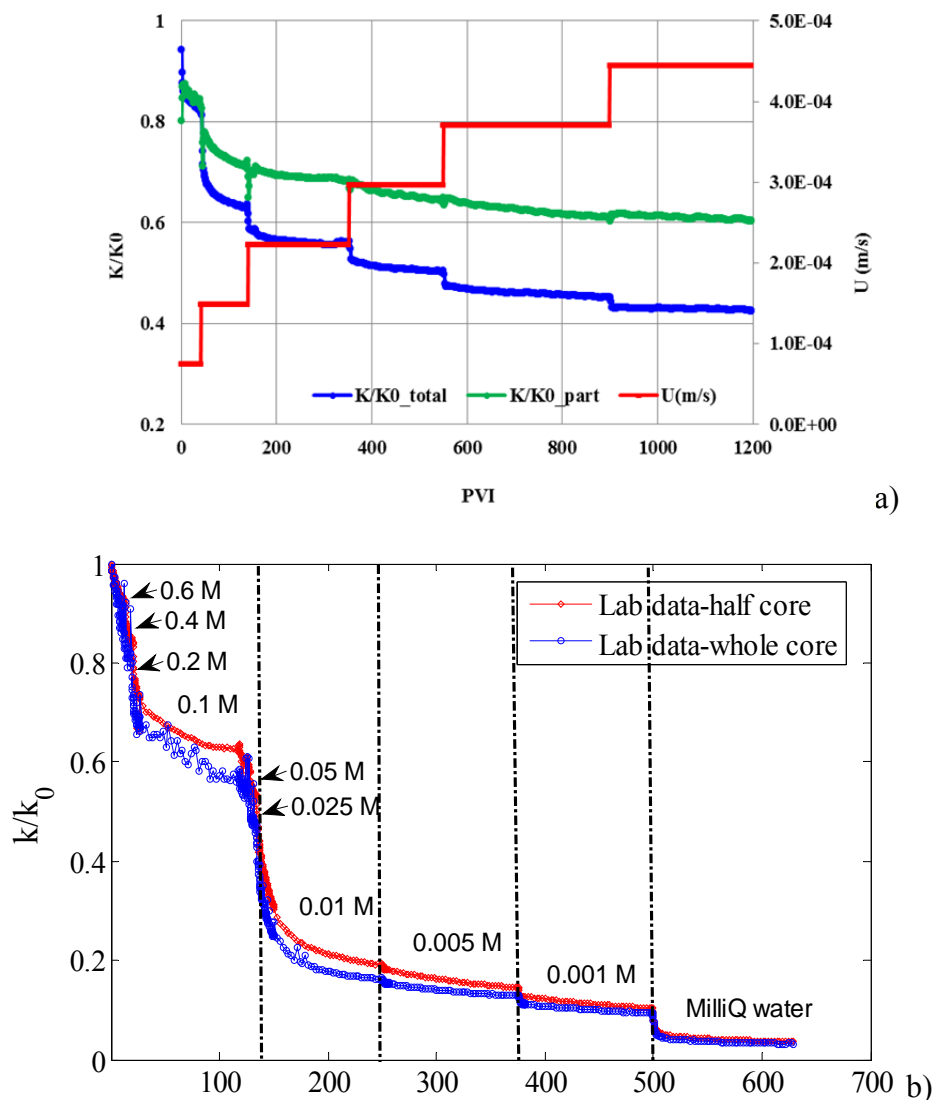


Fig. 2 Permeability behaviour during coreflood tests under variant flow rates and salinities: (a) Coreflood test under piecewise increasing flow rates (b) Coreflood test under piecewise decreasing salinities

Also, the deep bed filtration theory does not consider external cake formation if multi-sized particles are injected into porous media. Introducing external cake

formation process allows us to more precisely predict the multi-stage behaviour of impedance curve in field. The proposed bi-sized particle injection model aims to fill the gap by taking into account of injection of particles with two different sizes into porous media. The larger particles form the external filter cake instantly after the beginning of injection; while the smaller particles perform deep bed filtration simultaneously in the cake and in the porous media. From a certain transition time, the smaller particles no longer penetrate into the media, but only filtrate in the built-up cake.

Scope of the work The main achievements of the thesis include:

- A new analytical model and experimental study for fines migration accounting for the slow movement along the rock surface under variant flow rates (presented in Chapter 3)
- Development of a new analytical model for fines migration accounting for delayed particle release (presented in Chapter 3)
- Investigation of slow fines migration model in geothermal reservoirs including comprehensive temperature analysis, based on the analytical solution (presented in Chapter 4)
- Application of the analytical model for slow fines migration in CBM reservoir (presented in Chapter 5)
- Development of a new mathematical model of the cake filtration accounting for bi-sized particles injection into porous media (presented in Chapter 6)

1.1 Thesis structure

This is a PhD thesis by publication. Five journal papers, one book chapter and one SPE conference paper are included in the thesis. Among the seven works, five

papers have been published in peer reviewed journals, and one paper has been published in SPE proceedings. The book chapter has been submitted to Springer publishing house.

The main part of this thesis is divided into seven chapters. The first chapter contains the general aims and an introduction to show the importance of the work to the oil and gas industry. The second chapter presents the literature review on the mechanisms of fines migration induced formation damage, and the classical mathematical models. *Chapters three, four, five and six* are the novel original parts of the thesis. The main statements of scientific novelty presented in *Chapter seven* conclude the thesis.

Paper	Chapter	Title	Status
1	Chapter 3	Slow migration of mobilised fines during flow in reservoir rocks: Laboratory study	Published
2	Chapter 3	Slow migration of detached fine particles over rock surface in porous media	Published
3	Chapter 3	Fines mobilisation by low-salinity water injection: 3-point-pressure tests	Published
4	Chapter 3	Fines migration in aquifers and oilfields: laboratory and mathematical modelling	Submitted for publication
5	Chapter 4	Mathematical modelling of fines migration in geothermal reservoirs	Published
6	Chapter 5	Laboratory-based mathematical modelling of graded proppant injection in CBM reservoirs	Published
7	Chapter 6	Deep bed and cake filtration of two-size particle suspension in porous media	Published

The *first Chapter* demonstrates the importance of the performed research in this thesis to the petroleum, chemical, and environmental industries, and other areas. This chapter highlights the challenges in predicting the well performance by the current models. It allows formulating the main aim of the thesis, i.e. modelling the impedance behaviour which cannot be well described by the classical models. The main contextual statement in chapter one is to describe the goal of the PhD study.

The *second Chapter* presents detailed literature review on mechanisms of fines detachment and the consequent formation damage in injection wells during injection of sea water, produced water, low salinity water or any poor quality water. Water production growth and water management challenges in the petroleum industry are highlighted. Laboratory coreflood tests on reservoir samples for water injection and drilling fluid design, and also field data observations are reviewed. In addition, lessons learned from cross-flow filtration experiments in membrane science are briefly summarised. Different mathematical models of fines migration and their limitation in predicting the injectivity behaviour are reviewed and discussed. It shows the lack of comprehensive mathematical model for prediction of well injectivity decline.

Fines migration due to particle detachment often causes severe permeability damage in natural reservoirs. The damage happens during the mobilisation and migration of released fines that are strained in narrow pore throats. The delay in permeability stabilisation after flow rate variation is attributed to the slow drift of the mobilised fine particles near the rock surface. To account for this effect, the system of flow equations for suspended particle transport in porous media, with velocity smaller than the carrier fluid velocity, is derived in *Chapter three*. An analytical model for one dimensional flow including particle detachment and straining, under piecewise increasing velocity, is developed. Clean water injection tests, under piecewise increasing velocity, are also performed to confirm the observed long-term stabilisation. The laboratory data are in high agreement with the results of mathematical modelling. The effective particle speed is 500-1000 times smaller than the water velocity.

Salinity is another crucial parameter that can significantly affect fines migration in rocks. Delay in permeability stabilisation also takes place under salinity alterations. Several waterflooding tests, using the three-point method under piecewise decreasing salinities, are performed and discussed in details in *Chapter three*. Besides slow fines migration along the rock surface, the long term stabilisation of permeability can be attributed to the so-called Nernst-Planck diffusion. This diffusion occurs in a thin slot between two plates under the molecular-force action, which is significantly slower than the Brownian diffusion. Yet, a mathematical model that accounts for delay in particle mobilisation is not encountered in the literature as well. In Chapter three, the analytical model considering fines release delay is derived and the tuning results are compared with the previously derived model.

Temperature analysis on fines migration and consequent formation damage are performed in *Chapter four*. Temperature can significantly affect fines mobilisation due to its severe effect on zeta potential of the materials, at high temperatures. DLVO theory is a powerful tool to quantitatively estimate the magnitude of the electrostatic force between a particle and rock surface. Based on the torque balance equation, the analytical solutions of the proposed mathematical model, along with DLVO theory, are successfully applied to predict the permeability behaviour of sandstone under higher temperature, which corresponding to geothermal reservoir condition.

Chapter five presents the experimental studies conducted to analyse the effect of salinity change on fines migration in coal. The purpose of this study is to find a particular salinity range, where the salinity values are not too high to plug the core inlet by the injected particles (proppants), and not too low to cause formation damage by fines migration. The analytical solutions for slow fines migration, derived in Chapter three, are applied for tuning the experimental data. Successful treatment of

the test data by the analytical model allows reliable prediction of well behaviour during injection of graded particles.

External filter cake build-up and fine particles deep bed filtration occur during drilling, completion and water injection processes. To our knowledge, comprehensive analytical models for external cake formation including co-occurring deep bed filtration and cake build-up are not available in the literature. *Chapter six* proposes a new model accounting for injection of bi-sized particle suspension into porous media. This chapter derives an analytical model for external cake filtration (i.e., cake build-up and deep bed filtration). The new model incorporates the initial cake formation by large particles, deep bed filtration of small particles, internal cake growth inside external cake after the transition time, and possible formation of the mixture cake at a later stage. To validate the analytical model developed, a series of laboratory coreflood tests on the injection of two-sized particle suspensions have been performed. The values of impedance calculated using the analytical model agree well with the experimental data, and thus, validate the derived model.

1.2 How the publications are related to the thesis

The paper “Slow migration of mobilised fines during flow in reservoir rocks: laboratory study” presents the results of coreflooding tests with piecewise increasing velocities, in order to mobilise fines from natural cores until permeability stabilisation. It is observed that the times required for permeability stabilisation are much longer than one PVI in all the tests. This observation contradicts the classical model prediction, which assumes that particle and water have the same velocity, yielding the stabilisation time of one PVI. The permeability stabilisation time is shorter if the flow rate increases, because the drag force exerting on particles increases with flow rate.

In the paper “Slow migration of detached fine particles over rock surface in porous media”, the governing equations for one dimensional flow, accounting for particle mobilisation and consequent size exclusion under piecewise increasing flow rate, are derived. The long stabilisation time of permeability is explained by slow fines migration compared to the fluid velocity. The proposed model introduces a drift delay factor, which characterise the ratio between particle and fluid velocities. The analytical solutions are provided and validated by the experimental results.

The paper “Fines mobilisation by low-salinity water injection: 3-point-pressure tests” presents experimental results from coreflooding tests with piecewise decreasing salinities. Two sandstone cores were chosen to investigate formation damage using the 3-point pressure measurement method along the core. It was observed that formation damage in the studied cores, after their contact with low-ionic strength fluid, is caused by fines mobilisation, their migration in the porous medium and straining in narrow pores. Each coreflood is characterised by decrease in rock permeability, with stabilisation times much longer than one PVI. This indicates that the mobilised particle’s drift velocity is much smaller than that of the fluid.

The book chapter “Fines migration in aquifers and oilfields: laboratory and mathematical modelling” presents new mathematical models and experimental results of coreflooding, under piecewise decreasing salinities. Long permeability stabilisation time during coreflooding with fines migration, is explained by slow fines rolling and sliding, and also by the diffusive delay in particle mobilisation. The analytical models are derived for both phenomena. The laboratory fines-migration coreflood tests are carried out with measurements of breakthrough concentration of particles and pressure drop along the whole core and a fraction of its length. Tuning results of the two mathematical models, based on slow fines migration and delayed particle release,

respectively, and the combined model accounting for the two phenomena are compared. Treatment of the experimental data and analysis of the tuned coefficients show that the slow-particle model exhibits higher accuracy of matching and more typical strained-concentration dependencies of the tuned parameters than the delay-release model.

The temperature effects on reservoir fines mobilization, transport and straining are analysed in the paper “Mathematical modelling of fines migration in geothermal reservoirs”. Laboratory coreflood tests with piecewise decreasing ionic strength are performed, including the measurements of pressure drop along the core and accumulated effluent particle concentrations. Permeability stabilises after injection of numerous pore volumes, suggesting slow drift of mobilised particles if compared with the carrier water velocity. SEM-EDAX analysis of the produced fine particles shows that kaolinite and chlorite are the major minerals responsible for the permeability damage. The competitive effects of decreasing water viscosity and weakening electrostatic attraction, on the attached particle concentration during temperature increase, are observed. The microscale modelling of the fine particle mechanical equilibrium shows that, the electrostatic attraction effect on the fines attachment dominates over the fluid drag effect. This effect yields more fines release and consequent permeability reduction at high temperature, suggesting that geothermal reservoirs are more susceptible to formation damage induced by fines migration than the conventional petroleum fields. A mathematical model is derived accounting for “inherited” particles from the previous coreflooding stages. The obtained analytical solutions can be applied to predict well productivity index decline during reservoir exploitation. The maximum retention concentration function, based on mono-layer multi-sized particles assumption, is derived in the proposed model.

In the paper “Laboratory-based mathematical modelling of graded proppant injection in CBM reservoirs”, the analytical model for axisymmetric flow has been developed for exponential stress-permeability relationship. It accounts for permeability change out of the stimulated zone. Laboratory proppant injections into coal cores with different proppant sizes and water salinities have been conducted. It is found that the proppant suspension in low-salinity water exhibits weak particle–particle and particle–coal attractions, leading to core entrance plugging and external cake formation. Yet, injection of low-salinity water may incur mobilisation and straining of fines, causing substantial formation damage. In this work, laboratory tests are performed to observe the effect of salinity change on fines migration in coal. An interval is found, where salinity is not low enough to avoid significant formation damage due to fine migration, and is not high enough to avoid inlet plugged by the injected proppant. Matching the mathematical model derived in Chapter three with the experimental data, allows for reliable laboratory-based well performance prediction submitted to graded particle injection.

Build-up of an external cake on the borehole wall, along with deep bed filtration of small particles during drilling fluid invasion or water injection into oilfield, can cause permeability decline in the vicinity of the wellbore, and thus, serious formation damage. The paper “Deep bed and cake filtration of two-size particle suspension in porous media” presents a new mathematical model for the injection of two-sized particle suspension into rocks. The model accounts for deep bed filtration of small particles in porous media, build-up of external filter cake by large particles, filling of the cake by small particles and formation of a new cake by the mixed small and large particles at a later stage. Explicit analytical solutions have been derived. Two scenarios of cake formation are identified, and they correspond to the high and low

fractions of small particles injected, respectively. A laboratory test injecting two-sized suspension into a natural core was performed. The flow rate and pressure drop along the core were measured. The impedance profile from laboratory measurement was matched by the exact solution with high accuracy.

Finally, the above mentioned five journal papers, one book chapter and one SPE full-volume conference paper present results of numerous laboratory coreflood tests, with injection of clean water and particle suspensions. These publications also provide comprehensive analytical models for prediction of suspension transport and retention in porous media, which is necessary for decision making, design and implementation of water injection projects, and determining strategies to avoid and/or mitigate formation damage. The proposed models can be applied to the prediction of permeability behaviour during injection of seawater, fresh water, re-injection of produced water, waste disposal, and invasion of drilling fluids in oilfields, geothermal and CBM reservoirs.

1.3 References

- Abrams, A., 1977. Mud design to minimize rock impairment due to particle invasion. *Journal of Petroleum Technology*, 29: 586-592.
- Alotaibi, M.B., Nasr-El-Din, H.A. and Hill, A.D., 2009. Use of ester as a precursor to clean formate drill-in fluid damage in horizontal wells. *SPE Drilling & Completion*, 24(3): 404-412.
- Bai, T., Chen, Z., Aminossadati, S. M., Pan, Z., Liu, J., and Li, L., 2015. Characterization of coal fines generation: A micro-scale investigation. *Journal of Natural Gas Science and Engineering*, 27: 862–875.
- Byrne, M.T., Slayter, A.G. and, McCurdy, P., 2010. Improved selection criteria for sand control: When are " fines" fines? In: SPE-128038,. SPE International Symposium and Exhibition on Formation Damage Control, held in Lafayette, Louisiana, USA, 10–12 Feb.
- Byrne, M., Rojas, E., Kandasamy, R., Gibb, A., 2014. Fines migration in oil and gas reservoirs: Quantification and qualification through detailed study. In: SPE-168150,. SPE International Symposium and Exhibition on Formation Damage Control, held in Lafayette, Louisiana, USA, 26–28 Feb.
- Civan, F., 2007. *Reservoir formation damage : fundamentals, modeling, assessment, and mitigation*. Gulf Professional Pub., Amsterdam.
- Civan, F., 2014. *Reservoir formation damage (3rd ed.)*. Gulf Professional Publishing, Burlington, MA, USA.

- Dalmazzone, C.S., Follotec, A.L., Audibert-Hayet, A., Twynam, A.J. and Poitrenaud, H.M., 2007. Development of an optimized formulation for cleaning water injection wells drilled with oil-based systems, European Formation Damage Conference. Society of Petroleum Engineers, Scheveningen, The Netherlands.
- Ding, Y., Herzhaft, B. and Renard, G., 2006. Near-wellbore formation damage effects on well performance: A comparison between underbalanced and overbalanced drilling. *SPE Production and Operations*, 21(1): 51-57.
- Ding, Y., Longeron, D., Renard, G. and Audibert, A., 2004. Modeling of both near-wellbore damage and natural cleanup of horizontal wells drilled with water-based drilling fluids. *SPE Journal*, 9(3): 252-264.
- Ding, Y. and Renard, G., 2005. Evaluation of horizontal well performance after drilling-induced formation damage. *Journal of Energy Resources Technology, Transactions of the ASME*, 127(3): 257-263.
- Ding, Y., Renard, G. and Herzhaft, B., 2008. Quantification of uncertainties for drilling-induced formation damage. *SPE Production and Operations*, 23(2): 221-231.
- Ghalambor, A. and Economides, M.J., 2002. Formation damage abatement: a quarter-century perspective. *SPE Journal*, 7(1): 4-13.
- Guo, Z., Hussain, F. and Cinar, Y., 2015. Permeability variation associated with fines production from anthracite coal during water injection. *International Journal of Coal Geology*, 147: 46–57.
- Han, G., Ling, K., Wu, H., Gao, F., Zhu, F. and Zhang, M., 2015. An experimental study of coal-fines migration in cCoalbed-methane production wells. *Journal of Natural Gas Science and Engineering*, 26: 1542–1548.
- Hewitt, C.H., 1963. Analytical techniques for recognizing water sensitive reservoir rocks, *Journal of Petroleum Technology, Transactions of AIME*, 15(8): 813-817.
- Karimi, M., Ghalambor, A., Montgomery, M. and Moellendick, T.E., 2011. Formation damage and fluid loss reduction due to plastering effect of casing drilling, SPE European Formation Damage Conference. Society of Petroleum Engineers, Noordwijk, The Netherlands.
- Khilar, K.C. and Fogler, H.S., 1987. Colloidally induced fines migration in porous media. *Reviews in Chemical Engineering*, 4(1-2): 41-108.
- Khilar, K.C. and Fogler, H.S., 1998. *Migrations of fines in porous media (Vol. 12)*. Springer Science & Business Media.
- Lohne, A., Han, L., Van Der Zwaag, C., Van Velzen, H., Mathisen, A.M., Twynam, A., Hendriks, W., Bulgachev, R. and Hatzignatiou, D.G., 2010. Formation-damage and well-productivity simulation. *SPE Journal*, 15(3): 751-769.
- Monaghan, P.H., R.E. Salatheil, and B.E. Morgan, Laboratory studies of formation damage in sands containing clays. *Journal of Petroleum Technology, Transactions of AIME*, 11(2),209-215,1959.
- Mungan, N., Permeability reduction through changes in pH and salinity. *Journal of Petroleum Technology, Transactions of AIME*, 17, 1449-1453, 1965.
- Parn-anurak, S. and Engler, T.W., 2005. Modeling of fluid filtration and near-wellbore damage along a horizontal well. *Journal of Petroleum Science and Engineering*, 46(3): 149-160.
- Quintero, L., Jones, T.A., Clark, D. and Twynam, A.J., 2007. NAF filter cake removal using microemulsion technology, european formation damage conference. Society of Petroleum Engineers, Scheveningen, The Netherlands.
- Ruth, B.F., Montillon, G.H. and Montonna, R.E., 1933. Studies in filtration-I. critical analysis of filtration theory. *Industrial & Engineering Chemistry*, 25(1): 76-82.
- Salimi, S., Khansari, A.N., Ghalambor, A. and Tronvoll, J., 2009. Application of UBD technology to maximize recovery from horizontal wells in the naturally fractured carbonate reservoirs, IADC/SPE Managed Pressure Drilling and Underbalanced Operations Conference & Exhibition. 2009, IADC/SPE Managed Pressure Drilling and Underbalanced Operations Conference and Exhibition, San Antonio, Texas.

- Sharma, M.M. and Yortsos, Y.C., 1987. Fines migration in porous media. *AIChE Journal*, 33(10):1654-1662.
- Suri, A. and Sharma, M.M., 2004. Strategies for sizing particles in drilling and completion fluids. *SPE Journal*, 9(1): 13-23.
- Tien, C., 2012. *Principles of filtration*. Elsevier Science, Boston.
- Tien, C., Bai, R. and Ramarao, B.V., 1997. Analysis of cake growth in cake filtration: effect of fine particle retention. *AIChE Journal*, 43(1): 33-44.
- Valdya, R.N. and Fogler, H.S., 1992. Fines migration and formation damage: influence of pH and ion exchange. *SPE production engineering*, 7(4): 325-330.
- Wagner, M.R., Webb, T., Maharaj, M., Twynam, A., Green, T., Salamat, G. and Parlar, M., 2006. Horizontal drilling and openhole gravel packing with oil-based fluids - an industry milestone. *SPE Drilling and Completion*, 21(1): 32-43.

2 Literature Review

2.1 Introduction

Fines migration with consequent permeability reduction is a widely recognised formation damage mechanism, occurring in numerous petroleum and environmental processes. Fines migration takes place during oil and gas production in conventional and unconventional reservoirs, yielding significant reduction in the well productivity (Byrne et al., 2009, 2014; Bedrikovetsky et al., 2011*a,b*; 2012*a,b*; Zeinijahromi, 2012*a,b*; Civan, 2014; Bai et al., 2015; Guo et al., 2015; Han et al., 2015). The occurrence of natural and induced fines migration has also been widely reported for waterflooding of oilfields and invasion of drilling and completion fluids into the formation (Watson et al., 2008; Fleming et al., 2007; 2010*a,b*). Generally speaking, the fines migration phenomenon is known for its detrimental effects on wells. Despite clogging in production and injection wells remains a major operational issue, comprehensive and precise analytical models for fines migration behaviour are unavailable in the literature.

The literature review starts from the introduction of fines migration phenomenon and analysis of reservoir fines (Section 2.2). It is followed by the governing equations of fines migration in porous media (Section 2.3): traditional kinetics model for particle capture, which is the basics for the system of fines migration problems, is presented in Section 2.3.1; Section 2.3.2 presents the mechanisms of fines detachment; Section 2.3.3 reviews the models of the maximum retention function; and Section 2.3.4 introduces the delay effect of particle release.

Section 2.4 reviews the analytical solutions to the fines migration models accounting for slow drift and delayed release effects.

The main conclusion of the literature review, presented in Section 2.5, is the significance of the research project on analytical modelling of fines migration in porous media, due to wide spreading of these processes in petroleum, environmental and chemical engineering. The review is finalised by the statement that the solutions to the problems accounting for slow drift and delayed release effects are not available in the literature.

2.2 Fines migration in natural reservoirs

The distinguishing features of natural reservoir fines migration are mobilisation of the attached particles, their capture by straining in the rock and permeability decrease, with consequent decline of well productivity and injectivity (Fig. 1). Permeability decline during coreflooding with piecewise increasing velocity has been observed in many laboratory tests (Khilar and Fogler, 1998; Ochi and Vernoux, 1998, 1999). Similar effects occur during piecewise variation of water salinity or pH during coreflooding (Kia, 1987; Lever and Dawe, 1994). The phenomenon is attributed to the mobilisation and migration of attached fines in porous space until size exclusion in narrow pore throats, finally resulting in significant permeability decline (Muecke, 1979; Sarkar and Sharma, 1990; You et al. 2016). Fig. 1 shows the schematic for attached and strained fine particles in the porous space along with definitions for concentrations of attached, suspended and strained particles. Detachment of fines which coat the grain surfaces yields an insignificant increase in porosity and permeability, while the straining in narrow pore throats and the consequent blocking of conducting paths cause significant permeability decline. The main sources of movable fine particles in reservoirs are clays such as kaolinite, chlorite and illite; quartz and silica particles may be mobilised in low-consolidated sandstones (Arab et

al., 2014). Usually the kaolinite booklets of thin slices are situated on the grain surfaces (Fig. 3).

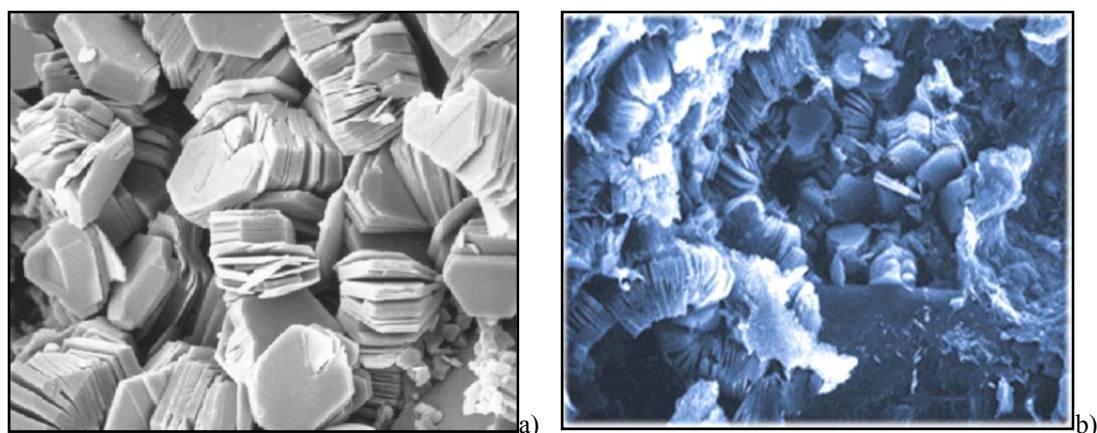


Fig. 3 Kaolinite particles attached to the grain surface (SEM image): (a) leaflet shape; (b) leaflets in the pore space

Typical result of SEM-EDX analyses for a core sample is illustrated in Fig. 4. Plate-like “booklets” characteristic of kaolinite is shown on SEM image (Fig. 4a). The so-called “peak height ratio” equivalent to the ratio of relative molar proportions of Al and Si shown on EDX spectrum (Fig. 4b) is close to unity. This suggests that the above “booklets” are identified as kaolinite, $\text{Al}_2(\text{Si}_2\text{O}_5)(\text{OH})_4$. Detachment of a thin large slice from the booklet may result in plugging of a large pore, so the mobilisation of small kaolinite volume may cause significant permeability impairment. Flakes of clay minerals are visible in the SEM image shown in Fig. 4c. Although their morphology indicates the presence of chlorite $(\text{Mg},\text{Al},\text{Fe})_{12}[(\text{Si},\text{Al})_8\text{O}_{20}](\text{OH})_{16}$, their EDAX spectra are more indicative of illite $\text{K}_{1-1.5}\text{Al}_4[\text{Si}_{7-6.5}\text{Al}_{1-1.5}\text{O}_{20}](\text{OH})_4$ (Fig. 4d). However, the moderate iron content is an indication of the formation of chlorite (Vortisch et al., 2003). Therefore, the observed clay particles can be identified as mixed-layer illite/chlorite mineral. A double-stick electrically-conductive carbon tape produces carbon peaks in both EDAX spectra in Figs. 5b and 5d.

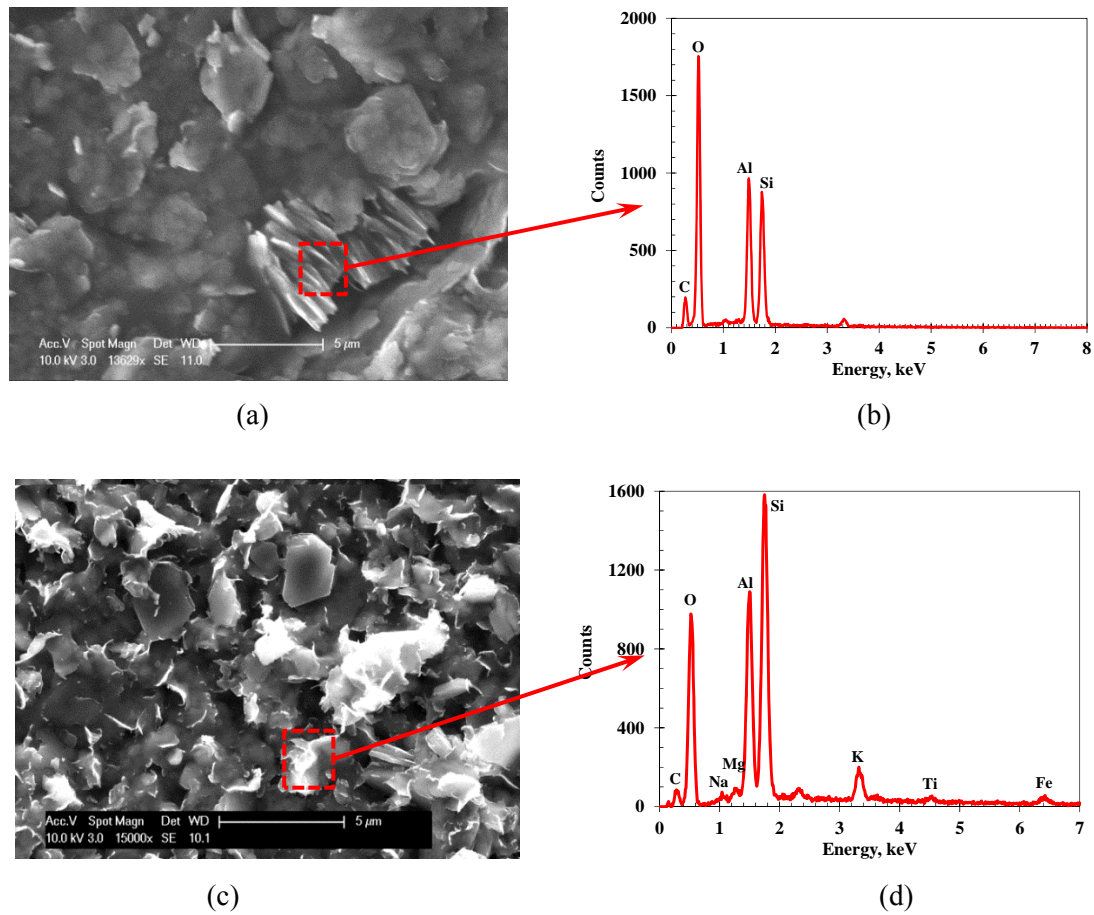


Fig. 4 SEM-EDAX results for the core sample: (a) SEM image for kaolinite; (b) EDAX spectra for kaolinite; (c) SEM image for illite/chlorite; and (d) EDAX spectra for illite/chlorite

2.3 Governing equations

Planning and design for injection and production in oil and gas reservoirs are supported by laboratory-based mathematical modelling. The classical filtration theory with particle detachment includes mass balance equation for suspended, attached and strained particles

$$\frac{\partial}{\partial t} [\phi c + \sigma_a + \sigma_s] + U \frac{\partial c}{\partial x} = 0 \quad (2.1)$$

where c , σ_a and σ_s stand for concentrations of suspended, attached and strained particles, respectively; ϕ is the porosity of the porous media, U is flow velocity of the carrier fluid which is equal to the particle speed, x and t represent distance and time, respectively.

2.3.1 Traditional kinetics model

The kinetics of simultaneous particles attachment and detachment is given by the relaxation equation (Bradford and Bettahar, 2005; Tufenkji, 2007; Bradford et al., 2012, 2013)

$$\frac{\partial \sigma_a}{\partial t} = \lambda_a c U - k_{\text{det}} \sigma_a \quad (2.2)$$

where λ_a is the filtration coefficient for attachment and k_{det} is the detachment coefficient (Tufenkji 2007; Bradford and Bettahar, 2005; Bradford et al., 2012).

The irreversible fines straining rate in narrow pore throats is expressed by the linear kinetics equation, in which the particle capture rate is proportional to the flux of suspended particles (Herzig et al, 1970; Bedrikovetsky, 2008; Yuan et al., 2011*a,b*; Yuan et al., 2012; Marquez et al., 2014)

$$\frac{\partial \sigma_s}{\partial t} = \lambda_s c U \quad (2.3)$$

where λ_s is the filtration coefficient for particle straining. Modified Darcy's law accounts for permeability decline due to both attachment and straining (Pang and Sharma, 1998; Bedrikovetsky et al., 2011) is expressed as

$$U = - \frac{k}{\mu(1 + \beta_s \sigma_s + \beta_a \sigma_a)} \frac{\partial p}{\partial x} \quad (2.4)$$

where k is the core permeability, p is the pressure, β_s and β_a are the formation damage coefficient of the strained and attached particles, respectively.

Fig. 1 illustrates the common assumption that the grain coating made of attached particles causes significantly lower permeability damage than straining: $\beta_s \gg \beta_a$, i.e. the combination of particle release and straining yields reduction in permeability. Therefore, the term accounting for permeability increase due to detachment in Eq. (2.4) is negligible, if compared with that of permeability decline due to straining.

Civan (2014, 2016) presents numerous generalisations for the governing equations (2.1-2.4) accounting for non-Newtonian behaviour of suspension fluxes, non-equilibrium for deep-bed filtration of high-concentration suspensions and colloids, particle bridging at thin pore throats, etc.

2.3.2 Mechanisms of fines detachment

The main assumption of the model for suspension transport in porous media with fines detachment is the introduction of a maximum (critical) retention function. This function relates the maximum value of the retained particle concentration with fluid salinity, flow velocity, pH, temperature..., i.e., $\sigma = \sigma_{cr}(U, \gamma, \text{pH}, T, \dots)$.

Two main forces contribute to the mobilisation of particles from pore surfaces in porous media, i.e., hydrodynamic and electrostatic forces (Khilar and Fogler, 1998). Flow rate is directly related to hydrodynamics. Salinity, pH, and temperature affect fines release through electrostatic force (Stuart, 1955; Aly and Esmail, 1993; Schembre et al., 2005, 2006a and 2006b; Leviton and Frey, 2006; Marshall, 2008; Leluk et al. 2010). The electrostatic forces are calculated using interaction energies between particles and surfaces. This indicates that the release of fines in porous media needs to be investigated at the interfacial scale.

2.3.2.1 Derjaguin–Landau–Verwey–Overbeek (DLVO) theory

At the interfacial scale, the Derjaguin–Landau–Verwey–Overbeek (DLVO) theory has been widely used to calculate the interaction energies between the particles and pore surfaces. The total energy between particles and surface is the sum of London-van der Waals, electrical double layer and born repulsive potentials (Derjaguin and Landau, 1941; Hogg et al., 1966; Gregory, 1981; Israelachvili, 1992; Elimelech et al., 1995; Hunter, 2001)

$$V = V_{LVA} + V_{DL} + V_{BR} \quad (2.5)$$

where V represents energy potential, the subscripts LVA , DL , and BR denote London-van der Waals, electrical double layer, and born repulsion, respectively.

The electrical attraction energy between two similar bodies is generally called London-van der Waals energy of interaction. This energy is the integration of all intermolecular interactions between polarised molecules, over a microscopic body. Several expressions for sphere-sphere and sphere-plate geometries have been summarised by Elimelech et al. (1995). According to the formula from Gregory (1981), the London-van der Waals potential is expressed as

$$V_{LW} = -\frac{A_{132}r_{s,wm}}{6h} \left[1 - \frac{5.32h}{\lambda} \ln \left(1 + \frac{\lambda}{5.32h} \right) \right] \quad (2.6)$$

where $r_{s,wm}$ is the weighted mean particles size; $\lambda = 100$ nm is the characteristic wavelength of interaction (Gregory, 1981); A_{132} is Hamaker constant for clay-water-sand system calculated using the equation presented by Israelachvili (2011)

$$A_{132} = \frac{3}{4} k_B T \left(\frac{\varepsilon_1 - \varepsilon_3}{\varepsilon_1 + \varepsilon_3} \right) \left(\frac{\varepsilon_2 - \varepsilon_3}{\varepsilon_2 + \varepsilon_3} \right) + \frac{3h\nu_e}{8\sqrt{2}} \frac{(n_1^2 - n_3^2)(n_2^2 - n_3^2)}{(n_1^2 + n_3^2)^{\frac{1}{2}}(n_2^2 + n_3^2)^{\frac{1}{2}} \left\{ (n_1^2 + n_3^2)^{\frac{1}{2}} + (n_2^2 + n_3^2)^{\frac{1}{2}} \right\}} \quad (2.7)$$

in which $k_B = 1.381 \times 10^{-23}$ J/K is Boltzmann constant; T is the absolute temperature of the system; $\varepsilon_1, \varepsilon_2$ and ε_3 are the static dielectric constants of clay, quartz and brine water respectively; n_1, n_2 and n_3 are the refractive indexes of clay, quartz and brine water respectively; the constant value of absorption frequency $\nu_e = 3.0 \times 10^{15}$ s⁻¹ is taken from Israelachvili (2011).

The electrical double layer repulsive energy between two similarly charged surfaces is a result of the overlap of diffuse double layer around charged bodies. The net charge on the particle surface affects the distribution of ions in the surrounding interfacial region. An "ion cloud" extends into solution around a charged surface effectively, "balancing" the surface charge over some distance away from the particle

(Fig. 5). The electric double layer (ion cloud) thickness around particles determines the minimum distance between two particles before repulsion.

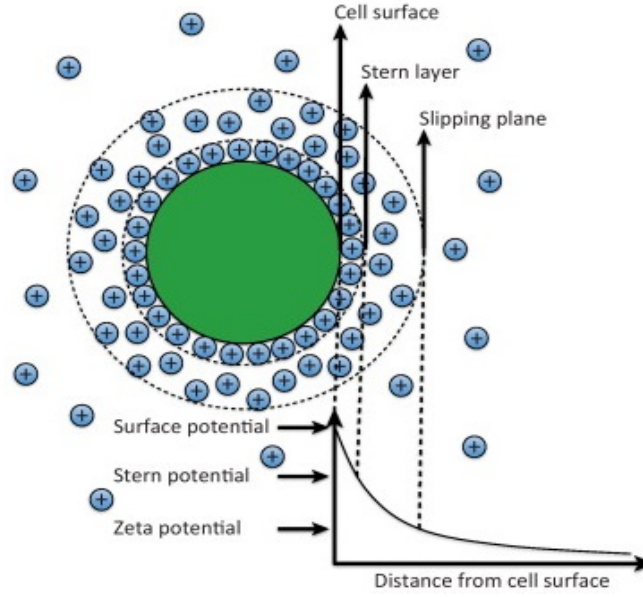


Fig. 5 The "Ion Cloud" around a particle (Vandamme et al., 2013)

Various expressions for Electrical Double layer energy have been presented in the literature (Elimelech et al., 1995). The expression of electrical double layer interaction between particles and surface of porous matrix is calculated according to Gregory (1975):

$$V_{EDL} = \frac{128\pi r_{s,wm} n_{\infty} k_B T}{\kappa^2} \gamma_s \gamma_b e^{-\kappa h} \quad (2.8)$$

where $\kappa = \sqrt{\frac{e^2 \sum n_{i0} z_i^2}{\epsilon_0 \epsilon_3 k_B T}}$ is the Debye-Hückel parameter (the so-called "inverse Debye length"); $e = 1.602 \times 10^{-19} C$ is the elementary electric charge; n_{i0} is the number concentration of ions "i" in bulk solution; z is the valence of a symmetrical electrolyte solution; $\epsilon_0 = 8.854 \times 10^{-12} F/m$ is the dielectric permittivity of vacuum; $n_{\infty} = 6.022 \times 10^{25} m^{-3}$ is the bulk number density of ions; $\gamma_s = \tanh\left(\frac{ze\zeta_s}{4k_B T}\right)$ and $\gamma_b = \tanh\left(\frac{ze\zeta_{pm}}{4k_B T}\right)$ are reduced zeta potentials for particles and porous matrix; ζ_s and ζ_{pm} are zeta potentials for particles and porous matrix.

The born repulsive potential is effective in short range, resulting from strong repulsive forces between atoms due to overlap of electron clouds as the particles approach the point of contact. This can be determined by the expression developed by Ruckenstein and Prieve (1976) for a sphere-plate system:

$$V_B = \frac{A_{132}\sigma_c^6}{7560} \left[\frac{8r_{s,wm}+h}{(2r_{s,wm}+h)^7} + \frac{6r_{s,wm}-h}{h^7} \right] \quad (2.9)$$

where $\sigma_c = 0.5$ nm is the collision diameter adopted from Elimelech et al. (1998).

Converting equations from potential energy to force is achieved by differentiating the equations for potential energy with respect to the distance between the particle and the pore surface (Fig. 6)

$$F = -\frac{dV}{dh} \quad (2.10)$$

where F is total electrostatic force, V is the total interaction energy, and h is the separation distance between the particle and rock surface.

Fig. 6 shows typical curves of potential energy and electrostatic force for both high and low salinities. Curves *I* in Figs. 6a and 6b represent the high salinity case, from which we can see deep primary minimum showing strong attraction. Curves *II* correspond to the low salinity case, showing the existence of secondary minimum and the presence of energy barrier between the primary and secondary minima. Elimelech et al. (1998) shows that a barrier height $20KT$ or more can hinder particles from moving towards the primary minimum, i.e., the particles reach equilibrium state at the secondary minimum.

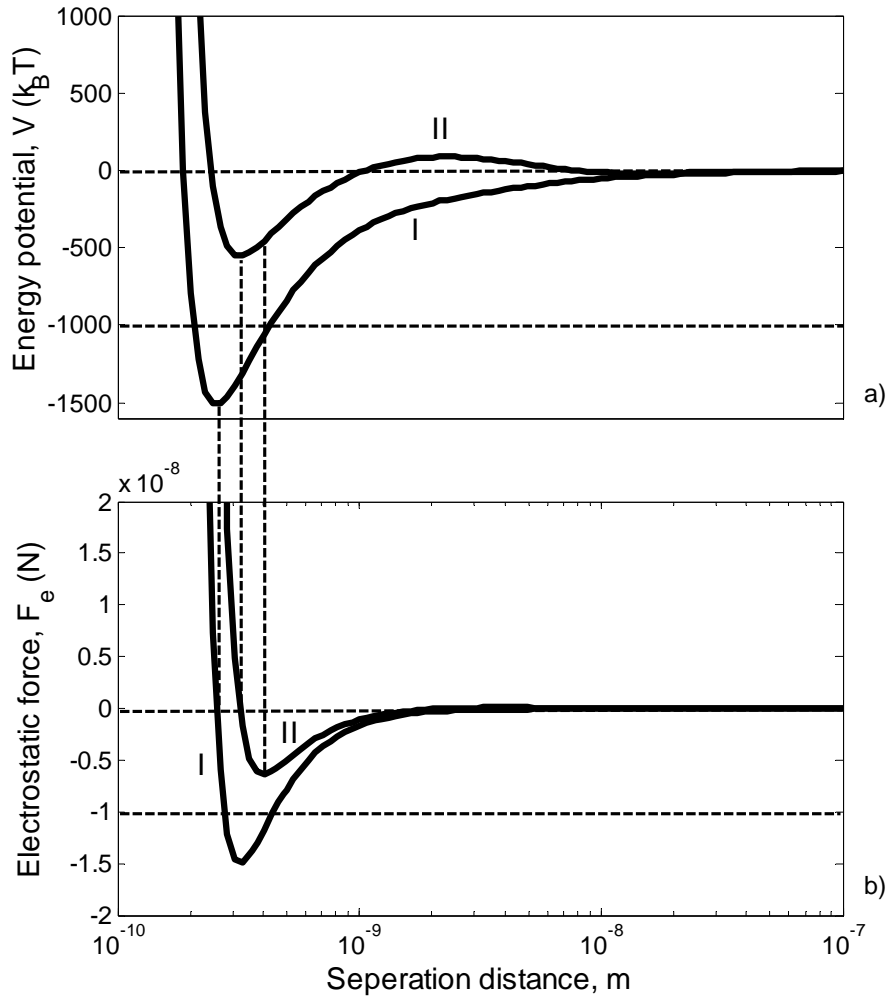


Fig. 6 Potential energy and electrostatic force calculated for the two tests by Ochi and Vernoux (1998): (a) potential energy; (b) electrostatic force

2.3.2.2 Hydrodynamic Forces

The hydrodynamic forces acting on fine particles from the fluid flow are responsible for the particles release. The total of lifting force (F_L), exerting on the particle perpendicular to the particle-grain interface, and the drag force (F_d), exerting on the particle tangent to the interface (Fig. 7), form the detaching hydrodynamic forces (Saffmann, 1965; O'Neill, 1968).

The drag force is given by the expression from the analytical solution of the Navier-Stokes equation for flow around a finite size particle on the plane (O'Neill, 1968; Altmann and Ripperger, 1997; Bergendahl and Grasso, 2003):

$$F_d = \frac{\omega \pi \mu r_s^2 u_p(r_p)}{(r_p - h_c)} \quad (2.11)$$

where μ is the viscosity of fluid, r_s is the particle radius, r_p is the pore radius, h_c is cake thickness on the pore wall, u_p is the average velocity and $\omega = 24 \times 1.7$ is the drag force coefficient.

The lifting force exerting on a particle suspended in fluid is given by:

$$F_L = \chi r_s^3 \sqrt{\frac{\rho \mu u^3}{H^3}} \quad (2.12)$$

where the lifting coefficient $\chi=89.5$ was reported by Kang et al. (2004), while Altmann and Ripperger (1997) provided a value of 1190. The expression of the lifting force on a small sphere contacting with a plane in a simple shear flow was obtained by Leighton and Acrivos (1985). All the above researchers derived their equations based on the pioneering works by Saffmann (1965, 1967).

2.3.2.3 Buoyancy force

Assuming the particle has ideal spherical shape, the buoyancy force is expressed as:

$$F_g = \frac{4}{3} r_s^3 \Delta \rho g \quad (2.13)$$

where $\Delta \rho$ is the difference of densities between the suspended particles and water.

2.3.2.4 Torques exerting on particles exposed to fluid flow

Fig. 7 shows the schematic of fines detachment from the grain surface, which causes the mobilisation and migration of reservoir fines (Das, et al., 1994). A fine particle attached on the grain surface is subject to the drag, electrostatic, lifting, and gravitational forces. Torque balance of detaching and attaching forces exerting on the particle can be expressed as

$$F_d(U, r_{scr}) l(r_{scr}) = F_e(r_{scr}) - F_L(U, r_{scr}) + F_g(r_{scr}), \quad l = l_d / l_n \quad (2.14)$$

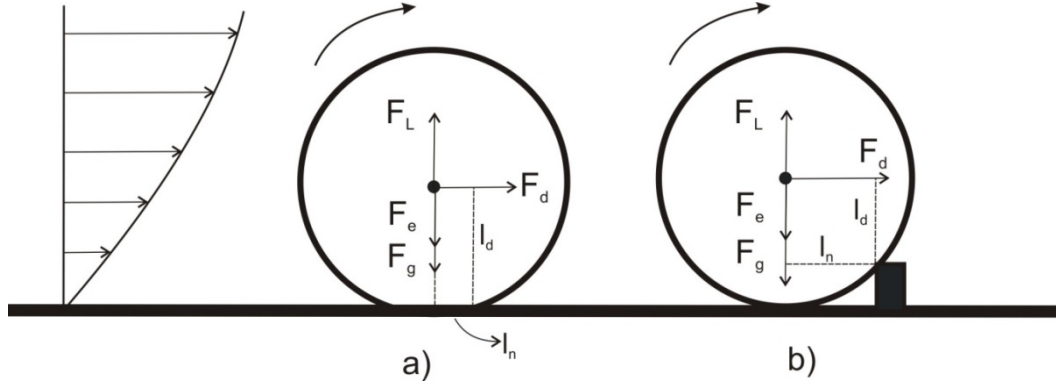


Fig. 7 Distribution of different-sized particles in a mono-layer on the grain surface, and forces acting on the particles; the torque balance on a fine particle attached to the pore wall: (a) normal lever l_n is the radius of the contact deformation area; (b) the asperity height determines the normal lever

Consider the deformation of elastic particles by the normal force (Fig. 7a), which equals the total of electrostatic, lifting, and gravitational forces. The right side of Eq. (2.14) is an expression for the normal force. Assume the particle rotates around a point of the contact area at the moment of mobilisation; the rotation touching point is located on the contact-area boundary. Following Derjaguin et al. (1975), Schechter (1992), Das et al. (1994), Freitas and Sharma (2001), and Bradford et al. (2013), the lever arm of the normal force l_n is assumed to be equal to the radius of the contact area of deformation by the normal force. It can be calculated from Hertz's theory as:

$$l_n^3 = \frac{F_n r_s}{4K} \quad K \equiv \frac{4}{3 \left(\frac{1-\nu_1^2}{E_1} + \frac{1-\nu_2^2}{E_2} \right)}. \quad (2.15)$$

where K is the composite Young's modulus, which depends on Poisson's ratio ν and Young's modulus E of the particle and of the surface (Prasad et al., 2002; Gercek, 2007), and the indices 1 and 2 refer to the particle and solid matrix surface, respectively. The lever arm of the drag force l_d can be calculated from the geometrical relation between particle radius r_s and l_n as $l_d = \sqrt{r_s^2 - l_n^2}$.

Another particle mobilisation scheme corresponds to the particle that rotates around the contacting asperity of the grain surface (Fig. 7*b*). In this case, the particle size and the asperity size determine the lever arm for the normal force l_n .

In this thesis, the first scheme accounting for rigid rock surface and particle deformation is adopted to study the fine particle detachment in porous media.

2.3.3 The maximum retention function

In order to be attached on a pore surface, a particle must be in stable equilibrium, where the net force on the particle is zero and it is at its lowest energy potential. Two such points exist for the system under consideration, corresponding to the secondary and primary energy minima, respectively (Fig. 6). Particles with sufficient kinetic energy can overcome the energy barrier, shown as Curves *II* in Fig. 6*a*. Afterwards, these particles are eventually constrained at the primary energy minimum; while the remaining particles deposit in the secondary energy minimum (Tufenkji and Elimelech, 2005; Li et al., 2006).

To remobilise a particle from the surface, the applied hydrodynamic torque acting on the single particle must overcome the torque of the total attaching forces (Elimelech et al., 1995; Khilar and Fogler, 1998; Bradford et al., 2011; Israelachvili, 2011; Yuan and Shapiro, 2011*a*). Once the latter happens, the particles are released instantly from the surface.

One obvious shortcoming of the attachment–detachment model accounting for particle detachment kinetics (2.1-2.4) is that, the retention concentration and permeability stabilise asymptotically when time tends to infinity; while the fines mobilisation after sharp increase of flow rate occurs almost instantly (Jaiswal et al., 2011). A prompt permeability response is observed during the coreflood tests with abrupt rate rise (Khilar and Fogler, 1998; Ochi and Vernoux, 1998). Thus, the

classical model including the kinetic detachment equation cannot characterise the mechanical equilibrium of particles, since the detachment term is not affected by the equilibrium state of a single particle.

The maximum retention concentration is a function of dimensionless ratio between the drag and normal forces, which is a phenomenological function of the porous medium and particles. The particle mobilisation, governed by this function, is determined by the torques exerting on the particles at rock surface. Therefore, the particle detachment kinetics in the classical attachment–detachment model (2.1-2.4) is substituted by this function, accounting for the particle mechanical equilibrium. Assuming constant porosity, and filtration and formation damage coefficients, the one-dimensional (1d) problem of deep bed filtration with limited particle retention, characterised by the net torque exerting on particles, allows for an analytical solution.

Till now, we have developed two models for the maximum retention concentration. One is derived under the assumption of multi-layer internal cake formed by mono-sized particles. The other corresponds to mono-layer particles with a size distribution. The details of these two models are reviewed below.

2.3.3.1 Multi-layer-mono-size-particle formed internal cake model of maximum retention concentration

This section presents formulae for the electrostatic, drag, lift, and gravitational forces related to particle equilibrium; then it derives equation for the maximum retention function for multi-layer mono-sized particles in cylindrical pores. At some moment, the particle is released by the drag and lifting forces from the cake surface. Consider an infinitesimal moment before the release-time. Fig. 8 exhibits the particle “rotation” around the tangent point with the neighbouring particle. The distance h between the particle and the cake increases from the minimum value to a certain value

where the particle- particle interaction is negligible, during the rotation. The particle dislodging occurs. The drag force torque must exceed the maximum torque of the normal force for the particle dislodging. The mechanical equilibrium of particle on the rock (grain, internal cake) surface involves the maximum value of electrostatic force. Therefore, the maximum value of electrostatic force must be taken for F_e -value in the mechanical equilibrium condition (2.14) (Fig. 6).

Usually it is assumed that the lever arms for drag and normal forces have the same order of magnitude. Their ratio is equal to $\sqrt{3}$ for regular arrangement of mono-sized particles in two-dimensions (Fig. 8). However, Kalantariasl et al. (2014) shows that, for solid particles, lever arm for drag force is almost equal to the particle radius, while the lever arm for normal forces is 100-700 times smaller than the particle radius.

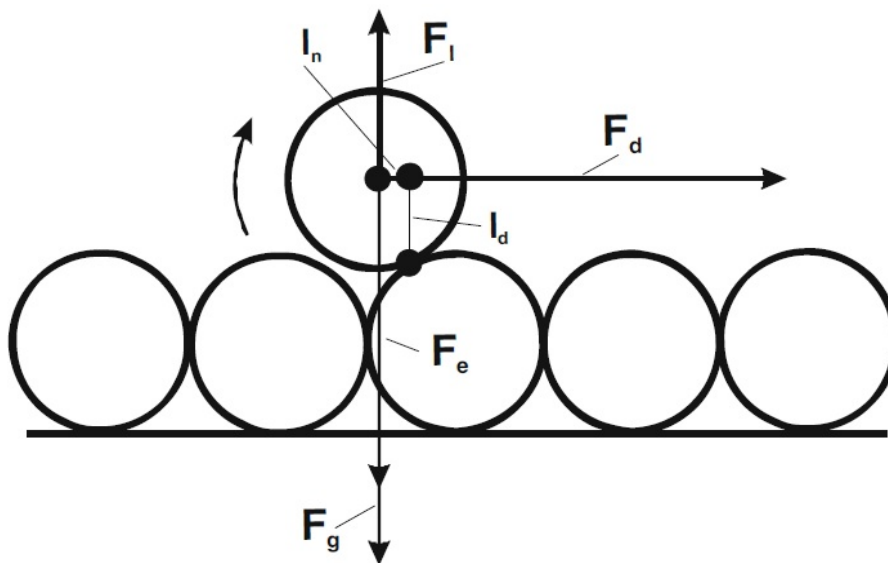


Fig. 8 Torques on the particles attached on the internal cake surface

A dimensionless parameter, particle erosion number, is defined as the ratio between the drag and normal forces. The drag force is given by Eq. (2.11), where r_s is an effective size of a particle with irregular shape. Substituting the relation between

the Darcy and interstitial velocities, and the estimate of the pore opening size H (Lake, 1989)

$$u = \frac{U}{\phi}, \quad H \approx \sqrt{k/\phi} \quad (2.16)$$

into (2.11), one obtains the dimensionless ratio between the drag and normal forces as

$$\varepsilon_p = \frac{\mu r_s^2 U}{\sqrt{k\phi} F_n} \approx \frac{F_d}{F_n} \quad (2.17)$$

During particle deposition process, the permeability is a function of deposited particle concentration on the surface (Pang and Sharma, 1997; Bedrikovetsky et al., 2011)

$$U = -\frac{k(\sigma_a)}{\mu} \frac{\partial p}{\partial x}, \quad k(\sigma_a) = k_0 k_r(\sigma_a) = k_0 (1 + \beta \sigma_a)^{-1} \quad (2.18)$$

which accounts for permeability damage effect caused by particle retention. The formula (2.17) becomes

$$\varepsilon_p = \frac{\mu r_s^2 U}{\sqrt{k_0 k_r(\sigma_a) \phi} F_n} \quad (2.19)$$

According to the torque balance equation (2.14), the dependences of the drag and lifting forces on velocity (2.11-2.12) and the dependences of the electrostatic force on salinity, pH and temperature indicate that, for each fluid condition, there exists a maximum retained concentration which relates to the equilibrium of torques exerting on particles. The maximum retention concentration can be expressed as a function of the ratio between the drag and normal forces (electrostatic force in particular, if the buoyancy force and lifting force are neglected) $\sigma_a = f(\varepsilon_p)$, i.e.

$$\sigma_a = f\left(\frac{\mu r_s^2 U}{\sqrt{k_0 k_r(\sigma_a) \phi} F_n}\right) \quad (2.20)$$

Eq. (2.20) contains the variable σ_a on both sides. This is a transcendental equation with respect to the unknown σ_a , for an arbitrary form of the functions $f(\varepsilon_p)$ and $k_r(\sigma_a)$. Expressing the maximum retention concentration $\sigma_a = \sigma_{cr}$ from Eq. (2.20) yields

$$\sigma_a = f\left(\frac{\mu r_s^2 U}{\sqrt{k_0 \phi F_n}}\right), \quad \varepsilon_p = \frac{\mu r_s^2 U}{\sqrt{k_0 \phi F_n}} \quad (2.21)$$

Finally, the maximum retention concentration is expressed as a function of the particle erosion number ε_p :

$$\sigma_a = f(\varepsilon_p), \quad \varepsilon_p = \frac{\mu r_s^2 U}{\sqrt{k_0 \phi F_n}}. \quad (2.22)$$

Fig. 9 illustrates the maximum retention concentration versus flow rate, calculated using the above model. The higher the velocity U , the higher the numerator in (2.22) for the erosion number ε_p , the higher the lifting force, and the lower the denominator in (2.22). Thus, the erosion number ε_p increases with the velocity U monotonically. The higher is U , the higher is the sum of drag and lifting forces in (2.14) and, consequently, the lower is the maximum retention concentration σ_{cr} . Hence, the maximum retention concentration decreases with the erosion number ε_p monotonically. The dependency (2.22) is named the maximum retention function.

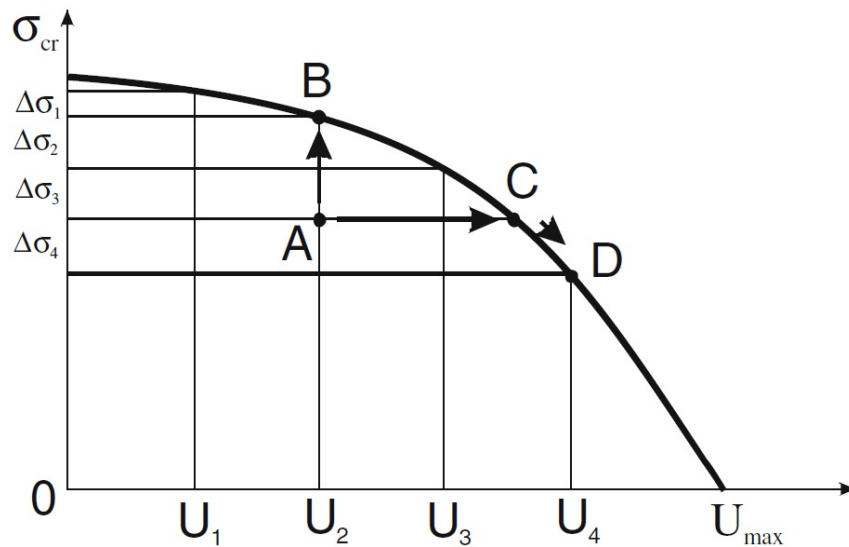


Fig. 9 The critical retention concentration calculated at variant flow rate, based on the multi-layer-mono-sized-particle model (Bedrikovetsky et al., 2011a)

In Fig. 9, point *A* below the maximum retention curve represents the state in a certain reservoir location. The state is “under-saturated”, i.e., the attaching torque of electrostatic and gravity forces exceeds the detaching torque of drag and lifting forces. If some suspended particles move along with constant velocity, the capture of these particles will occur at this location. Under constant injection rate, the gradual particle attachment leads to an increase of the interstitial flow velocity, and an increase of the drag and lifting forces as a result. The process of particle retention corresponds to the upward movement along the straight line from point *A* to *B* and stops until the “saturated” state point *B*.

The shift along the interval *AC* in Fig. 9 from *A* to *C* corresponds to the gradual velocity increase without particle attachment. The increase of velocity results in the increase of hydrodynamic forces. The torque equilibrium of particles is satisfied at point *C*, where the corresponding velocity is called the “critical velocity” for mobilised fines (Miranda and Underdown, 1993; Khilar and Fogler, 1998). It refers to the minimum velocity resulting in the rock erosion by fines mobilisation. Further increase of flow velocity leads to the movement along the maximum retention curve from point *C* to *D*.

2.3.3.2 Mono-layer-multi-size-particle model of maximum retention concentration

All the forces in Eq. (2.14) for mechanical equilibrium of attached particles depend on the particle size. Besides, the drag and lifting forces depend on flow velocity. Consequently, Eq. (2.14) is a transcendental equation for r_s and determines the critical particle size as (You et al., 2016)

$$r_s = r_{scr}(U, \gamma, pH, T \dots) \quad (2.23)$$

The function r_{scr} monotonically decreases with U , pH and T , and increases with γ , i.e., particles are dislodged by drag force with increasing velocity, pH or T and decreasing ionic strength in the order of particle size reduction.

Fig. 10 presents the results of these calculations. The higher is temperature, the lower is electrostatic attraction. Thus, a particle is detached at lower velocity where the temperature increases; so the curve 3 is located below the curve 1. Salinity increase yields the increase of electrostatic force; therefore curve 2 is located above the curve 1. During temperature increase under constant velocity, the drag force detaches the particles in the order of their size decreasing, i.e. large particles are mobilised first.

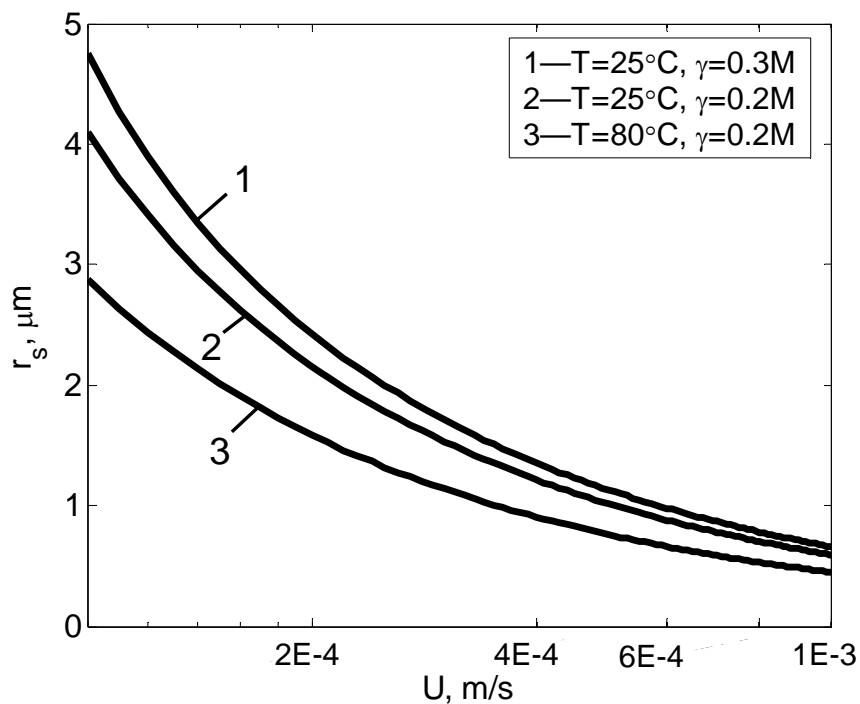
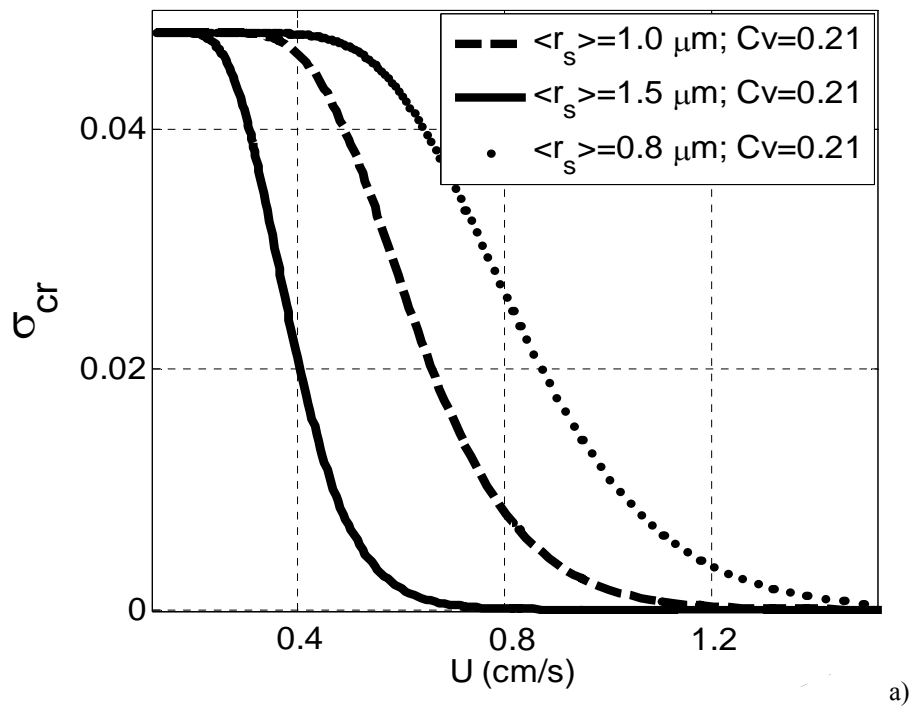


Fig. 10 The maximum retention function for mono-layer of size-distributed particles mobilised by the fluid flow with various velocities

Define the initial concentration distribution of attached particles with different sizes as $\Sigma_a(r_s)$. The larger particles are mobilised first and the smaller particles remain, determining the maximum retention function as:

$$\sigma_{cr}(U, \gamma) = \sigma_{a0} \int_0^{r_{scr}(U, \gamma)} \Sigma_a(r_s) dr_s \quad (2.24)$$

As shown in Fig. 11, the form of maximum retention function for the case of mono-layer fines is not convex. The calculated $\sigma_{cr}(U)$ -curves for three particle size distributions with the same variance coefficient support the above observation, that particle mobilisation during the fluid velocity increase occurs in the order of particle size decrease. The larger is a particle, the higher is the drag force and the less are the



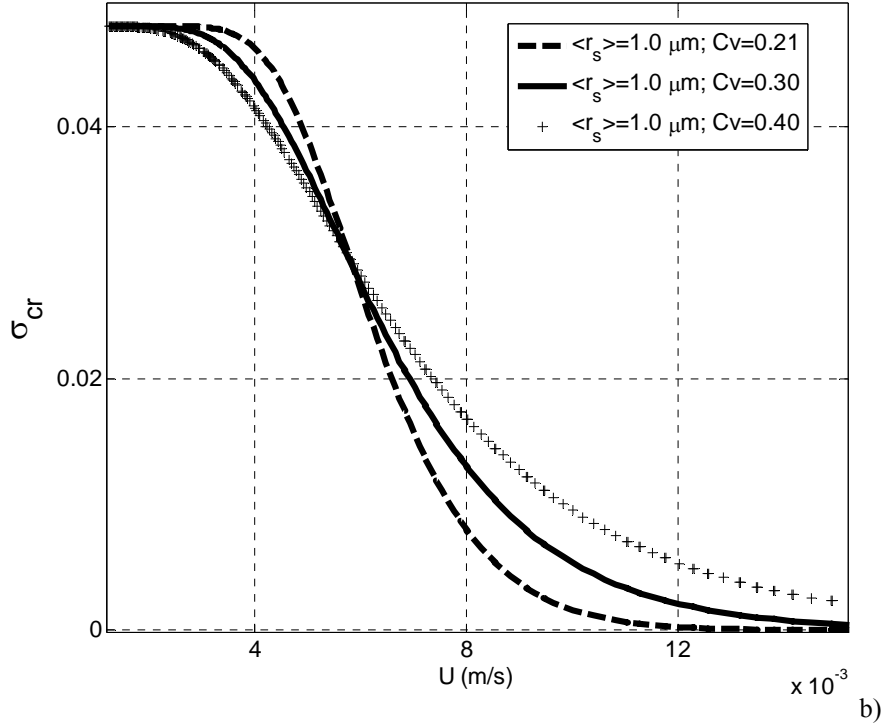


Fig. 11 The maximum retention function for the attached fines forming a mono-layer on the pore surface: (a) for log-normal size distributions with varying mean particle size; (b) for log-normal size distributions with varying variance coefficient

remained particles (Fig. 11a). Similar calculations for lognormal distributions with the same average particle size and different variance coefficients result in $\sigma_{cr}(U)$ -curves shown in Fig. 11b. The higher fraction of mobilised large particles corresponds to larger coefficient of variation C_v . For the low velocity range, $\sigma_{cr}(U)$ -curves for high values of standard deviation lie lower; whereas with the increase of fluid velocity $\sigma_{cr}(U)$ -curves shift to higher σ_{cr} -values. According to Eq. (2.14), $\sigma_{cr}(U)$ -curve has a step-shape for mono-sized particles ($C_v \rightarrow 0$), meaning that maximum retention function is a step-function. The wider is the attached particle size distribution, the wider is the transitional spread of the $\sigma_{cr}(U)$ -curves.

2.3.3.3 Using ionic strength sensitivity to characterise fines mobilisation system

Consider inflow performance in production wells. The well rate per unit of the reservoir depth is $q = 2\pi rU$. During production one observes two or more orders of

magnitude decrease of fluid velocity in the direction from well bore towards the drainage contour. The magnitude of this decrease is the function of the distance from the well. Variation of fluid viscosity with temperature affects detaching drag force which is a function of fluid velocity. Therefore, such rheological dependence of σ_{cr} should be studied in a wide range of fluid velocities. Having studied this relationship, one can reliably estimate well productivity index. However, the maximum available capacity of commercially available pumps limits the above studies at high fluid velocity variations.

Coreflood with lower ionic strength fluid also leads to particle mobilisation. Therefore, it is much easier to run such tests with significant variation of fluid ionic strength in the laboratory. The torque balance equation (2.14) has the following two solutions: $\sigma_{cr} = \sigma_{cr}(\gamma)$ and $\sigma_{cr} = \sigma_{cr}(U)$. Since $\sigma_{cr}(\gamma_0) = \sigma_{cr}(U_0)$, we obtain the following translation formula:

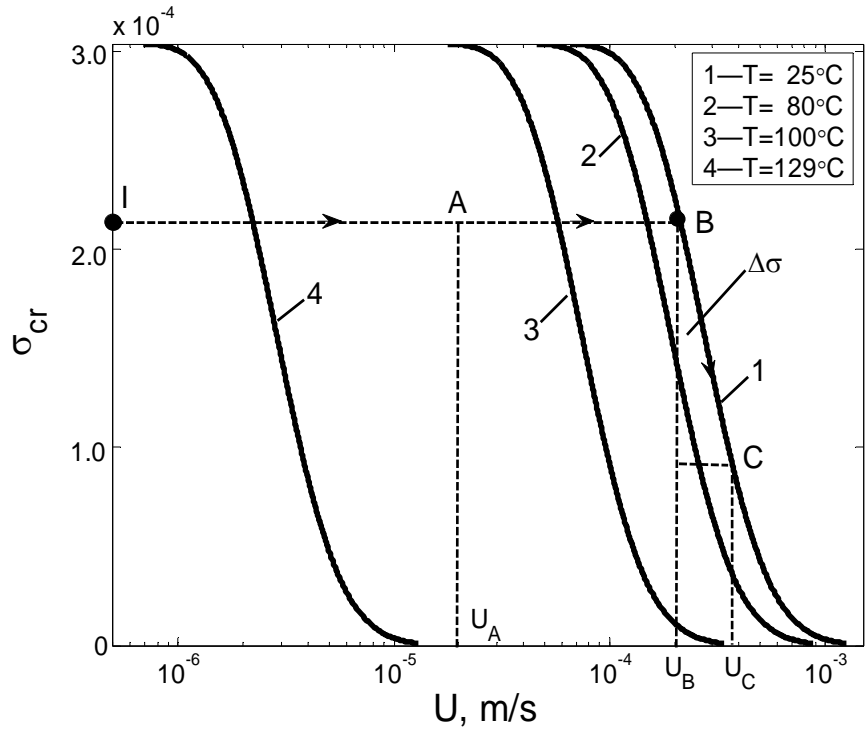
$$\sigma_{cr}(U, \gamma_0) = \sigma_{cr}(U_0, \gamma). \quad (2.25)$$

This formula translates $\sigma_{cr} = \sigma_{cr}(\gamma)$ to $\sigma_{cr} = \sigma_{cr}(U)$ and vice versa.

Below we describe such translation for a monolayer of multi-sized particles attached to the wall of pores. After running of coreflood tests with varying fluid ionic strength, one obtains $\sigma_{cr}(U_0, \gamma)$ relationship. Equation (2.23) determines critical particle radius as $r_{scr}(U, \gamma)$. It is possible to calculate $r_{scr}(U_0, \gamma) = r_{scr}(U, \gamma_0)$, corresponding to each value of γ , and corresponding velocity for fixed ionic strength γ_0 . Therefore, the relationship $\sigma_{cr}(U_0, \gamma)$ obtained experimentally can be re-calculated into $\sigma_{cr}(U, \gamma_0)$ relationship.

Fig. 12 shows an example of translation of the maximum retention function between the velocity effect and the salinity effect based on the transition principle

above. Curve 1 in Fig. 12b corresponds to $\sigma_{cr}(U_0, \gamma)$ at constant fluid velocity and ambient temperature. The translation curve 1 in Fig. 12a represents $\sigma_{cr}(U, \gamma_0)$ at constant fluid ionic strength and ambient temperature.



a)

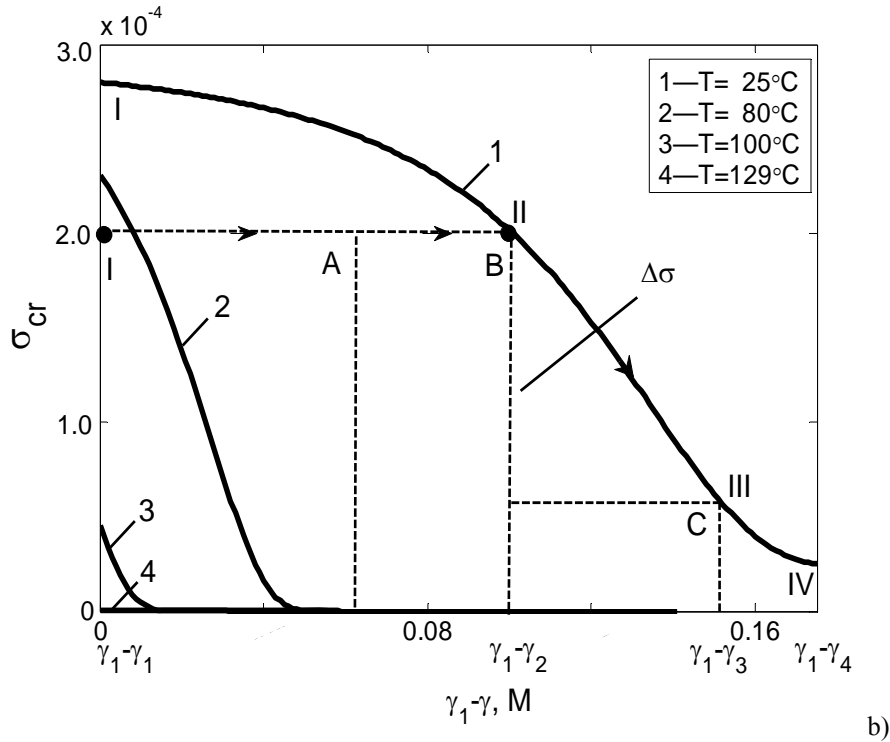


Fig. 12 Temperature- and salinity-dependence of maximum retention function: (a) maximum retention concentration vs velocity at different temperatures; (b) ionic strength dependency of maximum retention concentration ($\gamma_0 = 0.2 \text{ M NaCl}$) at different temperatures

2.3.4 Release delay effect of attached particles

The interaction between the ionic diffusion and thin film hydrodynamics has been observed in many field applications, e.g., wettability alteration or fines mobilisation by reduction of the ionic strength. These are the emerging technology in petroleum, mining and environmental industries, referred to as “low-salinity waterflooding” (LSF), which can improve the sweep efficiency. To our understanding, the LSF alters the wettability by decreasing the ionic strength and increasing the disjoining pressure (Mahani et al., 2015a,b). Experimental observations (Fig. 1 in Mahani et al., 2015a) indicate that replacing the electrolyte of a high ionic strength with that of a low ionic strength yields significant alteration of the rock wettability. Consequently, the grain surface turns to more hydrophilic, and thus, oil droplets may be detached from the solid surface. This phenomenon does not happen without ionic diffusion in thin films.

Mahani et al. (2015*a, b*) observed significant delay between salinity alternation and the corresponding contact angle change. It is attributed to saline water diffusion from the contact area between the deformed particle and rock surface. The so-called Nernst-Planck diffusion in thin slot between two plates under the molecular-force action is significantly slower than the Brownian diffusion, so the delay can be significant. The diffusive delay in particle mobilisation due to water salinity decrease can serve as another explanation for long stabilisation period. Yet, mathematical model that accounts for the delay effect in particle mobilisation is not available in the literature.

2.4 Analytical solutions for constant filtration and formation damage coefficient

The exact solution of the classical fines migration model (2.1-2.4) shows complete stabilisation of pressure drop after injection of one PV, while many laboratory observations report the stabilisation after 10-1000 *PVIs*. Therefore, the classical model for colloidal suspension flow in rocks allows good matching of the stabilised permeability but fails to predict the long stabilisation period.

In Keshavarz et al. (2014) and You et al. (2016), the long stabilisation times for permeability were explained by slow motion of mobilised particles on rock surface. Modification of the classical governing system consists of the substitution of the water flow velocity U in Eqs. (2.1-2.3) by the particle velocity $U_s < U$. The ratio of U_s and U is defined as drift delay factor α . Another important modification in the governing system is the introduction of the maximum retention function with delay, which corresponds to the Nernst-Planck diffusion (Mahani et al., 2015*a*) from the grain-particle contact area into the bulk of the fluid. The form of maximum retention function for mono-layer fines with a size distribution allows interpreting its non-

convex shape. The obtained system with slow fines migration and delayed maximum retention function allows for exact solutions for the cases of piecewise-constant velocity/pH/temperature increase or salinity decrease.

The analytical solution of the governing equation system (2.1-2.4) can be obtained by the method of characteristics (Bedrikovetsky, 1993). Fig. 13 illustrates the schematic of analytical solution to the slow fines migration model.

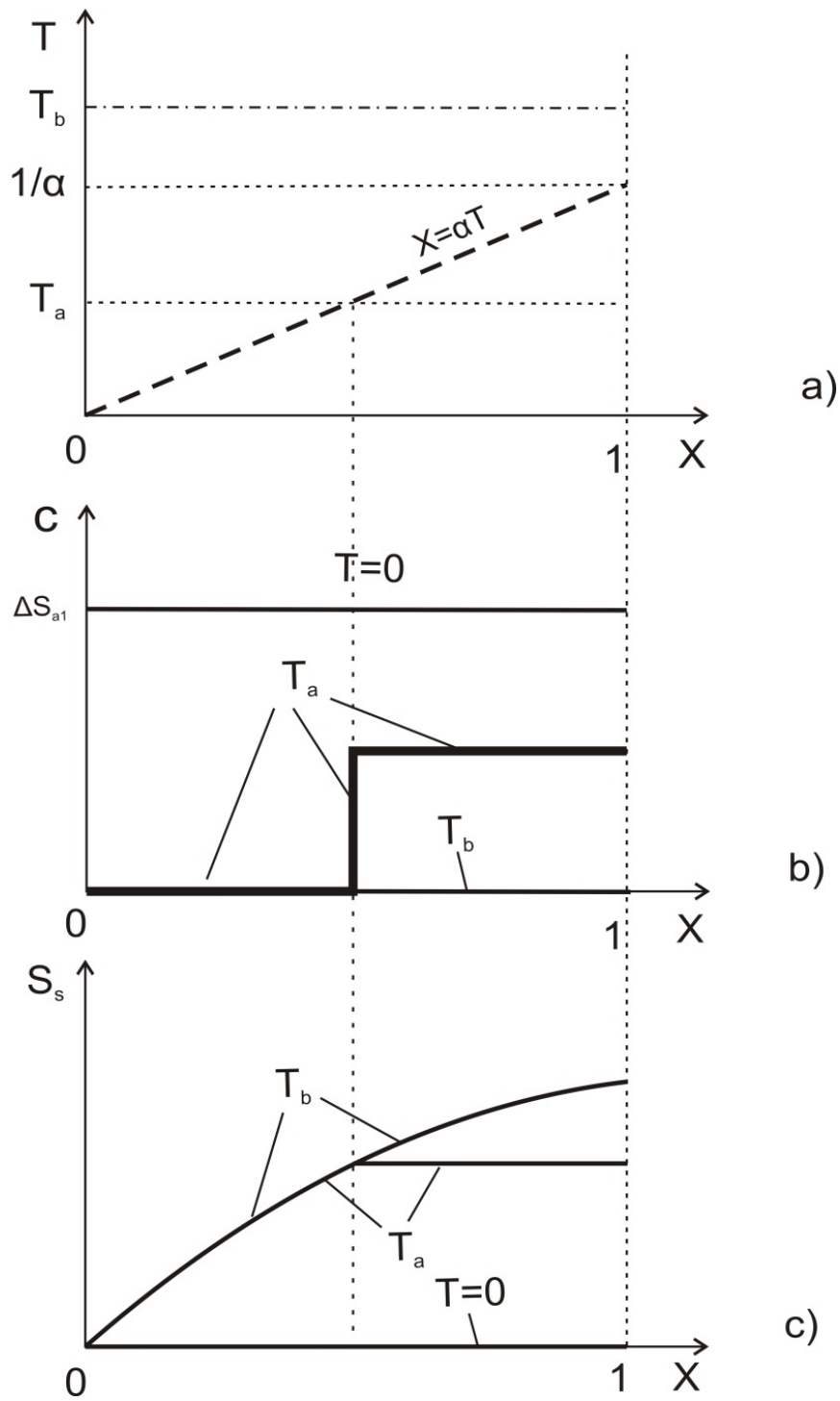


Fig. 13 Schematic for the analytical solution of 1d fines migration under piecewise-constant increasing velocity at times before and after the breakthrough (moments T_a and T_b , respectively): (a) trajectory of concentration fronts and characteristic lines in (X, T) -plane; (b) suspended concentration profiles at three moments $T=0$, T_a and T_b ; (c) strained concentration profiles at three moments

As shown in Fig. 13a, the concentration front of the injected clean fluid moves along the path $X = \alpha T$, where X and T stand for dimensionless distance and time, respectively. Behind the concentration front, particle concentration equals zero. The “last” mobilised particle arrives at the effluent at the moment $T = l/\alpha$. The mobilised particles have uniform concentration; they move with the same velocity under the condition that they have the same probability to be captured by smaller vacant pore throats. Therefore, the profile of suspended particle concentration is uniform during fluid flow, and concentration of suspension in zone I is independent of X (see the second line in Table 1). This leads to the conclusion that the concentration of particles strained in thin pores is independent of X ahead of the concentration front. Particle straining occurs for non-zero concentration of suspended particles. Therefore, the strained particles accumulate at a reservoir point X until the arrival of concentration front at this point; afterwards, the concentration of suspended particles remains unchanged. Therefore, the concentration of strained particles behind the concentration front keeps intact.

The profiles of suspended particle concentration at the moments $T = 0$, T_a (before the arrival of concentration front at the outlet of the core) and T_b (after the arrival of concentration front) are shown in Fig. 13b. We denote ΔS_{a1} as the initial concentration of the released particles. The profile of the concentration of suspended particles equals zero behind the concentration front, and is constant in front of this front. After the front arrival, the breakthrough concentration of suspended particles is zero due to the fact that all mobilised particles are either strained in narrow pore throats or transported to the core outlet.

Three profiles of strained particle concentration at the moments 0, T_a and T_b are shown in Fig. 13c. No strained particles are present in the media before the particle

mobilisation. The concentration of strained particles continues to grow until the moment of the front arrival and remains unchanged later. The duration of the particle straining process during the flow becomes longer, and the maximum value of accumulated strained particles grows with X . Hence, the profiles of strained particle concentration grow as X increases. The probability of particle capture ahead of the front remains constant. Thus, the strained profile is uniform, because the particle advective flux is uniform.

Fig. 14 illustrates the schematic of analytical solution to the combined model considering both slow fines migration and delayed particle release. Compared to the previous solution accounting for slow fines migration only (illustrated in Fig. 13), the current solution results in non-zero suspended concentration behind the front. Consequently, the retained concentration is not constant behind the front, due to continuous release of particles.

Tables 1, 2 and 3 list the main formulae of analytical solutions for the slow fines migration model and the combined models accounting for both slow fines migration and delayed particle release. In these tables, C , S_s , A and τ stand for the dimensionless suspended concentration, strained concentration, filtration coefficient and release delay time, respectively, and J denotes the impedance.

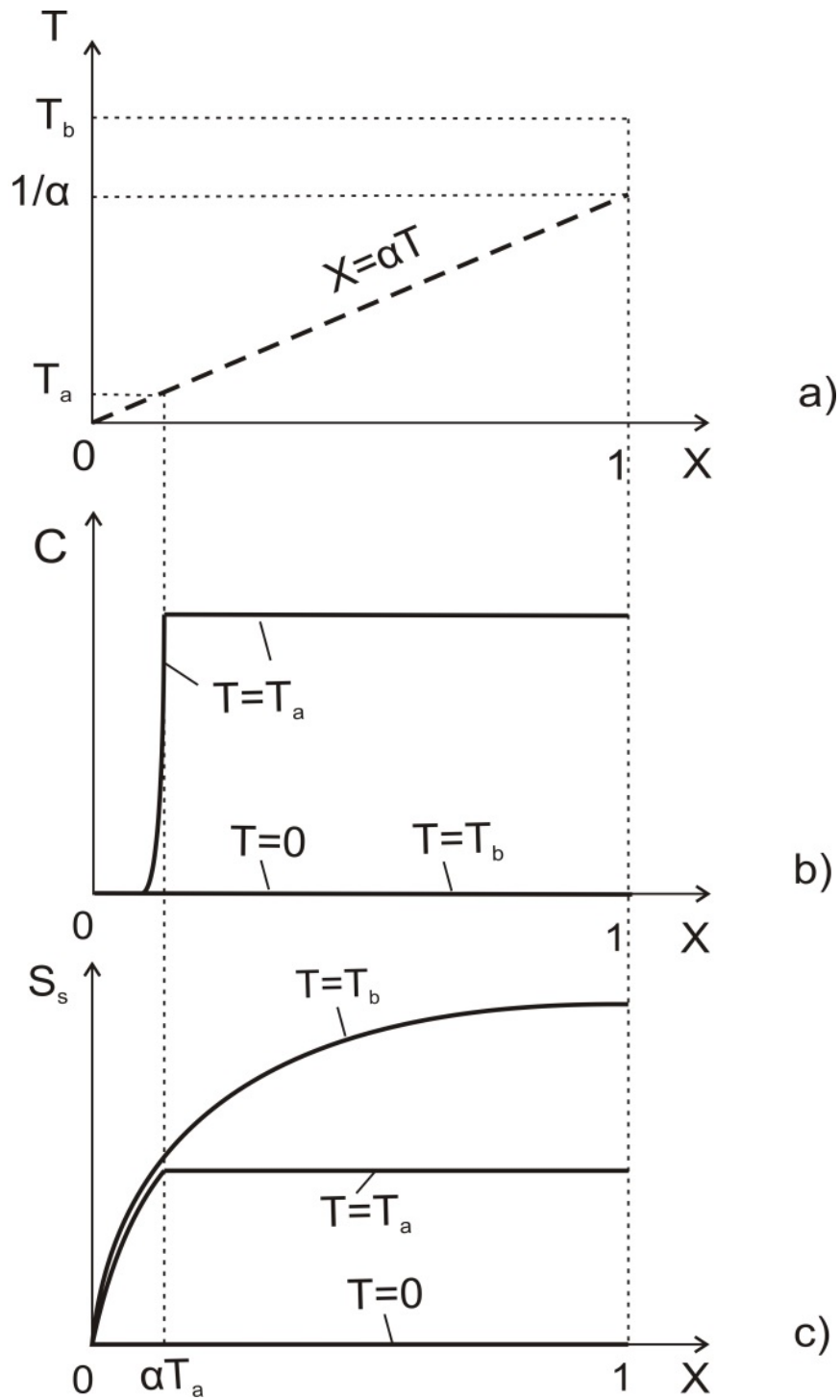


Fig. 14 Analytical slow-fines delay-release model: (a) trajectory of concentration fronts and characteristic lines in (X, T) plane; (b) suspended concentration profiles at three moments; (c) strained concentration profiles at three moments

Table 1 Analytical solution for the slow fines migration model

Term	Explicit formulae for 1d solution	(X,T) -domain
Suspension concentration during stage 1	$C = 0$	$X \leq \alpha_1 T$
	$C = \Delta S_{a1} e^{-\alpha_1 \Lambda_s T}$	$X > \alpha_1 T$
Retention concentration during stage 1	$S_s = \Delta S_{a1} (1 - e^{-\Lambda_s X})$	$X \leq \alpha_1 T$
	$S_s = \Delta S_{a1} (1 - e^{-\alpha_1 \Lambda_s T})$	$X > \alpha_1 T$
Impedance during stage 1	$J(T) = 1 + \beta_s \sigma_{a0} \Delta S_{a1} \left[1 - \frac{1}{\Lambda_s} - \left(1 - \frac{1}{\Lambda_s} - \alpha_1 T \right) e^{-\alpha_1 \Lambda_s T} \right]$	$T < \alpha_1^{-1}$
	$J(T) = 1 + \beta_s \sigma_{a0} \Delta S_{a1} \left[1 - \frac{1}{\Lambda_s} - \frac{e^{-\Lambda_s}}{\Lambda_s} \right]$	$T \geq \alpha_1^{-1}$
Suspension concentration during stage n	$C = 0$	$X \leq \alpha_1 T$
	$C = \Delta S_{an} e^{-\alpha_n \Lambda_s (T - T_n)}$	$X > \alpha_1 T$
Retention concentration during stage n	$S_s - S_{sn} = \Delta S_{an} (1 - e^{-\Lambda_s X})$	$X < \alpha_n (T - T_n)$
	$S_s - S_{sn} = \Delta S_{an} [1 - e^{-\alpha_n \Lambda_s (T - T_n)}]$	$X \geq \alpha_n (T - T_n)$
Impedance during stage n	$J(T) = J_{0n} + \beta_s \sigma_{a0} \Delta S_{an} \left[1 - \frac{1}{\Lambda_s} - \left(1 - \frac{1}{\Lambda_s} - \alpha_1 (T - T_n) \right) e^{-\alpha_n \Lambda_s (T - T_n)} \right]$	$T < T_n + \alpha_1^{-1}$
	$J(T) = J_{0n} + \beta_s \sigma_{a0} \Delta S_{an} \left[1 - \frac{1}{\Lambda_s} - \frac{e^{-\Lambda_s}}{\Lambda_s} \right]$	$T \geq T_n + \alpha_1^{-1}$

Table 2 Analytical solution for the combined model ($\alpha \Lambda \tau \neq 1$)

Term	Notation	Zones	Expression
Suspended concentration	$C(X,T)$	$T \leq X/\alpha$	$\frac{y}{\alpha\Lambda - b} \left(e^{-bT} - e^{-\alpha\Lambda T} \right)$
		$T > X/\alpha$	$\frac{y}{\alpha\Lambda - b} e^{-bT} \left(1 - e^{\left(\frac{b}{\alpha} - \Lambda\right)X} \right)$
Strained concentration	$S_s(X,T)$	$T \leq X/\alpha$	$\alpha\Lambda \left[\frac{y}{\alpha\Lambda(\alpha\Lambda - b)} e^{-\alpha\Lambda T} - \frac{y}{b(\alpha\Lambda - b)} e^{-bT} \right] - \alpha\Lambda \left[\frac{y}{\alpha\Lambda(\alpha\Lambda - b)} - \frac{y}{b(\alpha\Lambda - b)} \right]$
		$T > X/\alpha$	$\alpha\Lambda \left[\frac{y}{\alpha\Lambda(\alpha\Lambda - b)} e^{-\alpha\Lambda X} - \frac{y}{b(\alpha\Lambda - b)} e^{-b\frac{X}{\alpha}} \right] - \alpha\Lambda \left[\frac{y}{\alpha\Lambda(\alpha\Lambda - b)} - \frac{y}{b(\alpha\Lambda - b)} \right] \dots$ $+ \alpha\Lambda \left[-\frac{y}{b(\alpha\Lambda - b)} \left(1 - e^{\left(\frac{b}{\alpha} - \Lambda\right)X} \right) e^{-bT} \right] + \alpha\Lambda \left[\frac{y}{b(\alpha\Lambda - b)} \left(1 - e^{\left(\frac{b}{\alpha} - \Lambda\right)X} \right) e^{-b\frac{X}{\alpha}} \right]$
Permeability	$k(t_D)$		$k_0 \left(1 + \frac{\beta\phi}{\omega} \int_0^\omega S_s(x_D, t_D) dx_D \right)^{-1}$

Table 3 Analytical solution for the combined model ($\alpha\Lambda\tau = 1$)

Term	Notation	Zones	Expression
Suspended concentration	$C(X,T)$	$T \leq X/\alpha$	yTe^{-bT}
		$T > X/\alpha$	$\frac{y}{\alpha} e^{-bT} X$
Strained concentration	$S_s(X,T)$	$T \leq X/\alpha$	$-ye^{-bT}T + \frac{y}{b}(1 - e^{-bT})$
		$T > X/\alpha$	$\frac{y}{b} \left(1 - e^{-b\frac{X}{\alpha}} \right) - \frac{y}{\alpha} Xe^{-bT}$
Permeability	$k(t_D)$		$k_0 \left(1 + \frac{\beta\phi}{\omega} \int_0^\omega S_s(x_D, t_D) dx_D \right)^{-1}$

2.5 Summary

The distinguishing features of the natural reservoir fines migration are mobilisation of the attached particles, their capture by straining in the rock and permeability decrease with consequent decline of well productivity and injectivity. Permeability decline during coreflooding with piecewise increasing velocity has been reported in many laboratory tests (Ochi and Vernoux, 1998, 1999). Similar effects occur during piecewise variation of water salinity or pH during coreflooding (Lever and Dawe, 1994). This phenomenon is attributed to the release of attached particles and their migration in large pores until size exclusion in narrow pore throats, finally resulting in significant permeability decline (Muecke, 1979, Sarkar and Sharma, 1990).

Numerous laboratory studies exhibit the stabilisation periods of 10-1000 *PVIs*. However, the classical model shows that the permeability stabilises after one *PVI*. Therefore, the classical model fails to predict the long term stabilisation. Up to date, there have been no comprehensive mathematical models describing the long-term permeability stabilisation available in the literature. It encourages me to derive new models and their analytical solutions for fines migration in porous media.

In this thesis, the long-term permeability stabilisation is explained by slow particle drift along the rock surface. The drift delay factor corresponding to the ratio of particle velocity and fluid velocity is introduced into the classical model. Meanwhile, the delay effect of particle release induced by ion diffusion from the grain-particle contact area into the bulk of the fluid under salinity alteration is also considered in the new model. The obtained system including the slow fines migration and delayed release effects allows for exact solutions for the cases of piecewise velocity/pH/temperature increase or salinity decrease. Good matches between the

experimental and modelling results validate the proposed model for slow motion of released fine particles in porous media.

2.6 References

- Altmann, J. and Ripperger, S., 1997. Particle deposition and layer formation at the crossflow microfiltration. *Journal of Membrane Science*, 124(1): 119-128.
- Aly, K.M. and Esmail, E., 1993. Refractive index of salt water: effect of temperature. *Optical Materials*, 2(3): 195-199.
- Arab, D., Pourafshary, P., Ayatollahi, S. and Habibi, A., 2014. Remediation of colloid-facilitated contaminant transport in saturated porous media treated by nanoparticles. *International Journal of Environmental Science and Technology*, 11(1): 207-216.
- Bai, T., Chen, Z., Aminossadati, S.M., Pan, Z., Liu, J. and Li, L., 2015. Characterization of coal fines generation: A micro-scale investigation. *Journal of Natural Gas Science and Engineering*, 27: 862-875.
- Barenblatt, G.I., Entov, V.M. and Ryzhik, V.M., 1989. *Theory of fluid flows through natural rocks*. Kluwer Academic Publishers, Dordrecht, The Netherlands.
- Bedrikovetsky, P., 1993. *Mathematical theory of oil & gas recovery (with applications to ex-USSR oil & gas condensate fields)*. Kluwer Academic Publishers, London, UK.
- Bedrikovetsky, P., 2008. Upscaling of stochastic micro model for suspension transport in porous media. *Transport in Porous Media*, 75: 335-369.
- Bedrikovetsky, P., Siqueira, F.D., Furtado, C.A. and Souza, A.L.S., 2011a. Modified particle detachment model for colloidal transport in porous media. *Transport in Porous Media*, 86(2): 353-383.
- Bedrikovetsky, P., Vaz, A.S., Furtado, C.J. and Serra de Souza, A.R., 2011b. Formation-damage evaluation from nonlinear skin growth during coreflooding. *SPE Reservoir Evaluation & Engineering*, 14(2): 193-203.
- Bedrikovetsky, P., Zeinijahromi, A., Siqueira, F.D., Furtado, C.A. and de Souza, A.L.S., 2012a. Particle detachment under velocity alternation during suspension transport in porous media. *Transport in Porous Media*, 91(1): 173-197.
- Bedrikovetsky, P., Vaz, A., Machado, F., Zeinijahromi, A. and Borazjani, S., 2012b. Skin due to fines mobilization, migration, and straining during steady-state oil production. *Petroleum Science and Technology*, 30(15): 1539-1547.
- Bergendahl, J.A. and Grasso, D., 2003. Mechanistic basis for particle detachment from granular media. *Environmental Science & Technology*, 37(10): 2317-2322.
- Bradford, S.A. and Bettahar, M., 2005. Straining, attachment, and detachment of oocysts in saturated porous media. *Journal of Environmental Quality*, 34(2): 469-478.
- Bradford, S.A., Torkzaban, S., Kim, H. and Simunek, J., 2012. Modeling colloid and microorganism transport and release with transients in solution ionic strength. *Water Resources Research*, 48(9): W09509.
- Bradford, S.A., Torkzaban, S. and Shapiro, A., 2013. A theoretical analysis of colloid attachment and straining in chemically heterogeneous porous media. *Langmuir*, 29(23): 6944-6952.
- Byrne, M.T. and Waggoner, S.M., 2009, January. Fines migration in a high temperature gas reservoir-laboratory simulation and implications for completion design. In 8th European Formation Damage Conference. Society of Petroleum Engineers.
- Byrne, M., Rojas, E., Kandasamy, R. and Gibb, A., 2014, February. Fines Migration in Oil and Gas Reservoirs: Quantification and Qualification Through Detailed Study. In SPE International Symposium and Exhibition on Formation Damage Control. Society of Petroleum Engineers.
- Civan, F., 2014. *Reservoir formation damage (3rd ed.)*. Gulf Professional Publishing, Burlington, MA, USA.

- Civan, F., 2016. Modified Formulations of particle deposition and removal kinetics in saturated porous media. *Transport in Porous Media*, 111:381-410.
- Das, S.K., Schechter, R.S. and Sharma, M.M., 1994. The role of surface roughness and contact deformation on the hydrodynamic detachment of particles from surfaces. *Journal of Colloid and Interface Science*, 164(1): 63-77.
- Derjaguin, B.V. and Landau, L., 1941. Theory of the stability of strongly charged lyophobic sols and of the adhesion of strongly charged particles in solutions of electrolytes. *Acta physicochim. URSS*, 14(6): 633-662.
- Derjaguin, B.V., Muller, V.M. and Toporov, Y.P., 1975. Effect of contact deformations on the adhesion of particles. *Journal of Colloid and Interface Science*, 53(2): 314-326.
- Elimelech, M., Gregory, J. and Jia, X., 2013. Particle deposition and aggregation: measurement, modelling and simulation. Butterworth-Heinemann, Oxford, UK.
- Fleming, N., Mathisen, A.M., Eriksen, S.H., Moldrheim, E. and Johansen, T.R., 2007, January. Productivity impairment due to kaolinite mobilization: laboratory & field experience, Oseberg Sor. In European Formation Damage Conference. Society of Petroleum Engineers.
- Fleming, N., Ramstad, K., Kidd, S. and Hoeth, L.W., 2010a. Impact of successive squeezes on treatment lifetime and well productivity: comparative assessment of viscosified and nonviscosified treatments. *SPE Production & Operations*, 25(1): 99-110.
- Fleming, N., Ramstad, K., Mathisen, A.M., Selle, O.M., Tjomsland, T. and Fadnes, F.H., 2010b. Squeeze related well productivity impairment mechanisms & preventative/remedial measures utilised. In SPE International Conference on Oilfield Scale. Society of Petroleum Engineers.
- Freitas, A.M. and Sharma, M.M., 2001. Detachment of particles from surfaces: an AFM study. *Journal of Colloid and Interface Science*, 233(1): 73-82.
- Gercek, H., 2007. Poisson's ratio values for rocks. *International Journal of Rock Mechanics and Mining Sciences*, 44(1): 1-13.
- Gregory, J., 1981. Approximate expressions for retarded van der Waals interaction. *Journal of Colloid and Interface Science*, 83(1): 138-145.
- Guo, Z., Hussain, F. and Cinar, Y., 2015. Permeability variation associated with fines production from anthracite coal during water injection. *International Journal of Coal Geology*, 147: 46-57.
- Han, G., Ling, K., Wu, H., Gao, F., Zhu, F. and Zhang, M., 2015. An experimental study of coal-fines migration in coalbed-methane production wells. *Journal of Natural Gas Science and Engineering*, 26: 1542-1548.
- Herzig, J.P., Leclerc, D.M. and Goff, P.L., 1970. Flow of suspensions through porous media—application to deep filtration. *Industrial & Engineering Chemistry* 62(5): 8-35.
- Hogg, R., Healy, T.W. and Fuerstenau, D.W., 1966. Mutual coagulation of colloidal dispersions. *Transactions of the Faraday Society*, 62: 1638-1651.
- Hunter, R.J., 2013. Zeta potential in colloid science: principles and applications (Vol. 2). Academic press.
- Israelachvili, J.N., 2011. Intermolecular and surface forces: revised third edition. Elsevier, Amsterdam, The Netherlands.
- Jaiswal, D.K., Kumar, A. and Yadav, R.R., 2011. Analytical solution to the one-dimensional advection-diffusion equation with temporally dependent coefficients. *Journal of Water Resource and Protection*, 3(1): 76.
- Kalantariasl, A. and Bedrikovetsky, P., 2014. Stabilization of external filter cake by colloidal forces in “well-reservoir” system. *Industrial and Engineering Chemistry Research*, 53: 930-944.
- Kang, S.T., Subramani, A., Hoek, E.M., Deshusses, M.A. and Matsumoto, M.R., 2004. Direct observation of biofouling in cross-flow microfiltration: mechanisms of deposition and release. *Journal of Membrane Science*, 244(1): 151-165.

- Keshavarz, A., Yang, Y., Badalyan, A., Johnson, R. and Bedrikovetsky, P., 2014. Laboratory-based mathematical modelling of graded proppant injection in CBM reservoirs. *International Journal of Coal Geology*, 136: 1-16.
- Kia, S.F., Fogler, H.S. and Reed, M.G., 1987. Effect of salt composition on clay release in Berea sandstones. In *SPE International Symposium on Oilfield Chemistry*. Society of Petroleum Engineers.
- Khilar, K.C. and Fogler, H.S., 1998. *Migrations of fines in porous media*. Kluwer Academic Publishers, Dordrecht, The Netherlands.
- Lake, L.W., 1989. *Enhanced oil recovery*. Prentice Hall, Old Tappan, NJ.
- Leighton, D. and Acrivos, A., 1985. The lift on a small sphere touching a plane in the presence of a simple shear flow. *Zeitschrift für angewandte Mathematik und Physik ZAMP*, 36(1): 174-178.
- Leluk, K., Orzechowski, K., Jerie, K., Baranowski, A., SŁonka, T. and GŁowiński, J., 2010. Dielectric permittivity of kaolinite heated to high temperatures. *Journal of Physics and Chemistry of Solids*, 71(5): 827-831.
- Lever, A. and Dawe, R.A., 1984. Water-sensitivity and migration of fines in the hopeman sandstone. *Journal of Petroleum Geology*, 7(1): 97-107.
- Leviton, D.B. and Frey, B.J., 2006. Temperature-dependent absolute refractive index measurements of synthetic fused silica. In *SPIE Astronomical Telescopes+ Instrumentation* (pp. 62732K-62732K). International Society for Optics and Photonics.
- Li, X., Lin, C.L., Miller, J.D. and Johnson, W.P., 2006. Role of grain-to-grain contacts on profiles of retained colloids in porous media in the presence of an energy barrier to deposition. *Environmental Science & Technology*, 40(12): 3769-3774.
- Mahani, H., Berg, S., Ilic, D., Bartels, W.B. and Joekar-Niasar, V., 2015a. Kinetics of low-salinity-flooding effect. *SPE Journal*, 20(1): 8-20.
- Mahani, H., Keya, A.L., Berg, S., Bartels, W.B., Nasralla, R. and Rossen, W.R., 2015b. Insights into the mechanism of wettability alteration by low-salinity flooding (LSF) in carbonates. *Energy & Fuels*, 29(3): 1352-1367.
- Marquez, M., Williams, W., Knobles, M.M., Bedrikovetsky, P. and You, Z., 2014. Fines Migration in Fractured Wells: Integrating Modeling With Field and Laboratory Data. *SPE Production & Operations*, 29(4): 309-322.
- Marshall, W.L., 2008. Dielectric constant of water discovered to be simple function of density over extreme ranges from -35 to +600° C and to 1200 MPa (12000 atm), believed universal. *Nature Prec.*
- Muecke, T.W., 1979. Formation fines and factors controlling their movement in porous media. *Journal of Petroleum Technology*, 31(2): 144-150.
- Miranda, R.M. and Underdown, D.R., 1993. Laboratory measurement of critical rate: a novel approach for quantifying fines migration problems. In *SPE Production Operations Symposium*. Society of Petroleum Engineers.
- Muecke, T.W., 1979. Formation fines and factors controlling their movement in porous media. *Journal of Petroleum Technology*, 31(2): 144-150.
- Ochi, J. and Vernoux, J.F., 1998. Permeability decrease in sandstone reservoirs by fluid injection: hydrodynamic and chemical effects. *Journal of hydrology*, 208(3): 237-248.
- Ochi, J. and Vernoux, J.F., 1999. A two-dimensional network model to simulate permeability decrease under hydrodynamic effect of particle release and capture. *Transport in porous media*, 37(3): 303-325.
- Oliveira, M.A., Vaz, A.S., Siqueira, F.D., Yang, Y., You, Z. and Bedrikovetsky, P., 2014. Slow migration of mobilised fines during flow in reservoir rocks: Laboratory study. *Journal of Petroleum Science and Engineering*, 122: 534-541.
- O'Neill, M.E., 1968. A sphere in contact with a plane wall in a slow linear shear flow. *Chemical Engineering Science*, 23(11): 1293-1298.
- Pang, S. and Sharma, M.M., 1997. A model for predicting injectivity decline in water-injection wells. *SPE Formation Evaluation*, 12(3): 194-201.

- Prasad, M., Kopycinska, M., Rabe, U. and Arnold, W., 2002. Measurement of Young's modulus of clay minerals using atomic force acoustic microscopy. *Geophysical Research Letters*, 29(8): 13-1-13-4.
- Ruckenstein, E. and Prieve, D.C., 1976. Adsorption and desorption of particles and their chromatographic separation. *AIChE Journal*, 22(2): 276-283.
- Saffman, P.G.T., 1965. The lift on a small sphere in a slow shear flow. *Journal of fluid mechanics*, 22(2): 385-400.
- Saffman, P.G.T., 1967. The self-propulsion of a deformable body in a perfect fluid. *Journal of fluid mechanics*, 28(2): 385-389.
- Sarkar, A.K. and Sharma, M.M., 1990. Fines migration in two-phase flow. *Journal of petroleum technology*, 42(5): 646-652.
- Schembre, J.M. and Kovscek, A.R., 2005. Mechanism of formation damage at elevated temperature. *Journal of Energy Resources Technology*, 127(3): 171-180.
- Schembre, J.M., Tang, G.Q. and Kovscek, A.R., 2006a. Wettability alteration and oil recovery by water imbibition at elevated temperatures. *Journal of Petroleum Science and Engineering*, 52(1): 131-148.
- Schembre, J.M., Tang, G.Q. and Kovscek, A.R., 2006b. Interrelationship of temperature and wettability on the relative permeability of heavy oil in diatomaceous rocks (includes associated discussion and reply). *SPE Reservoir Evaluation & Engineering*, 9(3): 239-250.
- Sefrioui, N., Ahmadi, A., Omari, A. and Bertin, H., 2013. Numerical simulation of retention and release of colloids in porous media at the pore scale. *Colloids and Surfaces A: Physicochemical and Engineering Aspects*, 427: 33-40.
- Schechter, R.S., 1992. *Oil well stimulation*. Prentice Hall, NJ, USA.
- Stuart, M.R., 1955. Dielectric constant of quartz as a function of frequency and temperature. *Journal of Applied Physics*, 26(12): 1399-1404.
- Suri, A. and Sharma, M.M., 2004. Strategies for sizing particles in drilling and completion fluids. *SPE Journal*, 9(1): 13-23.
- Tien, C., Bai, R. and Ramarao, B.V., 1997. Analysis of cake growth in cake filtration: Effect of fine particle retention. *AIChE Journal*, 43(1): 33-44.
- Tufenkji, N. and Elimelech, M., 2005. Breakdown of colloid filtration theory: Role of the secondary energy minimum and surface charge heterogeneities. *Langmuir*, 21(3): 841-852.
- Tufenkji, N., 2007. Colloid and microbe migration in granular environments: a discussion of modelling methods. In *Colloidal Transport in Porous Media* (pp. 119-142). Springer, Berlin, Germany.
- Van Oort, E., Van Velzen, J.F.G. and Leerlooijer, K., 1993. Impairment by suspended solids invasion: testing and prediction. *SPE Production & Facilities*, 8(3): 178-184.
- Watson, R.B., Viste, P., Kageson-Loe, N.M., Fleming, N., Mathiasen, A.M. and Ramstad, K., 2008. Smart mud filtrate: an engineered solution to minimize near-wellbore formation damage due to kaolinite mobilization: laboratory and field experience, Oseberg Sør. In *SPE International Symposium and Exhibition on Formation Damage Control*. Society of Petroleum Engineers.
- You, Z., Bedrikovetsky, P., Badalyan, A. and Hand, M., 2015. Particle mobilization in porous media: Temperature effects on competing electrostatic and drag forces. *Geophysical Research Letters*, 42(8): 2852-2860.
- You, Z., Yang, Y., Badalyan, A., Bedrikovetsky, P. and Hand, M., 2016. Mathematical modelling of fines migration in geothermal reservoirs. *Geothermics*, 59: 123-133.
- Yuan, H. and Shapiro, A.A., 2011a. A mathematical model for non-monotonic deposition profiles in deep bed filtration systems. *Chemical Engineering Journal*, 166(1): 105-115.
- Yuan, H. and Shapiro, A.A., 2011b. Induced migration of fines during waterflooding in communicating layer-cake reservoirs. *Journal of Petroleum Science and Engineering*, 78(3): 618-626.

- Yuan, H., Shapiro, A., You, Z. and Badalyan, A., 2012. Estimating filtration coefficients for straining from percolation and random walk theories. *Chemical engineering journal*, 210: 63-73.
- Zeinjahromi, A., Vaz, A. and Bedrikovetsky, P., 2012a. Well impairment by fines migration in gas fields. *Journal of Petroleum Science and Engineering*, 88: 125-135.
- Zeinjahromi, A., Vaz, A., Bedrikovetsky, P. and Borazjani, S., 2012b. Effects of fines migration on well productivity during steady state production. *Journal of Porous Media*, 15(7): 665-679.

3 Analytical modelling of fines migration in porous media

3.1 Slow migration of mobilised fines during flow in reservoir rocks: Laboratory study

Oliveira, M. A., Vaz, A. S., Siqueira, F. D., **Yang, Y.**, You, Z., Bedrikovetsky, P.

Journal of Petroleum Science and Engineering, 122 (2014) 534-541

Statement of Authorship

Title of Paper	Slow migration of mobilised fines during flow in reservoir rocks: Laboratory study
Publication Status	<input checked="" type="checkbox"/> Published <input type="checkbox"/> Accepted for Publication <input type="checkbox"/> Submitted for Publication <input type="checkbox"/> Unpublished and Unsubmitted work written in manuscript style
Publication Details	Oliveira, M. A., Vaz, A. S., Siqueira, F. D., Yang, Y., You, Z. and Bedrikovetsky, P. (2014). Slow migration of mobilised fines during flow in reservoir rocks: Laboratory study. <i>Journal of Petroleum Science and Engineering</i> , 122, 534-541.

Author Contributions

By signing the Statement of Authorship, each author certifies that:

- the candidate's stated contribution to the publication is accurate (as detailed above);
- permission is granted for the candidate to include the publication in the thesis; and
- the sum of all co-author contributions is equal to 100% less the candidate's stated contribution

Name of Principal Author	Oliveira, M. A.
Contribution to the Paper	Performed laboratory tests
Signature	Date 19/JUL/2016

Name of Co-Author	Alexandre Vaz
Contribution to the Paper	Supervised laboratory work, helped in data interpretation
Signature	Date 18/JUL/2016

Name of Co-Author	Fernando Diogo de Siqueira
Contribution to the Paper	Supervised laboratory work, helped in data interpretation
Signature	Date 18/JUL/2016

Name of Co-Author (Candidate)	Yulong Yang
Contribution to the Paper	Helped in data interpretation
Overall percentage (%)	20%
Signature	Date 20/JUL/2016

Name of Co-Author	Zhenjiang You	
Contribution to the Paper	Helped in data interpretation	
Signature	Date	20/7/16

Name of Co-Author	Pavel Bedrikovetsky	
Contribution to the Paper	Supervised development of work, helped in data interpretation and manuscript evaluation	
Signature	Date	



ELSEVIER

Contents lists available at ScienceDirect

Journal of Petroleum Science and Engineering

journal homepage: www.elsevier.com/locate/petrol

Slow migration of mobilised fines during flow in reservoir rocks: Laboratory study



Maira A. Oliveira^a, Alexandre S.L. Vaz^a, Fernando D. Siqueira^a, Yulong Yang^b,
Zhenjiang You^b, Pavel Bedrikovetsky^{b,*}

^a Laboratory of Exploration and Production Engineering LENEP, North Fluminense State University UENF, Macaé, RJ, Brazil

^b Australian School of Petroleum, The University of Adelaide, 5000 SA, Australia

ARTICLE INFO

Article history:

Received 18 November 2013

Accepted 14 August 2014

Available online 28 August 2014

Keywords:

fines migration
particle detachment
laboratory study
formation damage
permeability decline
colloid

ABSTRACT

Permeability decline during high rate flows has been widely reported for corefloods and for production wells. The phenomenon is attributed to mobilisation of fine particles at elevated velocities, their migration in porous space with the following straining in thin pores and attachment to pore walls. Sixteen sets of corefloods with piecewise constant rate have been performed under increasing flow rate. The particularities of this study are long injection periods, allowing estimating permeability stabilisation times, and pressure measurements in intermediate core points, permitting for evaluation of the permeability profile variation along the core. It was found out that the mobilised particles drift with speeds significantly lower than the carrier fluid velocity, resulting in long permeability stabilisation periods.

© 2014 Elsevier B.V. All rights reserved.

1. Introduction

Detachment of the reservoir fines, their migration as colloids or suspensions in the carrier fluid with further straining in thin pore throats and attachment to pore walls occur in numerous petroleum production processes. The main features of the processes are the variation of colloidal suspension concentration in carrier fluid, which is important for produced water disposal in aquifers, and the permeability decline affecting well productivity and injectivity (Civan, 2007; Rousseau et al., 2008; Byrne and Waggoner, 2009). The above occurs during filtrate invasion into reservoirs during well drilling (Schechter, 1992; Watson et al., 2008), fines migration in oil and gas reservoirs (Schembre and Kovscek, 2005; Civan, 2007) and low quality water injection into oilfields (Nabzar et al., 1996; Pang and Sharma, 1997; Chauveteau et al., 1998). The role of fines migration during low-salinity waterflooding of oil reservoirs is a subject of the current intensive research (Tang and Morrow, 1999; Morrow and Buckley, 2011; Zeinijahromi et al., 2011; Yuan and Shapiro, 2011; Hussein et al., 2013). The permeability reduction due to fines migration can be used for water production control (Zeinijahromi et al., 2012). The list of fines migration applications can be significantly expanded.

The common view on the flow of mobilised fines in porous reservoirs is that the fine colloidal or suspension particles are transported in the carrier fluid. It means that the advective velocity of particles is equal to the carrier fluid velocity; the permeability stabilisation occurs after arrival of the “last” mobilised fine at the core outlet, i.e. after the injection of one pore volume. Several authors have mentioned the two-speed structure of the colloidal suspension flux, where the particles may undergo the near-surface motion with significantly reduced speed if compared to the carrier water velocity (Yuan and Shapiro, 2010). The particle drift near the rough pore walls as modelled by Navier–Stokes equations has the speed significantly lower than the injected water velocity (Sefriouri et al., 2013). However, the vast majority of mathematical models assume equality of particle and water velocities (Bradford et al., 2008, 2009). Besides, laboratory studies of slow fine particle migration in porous media are not available in the literature.

Several laboratory corefloods with increasing velocity in order to lift fines have been performed, yielding the clear understanding of mobilisation and straining phenomena (Priisholm et al., 1987; Ochi and Vernoux, 1998; Kuhn et al., 1998, etc.). The detailed overviews of those works are presented by Tiab et al. (2004) and Civan (2007). Yet, the permeability stabilisation periods cannot be evaluated from the results of these tests due to short injection times. Also, the permeability profile cannot be evaluated since only the pressure drop across the overall core has been measured.

In the current work, the corefloods with piecewise constant velocity in the mode of velocity increase in order to lift the natural

* Corresponding author. Tel.: +61 8 8313 3082.

E-mail address: pavel@asp.adelaide.edu.au (P. Bedrikovetsky).

reservoir fines are performed until the permeability stabilisation. It is found out that the permeability stabilisation periods significantly exceed one pore volume injected in all the tests, while the assumption of equality of particle and water velocities yields the stabilisation after injection of one pore volume. The delayed stabilisation is attributed to slow fines transport near pore walls. The stabilisation time decreases with the flow rate increase, which is explained by simultaneous increase of drag force driving the particles along the rock surface.

The structure of the paper is as follows. Brief physical description of colloidal suspension transport in porous media is given in Section 2. Section 3 presents the details of the laboratory set-up, rocks and fluids used and the methodology of laboratory tests. The test results are presented in Section 4. The paper is concluded by the discussions of results (Section 5), where the observed phenomena of delayed permeability stabilisation are attributed to the slow particle drift along the rock surface.

2. Physics of fines mobilisation, migration and straining

Following Muecke (1979), Sharma and Yortsos (1987), Chauveteau et al. (1998), Bergendahl and Grasso (2000), Freitas and Sharma (2001), Byrne et al. (2010), Bradford et al. (2011) and Bedrikovetsky et al. (2011, 2012), let us describe the main physical factors determining fines migration with consequent permeability decline in porous media. Detachment of fine particles, their migration with followed straining or attachment is shown in Fig. 1. The mobilised fine particle is retained by size exclusion if its size exceeds the pore size (Yuan et al., 2012; You et al., 2013). The fine particle intercepting a grain can also be attached, if there are available attachment sites on the grain surface. The forces exerting upon a single particle attached to the grain are shown in Fig. 1. The particle on the grain surface or on top of the internal cake formed by other attached particles is subject to electrostatic, drag, lifting and gravitational forces. The particle is attached if the attaching torque of electrostatic force and gravity exceeds the detaching torque of drag and lifting forces; otherwise the particle leaves the grain surface. The torque equilibrium is the condition of the particle mechanical equilibrium. The electrostatic force depends on the grain–particle disjoining distance that reaches the maximum at certain disjoining distance value. For the given values of drag, lifting and electrostatic forces, particle mobilisation is controlled by the maximum value of the attractive electrostatic

force. If the attaching torque exceeds the detaching torque, the disjoining distance is determined by the torque balance under given values of drag, lifting and electrostatic torques. From the torque balance criterion follows that under the mechanical equilibrium, there does exist the maximum concentration of retained particles that is a function of carrier fluid velocity, salinity, pH, temperature, etc. Particle detachment due to velocity, pH or temperature increase or salinity decrease is described by the maximum retention function decrease. Velocity increase yields an increase of drag and lifting forces; it may raise the detaching torque resulting in the particle mobilisation. The water salinity decrease causes a decrease of the electrostatic force with consequent decrease of the attaching torque and fines mobilisation. Increase of temperature and pH also causes weakening of electrostatic force with consequent fines mobilisation. The above phenomena of fines mobilisation by increasing velocity have been observed and discussed in laboratory studies by Miranda and Underdown (1993), Ochi and Vernoux (1998), Bradford et al. (2011), while the fines lifting due to salinity decrease or temperature and pH increase is presented by Lever and Dawe (1984), Sarkar and Sharma (1990), Valdya and Fogler (1992), Khilar and Fogler (1998) and Civan (2010).

The classical filtration theory introduces critical velocity as the minimum velocity, where fines mobilisation occurs (Miranda and Underdown, 1993). Critical salinity is the salinity threshold below which the fines are lifted (Khilar and Fogler, 1998). The particle detachment rate is proportional to the difference between the current and critical values of velocity, salinity, pH, etc. The proportionality coefficients correspond to relaxation times, which are empirical coefficients and are obtained from the fitting. The model exhibits the delay in permeability response to an abrupt change of the parameters, while several laboratory studies reveal an instant permeability response (Lever and Dawe, 1984; Ochi and Vernoux, 1998; Bedrikovetsky et al., 2012). The above mentioned model of maximum retention function is free of this shortcoming.

If the migrating particle intercepts the grain and the attaching torque exceeds the detaching torque, the particle becomes attached to the grain. The size exclusion mechanism of the particle has been mentioned before. Another mechanism of particle retention is diffusion into the dead-end pores, where the particles may remain not being accessible to the flow in skeleton pores. In the next section we present the methodology and set-up of the laboratory study of fines mobilisation under increasing flow velocity followed by migration and capture.

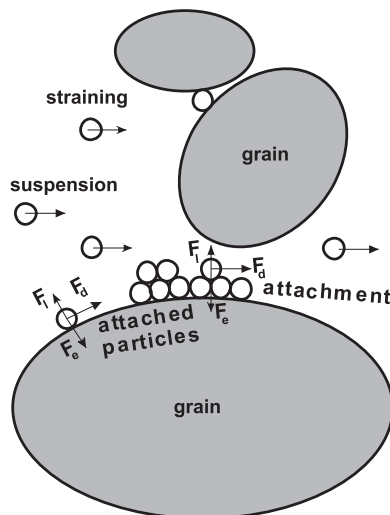


Fig. 1. Fine particles detachment from grains, migration in carrier water, attachment to grains and straining in thin pores.

3. Laboratory study

In this section we describe laboratory set-up (Section 3.1), characteristics of rock and fluids (Section 3.2) and methodology of flow testing under alternate velocities (Section 3.3).

3.1. Set-up

The schematic of laboratory set-up with specification of all key elements is shown in Fig. 2. Fig. 3 is the photo of set-up. The injected fluid is placed in Beaker 1 and is injected by PU-2087 pump Jasco under constant rate. The core-holder Mantec (Lab-conte) with two intermediate ports for pressure measurements is controlled by valves 14 and 15. The overburden pressure in core-holder is provided by manual pump Fluke 10 and is monitored by manometer 11. Pressure transducers 5, 6 and 7 measure pressure drops across the overall core, between the entrance and second ports and across the first core section, respectively. The Yokogawa transducers are calibrated to measure the pore pressure from zero to 500 psi. The data acquisition system 8 delivers a digital form for

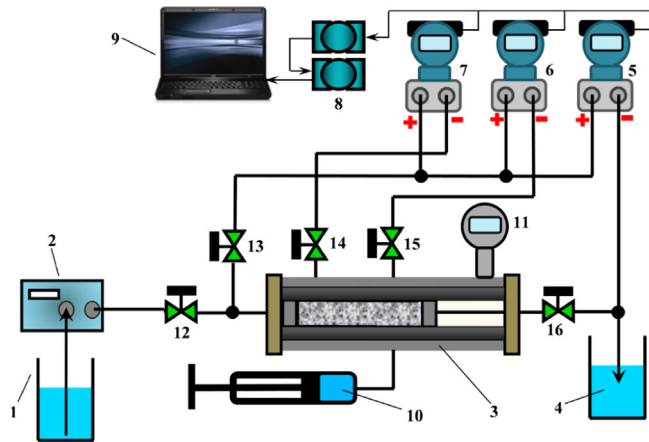


Fig. 2. Schematic of laboratory set-up for fines migration in porous media: 1 – injected fluid, 2 – pump, 3 – core-holder with core, 4 – produced fluid, 5, 6, 7 – pressure transducers, 8 – data acquisition system, 9 – PC with LabView, 10 – manual pump to maintain overburden pressure, 11 – manometer, 12–16 – control valves.

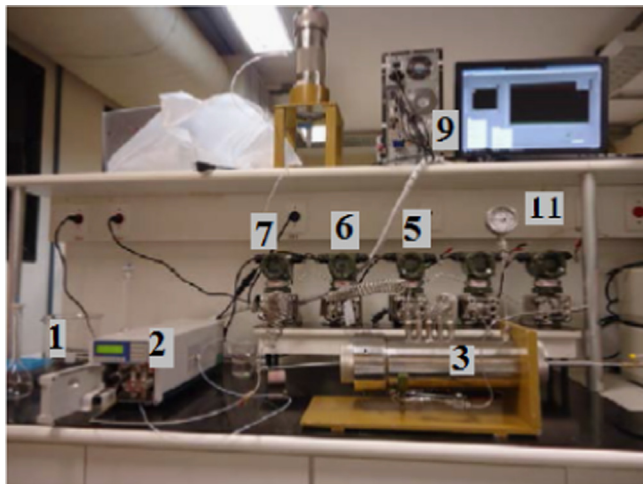


Fig. 3. Set-up for investigation of fines migration in porous media.

the measurements of three pressure transducers and transfers it to PC 9. The data are treated by the software LabView installed in PC. The effluent fluid is collected in Beaker 4 for further electrical resistance, pH, breakthrough concentration and fine particle size distribution measurements.

3.2. Core and fluid

Corefloods in 16 Berea cores with alternate velocities have been performed. Some core and brine properties for Core 12 are presented in Table 1. Table 2 shows initial core permeability and brine salinities for 16 tests. The cores 8–20 and 21–24 have been cut from two different blocks. The permeability values in the first block are lower than those in the second block. Cores have diameters determined from the core-holder size – 0.038 m. Core length varies from 0.044 to 0.072 m. Fresh Milli-Q type ultrapure water has been used for preparing the solution of sodium chloride. The brine has been filtered using 0.22 μm filter.

3.3. Methodology of laboratory study

In order to determine porosity, dry cores are weighted, saturated by brine with a determined salinity under vacuum and

weighted again. Dry Berea core has been saturated by brine at low velocity (at the injection rate 0.5 mL/m). The salinity varies from test to test from 6 to 30 g/L. The brine pH is below 7 (Table 1). The

Table 1
General water and core data for Test 12.

Parameter	Test 12
Salinity	10.0 g/L NaCl
pH	6.4
Total core length	7.2 cm
Intermediate point core length	0.7 cm and 2.9 cm
Porosity	19%
Cross-sectional area	11.53 cm ²
Solution viscosity	1.0 cP
Initial permeability	58 mD

Table 2
Stabilised times in different tests.

Test no.	K_0 (mD)	Q (ml/min)	Duration of tests (pvi)	Stabilisation time (pvi)	Brian salinity (g/L)	K_{st} (mD)
8	57	10	303	20	10	40
			595	16	10	36
			585	20	10	32
9	70	10	281	16	10	61
			623	14	10	55
			706	18	10	50
10	44	10	200	16	6	38
			505	15	6	33
			778	20	6	31
11	30	10	18	16	10	30
			469	20	10	27
			710	14	10	26
12	58	10	91	25	10	31
			361	17	10	26
			455	30	10	24
13	61	10	127	11	30	42
			752	19	30	35
			563	22	30	32
14	44.9	10	146	14	30	40
			628	17	30	34
			123	14	10	46
15	56	10	451	23	10	38
			485	15	10	34
			129	14	6	39
16	50	10	420	20	6	33
			527	20	6	30
			133	27	6	43
18	60	10	599	23	6	35
			803	18	6	34
			146	23	6	45
19	71	10	595	25	6	36
			627	19	6	31
			120	12	10	32
20	75	10	72	19	10	173
			306	18	10	155
			421	21	10	122
21	270	10	450	23	10	118
			44	13	10	106
			97	18	10	84
22	109	5	213	12	10	71
			198	10	10	67
			367	11	10	59
23	247	10	1278	12	10	56
			86	11	3	180
			258	12	3	148
24	250	10	441	12	3	113
			77	10	10	188
			317	21	10	148
			300	13	10	111
			310	20	10	102

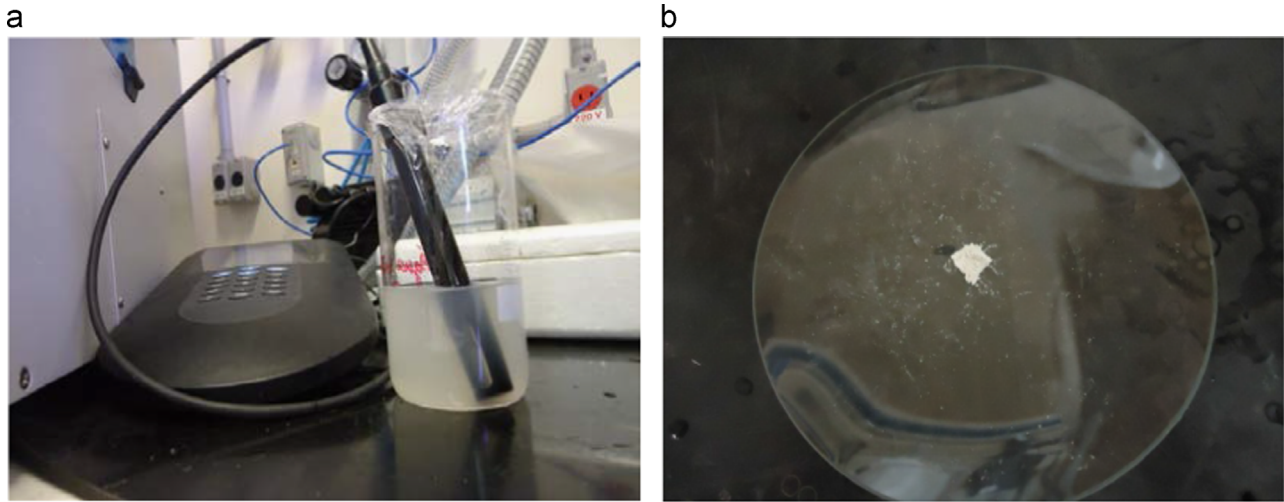


Fig. 4. Analysis of effluent fluids: (a) conductivity measurements; (b) residual fines after produced fluid evaporation to be submitted to XRD analysis.

fines are not lifted at such low velocity, low pH and high salinity. Afterwards, the cores are submitted to the low velocity flow with the rate varying from 0.5 to 2.0 mL/min for determining the stable initial permeability. Subsequently, the cores are flooded with several rates sequentially (Table 2). The first flood is always performed with the rate 1 mL/min during short period where the permeability remains constant. Pressure at the core inlet, outlet and in two intermediate ports is measured during the coreflooding (see the schematic in Fig. 2). Measurements of pressure in intermediate core points provide more information for tuning the mathematical model and also allow estimating the permeability profile (Bedrikovetsky et al., 2001). The produced fluid salinity is determined from electric conductivity (Fig. 4a). The produced fluid pH is also measured.

The breakthrough concentrations of produced fines are too low to be measured with certain accuracy. Therefore, the fines have been removed from the core with high breakthrough concentration after water injection with three rates by injection of low salinity water (0.5 g/L). Fig. 4a shows semi-transparent effluent suspension with significant turbidity. Particle size distribution in the effluent suspension is measured by the Particle Analyser CILAS 1180 (Fig. 5). Then the produced water is evaporated in order to extract fine particles (Fig. 4b). Mineralogy of the fines is determined by XRD analysis (Fig. 6).

The obtained laboratory data are presented in the next section.

4. Results

Particle size distribution as obtained from the effluent suspension (Fig. 4a) is presented in Fig. 5. Diameters corresponding to 10%, 50% and 90% cuts are 0.38 μm , 1.35 μm and 5.03 μm , respectively; the medium particle diameter is 2.14 μm . The core permeability is $k_0=247$ mD, porosity is $\phi=0.20$. The medium pore diameter is $D_p=10 \times (k/\phi)^{1/2}=11.1$ μm (see Amix et al. (1964) for determining pore size from the permeability and porosity). According to the “golden rule of filtration”, the particles with diameter less than $D_p/7$ filtrate without being captured, the particles with diameter larger than $D_p/3$ are captured after migration for a distance that is negligibly smaller than the core length and do not appear at the effluent and the intermediate size particles are performing the deep bed filtration (Van Oort et al., 1993). The fines size distribution in Fig. 5 shows that a significant fraction of fines has the diameter less than $D_p/7=1.6$ μm ; the fraction of large particles with diameter above $D_p/3=3.7$ μm is

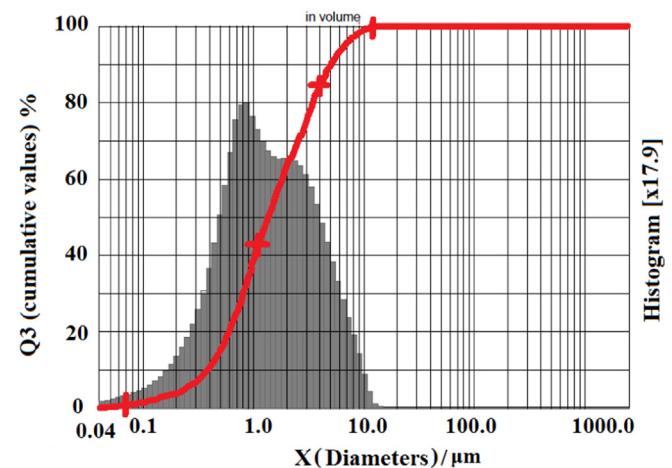


Fig. 5. Size distribution of produced fines.

significantly lower than one. The jamming ratio between the mean pore and particle diameters in the effluent $11.2/2.14=5.1$ is typical for deep bed filtration (Bradford et al., 2008, 2009, 2011).

The dry residue of the evaporated produced suspension (Fig. 4b) is submitted to XRD analysis. The qualitative results are shown in Fig. 6. Besides the salt crystals, the residue contains the leaflets of kaolinite clay and quartz particles from sandstones. Salt presence is attributed to the injected brine. The data refinement shows 79 mass% of NaCl crystals, 18% of kaolinite and 3% of quartz.

The results of pressure measurements are shown in Fig. 7. Rates 10, 20 and 30 mL/min have been applied in Test 12. The so-called dimensionless impedance is used to describe medium permeability of different core sections

$$J(t_D) = \frac{\Delta p(t_D) q(0)}{q(t_D) \Delta p(0)} = \frac{k_0}{k(t_D)}; \quad \Delta p(t_D) = p(0, t_D) - p(L, t_D)$$

where p is pressure, q is rate, the sign Δ corresponds to the difference between the upstream and downstream pressure values. The impedance is the ratio between the initial and current permeability values. The impedance history $J(t_D)$ for the overall core and its sections is presented in Fig. 7a. The pressure drop across the overall core and its sections is shown in Fig. 7b. Fig. 7c–e correspond to time zoom from the beginning of injections with a constant rate.

Let us define the pressure drop/permeability stabilisation time. The typical time interval between two sequential samplings is 10 PVI for the rates used in the coreflood tests. The precision of

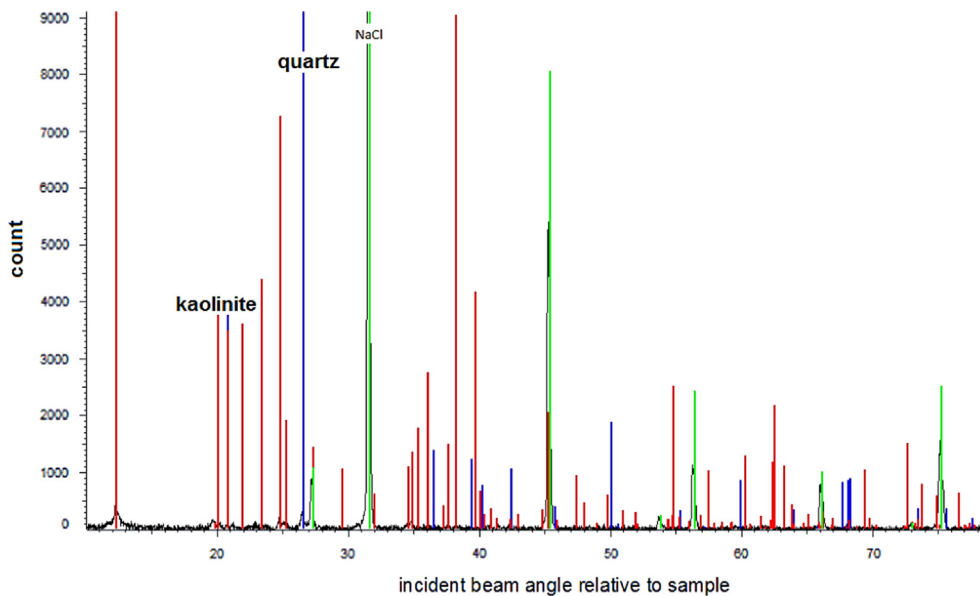


Fig. 6. Results of XRD analysis of the fines from produced fluid.

pressure measurements is 0.5 psi. The system is stabilised if the pressure drop does not grow anymore. The following criterion is assumed for stabilisation – pressure drop rise divided by the time between two sequential samplings does not exceed 0.5/10 psi. The calculated stabilisation times t_{Dst} , $J(t_{Dst})=J_{st}$ are shown in the fifth column of Table 2. Column seven presents the stabilised permeability as calculated from the stabilised impedance. The plots of permeability versus velocity for Test 12 are shown in Fig. 8. Stabilisation times versus velocity as obtained from all tests listed in Table 2 are shown in Fig. 9.

5. Discussions

The size distribution of produced fines is in qualitative agreement with the 1/3–1/7 filtration rule. It corresponds to the possibility for mobilised particles to migrate along the core and be produced at the effluent. It allows attributing the pressure drop increase during the constant rate flow to pore straining and rock clogging by the mobilised and migrating fines.

Numerous laboratory studies indicate simultaneous presence of clay and sandstone particles in produced water residue after evaporation (Lever and Dawe, 1984; Khilar and Fogler, 1998). XRD analysis of the residue fines presented in Fig. 6 also shows the presence of kaolinite clay and quartz sandstone particles.

The impedance curves in Fig. 7 indicate almost instant permeability response to the abrupt permeability alteration. So, the fine particles detachment occurs during time periods that are negligibly shorter than flow times. Fig. 7b shows pressure drop along the core, its third section and across Sections 2 and 3. Fig. 7c–e presents zoom-in for each constant rate injection during small time period from the beginning of each injection. Pressure drop gradually increases during each constant-rate injection for core and all sections; the gradual permeability decrease is explained by fines migration and straining.

The stabilised values of permeability for the overall core and its sections are shown in Fig. 8. The higher is the flow rate the lower is the permeability. It is explained by accumulation of strained particles sequentially mobilised under the increasing flow rate.

Fig. 7 shows that the impedance curve for the third core section is above that for the second and third sections; the overall core

impedance curve is the lowest. Consequently, the average permeability of the overall core is higher than that for the second and third sections; the third section has the lowest permeability. The same relationship is revealed from Fig. 8, which shows the stabilised permeability of the core and its sections after long-term injection. Let us explain the phenomenon. The mobilised fines move along the core with a certain speed. This is the velocity of the clean water front moving from the core inlet along the core from the beginning of injection. Particle size exclusion causing permeability reduction is going on ahead of the front, the suspended fines are absent behind the front. The larger is the distance between the core inlet and a point in the core, the longer is the period if particle straining occurs at this point, and the lower is the final permeability. The profile of the final permeability along the core is given by a declining curve.

Now let us discuss the obtained values of stabilisation times with consequent conclusions about the fines drift velocity. It is assumed that the fines are lifted by an abrupt velocity alternation during the time period that is negligibly smaller than the reference time of flow in the core. Therefore, the concentration front of the injected particle-free water moves with the water velocity from the core inlet at the beginning of injection. The diffusive front thickness is significantly smaller than the core length. Size exclusion of mobilised fines stops at the moment of concentration front breakthrough, i.e. after one pore volume injected. The assumption that mobilised particles are transported by carrier water results in one pore volume value for stabilisation time.

However, the observed stabilisation times highly exceed one (Table 2). It shows that the mobilised particles drift with a speed that is significantly lower than the velocity of the carrier water. This drift can be a total of different micro-motions, such as rolling over the rock surface or sliding along the pore wall segments (Yuan and Shapiro, 2010). The particle can be mobilised and move with the carrier fluid until the neighbouring asperity, either leaving it or remaining attached. The range of the transition time in PVI, which is equal to the ratio between the velocities of the carrier water and the drift, varies from 10 to 27 (Table 2).

Fig. 9 shows stabilisation time versus velocity of the carrier fluid for the conditions of all tests performed. The upper curve corresponds to the cores with higher permeability values that have been cut off the second rock block (Tests 21–24, see Table 2). The lower

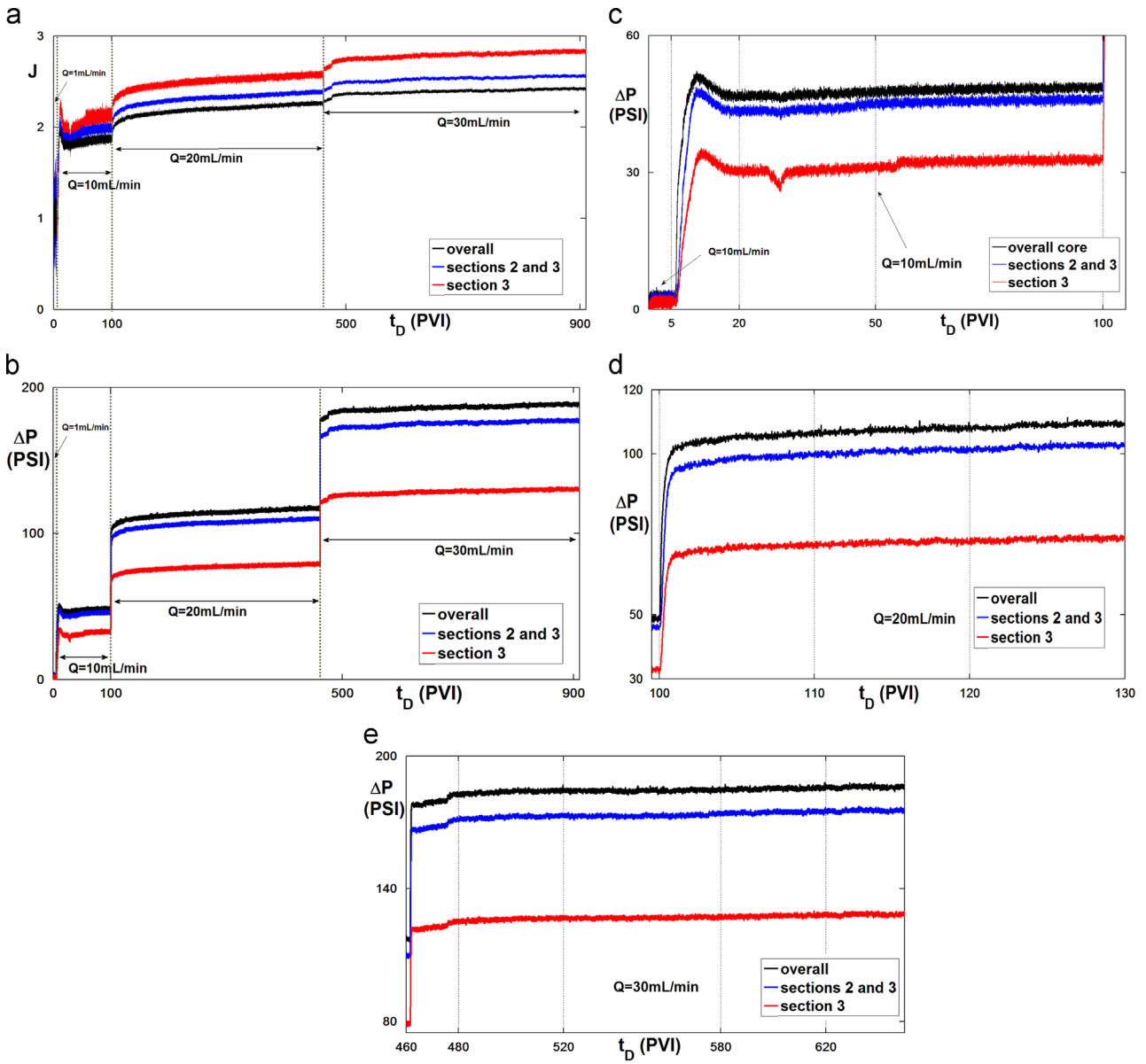


Fig. 7. Comparison of the model tuned predictions with impedance's data from Test 12: (a) impedance history; (b) pressure drops across the core and its sections versus PVI; (c) history of pressure drops across the core and its sections for rate 10 mL/min; (d) zoom for pressure drops across the core and its sections for rate 20 mL/min for small times; (e) pressure drops for rate 30 mL/min for small times.

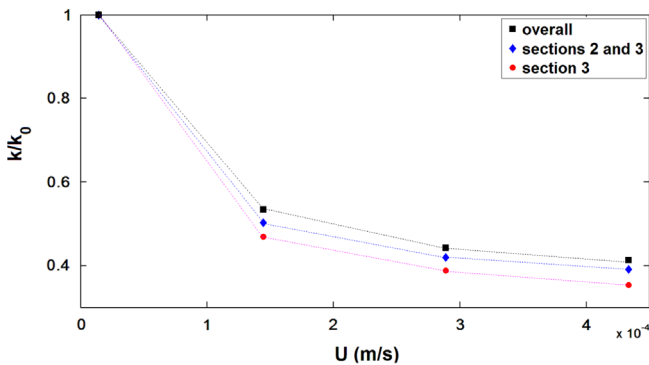


Fig. 8. Stabilised permeability versus velocity as obtained from pressure drop measurements across the overall core and its sections (Test 12).

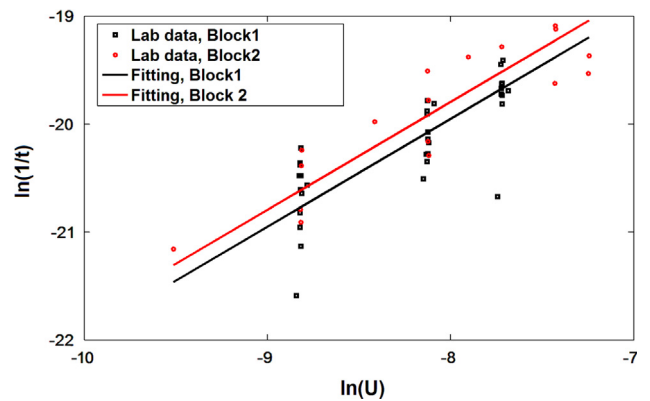


Fig. 9. Permeability stabilisation time versus flow velocity for 16 tests.

curve corresponds to the cores with lower permeability values that have been cut off the first rock block (Tests 8–20). The points are not expected to be located exactly on two curves, since the

transition times for the different points have been calculated from tests with different cores. However, the curves show the following tendency: the higher is the carrier fluid velocity, the smaller is the

transition time or, the higher is the particle drift speed. It is explained by the proportionality between the flow velocity and the drag force exerting on the particles at the rock surface.

During the injection of suspensions in porous media, the breakthrough time varies around one PVI. Small deviation of the breakthrough time from unity is explained by accessibility of the pore space for finite size particles (Ilina et al., 2008) or by the interplay between the particle capture and diffusion (Altoe et al., 2006). So, the injected particles move with the carrier fluid. On the contrary, for conditions of the laboratory tests presented in the current work, the detached particles perform a slow motion near to pore walls. Nevertheless, the above does not exclude the possibility for particle detachment into the main stream of the carrier fluid resulting in faster particle transport. It may occur at higher flow velocities and requires further laboratory investigation.

General tendency of the impedance growth during injection with velocity increase is evident from Fig. 7. However, some short time impedance decrease has been observed during the test. Fig. 7a shows the $J(t_D)$ -curve decline after the rate switching from 1 mL/min to 10 mL/min. We explain it by formation of multi-particle bridges at the pore throat entrances during the induced fines migration. The abrupt rate increase may destruct the bridge and yield the fines mobilisation, resulting in a temporary permeability improvement. The effect is observed mostly at low velocities (Fig. 7). It agrees well with the above mentioned explanation of the short time impedance decline, since bridging occurs at low velocities (Tiab et al., 2004; Civan, 2007).

The explanation of permeability decline due to fines migration during the flow with increasing injection rate can be verified by applying the NMR (T2 distribution) test on each core. A possible shift in T2 distribution could be used to indicate pore plugging by the migrating fine particles (see Arns et al., 2005).

6. Conclusions

Corefloods under sequentially increasing velocity with pressure drop measurements allow drawing the following conclusions:

- (1) Corefloods exhibit almost instant permeability response to abrupt rate change, suggesting that the fine particles are mobilised instantly
- (2) Stabilisation time highly exceeds one pore volume, suggesting that fine particles migrate with the velocity that is significantly lower than the carrier water velocity
- (3) The higher is the velocity, the lower is the stabilisation time. It is explained by the proportionality between the velocity and the drag force driving mobilised particles near to pore walls;
- (4) The *post-mortem* permeability decreases along the core, since more remote core points are exposed to straining by lifted fines for longer period.

Acknowledgements

Many thanks go to Drs. A. Zeinijahromi, A. Badalyan and T. Carageorgos for long-term co-operation in formation damage and colloidal flows. The authors are also grateful to Dr. A. Badalyan for help in preparing the manuscript. F. Siqueira acknowledges Brazilian programs CAPES and ANP PRH for sponsorship of Ph.D. study and the visit to University of Adelaide.

References

Altoe, J.E., Bedrikovetsky, P.G., Siqueira, A.G., de Souza, A.L., Shecaira, F., 2006. Correction of basic equations for deep bed filtration with dispersion. *J. Pet. Sci. Eng.* 51, 68–84.

- Amix, B., Bass, R., Whiting, A., 1964. *Applied Reservoir Engineering*. McGraw Hill Book Co, NY.
- Arns, C.H., Knackstedt, M.A., Martys, N.S., 2005. Cross-property correlations and permeability estimation in sandstone. *Phys. Rev. E* 72, 046304.
- Bedrikovetsky, P.G., Marchesin, D., Checaira, F., Serra, A.L., Resende, E., 2001. Characterization of deep bed filtration system from laboratory pressure drop measurements. *J. Pet. Sci. Eng.* 64, 167–177.
- Bedrikovetsky, P., Siqueira, F.D., Furtado, C., de Souza, A.L.S., 2011. Modified particle detachment model for colloidal transport in porous media. *J. Transp. Porous Med.* 86, 353–383.
- Bedrikovetsky, P., Zeinijahromi, A., Siqueira, F.D., Furtado, C., de Souza, A.L.S., 2012. Particle detachment under velocity alternation during suspension transport in porous media. *J. Transp. Porous Med.* 91 (1), 173–197.
- Bergendahl, J., Grasso, D., 2000. Prediction of colloid detachment in a model porous media: hydrodynamics. *Chem. Eng. Sci.* 55, 1523–1532.
- Bradford, S., Torkzaban, S., 2008. Colloid transport and retention in unsaturated porous media: a review of interface-, collector-, and pore-scale processes and models. *Vadose Zone J.* 7, 667–681.
- Bradford, S., Kim, H., Haznedaroglu, B., Torkzaban, S., Walker, S., 2009. Coupled factors influencing concentration-dependent colloid transport and retention in saturated porous media. *Env. Sci. Technol.* 43, 6996–7002.
- Bradford, S., Torkzaban, S., Wiegmann, P., 2011. Pore-scale simulations to determine the applied hydrodynamic torque and colloidal mobilisation. *Vadose Zone J.* 10, 252–261.
- Byrne, M., Waggoner, S., 2009. Fines migration in a high temperature gas reservoir – laboratory simulation and implications for completion design. SPE 121897. In: *Proceeding of the SPE 8th European Formation Damage Conference*. Scheveningen, The Netherlands, 27–29 May.
- Byrne, M., Slayter, A., McCurdy, P., 2010. Improved selection criteria for sand control: when are “Fines” fines? SPE 128038. In: *Proceedings of the SPE International Symposium and Exhibition on Formation Damage Control*. Lafayette, Louisiana, USA, 10–12 February.
- Chauveteau, G., Nabzar, L., Coste, J., 1998. Physics and modeling of permeability damage induced by particle deposition. SPE 39463. In: *Proceeding of the SPE Formation Damage Control Conference*. Lafayette, Louisiana, USA, 18–19 February, pp. 409–419.
- Civan, F., 2007. *Reservoir Formation Damage: Fundamentals, Modeling, Assessment, and Mitigation*. Gulf Professional Publishing, Elsevier, Burlington.
- Civan, F., 2010. Non-isothermal permeability impairment by fines migration and deposition in porous media including dispersive transport. *J. Transp. Porous Med.* 85, 233–258.
- Freitas, A., Sharma, M., 2001. Detachment of particles from surfaces: an Afm study. *J. Colloid Interface Sci.* 233, 73–82.
- Hussein, F., Zeinijahromi, A., Bedrikovetsky, P., Cinar, Y., Badalyan, A., Carageorgos, T., 2013. An experimental study of improved oil recovery through fines-assisted waterflooding. *J. Pet. Sci. Eng.* 109, 187–197.
- Ilina, T., Panfilov, M., Buès, M., Panfilova, I., 2008. A pseudo two-phase model for colloid facilitated transport in porous media. *J. Transp. Porous Med.* 71 (3), 311–329.
- Khilar, K., Fogler, H., 1998. *Migrations of Fines in Porous Media*. Kluwer Academic Publishers, Dordrecht/London/Boston.
- Kuhn, M., Vernoux, J.F., Kellner, T., Isenbeck-Schroter, M., Schulz, H., 1998. Onsite experimental simulation of brine injection into a clastic reservoir as applied to geothermal exploitation in Germany. *Appl. Geochem.* 13 (4), 477–490.
- Lever, A., Dawe, R., 1984. Water-sensitivity and migration of fines in the Hopeman sandstone. *J. Pet. Geol.* 7, 97–107.
- Miranda, R.M., Underdown, D.R., 1993. Laboratory measurement of critical rate: a novel approach for quantifying fines migration problems. SPE 25432. In: *Proceeding of the SPE Production Operations Symposium*. Oklahoma City, Oklahoma, USA, 21–23 March.
- Morrow, N., Buckley, J., 2011. Improved oil recovery by low-salinity waterflooding. *J. Pet. Technol.* 63 (5), 106–112.
- Muecke, T.W., 1979. Formation fines and factors controlling their movement in porous rocks. *J. Pet. Technol.* 32 (2), 144–150.
- Nabzar, L., Chauveteau, G., Roque, C., 1996. A new model for formation damage by particle retention. SPE 1283. In: *Proceeding of the SPE Formation Damage Control Symposium*. Lafayette, Louisiana, USA, 14–15 February.
- Ochi, J., Vernoux, J.-F., 1998. Permeability decrease in sandstone reservoirs by fluid injection: hydrodynamic and chemical effects. *J. Hydrol.*, 208 pp. 237–248.
- Pang, S., Sharma, M.M., 1997. A model for predicting injectivity decline in water-injection wells. SPEFE 12, 194–201.
- Priisholm, S., Nielsen, B.L., Haslund, O., 1987. Fines migration, blocking and clay swelling of potential geothermal sandstone reservoirs, Denmark. SPE Form. Eval. June, 168–178.
- Rousseau, D., Latifa, H., Nabzar, L., 2008. Injectivity decline from produced-water reinjection: new insights on in-depth particle-deposition mechanisms. SPE Prod. Oper. 23, 525–531.
- Sarkar, A., Sharma, M., 1990. Fines migration in two-phase flow. *J. Pet. Technol.* May, 646–652.
- Schembre, J.M., Kovscek, A.R., 2005. A mechanism of formation damage at elevated temperature. *J. Energy Resour. Technol., ASME Trans.* 127 (3), 171–180.
- Sefriouri, N., Ahmadi, A., Omari, A., Bertin, H., 2013. Numerical simulation of retention and release of colloids in porousmedia at the pore scale. *J. Colloids Surf. A: Phys. Eng. Asp.* 427, 33–40.
- Sharma, M.M., Yortsos, Y.C., 1987. Fines migration in porous media. *AIChE J.* 33, 1654–1662.

- Schechter, R.S., 1992. Oil Well Stimulation. Prentice Hall, Englewood Cliffs, New Jersey p. 602.
- Tang, G., Morrow, N., 1999. Influence of brine composition and fines migration on crude oil/brine/rock interactions and oil recovery. *J. Pet. Sci. Eng.* 24 (2–4), 99–111.
- Tiab, D., Donaldson, E.C., Knovel, 2004. *Petrophysics: Theory and Practice of Measuring Reservoir Rock and Fluid Transport Properties*. Gulf Professional Publishing, MA, USA.
- Valdya, R., Fogler, H., 1992. Fines migration and formation damage: influence of pH and ion exchange. *SPEPE* 7, 325–330.
- Van Oort, E., Van Velsen, J.F.G., Leerlooijer, K., 1993. Impairment by suspended solids invasion: testing and prediction. *SPE Prod. Facil.* August, 178–184.
- Watson, R.B., Viste, P., Kaageson-Loe, N., Fleming, N., Mathisen, A.M., Ramstad, K., 2008. Smart Mud Filtrate: An Engineered Solution To Minimize Near-Wellbore Formation Damage Due to Kaolinite Mobilization Laboratory and Field Experience—Oseberg Sør. SPE paper 112455 presented at 2008 SPE Formation Damage Control Conference and Exhibition, Lafayette, Louisiana, February 13–15.
- You, Z., Badalyan, A., Bedrikovetsky, P., 2013. Size-exclusion colloidal transport in porous media – stochastic modeling and experimental study. *SPE J.* 18, 620–633.
- Yuan, H., Shapiro, A., 2010. A Mathematical model for non-monotonic deposition profiles in deep bed filtration systems. *Chem. Eng. J.* 166, 105–115.
- Yuan, H., Shapiro, A., You, Z., Badalyan, A., 2012. Estimating filtration coefficients for straining from percolation and random walk theories. *Chem. Eng. J.* 210, 63–73.
- Yuan, H., Shapiro, A.A., 2011. Induced migration of fines during waterflooding in communicating layer-cake reservoirs. *J. Pet. Sci. Eng.* 78 (3–4), 618–626.
- Zeinijahromi, A., Lemon, P., Bedrikovetsky, P., 2011. Effects of induced migration of fines on water cut during waterflooding. *J. Pet. Sci. Eng.* 78, 609–617.
- Zeinijahromi, A., Vaz, A., Bedrikovetsky, P., 2012. Well impairment by fines production in gas fields. *J. Pet. Sci. Eng.* 88–89, 125–135.

3.2 Slow migration of detached fine particles over rock surface in porous media

Yang, Y., Siqueira, F. D., Vaz, A., You, Z., Bedrikovetsky, P.

Journal of Natural Gas Science and Engineering, accepted on 22/07/2016

Statement of Authorship

Title of Paper	Slow migration of detached fine particles over rock surface in porous media
Publication Status	<input type="checkbox"/> Published <input type="checkbox"/> Accepted for Publication <input checked="" type="checkbox"/> Submitted for Publication <input type="checkbox"/> Unpublished and Unsubmitted work written in manuscript style
Publication Details	Yang, Y., Siqueira, F. D., Vaz, A., You, Z. and Bedrikovetsky, P. (2016) Slow migration of detached fine particles over rock surface in porous media, submitted to Journal of Natural Gas Science and Engineering (minor review).

Author Contributions

By signing the Statement of Authorship, each author certifies that:

- i. the candidate's stated contribution to the publication is accurate (as detailed above);
- ii. permission is granted for the candidate to include the publication in the thesis; and
- iii. the sum of all co-author contributions is equal to 100% less the candidate's stated contribution

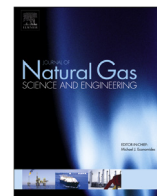
Name of Principal Author (Candidate)	Yulong Yang	
Contribution to the Paper	Derived analytical solution and performed data treatment	
Overall percentage (%)	50%	
Signature		Date 20/JUL/2016

Name of Co-Author (Candidate)	Fernando Diogo de Siqueira	
Contribution to the Paper	Supervised development of work, derived analytical solution and performed data treatment	
Signature		Date 18/JUL/2016

Name of Co-Author	Alexandre Vaz	
Contribution to the Paper	Supervised development of work, helped in data interpretation and manuscript evaluation	
Signature		Date 18/JUL/2016

Name of Co-Author	Zhenjiang You	
Contribution to the Paper	Supervised development of work, helped in data interpretation and manuscript evaluation	
Signature		Date 20/7/16

Name of Co-Author	Pavel Bedrikovetsky
Contribution to the Paper	Supervised development of work, helped in data interpretation and manuscript evaluation
Signature	21/07/2016



Slow migration of detached fine particles over rock surface in porous media



Yulong Yang^a, Fernando D. Siqueira^b, Alexandre S.L. Vaz^b, Zhenjiang You^a, Pavel Bedrikovetsky^{a,*}

^a Australian School of Petroleum, The University of Adelaide, Adelaide, SA, 5005, Australia

^b North Fluminense State University, Lenep-UENF, Rod. Amaral Peixoto Km 163, Imboassica, Macaé, RJ, 27.925-310, Brazil

ARTICLE INFO

Article history:

Received 13 April 2016

Received in revised form

7 June 2016

Accepted 23 July 2016

Available online 26 July 2016

Keywords:

Fines migration

Formation damage

Colloid

Porous media

Particle detachment

DLVO force

Suspension

Mathematical model

Permeability decline

ABSTRACT

Fines migration involving particle detachment in natural reservoirs usually exhibits significant permeability damage. This occurs due to mobilization and migration of detached colloidal or suspended fines that were strained in thin pore throats. Numerous laboratory coreflood tests show that the time for permeability stabilization accounts for hundreds of injected pore volumes. However, classical filtration theory assumes that the released fines are transported by the bulk of the carrier fluid, thus stabilizing the permeability after the injection of one pore volume. The current paper attributes the stabilization delay to the slow drift of the mobilized fines near the pore walls. We propose basic flow equations for single-phase particle transport in porous media with velocity lower than the carrier fluid velocity. We derive an analytical model for one dimensional flow with particle release and straining under piecewise-constant increasing velocity. The laboratory data are in high agreement with the results of mathematical modelling. The effective particle speed is 500–1000 times lower than the water velocity.

© 2016 Elsevier B.V. All rights reserved.

1. Introduction

Fines migration and the consequent permeability reduction can cause formation damage in numerous petroleum, environmental, and water-resource technologies. Fines migration occurs during oil and gas production in conventional and unconventional reservoirs, significantly reducing well productivity (Byrne and Waggoner, 2009; Byrne et al., 2010, 2014; Civan, 2014; Bai et al., 2015; Guo et al., 2015; Han et al., 2015; You et al., 2016). The literature has widely reported natural- and induced fines migration in the waterflooding of oilfields and the invasion of drilling and completion fluids into the formation (Watson et al., 2008; Fleming et al., 2007, 2010a, 2010b). Despite significant progress in the oil, gas and water production technologies, clogging of production and injection wells still remains a major operational issue.

The distinguishing features of the natural-reservoir fines migration are mobilization of the attached particles, their capture

by straining in thin pore throats, and consequent decline of well productivity and injectivity (Fig. 1). Permeability decline during corefloods that have piecewise-constant increasing velocity have been observed in numerous laboratory studies (Ochi and Vernoux, 1998, 1999). Similar effects occur during piecewise-constant change of water salinity or pH during coreflooding (Lever and Dawe, 1984; You et al., 2015). This is attributed to mobilization of the attachment fine particles and their migration in pore space until size exclusion in thin pore throats, finally resulting in significant permeability decline. Fig. 1 shows the schematic for attached and size-excluded fine particles in the porous space, along with definitions of the concentrations of attached, suspended and strained particles. Detachment of fines that coat the grain surfaces yields an insignificant increase in porosity and permeability, whereas the straining in thin pore throats and consequent plugging of conducting paths causes significant permeability decline. The main sources of movable fine particles in natural reservoirs are kaolinite and illite clays (Lagasca and Kovscek, 2014; Arab et al., 2014). Usually the kaolinite booklets of thin slices are situated on the grain surfaces (Fig. 2). Detachment of a large, thin slice from the booklet can result in plugging of the large pore, so that the

* Corresponding author.

E-mail address: pavel@asp.adelaide.edu.au (P. Bedrikovetsky).

mobilization of a limited kaolinite volume can significantly impair permeability.

Figs. 3a and 4a show typical decreasing permeability curves during the velocity increase; the velocity variations are presented in Figs. 3b and 4b.

Planning and design of injection and production in oil and gas reservoirs are supported by laboratory-based mathematical modelling. Classical filtration theory involving particle detachment includes the following mass balance equation for suspended, attached and strained particles

$$\frac{\partial}{\partial t} [\phi c + \sigma_a + \sigma_s] + U \frac{\partial c}{\partial x} = 0, \tag{1}$$

where c , σ_a , and σ_s are concentrations of suspended, attached and strained particles, respectively and U is flow velocity of the carrier fluid that coincides with particle speed.

The following relaxation equation captures the kinetics of simultaneous particles' attachment and detachment is given by Bradford and Bettahar (2005), Tufenkji (2007), Zheng et al. (2014)

$$\frac{\partial \sigma_a}{\partial t} = \lambda_a c U - k_{det} \sigma_a. \tag{2}$$

where λ_a is the filtration coefficient for attachment and k_{det} is the detachment coefficient (Bradford and Bettahar, 2005; Tufenkji, 2007; Bradford et al., 2012).

The following linear kinetics equation expresses the irreversible fines straining rate in thin pore throats, where the straining rate is proportional to the advective flux of suspended particles (Herzig et al., 1970; Yuan and Shapiro, 2011a, b)

$$\frac{\partial \sigma_s}{\partial t} = \lambda_s c U, \tag{3}$$

where λ_s is the filtration coefficient for straining (size exclusion).

Modified Darcy's law accounts for permeability damage due to both attachment and straining (Pang and Sharma, 1997):

$$U = -\frac{k}{\mu(1 + \beta_s \sigma_s + \beta_a \sigma_a)} \frac{\partial p}{\partial x}. \tag{4}$$

Eq. (4) follows from Taylor's series for the normalized reciprocal for permeability $k/k(\sigma_a, \sigma_s)$ with respect to small independent variables σ_a and σ_s ; the corresponding partial derivatives over variables σ_a and σ_s , β_a and β_s are called the formation damage coefficients for attachment and straining, respectively.

Fig. 1 illustrates the accepted assumption that permeability damage due to grain coating by attached particles is significantly lower than that due to straining: $\beta_s \gg \beta_a$, i.e., the combination of particle detachment and straining yields the decline in permeability. Therefore, the term that represents permeability increase due to detachment in Eq. (4) is negligible in comparison with that of

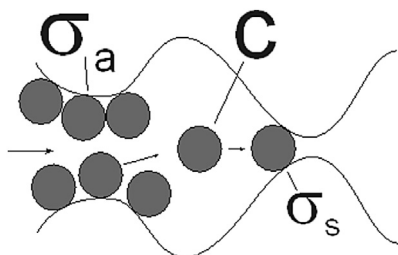


Fig. 1. Schema for fine particle detachment and straining that yields the permeability decline.



Fig. 2. Kaolinite particles attached to the grain surface (SEM image).

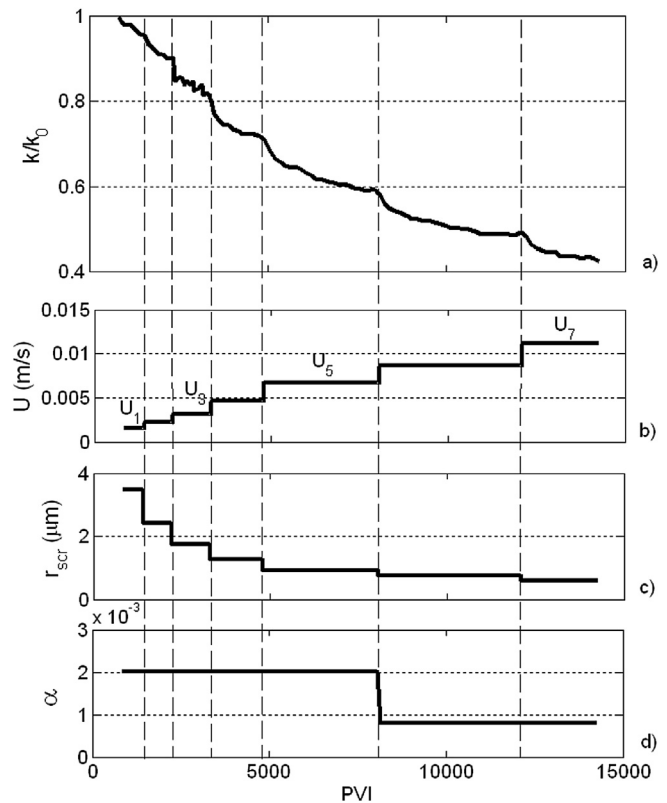


Fig. 3. Time variation of measured and calculated parameters during coreflood with piecewise-increasing velocity during test BS012 from Ochi and Vernoux (1998): (a) experimentally determined permeability decline with time; (b) increasing velocity during the test; (c) decrease in the critical mobilized fines radius as velocity increases, calculated from the torque balance; (d) delay drift factor from the model adjustment.

permeability decline due to straining.

The quasi-linear system of partial differential equations (1)–(4) depicts a delayed reaction to an abrupt injection rate alteration, whereas the laboratory tests show an immediate permeability and breakthrough concentration response to an abrupt velocity alteration (Ochi and Vernoux, 1998; Bedrikovetsky et al., 2012). This discrepancy has been resolved in the modified model for particle detachment, by introducing the maximum attached concentration as a velocity function $\sigma_a = \sigma_{cr}(U)$ (Bedrikovetsky et al., 2011). If the maximum value $\sigma_{cr}(U)$ exceeds the attached concentration, particle attachment occurs, and the detached particles follow the classical filtration equation (3); otherwise the maximum attached

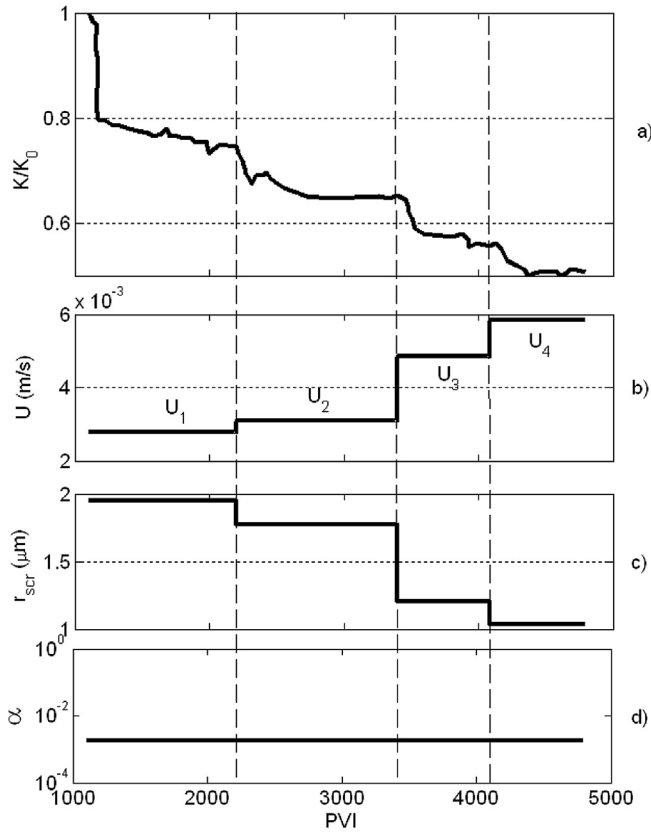


Fig. 4. Time variation of measured and calculated parameters during coreflood with piecewise-constant increasing velocity during test BS013 from [Ochi and Vernoux \(1998\)](#): (a) permeability decline with time as calculated from experimental data; (b) increasing piecewise-constant velocity during the test; (c) decrease in radius of the mobilized fines as velocity increases, as calculated from mechanical equilibrium Eq. (6); (d) delay drift factor α obtained by the model adjustment.

concentration holds. Therefore, dependency $\sigma_a = \sigma_{cr}(U)$ is called the maximum retention function. Hence, the following equation describes the above attachment-detachment scenario:

$$\begin{aligned} \frac{\partial \sigma_a}{\partial t} &= \lambda_a U c, \quad \sigma_a < \sigma_{cr}(U) \\ \sigma_a &= \sigma_{cr}(U) \end{aligned} \quad (5)$$

The maximum retention function decreases as flow velocity increases. Therefore, the velocity increase causes immediate release of the attached fine-particle excess.

The function $\sigma_{cr}(U)$ is an empirical phenomenological function of the model, which can be determined by the inverse-problem solution using the fines-migration test data. However, it can be approximated through a simplified geometry of porous space using torque balance of attaching and detaching forces exerted on the particle attached to the rock surface ([Fig. 5](#)) ([Freitas and Sharma, 2001](#); [Bergendahl and Grasso, 2003](#); [Bradford et al., 2012, 2013](#); [Kalantariasl et al., 2015](#)):

$$F_d(U, r_{scr})l(r_{scr}) = F_e(r_{scr}) - F_l(U, r_{scr}) + F_g(r_{scr}), \quad l = l_d/l_n. \quad (6)$$

Here F_d , F_e , F_l , and F_g are drag, electrostatic, lift, and gravitational forces, respectively; l_d and l_n are the lever arms for drag and normal forces (see Appendix for expressions of the forces in Eq. (6)).

Substitution of the expressions for drag, electrostatic, lift, and gravitational forces into the torque balance equation (6) yields the

expression of the maximum retention function (for detailed derivations, see [Bedrikovetsky et al., 2011](#)). The maximum retention function (5) for the case of poly-layer attachment of single-radius particles in rock with mono-sized cylindrical capillaries is a quadratic polynomial of the flow velocity.

Expression (5) for the maximum retention function substitutes the equation for simultaneous attachment and detachment (2) in the mathematical model for colloidal-suspension transport. The modified model consists of three equations (1), (3) and (5) for three unknown concentrations c , σ_a , and σ_s . Eq. (4) for pressure separates from system (1, 3, 5), which is independent of pressure. The one dimensional flow problem with attachment and detachment allows for exact solution; matching the laboratory coreflood data determining the maximum retention function. The laboratory- and theoretically-determined maximum retention functions are in close agreement, which validates the maximum retention function as a mathematical model for particle detachment ([Zeinijahromi et al., 2012](#); [Nguyen et al., 2013](#)). Nevertheless, the exact solution of the system (1, 3, 4, 5) shows complete pressure drop stabilization after injection of one pore volume ([Bedrikovetsky et al., 2011](#)), whereas numerous laboratory studies have exhibited 30–500 PVI periods of stabilization ([Ochi and Vernoux, 1998, 1999](#); [Oliveira et al., 2014](#)). [Fig. 3a](#) shows the permeability stabilization times 70–3000 PVI for different injection velocities ([Ochi and Vernoux, 1998](#)). The stabilization times for flow exhibited in [Fig. 4a](#) vary from 300 to 1200 PVI. Therefore, the modified model for suspension-colloidal transport in porous media (1, 3, 5) accurately predicts stabilized permeability but fails for predicting long stabilization periods.

Several works claim that slow surface motion of the mobilized particles accompanies the simultaneous fast particle transport in the bulk of the aqueous suspension. [Li et al. \(2006\)](#) asserted that the slow surface motion is due to particles in the secondary energy minimum. [Yuan and Shapiro \(2011a\)](#) and [Bradford et al. \(2012\)](#) introduced slow particle velocity in the classical suspension flow model; the two-speed model successfully matches the laboratory data on breakthrough concentration. The Navier-Stokes-based simulation of colloidal behavior at the pore scale, performed by [Sefrioui et al. \(2013\)](#), also yields particle transport speeds significantly lower than the water velocity. However, classical filtration theory along with the modified particle detachment model assumes the particle transport occurring with the carrier fluid velocity ([Tufenkji, 2007](#); [Civan, 2014](#)).

In the current paper, the long periods for permeability stabilization are explained by slow surface motion of mobilized fine particles. Further modification of the governing system consists of the substitution of water flow velocity U in Eqs. (1), (3) and (5) by the particle velocity $U_s < U$ ([Fig. 6](#)). Another modification of the governing system is the introduction of a maximum retention function for the mono-layer of size-distributed fines, allowing explaining its non-convex form. The obtained system allows for exact solution in the case of piecewise-constant velocity increase. High agreement between the laboratory and modelling data validates the proposed model for slow surface motion of released fine particles in porous media.

The structure of the paper is as follows. Section 2 presents a brief physical description of fine particle detachment in porous media and introduces the maximum retention function for a mono-layer of size-distributed particles. Qualitative analysis of the laboratory results presented in this section yields modification of the mathematical model for fines migration in porous media. Section 3 presents those basic transport equations. Section 4 derives the analytical model for one-dimensional flow under piecewise-constant flow velocity increase with consequent fines release and permeability impairment. Section 5 describes the laboratory

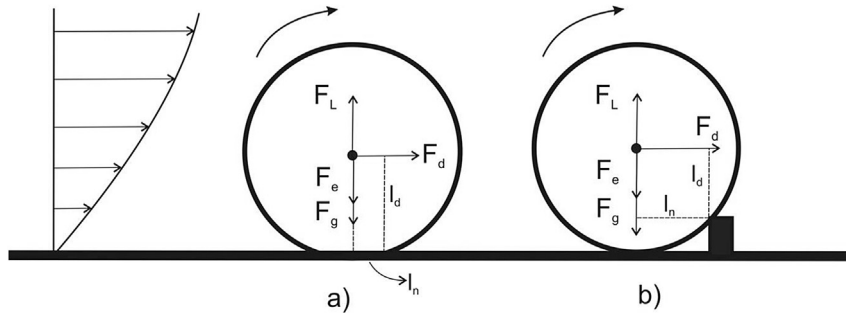


Fig. 5. Distribution of different-sized particles in a mono-layer on the grain surface, and forces acting on the particles; torque and force balance on a fine particle attached to the pore wall: (a) normal lever l_n is the radius of the contact deformation area; (b) the asperity height determines the normal lever.

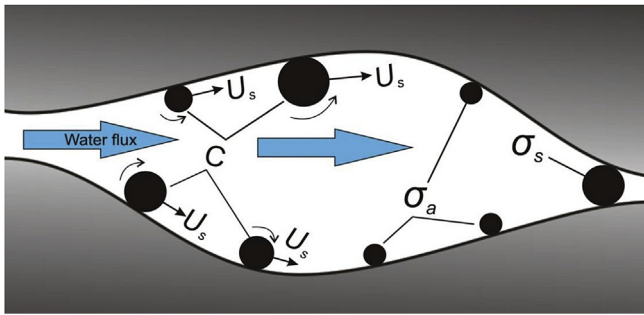


Fig. 6. Fines mobilization, migration, and straining in porous media.

coreflood tests with fines mobilization along with the successful adjustment of the analytical model. Discussions and conclusions finalize the paper.

2. Fines detachment, transport, and straining in porous media

We now discuss the micro-scale physics of particle detachment. Figs. 1 and 5 show the schematic of reservoir-fines detachment from the grain surfaces, causing their mobilization and migration. A fine particle on the grain surface is subjected to drag, lift, electrostatic, and gravitational forces. Further in the paper, we apply the DLVO (Derjaguin-Landau-Verwey-Overbeek) theory (Derjaguin and Landau, 1941; Elimelech et al., 1995; Khilar and Fogler, 1998; Israelachvili, 2011) for calculating the electrostatic forces. We use the formula for drag force from Bergendahl and Grasso (2003) and Bradford et al. (2013). Leighton and Acrivos (1985) and Akhatov et al. (2008) presented the expression for lift. The Appendix gives the expressions for all forces.

Consider the deformation of elastic particles by the normal force, which equals the total of electrostatic, lift, and gravitational forces. The right hand side of Eq. (6) is an expression for the normal force. It is assumed that the particle rotates around a point of the contact circle at the moment of mobilization; the rotation touching point is located on the contact-area boundary. Following Derjaguin et al. (1975), Schechter (1992), Freitas and Sharma (2001), and Bradford et al. (2013), the lever arm is assumed to be equal to the radius of the contact area of deformation by the normal force. Hertz's theory calculates the radius that is the lever arm l_n :

$$l_n^3 = \frac{F_n r_s}{4K}, \quad l_d = \sqrt{r_s^2 - l_n^2}, \quad K \equiv \frac{4}{3 \left(\frac{1-\nu_1^2}{E_1} + \frac{1-\nu_2^2}{E_2} \right)} \quad (7)$$

where K is the composite Young modulus that depends on Poisson's

ratio ν and Young's elasticity modulus E of the particle and of the surface, and indices 1 and 2 refer to the particle and solid matrix surface, respectively.

Another particle mobilization schema corresponds to the particle that rotates around the contacting asperity of the grain surface (Fig. 5b). Thus, the elastic particle and rock properties in the first case and the asperity size in the second case determine the lever arm for the normal force l_n .

We consider the parameters in Eq. (6) that correspond to the conditions of laboratory tests performed by Ochi and Vernoux (1998). Berea sandstone cores were used, and kaolinite fine particles were mobilized in the course of the velocity increase during coreflooding. We use the following values for electrostatic constants of kaolinite and quartz: Hamaker constant is $2.6 \times 10^{-20} \text{ J}$ (Welzen et al., 1981; Kia et al., 1987); atomic collision diameter is $0.4 \times 10^{-9} \text{ m}$ (Das et al., 1994); surface potentials ψ_{01} and ψ_{02} are $(-55 \text{ mv}, -50 \text{ mv})$ and $(-70 \text{ mv}, -80 \text{ mv})$ for tests BS012 and BS013, respectively (Ochi and Vernoux, 1998); and salinities are 0.1 and 0.01 mol/L for tests BS012 and BS013. Other constants are taken from Israelachvili (2011) and Khilar and Fogler (1998); permittivity of free space (vacuum) $\epsilon_0 = 8.854 \times 10^{-12} \text{ C}^{-2} \text{ J}^{-1} \text{ m}^{-1}$; dielectric constant for water $D = 78.0$. Temperature is $T = 25 \text{ }^\circ\text{C}$; Boltzmann constant is $k_B = 1.3806504 \times 10^{-23} \text{ J/K}$; and electron charge is $e = 1.6 \times 10^{-19} \text{ C}$. We use the following constants to calculate the lever arm ratio (7): Young's moduli for kaolinite and for quartz are 6.2 GPa and 12 GPa, respectively (Prasad, 2002); and Poisson's ratios are 0.281 and 0.241 (Gercek, 2007). Fig. 7a and b presents the plots of electrostatic potential and force versus separation particle-grain distance, that were calculated using the above parameters.

Eq. (A-5) expresses electrostatic force F_e is via energy potential V . Therefore, minimum and maximum points of the potential correspond to zero-values of electrostatic force. The inflection point of the potential curve corresponds to the minimum of force.

The calculations reveal no secondary minimum and favorable attachment conditions for test BS012. For the conditions of test BS013, primary and secondary minimum energies are 550 kT and 19 kT, respectively. The energy barrier is 87 kT, which exceeds values allowing the particle jumps from secondary minimum to primary minimum, i.e., the attachment conditions are unfavorable (Elimelech et al., 1995).

All forces in Eq. (6) for mechanical equilibrium are particle-size dependent. However, drag and lift forces are also flow-velocity dependent. This allows the critical radius of the particle mobilized by the flow with velocity U to be expressed as: $r_{scr} = r_{scr}(U)$. Eq. (6) is a transcendent equation for implicit dependency $r_{scr} = r_{scr}(U)$ and can be solved using the stationary iterative numerical procedure (see Varga, 1962).

Fig. 8 shows the form of the dependency $r_{scr} = r_{scr}(U)$ as obtained using the above constants. The solution shows that the higher the

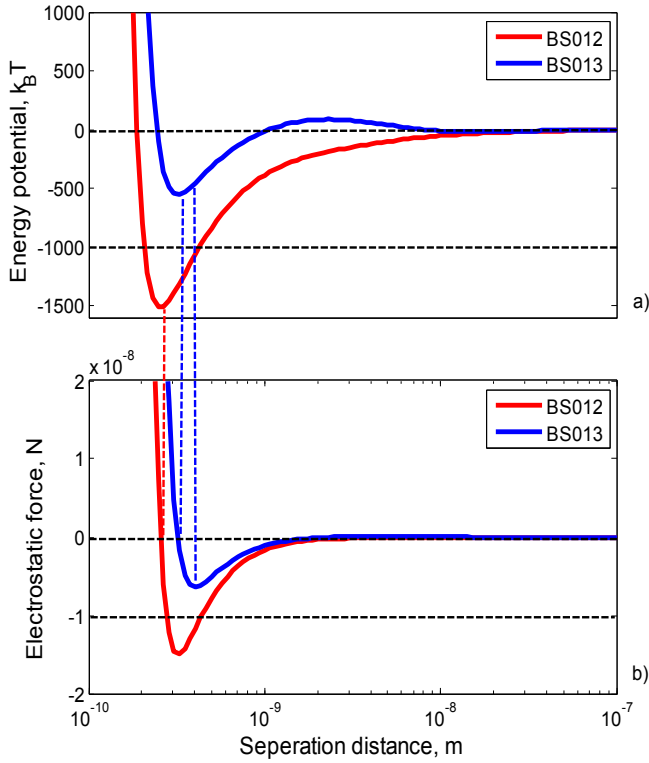


Fig. 7. Calculation of potential energy and electrostatic force for the two tests: (a) energy potential; (b) electrostatic force.

velocity, the smaller the mobilized particle, i.e., $r_{scr}(U)$ is monotonically decreasing. Therefore, the particles are mobilized in order of decreasing of size during the increase in flux velocity. Thus, the particles that remain on the surface during the flow with velocity U are smaller than $r_{scr}(U)$.

The attaching electrostatic force increases as the Hamaker constant increases. Thus, the higher the Hamaker constant, the larger the particle removed under a given velocity U . Therefore, the curve $r_{scr}(U)$ shifts to the right as the Hamaker constant increases (Fig. 8).

Let the initial concentration distribution of attached particle sizes be denoted by $\Sigma_a(r_s)$. The model assumes that the attached

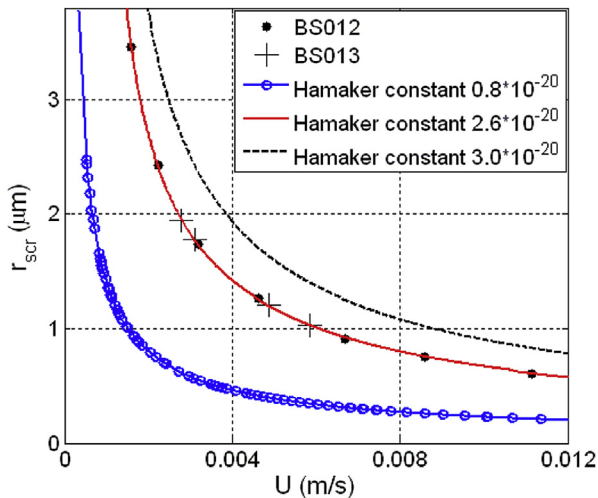


Fig. 8. Minimum size of the fine particles lifted by the flux with velocity U .

particles form a mono-layer on the rock surface. From the above discussion, it follows that the critical retention concentration includes all particles with radii smaller than $r_{scr}(U)$:

$$\sigma_{cr}(U) = \int_0^{r_{scr}(U)} \Sigma_a(r_s) dr_s. \quad (8)$$

Following Jensen et al. (2000), we assume that the attached particles have been created by the breakage algorithm, i.e., the attached particle sizes $\Sigma_a(r_s)$ follow a log-normal distribution. Fig. 9 shows the maximum retention function for various size distributions of the attached particles as calculated by (8) using the above mentioned values for electrostatic and elastic constants.

The maximum retention function $\sigma_{cr}(U)$ for single-size particles that form the poly-layer coating on the surface of cylindrical pores is a quadratic polynomial (Bedrikovetsky et al., 2011). Introduction of size distributions for spherical particles and cylindrical pores results in the convex maximum retention curves.

The maximum retention function for mono-layer fines is not convex (Fig. 9). Fig. 9a shows the maximum retention curves for three fines distributions that have the same variance coefficients but different average particle sizes. The larger the particle, the lower the maximum retention function. This result agrees with the above assertion that the particles are mobilized by descending size, by a flux with increasing velocity. Fig. 9b shows the maximum retention curves that originated from log-normal distributions of particle size and have the same average size and different variance coefficients. The fraction of large particles is higher for the curve with larger variance coefficient. Therefore, the higher the standard deviation, the lower the maximum retention function at low velocities; the maximum retention function increases as the variance coefficient increases at high velocities. As Eq. (8) shows, the maximum retention function for mono-sized particles is a step-function; the larger the particle size deviation, the wider the transitional spread of the maximum retention curve.

The phenomenological model for fines detachment in porous media (1, 3–5) assumes the existence of a maximum retention function and that its form is unconstrained.

We now consider the injection of particle-free water with increasing piecewise-constant velocity into the rock with concentration σ_{a0} of the movable attached fines (Fig. 9c). There is no particle release for small flow velocities, i.e., the attaching torque (6) exceeds the detaching torque for all size particles. The horizontal arrow in Fig. 9c corresponds to velocity increase from zero to the critical velocity U_0 without particle mobilization, i.e., the attached concentration remains constant. The critical velocity is the minimum velocity yielding the first fine appearance in the core effluent. The critical velocity U_0 is determined by the initial concentration of attached fines in the rock

$$\sigma_{a0} = \sigma_{cr}(U_0). \quad (9)$$

Flow velocity increase above U_0 corresponds to movement to the right and down along the maximum retention curve. The abrupt flow velocity increase from U_1 to U_2 yields immediate mobilization of particles with concentration $[\sigma_{cr}(U_1) - \sigma_{cr}(U_2)]$. Particle mobilization yields an increase in suspended concentration of $[\sigma_{cr}(U_1) - \sigma_{cr}(U_2)]/\phi$. The mobilized particles drift along the rock surface with velocity U_s , which is smaller than the flux velocity U . The mobilized particle migrates until being strained by a pore throat with radius smaller than that of the particle. Particle straining in thin pore throats occurs. This results in plugging of the conductive pore path and decrease in permeability. Eq. (4) defines the permeability decline due to the strained concentration

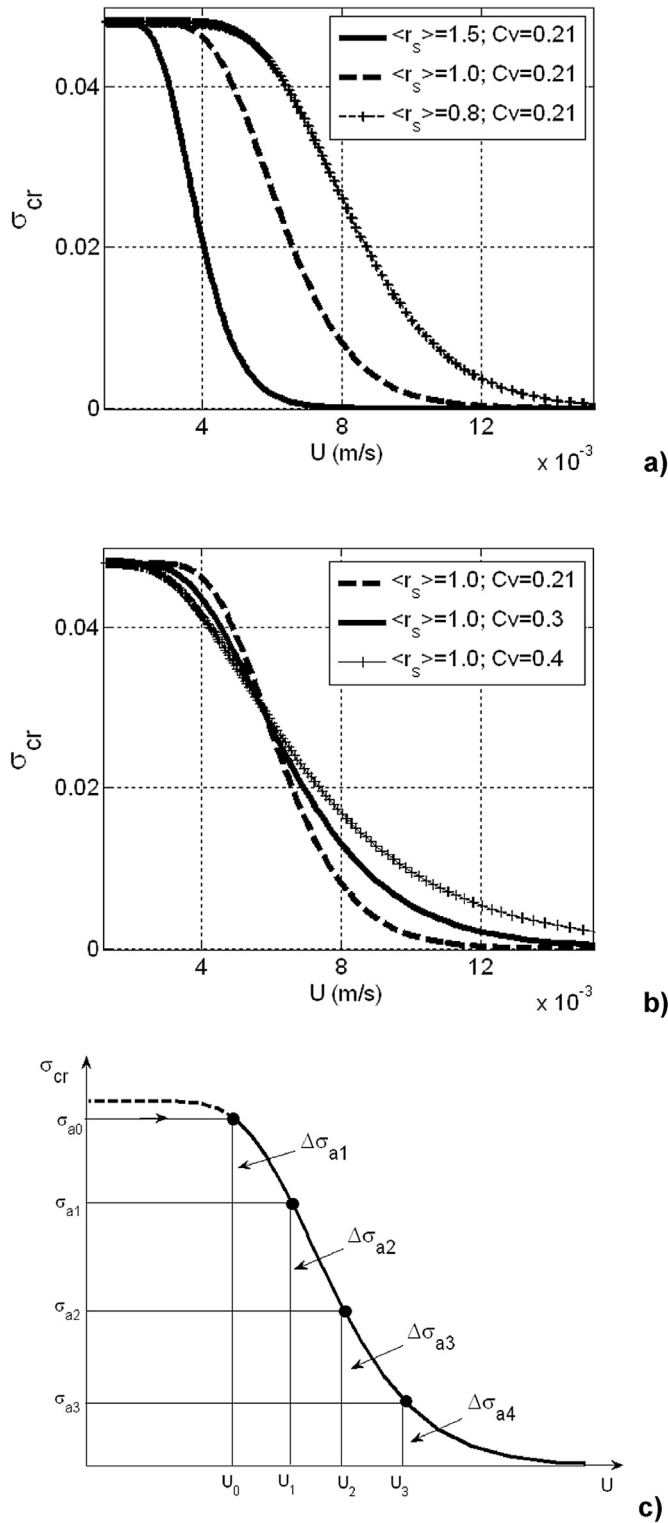


Fig. 9. Form of maximum retention function for the attached fine particles that form a mono-layer on the pore surface: (a) log-normal particle size distribution with varying mean particle size; (b) log-normal particle size distribution with varying variance coefficient; (c) schematic for determining the maximum retention function.

increase. Fig. 10a,b shows the stabilized permeability values for different flow velocities as obtained from the pressure drops across the core and velocities of the two coreflooding tests shown in Fig. 3a and 4a, respectively. The higher the velocity, the larger the

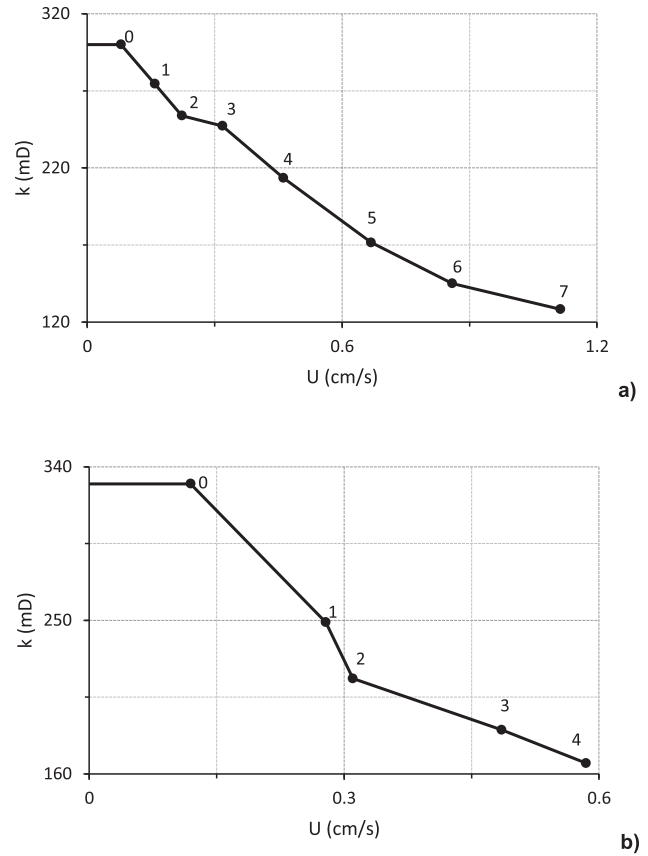


Fig. 10. Stabilized permeability versus velocity: (a) test BS012; (b) test BS013.

strained concentration, and the lower the permeability.

The impedance J denotes the dimensionless pressure drop along the core, normalized by the initial pressure drop:

$$J(T) = \frac{\Delta P(T)U(0)}{U(T)\Delta P(0)} = \frac{k_0}{\langle k \rangle(T)} \tag{10}$$

where $\langle k \rangle(T)$ is the average core permeability. The permeability decline curves in Figs. 3a and 4a are re-calculated into the impedance growth curves in Fig. 11a and b, respectively.

Applying increasing velocity U_n , $n = 1,2,3 \dots$ results in the increase of the pressure drop across the core from Δp_{n-1} to Δp_n , or in permeability decline from k_{n-1} to k_n . Thus, the existence of the maximum attached concentration as a monotonically decreasing flow velocity function (Fig. 9) explains permeability decline during the flow velocity increase.

Figs. 3a and 4a show that permeability stabilization occurs after injection of numerous pore volumes. According to classical filtration theory, the particle mobilized at the core inlet and transported by the carrier water, is either strained or arrives at the outlet after injection of one pore volume, i.e., it appears at the effluent after the flight time along the overall core. However, the permeability stabilization time in Figs. 3, 4 and 10 highly exceeds one pore volume injected. This suggests that the particle transport velocity is significantly lower than the carrier fluid velocity.

The next section introduces the mathematical model for suspension-colloidal transport in porous media with maximum retention function, modelling the particle detachment and slow particle drift with velocity $U_s < U$.

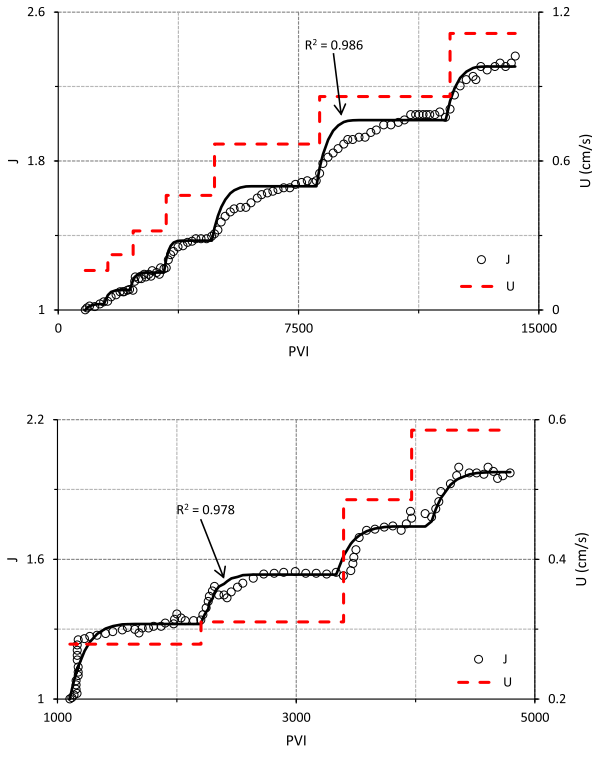


Fig. 11. Pressure drop across the core as obtained from coreflood versus the mathematical model: (a) test BS012; (b) test BS013.

3. Basic governing equations for colloidal transport and detachment in porous media

The above physical analysis supports the following assumptions for a mathematical model of suspension-colloidal transport and detachment in porous media (Yuan and Shapiro, 2011a; Yuan et al., 2012):

- the existence of a function that accurately characterizes the maximum retention concentration for particles attached to a rock surface;
- no re-attachment of the mobilized fines;
- no diffusion of fine particles in long cores;
- incompressibility of the carrier fluid;
- small concentrations of suspended, attached, and strained particles do not perturb the volume of the incompressible carrier fluid;
- viscosity and density of suspension are equal to those of injected water;
- mobilized particles move with velocity U_s , which is lower than the carrier fluid velocity U .

The last assumption implies that all particles drift near to the rock surface with the speed, which is lower than the carrier water velocity, i.e., the suspended concentration of fines carried by a water stream is significantly lower than the drifted particle concentration (Fig. 6). The drift speed U_s is a phenomenological parameter of the model that can be derived from experimental observations.

The assumption $U_s < U$ expresses the difference between the above formulated assumptions and those for the modified model (1, 3–5). Therefore, the system of governing equations includes a mass balance equation for suspended, attached, and strained fines

where the suspended particles are transported by water flux with reduced velocity U_s along the rock surface:

$$\frac{\partial(\phi c + \sigma_s + \sigma_a)}{\partial t} + U_s \frac{\partial c}{\partial x} = 0. \quad (11)$$

The straining rate is proportional to particle advection flux that is cU_s (Herzig et al., 1970; Zheng et al., 2014):

$$\frac{\partial \sigma_s}{\partial t} = \lambda(\sigma_s)U_s c. \quad (12)$$

The attachment rate from Eq. (5) is also proportional to particle advection flux cU_s , if the attached concentration is lower than the maximum retention concentration:

$$\begin{aligned} \frac{\partial \sigma_a}{\partial t} &= \lambda_a U_s c, \quad \sigma_a < \sigma_{cr}(U) \\ \sigma_a &= \sigma_{cr}(U) \end{aligned} \quad (13)$$

Otherwise, the maximum retention concentration given by Eq. (13) holds.

The four equations (4), (11)–(13) for four unknowns c , σ_a , σ_s , and p form a closed system, which constitutes the mathematical model for fines migration in porous media.

Introduce the following dimensionless parameters

$$\begin{aligned} X &= \frac{x}{L}, \quad T = \frac{1}{\phi L} \int_0^t U(y) dy, \quad C = \frac{c\phi}{\sigma_{a0}}, \\ S_a &= \frac{\sigma_a}{\sigma_{a0}}, \quad S_s = \frac{\sigma_s}{\sigma_{a0}}, \quad P = \frac{kp}{\mu LU}, \\ \alpha_n &= \frac{U_{sn}}{U_n}, \quad A_a = \lambda_a L, \quad A_s = \lambda_s L, \end{aligned} \quad (14)$$

where the particle drift velocities U_{sn} and the delay factors α_n , $n = 1, 2, 3, \dots$ correspond to flow velocities U_n ; T is the accumulated dimensionless volume of the injected water. For the case of piecewise-constant flow velocity $U(t)$, the dimensionless $T(t)$ is piecewise-linear function.

Substitution of dimensionless parameters (14) into governing equations (4), (11)–(13) results in the following dimensionless system:

$$\frac{\partial(C + S_s + S_a)}{\partial T} + \alpha_n \frac{\partial C}{\partial X} = 0 \quad (15)$$

$$\frac{\partial S_s}{\partial T} = A_s \alpha_n C \quad (16)$$

$$\begin{aligned} \frac{\partial S_a}{\partial T} &= A_a \alpha_n C, \quad S_a < S_{cr}(U) \\ S_a &= S_{cr}(U) \end{aligned} \quad (17)$$

$$1 = \frac{1}{1 + \beta_s \sigma_{a0} S_s} \frac{\partial P}{\partial X}. \quad (18)$$

The next section solves dimensionless governing system (15–18) is solved for the conditions of laboratory tests with piecewise-constant increasing velocity.

4. Analytical model for one-dimensional colloidal flow with detachment and straining

We now consider coreflooding where velocity U_1 is higher than

Table 1
Analytical model for one-dimensional fines migration with increase in piecewise-constant velocity.

Term	Explicit formulae	(X,T)-Domain
Suspension concentration during stage 1	$C = 0$ $C = \Delta S_{a1} e^{-\alpha_1 A_s T}$	$X \leq \alpha_1 T$ $X > \alpha_1 T$
Retention concentration during stage 1	$S_s = \Delta S_{a1} (1 - e^{-A_s X})$ $S_s = \Delta S_{a1} (1 - e^{-\alpha_1 A_s T})$	$X \leq \alpha_1 T$ $X > \alpha_1 T$
Impedance during stage 1	$J(T) = 1 + \beta_s \sigma_{a0} \Delta S_{a1} \left[1 - \frac{1}{A_s} - \left(1 - \frac{1}{A_s} - \alpha_1 T \right) e^{-\alpha_1 A_s T} \right]$ $J(T) = 1 + \beta_s \sigma_{a0} \Delta S_{a1} \left[1 - \frac{1}{A_s} - \frac{e^{-A_s}}{A_s} \right]$	$T < \alpha_1^{-1}$ $T \geq \alpha_1^{-1}$
Suspension concentration during stage n	$C = 0$ $C = \Delta S_{an} e^{-\alpha_n A_s (T - T_n)}$	$X \leq \alpha_1 T$ $X > \alpha_1 T$
Retention concentration during stage n	$S_s - S_{sn} = \Delta S_{an} (1 - e^{-A_s X})$ $S_s - S_{sn} = \Delta S_{an} [1 - e^{-\alpha_n A_s (T - T_n)}]$	$X < \alpha_n (T - T_n)$ $X \geq \alpha_n (T - T_n)$
Impedance during stage n	$J(T) = J_{0n} + \beta_s \sigma_{a0} \Delta S_{an} \left[1 - \frac{1}{A_s} - \left(1 - \frac{1}{A_s} - \alpha_1 (T - T_n) \right) e^{-\alpha_n A_s (T - T_n)} \right]$ $J(T) = J_{0n} + \beta_s \sigma_{a0} \Delta S_{an} \left[1 - \frac{1}{A_s} - \frac{e^{-A_s}}{A_s} \right]$	$T < T_n + \alpha_1^{-1}$ $T \geq T_n + \alpha_1^{-1}$

the critical velocity, i.e., $\sigma_{a0} > \sigma_{cr}(U_1)$. The excess of the attached concentration is instantly released into the colloidal suspension. The model assumes that straining to be irreversible. The initial concentration of strained particles is accounted for in initial porosity and permeability. The attached concentration S_a remains constant during the constant-rate injection. Thus, the initial conditions are:

$$T = 0 : \quad C = \Delta S_{a1} = S_{a0} - S_{cr}(U_1), \quad (19)$$

$$S_s = 0, \quad S_a = S_{cr}(U_1)$$

The inlet boundary condition corresponds to injection of particle-free water:

$$X = 0 : \quad c = 0. \quad (20)$$

Substituting the expression for straining rate (16) into mass balance equation (15) and accounting for steady state distribution of S_a yields The linear first-order hyperbolic equation

$$\frac{\partial C}{\partial T} + \alpha_1 \frac{\partial C}{\partial X} = -A_s \alpha_1 C. \quad (21)$$

The next section solves Eq. (21) subject to initial and boundary conditions (19, 20) by the method of characteristics.

4.1. Exact solution for constant-rate injection

The characteristic speed in Eq. (21) is equal to α_1 . The solution $C(X,T)$ is presented in Table 1. Eq. (16) determines the strained concentration $S_s(X,T)$ by integration in T .

The concentration front of the injected particle-free water propagates along the trajectory $X = \alpha_1 T$ (Fig. 12a). The concentration equals zero in zone II behind the concentration front. The moment $T = 1/\alpha_1$ corresponds to arrival of the “last” released fine at the core outlet. The released particles with uniform concentration move with the same velocity subject to capture in the vacant pores with the same probability. Therefore, the suspended concentration profile remains uniform during the flow, and suspension concentration in zone I is independent of X (see row 2 in Table 1).

Because the suspended concentration profile is uniform, strained concentration is independent of X ahead of the concentration front. Straining occurs for non-zero suspended concentration. Thus, the strained particles accumulate until the arrival of the concentration front. Afterwards, the strained concentration remains the same, implying that it is steady state behind the concentration front.

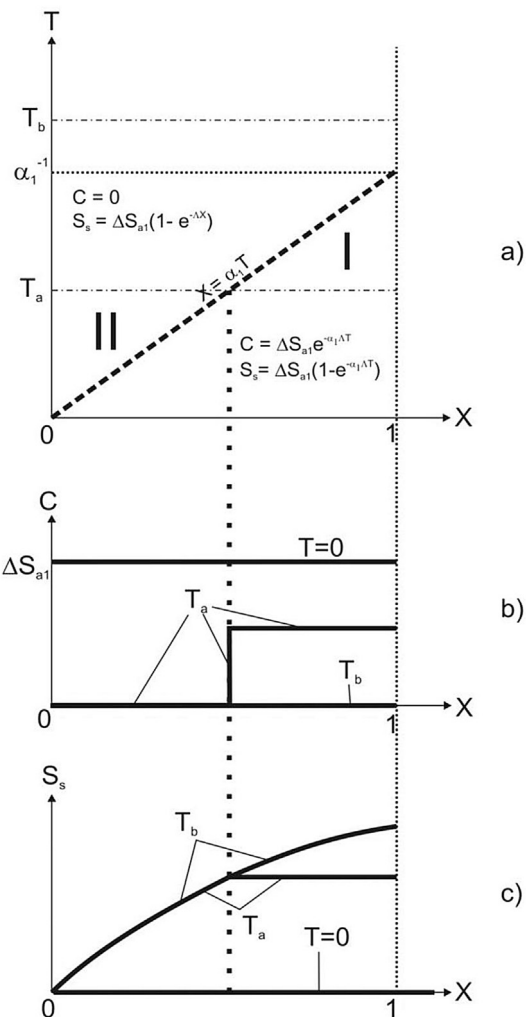


Fig. 12. Solution of fines migration problem under elevated velocity: (a) trajectory of fronts and characteristic lines in the (X,T) -plane; (b) suspended concentration profiles at three moments; (c) strained concentration profiles at three moments.

Fig. 12b shows suspended concentration profiles at $T = 0$, at the moment T_a before the front arrival at the core outlet, and at the moment T_b after the front's arrival. The initial concentration equals

ΔS_{a1} . The suspended concentration profile before the front's arrival is zero behind the front and constant ahead of the front. The suspended concentration becomes zero after front's arrival, because all particles become either strained or produced at the effluent.

Fig. 12c shows three profiles of strained concentration at times 0, T_a , and T_b . There are no strained particles in the rock before the fines mobilization. The strained concentration grows with time until the front's arrival moment and remains constant afterwards. The larger the value of X the more prolonged the straining process and the higher the maximum concentration of accumulated strained particles. Thus, the strained-concentration profiles grow as X increases. The profile is uniform ahead of the front, because the particle advective flux is uniform along with the particle capture probability.

The breakthrough concentration history is shown in Fig. 13. The distance that particle travels until its arrival at the outlet increases with time; thus, breakthrough concentration decreases. The filtration coefficient λ_s equals the straining probability per unit length of the particle trajectory (Herzig et al., 1970). Therefore, the captured-particle concentration increases with time, yielding the decrease in the breakthrough concentration.

At the moment

$$T_{st,1} = \frac{1}{\alpha_1}, \quad (22)$$

all mobilized fines either are strained or exit the core, i.e., suspended concentration becomes zero. The rock permeability stabilizes at this moment.

We now calculate the impedance from Eq. (10). From (18), for the time interval with constant flow velocity, the impedance is:

$$J(T) = \int_0^1 \left(-\frac{\partial P}{\partial X} \right) dX = 1 + \beta_s \sigma_{a0} \int_0^1 S_s(X, T) dX. \quad (23)$$

Substituting the solution of retention concentration (rows 4 and 5 in Table 1) into Eq. (23) and integrating in X yields the explicit formula for the impedance increase during the injection:

$$J(T) = 1 + \beta_s \sigma_{a0} \Delta S_{a1} \left[1 - \frac{1}{A_s} - \left(1 - \frac{1}{A_s} - \alpha_1 T \right) e^{-\alpha_1 A_s T} \right], \quad T < \alpha_1^{-1}. \quad (24)$$

Substituting the expression for stabilization time (22) into Eq. (24) yields the stabilized impedance value

$$J(T_{st1}) = 1 + \beta_s \sigma_{a0} \Delta S_{a1} \left(1 - \frac{1}{A_s} + \frac{e^{-A_s}}{A_s} \right), \quad T \geq \alpha_1^{-1}. \quad (25)$$

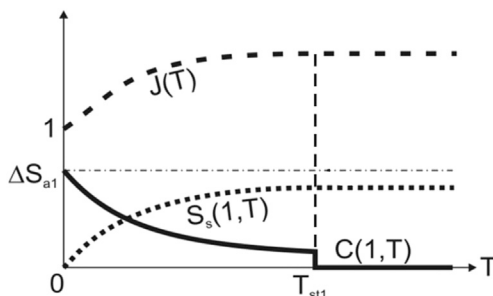


Fig. 13. Histories for breakthrough concentration C , strained concentration S_s at the outlet, and dimensionless pressure drop across the core J .

The dimensionless pressure drop across the core monotonically increases from one to the maximum value, which is attained at time $1/\alpha_1$, when the “last” mobilized particle arrives at the core outlet (Fig. 13). Afterwards, the pressure drop remains constant.

4.2. Exact solution for multiple injections

The solution of problem (15–18) after changing velocity from U_{n-1} to U_n is analogous to the solution of the first stage under velocity U_1 . The only difference is that the strained concentration for $T > T_n$ is the total of the strained concentration before the velocity alteration at time $T = T_n - 0$ and the concentration of particles that have been strained during time $T > T_n$. The model assumes that velocity alteration occurs after permeability stabilization.

We now consider the change in flow velocity from U_{n-1} to U_n . This results in release of the particles with concentration $\Delta \sigma_{an}$ that equals $[\sigma_{cr}(U_{n-1}) - \sigma_{cr}(U_n)]$. The initial condition corresponds to detachment of the attached particles into the suspension and to the “heritage” of the strained concentration from the previous injection with velocity U_{n-1} :

$$T = T_n : \quad \begin{aligned} C &= \Delta S_{an} = S_{cr}(U_{n-1}) - S_{cr}(U_n), \\ S_s &= S_s(X, T_n - 0), \quad S_a = S_{cr}(U_n) \end{aligned} \quad (26)$$

Substitution of strained concentration from Table 1 into Darcy's law (18) and integration of the pressure gradient expression in X along the core yield the impedance for $T > T_n$:

$$\begin{aligned} T < T_n + \alpha_n^{-1} : \\ J(T) &= J_{0n} + \beta_s \sigma_{a0} \Delta S_{an} \left[1 - \frac{1}{A_s} - \left(1 - \frac{1}{A_s} - \alpha_n (T - T_n) \right) e^{-\alpha_n A_s (T - T_n)} \right] \end{aligned} \quad (27)$$

Substitution of stabilized time $T = T_n + 1/\alpha_n$ into Eq. (27) yields the stabilized impedance after the n -th injection with velocity U_n .

The next section uses the analytical-model based formulae for impedance (rows 12 and 13 in Table 1) in order to match the laboratory test data.

5. Determination of the model rheological functions from the experiments

Two laboratory corefloods were performed using the Berea cores for real bottom-hole pressures and temperatures in order to reproduce the injection of water in the well. The details of laboratory set-up, materials, and procedures can be found in Ochi and Vernoux (1998). Seven velocities in test BS012 and four velocities in test BS013 were applied (Figs. 3b and 4b). The tests were performed in accordance to initial and boundary conditions (19, 20): clean particle-free water was injected with piecewise-constant increasing velocity; the pressure drop across the core was monitored during the injection. Two Berea sandstone cores from the same block were used in both tests. It was found that the kaolinite fines were lifted under the increasing velocities from the quartz grains. The analytical model presented in the previous Section matches the pressure drop across the core during the injection with different velocities. The model constants were adjusted by minimizing the deviation between the modelled and measured pressure drop histories.

5.1. Tuning the model by applying laboratory coreflood data

The model assumes that the filtration and formation-damage coefficients are constant, i.e., they are independent of velocity and retained concentrations. However, the drift delay factor is not

assumed to be constant, i.e., the rock surface alteration during the particle detachment yields the drift velocity change.

From (4), for stabilized permeability values k_n fulfil the following relationship

$$\beta[\sigma_{cr}(U_{n-1})]\Delta\sigma_{an} = \frac{k_{n-1}}{k_n} - 1. \tag{28}$$

The least square tuning of the pressure drop data as monitored across the core during corefloods with different rates yield the filtration coefficient λ_s , the products $\beta_s\Delta\sigma_{cr}(U_n)$, $n = 1, 2, \dots$, and the drift delay factors α_n for different velocities U_n . To solve the optimization problem, we applied the reflective trust region algorithm (Coleman and Li, 1996) using the software Matlab (Mathworks, 2010).

Figs. 3a and 4a present the average permeability as calculated from the pressure drop across the core (Ochi and Vernoux, 1998). It allows calculating the impedance (10). The impedance values $J(T)$ calculated from experimental data are depicted using circles in Fig. 11.

We assume a typical mass concentration of 0.06 for movable kaolinite clay in the Berea sandstone (Khilar and Fogler, 1998). Assuming typical porosity of 0.2 for the Berea core, we calculate the attached volumetric concentration $\sigma_{a0} = 0.06 \times 0.8 = 0.048$. This is the critical retention value that corresponds to the critical velocity $U_0 < U_1$, as shown in Eq. (9). Finally, the formation-damage coefficient for straining is found from the condition of full removal of attached fine particles from the rock at the maximum velocity during the last injection:

$$\beta_s = \frac{1}{\sigma_{a0}} \sum_{n=1}^N (\beta_s \Delta\sigma_{an}), \tag{29}$$

where the groups $\beta_s\Delta\sigma_{an}$ are obtained by the tuning. The values of released concentrations $\Delta\sigma_{an}$ allow calculating maximum retention function $\sigma_{cr}(U)$:

$$\sigma_{cr}(U_n) = \sigma_{a0} - \sum_{n=1}^N \Delta\sigma(U_n). \tag{30}$$

5.2. Analysis of the results

Table 2 presents the results of the impedance history matching for two cores. The continuous impedance curves in Fig. 11 correspond to prediction by the adjusted model. Velocity dependencies of the drift delay factor as obtained from the tuning are presented in Figs. 3d and 4d for floods in two cores. The dependency is monotonically decreasing.

Fig. 11 indicates that the model closely matches the experimental data; the coefficient of determination R^2 is close to one. Comparing the impedance data with fixed drift delay factors $\alpha_n = \text{constant}$ yields significantly lower values of R^2 criterion. Fixed values of drift delay factor for each period of the constant-velocity injection were assumed during the model adjustment.

Fig. 14 shows the maximum retention function as obtained by tuning and further analytical modelling applying formula (30) for both cores. The higher the velocity, the higher the drag and lift forces detaching the fines from the rock grains and the smaller the concentration of “remaining” attached fine particles.

The maximum retention curves are not convex, which can be explained by the mono-layer different-sized fines attached to the grain surfaces, using the mechanical equilibrium model (6, 8).

The model allows determining the size distribution of attached

Table 2
Adjusted values of the model parameters.

Parameter	Value for the test BS012	Value for the test BS013
α_1	0.0020	0.0018
α_2	0.0020	0.0018
α_3	0.0020	0.0018
α_4	0.0020	0.0018
α_5	0.0020	–
α_6	0.0008	–
α_7	0.0008	–
$\Delta\sigma_{a1}$	0.0017	0.0206
$\Delta\sigma_{a2}$	0.0039	0.0102
$\Delta\sigma_{a3}$	0.0045	0.0086
$\Delta\sigma_{a4}$	0.0076	0.0086
$\Delta\sigma_{a5}$	0.0114	–
$\Delta\sigma_{a6}$	0.0114	–
$\Delta\sigma_{a7}$	0.0076	–
λL	2.2869	3.0069
β	30.9328	22.9161

fines $\Sigma_a(r_s)$ from the maximum retention function $\sigma_{cr}(U)$; the minimum mobilized size $r_{scr}(U)$ is determined from Eq. (6), and the size distribution $\Sigma_a(r_s)$ is calculated from (8) by regularized numerical differentiation (Coleman and Li, 1996).

The velocity U was not changed continuously in the tests: the first coreflood test applies seven values for velocity; the second test applies four values. Therefore, the resulting fines size distributions are given by histogram in Fig. 15. Figs. 3c and 4c show that minimum radius of particles detached by flow with velocity U decreases as velocity increases.

Fig. 16 compares various forces exerting on the particles at the critical condition of their mobilization for the matched systems in

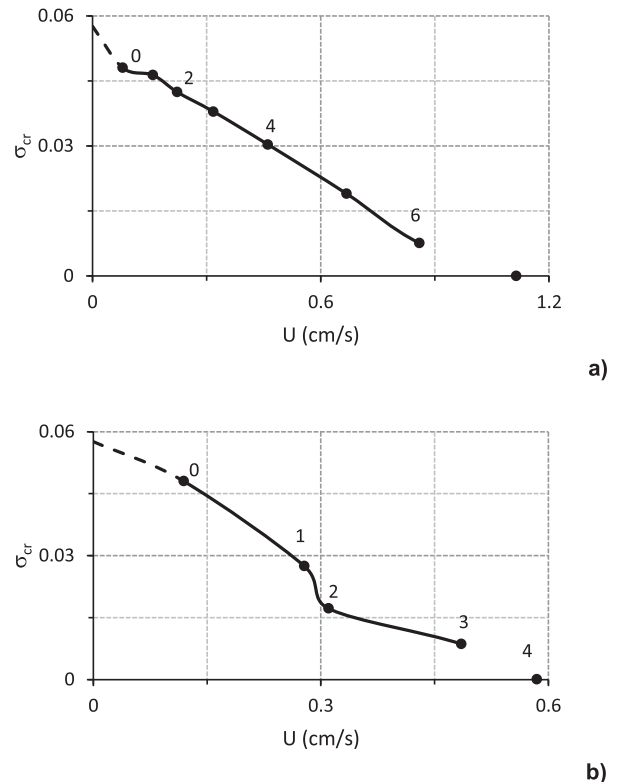


Fig. 14. Maximum retention curves $\sigma_{cr}(U)$ as obtained from test data: (a) coreflood test BS012; (b) test BS013.

two coreflood tests. The ranges of particle radii cover those presented by attached particle size distributions (Fig. 15). Electrostatic force is two orders of magnitude larger than drag force. Lift and gravitational forces are negligible compared to drag force. The lever arm ratio significantly exceeds one, thus small drag torque can exceed the torque of electrostatic force.

This graph allows parameterizing the maximum retention function by the critical particle radius $\sigma_{cr}(U) = \sigma_{cr}(r_{scr}(U))$. The value $\sigma_{cr}(r_{scr})$ is an accumulation function of retained concentration for all particles with radius smaller than r_{scr} . Fig. 15 shows the corresponding histogram. This function shows the concentration distribution of initial reservoir fines for various radii. It allows interpreting the maximum retention function for different-sized fines particles attached to pore walls: $\sigma_{cr}(U)$ is the concentration of attached particles that cannot be mobilized by flow with velocity U ; these particles have radii smaller than $r_{scr}(U)$. Figs. 3c and 4c show that minimum radius of particles detached by flow with velocity U decreases as U increases.

Table 2 shows that the values of filtration and formation-damage coefficients remain within the common ranges (Pang and Sharma, 1997).

6. Discussion and summary

The mathematical model that includes the maximum retention function for particle detachment and particle transport, with the velocity of carrier fluid (1, 3, 5), exhibits permeability stabilization after 1 PVI. However, the laboratory tests showed stabilization periods that significantly exceed 1 PVI. We attribute this to particle movement that is slower than carrier fluid velocity. When the two-

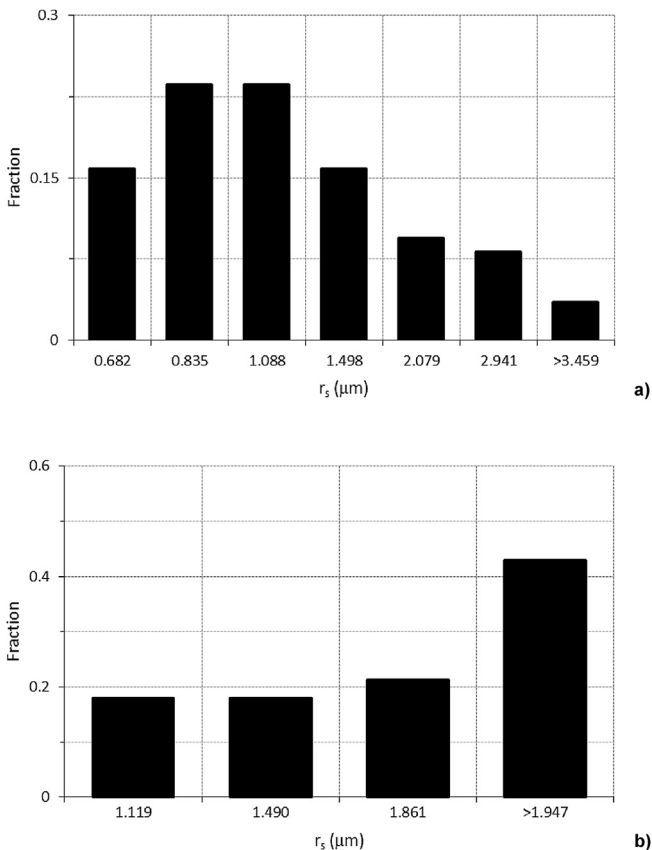


Fig. 15. Histograms of movable fines on the matrix surface: (a) test BS012; (b) test BS013.

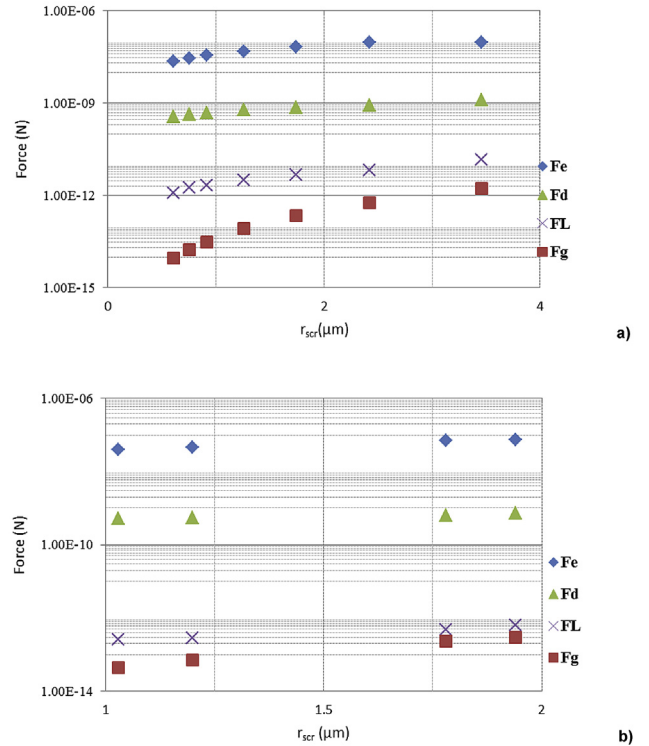


Fig. 16. Forces acting on the attached particles: (a) for test BS012; (b) for test BS013.

speed model containing six constants of mass exchange between slow and fast particles, two filtration coefficients and two detachment coefficients for fast and slow particles, is applied, it describes the effects of slow fine particles migration (Yuan and Shapiro, 2011a, b; Bradford et al., 2012). However, the breakthrough curves cannot provide the unique tuning of the model. Significantly more complex tests that measure pressure drop and retained concentration are also required for complete characterization of the two-speed model. Yet, only histories of pressure drop across the core are available in the majority of fines migration laboratory studies. Therefore, the current work considers the special case corresponding to rapid mass exchange between fast and slow particle populations across each pore, which is assumed to be significantly faster than particle capture by the rock with free run along numerous pore lengths. It results in equal particle concentrations in the fast and slow fluxes, leading to a single-velocity model that reflects the average particle speed.

The particle velocity in the proposed model (11–13) significantly differs from the carrier fluid velocity. Matching the laboratory data by the analytical model data reveals that the particle velocities are significantly smaller than the carrier fluid velocity. With drift delay factors α_n varying from 0.0008 to 0.002, the delay times vary from 500 PVI to 1250 PVI.

In general, water carries the fraction of the mobilized particles, and another fraction moves along the grain surfaces with significantly lower speed. The fines size distribution, flow velocity and the electrostatic fines-rock interaction determine the fraction value. The near-rock-surface drift of detached fines is a combination of rolling, sliding, temporary detachment into fluid, and return to the surface due to collision with asperities, etc. (Li et al., 2006; Yuan and Shapiro, 2011b; Sefrioui et al., 2013).

It follows from the torque balance for an immobile particle situated at the matrix surface, that for each carrier fluid velocity, there exists such a critical particle radius, in which all larger particles are

removed from the surface: $r_{scr} = r_{scr}(U)$ (Fig. 8). It allows the maximum retention function for a mono-layer of attached different-size particles to be defined as the concentration of attached particles with size smaller than the critical size. From the definition follows the calculation method for the maximum retention function from size distribution of attached movable particles. It also allows solving the inverse problem of determining the size distribution of attached movable particles from the maximum retention function.

The maximum retention function for different-size fine particles attached to pore walls in a monolayer depends on attached fines radius histogram, on electrostatic constants of the particle-rock interaction, and on particle and rock Young's moduli and Poisson's ratios.

The larger the particles, the lower the maximum retention function. The higher the variance coefficient for particle size distribution, the lower the maximum retention function for low velocities and the higher the maximum retention function for high velocities.

The maximum retention function for poly-layer attachment of mono-sized particles is convex, whereas that for the mono-layer of poly-dispersed particles can be any monotonically decreasing curve. The maximum retention curve for mono-layer deposit and log-normal particle size distribution is convex for small velocities and is concave for high velocities (Fig. 9).

The one dimensional problem for flow with piecewise-constant increasing velocity, instant particle release, and the consequent rock straining allows for exact analytical solution. The concentration fronts starts at the core inlet at the moment of abrupt velocity alternation, coincides with the trajectory of the drifting particle, and separates the particle-free region behind the front and the region ahead of the front, where the suspended concentration profile is uniform.

The mathematical model assumes a constant drift-delay factor. In reality, the drift-delay factor depends on the particle size and the geometry of the porous media, which changes during straining. The smaller the particle the closer to the wall it moves, the lower its speed, and the lower the drift delay factor. The velocity increased with time in the investigated laboratory tests; thus, the radii of the released particles decrease. This explains the decreasing drift-delay factor in Fig. 1d. The next step in the model's development would be the introduction of a phenomenological function for the drift-delay factor: $\alpha = \alpha(r_s, \sigma_s)$.

The pressure drop history during coreflooding that involves a piecewise-constant increasing velocity closely matches the mathematical modelling data. However, good agreement between the laboratory data and the matched modelling prediction provides just a preliminary validation of the mathematical model. The laboratory tests with measurements of retention profiles, breakthrough concentration history and particle size distribution must be performed and matched by the analytical solutions listed in Table 1 in order to validate the model with the particle drift velocity that differs from the carrier flow velocity. To our knowledge, no such tests have appeared in the literature.

7. Conclusions

The analytical modelling of fines release with piecewise-constant increasing velocity during coreflooding and its comparison with laboratory test results allow drawing the following conclusions:

- Low-velocity fines migration in porous media explains the long permeability-stabilization periods.
- The higher the flow velocity the smaller the mobilized particles.

- The maximum retention function for size-distributed fine particles attached to pore walls in a mono-layer is expressed by an explicit formula that includes the size distribution of attached particles and the critical detached size curve. This function is equal to accumulated concentration of particles smaller than that mobilized by the flux with a given flow with velocity U .
- The larger the fine particle size, the smaller the critical retention function. The larger the variance coefficient for particle sizes, the higher the maximum retention function at high velocities and the lower the maximum retention function at low velocities.
- Size distribution of the attached movable particles can be determined from the maximum retention function and the critical detached size curve.
- Matching the pressure drop curves as obtained from two laboratory coreflows by the proposed model exhibit high agreement with coefficient of determination exceeding 0.98.

Acknowledgements

The authors thank Dr. Alex Badalyan and Dr. Themis Carageorgos (University of Adelaide) for fruitful discussions and co-operation. The PhD work of Y. Yang was sponsored by the China Scholarship Council (CSC). The PhD work of F.D. Siqueira was sponsored by PRH-20/ANP; his visit to the University of Adelaide was sponsored by PDSE/CAPES. Pavel Bedrikovetsky acknowledges the program "Science without Boundaries" and CAPES, Brazil for providing 2014–2016 scholarship. Open Fund of State Key Laboratory of Oil and Gas Reservoir Geology and Exploitation (Chengdu University of Technology) (PLC201409) is gratefully acknowledged by Z. You and Y. Yang. Many thanks go to David H. Levin (Murphy, NC, USA) who provided professional English-language editing of this article.

Appendix. Forces acting on a particle at the pore surface

Fig. 5 shows a fine particle attached to the pore wall. Such a particle is subject to the drag, lift, buoyancy and electrostatic forces. Fig. 5a corresponds to the case of attractive electrostatic force and a deformable particle. Fig. 5b shows a non-deformable particle secured by the rock surface asperity and revolving around it at the moment of detachment. Electrostatic and gravitational forces attach a particle to the surface, whereas drag and lift forces attempt to detach it. Below are the expressions for all of these forces and the mechanical equilibrium condition.

Drag force

The expression for drag force acting on a particle on the plane surface is obtained from the asymptotic solution of the Navier-Stokes equations by O'Neill (1968). This expression is widely used in the modelling of particle attachment and detachment in porous media (Bergendahl and Grasso, 2003; Bradford et al., 2013)

$$F_d = \omega \pi \mu r_s u_t |_{H-r_s}. \quad (\text{A-1})$$

Here μ is the fluid viscosity, r_s is the particle radius, H is a half-width of the channel, u_t is the tangential cross flow velocity of the fluid in the center of the particle and the drag factor ω equals 6×1.7 . The case of $\omega = 6$ corresponds to the Stokes formula for a particle in the uniform boundary-free flux.

Velocities in the center of the particle situated on the pore wall are

$$u_t|_{H-r_s} = \frac{3r_s\bar{u}}{H}, \quad u_t|_{r_w-r_s} = \frac{2r_s q}{\pi r_w^3}, \quad (\text{A-2})$$

for Hele-Shaw flow in a slot and for Poiseuille flow in a tube, respectively. Here \bar{u} is average velocity through a slot.

Lift force

The lift force exerting on a spherical particle on the plane surface is

$$F_l = \chi \left[\rho \mu \left(r_s u_t|_{H-r_s} \right)^3 \right]^{1/2}, \quad (\text{A-3})$$

where ρ is the carrier water density. Kang et al. (2004) calculated the lift factor χ as 81.2 by, whereas Altmann and Ripperger (1997) gave a value of 0.761; ρ is the carrier water density. Akhatov et al. (2008) derived similar expression for the lift. The above references derived their equations from the work by Saffmann (1968).

Buoyancy force

The net gravitational force acting on a spherical particle in water is

$$F_g = \frac{4}{3} \Delta \rho g r_s^3. \quad (\text{A-4})$$

Here $\Delta \rho$ is the density difference between the particle matter and carrier water.

Electrostatic forces

The total electrostatic force is the derivative from the overall potential energy:

$$F_e = -\frac{\partial V}{\partial h}, \quad (\text{A-5})$$

where the total energy is the sum of the London-van-der-Waals, double electric layer and Born potentials, given by the so-called DLVO (Derjaguin-Landau-Verwey-Overbeek) theory (Derjaguin and Landau, 1941; Elimelech et al., 1995; Khilar and Fogler, 1998; Israelachvili, 2011):

$$V_{LVA} = -\frac{A_{132}}{6} \left[\frac{2(1+Z)}{Z(2+Z)} + \ln \left(\frac{Z}{2+Z} \right) \right], \quad Z = \frac{h}{r_s} \quad (\text{A-6})$$

$$V_{DLR} = \frac{\epsilon_0 D e r_s}{4} \left[2\psi_{01}\psi_{02} \ln \left(\frac{1 + \exp(-\kappa h)}{1 - \exp(-\kappa h)} \right) - (\psi_{01}^2 + \psi_{02}^2) \ln(1 - \exp(-2\kappa h)) \right] \quad (\text{A-7})$$

$$V_{BR} = \frac{A_{132}}{7560} \left(\frac{\sigma_{lj}}{r_s} \right)^6 \left[\frac{8+Z}{(2+Z)^7} + \frac{6-Z}{Z^7} \right] \quad (\text{A-8})$$

$$V = V_{LVA} + V_{DLR} + V_{BR} \quad (\text{A-9})$$

Here A_{132} is the Hamaker constant, h is the surface-to-surface separation length, Z is its dimensionless value, ϵ_0 is the electric constant (permittivity of free space), D is the dielectric constant, ψ_{01} and ψ_{02} are the surface potentials of particles and collectors-grains,

respectively, and σ_{lj} is the atomic collision diameter in Lennard-Jones potential. The inverse Debye length κ is

$$\kappa = \sqrt{\left(\frac{e^2 \sum v_i z_i^2}{\epsilon_0 D k_B T} \right)}, \quad (\text{A-10})$$

where k_B is the Boltzmann's constant, v_i is a bulk i -th ion concentration as defined by the number of ions per unit volume, z_i is a valence of the i -th ion and e is the electron charge $e = 1.6 \times 10^{-19}$ C.

For aqueous solutions under normal temperature, the above formula simplifies to

$$\kappa = 0.73 \times 10^8 \sqrt{\sum C_{mi} z_i^2}, \quad (\text{A-11})$$

where C_{mi} is the molar concentration of i -th ion in mol/m^3 (Elimelech et al., 1995).

The main text uses force expressions (A1–A11) to determine the conditions of mechanical equilibrium of particles on the pore walls (6) in order to calculate the maximum retention function (9).

Nomenclature

A_{132}	Hamaker constant for interaction between material 1 and 2 in medium 3 ($\text{kg m}^2 \text{s}^{-2}$)
c	Suspended particle concentration (m^{-3})
C	Dimensionless suspended particle concentration
C_{mi}	Molar concentration of i -th ion (m^{-3})
D_e	Dielectric constant
e	electron charge (C)
E	Young's modulus ($\text{kg m}^{-1} \text{s}^{-2}$)
F	Force (N)
h	Particle-surface separation distance (m)
H	Half width of the channel (m)
J	Impedance (normalized reciprocal of mean permeability)
k	Permeability (m^2)
k_{det}	Detachment coefficient
$\langle k \rangle$	Mean permeability (m^2)
k_B	Boltzmann constant ($\text{kg m}^2 \text{s}^{-2} \text{K}^{-1}$)
k_n	Number of data points in each stage
K	Composite Young's modulus ($\text{kg m}^{-1} \text{s}^{-2}$)
l	Lever arm ratio
l_n	Normal lever (m)
l_d	Tangential (drag) lever (m)
L	Core length (m)
p	Pressure (Pa)
P	Dimensionless pressure
n	Serial number of different-rate flow
r_s	Radius of a particle (m)
r_{scr}	Critical radius of a particle that can be removed at certain velocity (m)
S	Dimensionless retained particle concentration
ΔS_{a1}	Dimensionless mobilized concentration of detached particles with velocity switch from U_0 to U_1
t	Time (s)
T	Dimensionless time
$t_{st,n}$	Stabilization time for n th flow rate (s)
$T_{st,n}$	Dimensionless stabilization time for n th flow rate
t_n	Initial time of n th flow rate (s)
T_n	Dimensionless initial time of n th flow rate
\bar{u}	Average velocity through a slot
u_t	The tangential cross flow velocity of fluid in the center of the particle
U	Darcy's velocity (m s^{-1})

U_s	Particle's seepage velocity (m s^{-1})
V	Potential energy ($\text{kg m}^2 \text{s}^{-2}$)
x	Linear coordinate (m)
X	Dimensionless linear coordinate
z_i	Electrolyte valence of the i -th ion

Greek symbols

α	Drift delay factor
β	Formation-damage coefficient
ϵ_0	Free space permittivity ($\text{C}^{-2} \text{J}^{-1} \text{m}^{-1}$)
κ	Debye length (m^{-1})
λ	Filtration coefficient (m^{-1})
Λ	Dimensionless filtration coefficient
μ	Dynamic viscosity ($\text{kg m}^{-1} \text{s}^{-1}$)
ν	Poisson's ratio
ρ	Fluid density (kg m^{-3})
ρ_s	Particle density (kg m^{-3})
σ_{cr}	Critical retention concentration (m^{-3})
$\Sigma_a(r_s)$	Size distribution of attached particles (m^{-4})
σ	Concentration of retained particles (m^{-3})
$\Delta\sigma_n$	Mobilized concentration of detached particles with velocity switch from U_{n-1} to U_n
σ_{LJ}	Atomic collision diameter (m)
ν_i	The number of ions per unit volume
χ	Lifting factor
ϕ	Porosity
Ψ_{01}	Particle surface potential
Ψ_{02}	Collector surface potential
ω	Drag factor

Subscripts

a	Attached (for fine particles)
l	Lift (for force)
e	Electrostatic (for force)
n	Normal (for force), flow rate number (for velocities, inherited retained concentrations, particle – fluid velocity ratios, inherited impedances)
s	Strained (for fine particles)
0	Initial value or condition (for permeability, retained concentrations)
d	Drag (for force)
g	Gravitational (for force)
BR	Born repulsion (for potential energy)
DLR	Electrostatic double layer (for potential energy)
LVA	London-van der Waal (for potential energy)

References

- Akhatov, I.S., Hoey, J.M., Swenson, O.F., Schulz, D.L., 2008. Aerosol focusing on micro-capillaries: theory and experiment. *J. Aerosol Sci.* 39, 691–709.
- Altmann, J., Ripperger, S., 1997. Particle deposition and layer formation at the cross flow micro filtration. *J. Membr. Sci.* 124, 119–128.
- Arab, D., Pourafshary, P., Ayatollahi, Sh, Habibi, A., 2014. Remediation of colloid-facilitated contaminant transport in saturated porous media treated with nanoparticles. *Int. J. Environ. Sci. Technol.* 11 (1), 207–216.
- Bai, T., Chen, Z., Aminossadati, S.M., Pan, Z., Liu, J., Li, L., 2015. Characterization of coal fines generation: a micro-scale investigation. *J. Nat. Gas. Sci. Eng.* 27, 862–875.
- Bedrikovetsky, P., Siqueira, F.D., Furtado, C.A., Souza, A.L.S., 2011. Modified particle detachment model for colloidal transport in porous media. *Transp. Porous Media* 86 (2), 353–383.
- Bedrikovetsky, P., Zeinijahromi, A., Siqueira, F.D., Furtado, C., de Souza, A.L.S., 2012. Particle detachment under velocity alternation during suspension transport in porous media. *Transp. Porous Media* 91 (1), 173–197.
- Bergendahl, J.A., Grasso, D., 2003. Mechanistic basis for particle detachment from granular media. *Environ. Sci. Technol.* 37 (10), 2317–2322.
- Bradford, S.A., Bettahar, M., 2005. Straining, attachment, and detachment of cryptosporidium oocysts in saturated porous media. *J. Environ. Qual.* 34 (2), 469–478.
- Bradford, S.A., Torkzaban, S., Kim, H., Simunek, J., 2012. Modeling colloid and microorganism transport and release with transients in solution ionic strength. *Water resour. Res.* 48, W09509.
- Bradford, S.A., Torkzaban, S., Shapiro, A., 2013. A theoretical analysis of colloid attachment and straining in chemically heterogeneous porous media. *Langmuir* 29 (23), 6944–6952.
- Byrne, M.T., Waggoner, S.M., 2009. Fines migration in a high temperature gas reservoir - laboratory simulation and implications for completion design. In: SPE-121897. SPE European Formation Damage Conference Held in Scheveningen, the Netherlands, 27–29 May.
- Byrne, M.T., Slayter, A.G., McCurdy, P., 2010. Improved selection criteria for sand control: when are “fines” fines?. In: SPE-128038. SPE International Symposium and Exhibition on Formation Damage Control Held in Lafayette, Louisiana, USA, 10–12 Feb.
- Byrne, M., Rojas, E., Kandasamy, R., Gibb, A., 2014. Fines migration in oil and gas reservoirs: quantification and qualification through detailed study. In: SPE-168150. SPE International Symposium and Exhibition on Formation Damage Control Held in Lafayette, Louisiana, USA, 26–28 Feb.
- Civan, F., 2014. Reservoir Formation Damage, third ed. Gulf Professional Publishing, Burlington, MA, USA.
- Coleman, T.F., Li, Y., 1996. An interior, trust region approach for nonlinear minimization subject to bounds. *SIAM J. Optim.* 6 (2), 418–445.
- Das, S.K., Schechter, R.S., Sharma, M.M., 1994. The role of surface roughness and contact deformation on the hydrodynamic detachment of particles from surfaces. *J. Coll. Interface Sci.* 164 (1), 63–77.
- Derjaguin, B.V., Landau, L.D., 1941. Theory of the stability of strongly charged lyophobic sols and of the adhesion of strongly charged particles in solutions of electrolytes. *J. Acta Physicochim. URSS* 14, 633–662.
- Derjaguin, B.V., Muller, V.M., Toporov, Yu.P., 1975. Effect of contact deformations on the adhesion of particles. *J. Coll. Interface Sci.* 53 (2), 314–326.
- Elimelech, M., Gregory, J., Jia, X., Williams, R.A., 1995. Particle Deposition and Aggregation. Butterworth-Heinemann, Boston.
- Fleming, N., Mathisen, A.M., Eriksen, S.H., Moldrheim, E., Johansen, T.R., 2007. Productivity impairment due to kaolinite mobilization: laboratory & field experience, Oseberg Sor. In: SPE 117415. SPE European Formation Damage Conference, The Hague, The Netherlands, 19–21 May.
- Fleming, N., Ramstad, K., Kidd, S., Hoeth, L.W., 2010a. Impact of successive squeezes on treatment lifetime and well productivity: comparative assessment of viscosified and nonviscosified treatments. *SPE Prod. Oper.* 25 (01), 99–110.
- Fleming, N., Ramstad, K., Mathisen, A.M., Selle, O.M., Tjomsland, T., Fadnes, F.H., 2010b. Squeeze related well productivity impairment mechanisms & preventative/remedial measures utilised. In: SPE-129765. SPE International Conference on Oil Field Scale, Aberdeen, UK, 26–27 May.
- Freitas, A.M., Sharma, M.M., 2001. Detachment of particles from surfaces: an AFM study. *J. Coll. Interface Sci.* 233 (1), 73–82.
- Gercek, H., 2007. Poisson's ratio values for rocks. *Intern. J. Rock Mech. Min. Sci.* 44, 1–13.
- Guo, Z., Hussain, F., Cinar, Y., 2015. Permeability variation associated with fines production from anthracite coal during water injection. *Intern. J. Coal Geol.* 147, 46–57.
- Han, G., Ling, K., Wu, H., Gao, F., Zhu, F., Zhang, M., 2015. An experimental study of coal-fines migration in Coalbed-methane production wells. *J. Nat. Gas. Sci. Eng.* 26, 1542–1548.
- Herzig, J.P., Leclerc, D.M., Le Goff, P., 1970. Flow of suspensions through porous media - application to deep filtration. *Ind. Eng. Chem.* 65 (5), 8–35.
- Israelachvili, J., 2011. Intermolecular and Surface Forces, third ed. Academic Press, London.
- Jensen, J., Lake, L.W., Corbett, P., Goggin, D., 2000. Statistics for petroleum engineers and geoscientists. In: Handbook of Petroleum Exploration and Production, second ed. Elsevier B.V., Amsterdam.
- Kalantariasl, A., Farajzadeh, R., You, Z., Bedrikovetsky, P., 2015. Nonuniform external filter cake in long injection wells. *Ind. Eng. Chem. Res.* 54, 3051–3061.
- Kang, S.-T., Subramani, A., Hoek, E.M.V., Deshusses, M.A., Matsumoto, M.R., 2004. Direct observation of biofouling in cross-flow microfiltration: mechanisms of deposition and release. *J. Membr. Sci.* 244, 151–165.
- Kia, S.F., Fogler, H.S., Reed, M.G., Vaidya, R.N., 1987. Effect of salt composition on clay release in Berea sandstones. *SPE Prod. Eng.* 2 (4), 277–283.
- Khilar, K.C., Fogler, S., 1998. Migration of Fines in Porous Media. Kluwer Academic Publishers, Dordrecht.
- Lagasca, J., Kovscek, A., 2014. Fines migration and compaction in diatomaceous rocks. *J. Petrol. Sci. Eng.* 122, 108–118.
- Leighton, L.A., Acrivos, A., 1985. The lift on a small sphere touching a plane in the presence of a simple shear flow. *Z. Agnew. Math. Phys.* 36, 174178.
- Lever, A., Dawe, R.A., 1984. Water-sensitivity and migration of fines in the hopeman sandstone. *J. Pet. Geol.* 7 (1), 97–107.
- Li, X., Lin, C.-L., Miller, J.D., Johnson, W.P., 2006. Role of grain-to-grain contacts on profiles of retained colloids in porous media in the presence of an energy barrier to deposition. *Environ. Sci. Technol.* 40 (12), 3769–3774.
- MATLAB and Optimization Toolbox R2010b, The MathWorks, Inc., Natick, Massachusetts, United States.
- Nguyen, T.K., Zeinijahromi, A., Bedrikovetsky, 2013. Fines-migration-assisted improved gas recovery during gas field depletion. *J. Petrol. Sci. Eng.* 109, 26–37.
- Ochi, J., Vernoux, J.-F., 1998. Permeability decrease in sandstone reservoirs by fluid injection: hydrodynamic and chemical effects. *J. Hydrol.* 208 (3–4), 237–248.
- Ochi, J., Vernoux, J.-F., 1999. A two-dimensional network model to simulate permeability decrease under hydrodynamic effect of particle release and

- capture. *Transp. Porous Med.* 37 (3), 303–325.
- Oliveira, M., Vaz, A., Siqueira, F., Yang, Y., You, Z., Bedrikovetsky, P., 2014. Slow migration of mobilised fines during flow in reservoir rocks: laboratory study. *J. Petrol. Sci. Eng.* 122, 534–541.
- O'Neill, M.E., 1968. A sphere in contact with a plane wall in a slow linear shear flow. *Chem. Eng. Sci.* 23, 1293–1298.
- Pang, S., Sharma, M., 1997. A Model for predicting injectivity decline in water-injection wells. *SPE Form. Eval.* 12 (3), 194–201.
- Prasad, M., 2002. Measurement of Young's modulus of clay minerals using atomic force acoustic microscopy. *Geophys. Res. Lett.* 29 (8), 1172, 131–134.
- Saffman, P.G., 1968. Correction to "The lift on a small sphere in a slow shear flow". *J. Fluid Mech.* 31, 624.
- Sefrioui, N., Ahmadi, A., Omari, A., Bertin, H., 2013. Numerical simulation of retention and release of colloids in porous media at the pore scale. *Coll. Surf. A Physicochem. Eng. Asp.* 427, 33–40.
- Schechter, R.S., 1992. *Oil Well Stimulation*. Prentice Hall, NJ.
- Tufenkji, N., 2007. Colloid and microbe migration in granular environments: a discussion of modelling methods. In: Frimmel, F.H., von der Kammer, F., Flemming, F.-C. (Eds.), *Colloidal Transport in Porous Media*. Springer-Verlag, Berlin, pp. 119–142. Chap. 5.
- Varga, R., 1962. *Matrix Iterative Analysis*. Englewood Cliffs, Prentice-Hall, NJ.
- Watson, R.B., Viste, P., Kageson-Loe, N.M., Fleming, N., Mathiasen, A.M., Ramstad, K., 2008. Smart mud filtrate: an engineered solution to minimize near-wellbore formation damage due to kaolinite mobilization: laboratory and field experience, Oseberg Sør. In: *SPE-112455. SPE International Symposium and Exhibition on Formation Damage Control*. Lafayette, Louisiana, USA, 13–15 Feb.
- Welzen, J.T.A.M., Stein, H.N., Stevels, J.M., Siskens, C.A.M., 1981. The influence of surface-active agents on kaolinite. *J. Coll. Interface Sci.* 81 (2), 455–467.
- You, Z., Bedrikovetsky, P., Badalyan, A., Hand, M., 2015. Particle mobilization in porous media: temperature effects on competing electrostatic and drag forces. *Geophys. Res. Lett.* 42, 2852–2860.
- You, Z., Yang, Y., Badalyan, A., Bedrikovetsky, P., Hand, M., 2016. Mathematical modelling of fines migration in geothermal reservoirs. *Geothermics* 59, 123–133.
- Yuan, H., Shapiro, A., 2011a. A mathematical model for non-monotonic deposition profiles in deep-bed filtration systems. *Chem. Eng. J.* 166 (1), 105–115.
- Yuan, H., Shapiro, A., 2011b. Induced migration of fines during waterflooding in communicating layer-cake reservoirs. *J. Pet. Sci. Eng.* 78 (3–4), 618–626.
- Yuan, H., Shapiro, A., You, Z., Badalyan, A., 2012. Estimating filtration coefficients for straining from percolation and random walk theories. *Chem. Eng. J.* 210, 63–73.
- Zeinijahromi, A., Vaz, A., Bedrikovetsky, P.G., Borazjani, S., 2012. Effects of fines migration on well productivity during steady state production. *J. Porous Media* 15 (7), 665–679.
- Zheng, X., Shan, B., Chen, L., Sun, Y., Zhang, S., 2014. Attachment–detachment dynamics of suspended particle in porous media: experiment and modeling. *J. Hydrol.* 511, 199–204.

3.3 Fines mobilisation by low-salinity water injection: 3-point-pressure tests

Bhattacharya, S. S., Paitaridis, J., Pedler, A., Badalyan, A., **Yang, Y.**, Carageorgos, T., Lemon, N.

SPE International Conference and Exhibition on Formation Damage Control, 02/2016

Statement of Authorship

Title of Paper	Fines Mobilisation by Low-Salinity Water Injection: 3-Point-Pressure Tests
Publication Status	<input type="checkbox"/> Published <input type="checkbox"/> Accepted for Publication <input checked="" type="checkbox"/> Submitted for Publication <input type="checkbox"/> Unpublished and Unsubmitted work written in manuscript style
Publication Details	Bhattacharya, S. S., Paitaridis, J., Pedler, A., Badalyan, A., Yang, Y., Carageorgos, T., Bedrikovetsky, P., Warren, D., Lemon, N., 2016. Fines Mobilisation by Low-Salinity Water Injection: 3-Point-Pressure Tests. SPE-178947-MS. SPE International Conference and Exhibition on Formation Damage Control, 24-26 February, Lafayette, Louisiana, USA.

Author Contributions

By signing the Statement of Authorship, each author certifies that:

- i. the candidate's stated contribution to the publication is accurate (as detailed above);
- ii. permission is granted for the candidate to include the publication in the thesis; and
- iii. the sum of all co-author contributions is equal to 100% less the candidate's stated contribution

Name of Principal Author	Siddharth Bhattacharya		
Contribution to the Paper	Performed laboratory tests and data analysis		
Signature		Date	21/07/2016

Name of Principal Author	John Paitaridis		
Contribution to the Paper	Performed laboratory tests and data analysis		
Signature		Date	11/07/2016

Name of Principal Author	Adam Pedler		
Contribution to the Paper	Performed laboratory tests and data analysis		
Signature		Date	11/7/16

Name of Co-Author	Alex Badalyan		
Contribution to the Paper	Supervised lab tests, helped in data interpretation and manuscript preparation		
Signature		Date	20.07.2016

Name of Co-Author (Candidate)	Yulong Yang	
Contribution to the Paper	helped in data interpretation and manuscript evaluation	
Overall percentage (%)	20%	
Signature		Date 20/07/2016

Name of Co-Author	Themis Carageorgos	
Contribution to the Paper	Supervised lab tests, helped in data interpretation and manuscript evaluation	
Signature		Date 20/07/2016

Name of Co-Author	Pavel Bedrikovetsky	
Contribution to the Paper	Supervised development of work, helped in data interpretation and manuscript evaluation	
Signature		Date 21/07/2016

Name of Co-Author	David Warren	
Contribution to the Paper	Supervised development of work, helped in data interpretation and manuscript evaluation	
Signature		Date 11/07/2016

Name of Co-Author	Nick Lemon	
Contribution to the Paper	Supervised development of work, helped in data interpretation and manuscript evaluation	
Signature		Date 11/07/2016

Bhattacharya, S.S., Paitaridis, J., Pedler, A., Badalyan, A., Yang, Y., Carageorgos, T., Bedrikovetsky, P., Warren, D. & Lemon, N. (2016, February 24-26). Fines Mobilisation by Low-Salinity Water Injection: 3-Point-Pressure Tests. *SPE International Conference & Exhibition on Formation Damage Control* held in Lafayette, Louisiana, USA.

NOTE:

This publication is included on pages 86 - 96 in the print copy of the thesis held in the University of Adelaide Library.

It is also available online to authorised users at:

<http://dx.doi.org/10.2118/178974-MS>

3.4 Fines migration in aquifers and oilfields: laboratory and mathematical modelling

Yang, Y., Siqueira, F. D., Vaz, A., Badalyan, A., You, Z., Zeinijahromi, A., Carageorgos T., Bedrikovetsky, P.

Springer, submitted 06/2016

Statement of Authorship

Title of Paper	Fines migration in aquifers and oilfields: laboratory and mathematical modelling
Publication Status	<input type="checkbox"/> Published <input type="checkbox"/> Accepted for Publication <input checked="" type="checkbox"/> Submitted for Publication <input type="checkbox"/> Unpublished and Unsubmitted work written in manuscript style
Publication Details	Yang, Y., Siqueira, F. D., Vaz, A., Badalyan, A., You, Z., Zeinijahromi, A., Carageorgos T., Bedrikovetsky, P., Fines migration in aquifers and oilfields: laboratory and mathematical modelling, Springer.

Author Contributions

By signing the Statement of Authorship, each author certifies that:

- i. the candidate's stated contribution to the publication is accurate (as detailed above);
- ii. permission is granted for the candidate to include the publication in the thesis; and
- iii. the sum of all co-author contributions is equal to 100% less the candidate's stated contribution

Name of Principal Author (Candidate)	Yulong Yang	
Contribution to the Paper	Derived analytical model and performed laboratory data treatment	
Overall percentage (%)	50%	
Signature		Date 20/JUL/2016

Name of Co-Author	Fernando Diogo de Siqueira	
Contribution to the Paper	Supervised development of work, consulted in analytical solution derivation and data treatment	
Signature		Date 18/JUL/2016

Name of Co-Author	Alexandre Vaz	
Contribution to the Paper	Supervised development of work, consulted in data interpretation and manuscript evaluation	
Signature		Date 18/JUL/2016

Name of Co-Author	Alex Badalyan	
Contribution to the Paper	Performed lab tests, consulted in data interpretation and manuscript evaluation	
Signature		Date 20.07.2016

Name of Co-Author	Zhenjiang You	
Contribution to the Paper	Supervised development of work, consulted in data interpretation and manuscript evaluation	
Signature	Date	20/7/16

Name of Co-Author	Abbas Zeinijahromi	
Contribution to the Paper	Supervised development of work, consulted in data interpretation and manuscript evaluation	
Signature	Date	20/07/16

Name of Co-Author	Themis Carageorgos	
Contribution to the Paper	Supervised development of work, consulted in data interpretation and manuscript evaluation	
Signature	Date	20/07/2016

Name of Co-Author	Pavel Bedrikovetsky	
Contribution to the Paper	Supervised development of work, consulted in data interpretation and manuscript evaluation	
Signature	21/07/2016	

Fines migration in aquifers and oilfields: laboratory and mathematical modelling

Yang, Y.^a, Siqueira, F. D.^b, Vaz, A.^b, Badalyan, A.^a, You, Z.^a, Zeinijahromi, A.^a, Carageorgos T.^a, Bedrikovetsky, P.^a

^a Australian School of Petroleum, University of Adelaide, Adelaide 5005, Australia

^b North Fluminense State University of Rio de Janeiro, Lenep-UENF, Rod. Amaral Peixoto km 163, Imboassica - Macaé, RJ, 27.925-310 Brazil

Abstract: Migration of natural reservoir fines is one of the main causes of formation damage in oil and gas fields. Yet, the phenomenon can be employed for enhancing reservoir sweep and water production control. Permeability decline due to fine particles' detachment from reservoir rocks, mobilisation, migration, and straining has been widely reported in the petroleum industry since the 1960s, and is being researched intensively worldwide. The topic of colloidal suspension flows with particle detachment is also of wide interest in environmental, chemical and civil engineering.

The current work begins with a detailed introduction on laboratory and mathematical modelling of fines migration, along with new mathematical models and experimental results. Each of the next three chapters explores a particular cause of fines migration. Chapter 2 covers high velocity that gives high production rate. Chapter 3 covers low salinity water injection. Chapter 4 covers high temperature effect on production rate and low-salinity water injection in geothermal reservoirs. The long permeability stabilisation period during coreflooding with fines migration is explained by slow fines rolling and sliding and by diffusive delay in particle mobilisation. Analytical models are derived for both phenomena. Laboratory fines-migration corefloods are carried out while measuring breakthrough fines concentration and pressure drop across the whole core and its section. Matching of the experimental data and analysis of the tuned coefficients show that the slow-particle model exhibits higher accuracy of matching and more typical strained-concentration dependencies of the tuned parameters than does the delay-release model.

Contents

1. Introduction
2. Fines mobilisation, migration and straining under high velocities
3. Fines detachment and migration at low salinities
4. Detachment and migration of reservoir fines at high temperatures

References

Index

Tables and Figures

1. Introduction

Fines migration with consequent permeability reduction has been widely recognised to cause formation damage in numerous technologies for petroleum, environmental and water resource processes. Fines migration takes place during oil and gas production in conventional and unconventional reservoirs, significantly reducing well productivity (Byrne et al., 2009, 2014; Civan, 2014; Bai et al., 2015; Guo et al., 2015; Han et al., 2015). The occurrence of natural and induced fines migration has also been widely reported in waterflooding of oilfields and invasion of drilling and completion fluids into the formation (Watson et al., 2008; Fleming et al., 2007, 2010a, 2010b). Despite significant progress in the above-mentioned technologies, clogging of production and injection wells remains a major operational issue.

The distinguishing features of natural reservoir fines migration are mobilisation of the attached particles, their capture by straining in the rock, permeability reduction, and consequent decline in well productivity and injectivity (Fig. 1). Permeability decline during coreflooding with piecewise increasing velocity has been observed in several laboratory studies (Ochi and Vernoux, 1998, 1999). Similar effects occur during piecewise change in water salinity or pH during coreflooding (Lever and Dawe, 1994). Permeability reduction, due to velocity increase, salinity decrease and pH increase, is attributed to mobilisation of the attached fine particles and their migration in pore space until size exclusion in thin pore throats, finally resulting in significant permeability decline (Muecke, 1979; Sarkar and Sharma, 1990). Fig. 1 shows a schematic for attached and size-excluded fine particles in the porous space, along with definitions of the concentrations of attached, suspended, and strained particles. Detachment of fines from the grain surfaces yields an insignificant increase in permeability, whereas the straining in thin pore throats and consequent plugging of conducting paths causes significant permeability decline. The main sources of movable fine particles in natural reservoirs are kaolinite, chlorite, and illite clays; quartz and silica particles can be mobilised in low-consolidated sandstones (Arab et al., 2014). Kaolinite booklets of thin slices, when present, are usually situated on grain surfaces (Fig. 2). Detachment of a thin, large slice from the booklet can result in plugging of a large pore.

Figs. 3a and 3e show typical decreasing permeability curves during velocity increase.

Planning and design of the above-mentioned technologies are supported by laboratory-based mathematical modelling. Classical filtration theory with particle detachment includes a mass balance equation for suspended, attached, and strained particles:

$$\frac{\partial}{\partial t} [\phi c + \sigma_a + \sigma_s] + U \frac{\partial c}{\partial x} = 0, \quad (1)$$

where c , σ_a , and σ_s are the concentrations of suspended, attached, and strained particles, respectively, and U is flow velocity of the carrier fluid that coincides with particle speed.

The kinetics of simultaneous particle attachment and detachment is given by the relaxation equation (Bradford and Bettahar, 2005; Tufenkji, 2007; Bradford et al., 2012, 2013)

$$\frac{\partial \sigma_a}{\partial t} = \lambda_a c U - k_{\text{det}} \sigma_a, \quad (2)$$

where λ_a is the filtration coefficient for attachment and k_{det} is the detachment coefficient.

The irreversible fines straining rate in thin pore throats is expressed by the linear kinetics equation where the straining rate is proportional to the advective flux of suspended particles (Herzig et al, 1970; Yuan et al., 2011a,b):

$$\frac{\partial \sigma_s}{\partial t} = \lambda_s c U. \quad (3)$$

Modified Darcy's Law accounts for permeability damage due to both attachment and straining (Pang and Sharma, 1998):

$$U = - \frac{k}{\mu(1 + \beta_s \sigma_s + \beta_a \sigma_a)} \frac{\partial p}{\partial x}. \quad (4)$$

Fig. 1 illustrates the common assumption that the coating of grain by attached particles causes significantly lower permeability damage than straining: $\beta_s \gg \beta_a$, i.e., the combination of particle detachment and straining is primarily responsible for the decline in permeability. Therefore, the term in Eq. (4) that accounts for permeability increase due to detachment is negligible.

Civan (2014, 2016) presented numerous generalisations for the governing equations (1-4) accounting for non-Newtonian behaviour of suspension fluxes, non-equilibrium for deep-bed filtration of high-concentration suspensions and colloids, and particle bridging at thin pore throats.

A quasi-linear system of partial differential equations (1-4) exhibits the delayed reaction to an abrupt injection rate alteration, whereas laboratory tests have shown an instant permeability and breakthrough concentration response to an abrupt velocity alteration (Ochi and Vernoux, 1998; Bedrikovetsky et al., 2012). This discrepancy between the modelling and laboratory data, and the corresponding shortcoming in the theory, has been resolved in the modified model for particle detachment by introducing the maximum attached concentration as a velocity function $\sigma_a = \sigma_{cr}(U)$ (Bedrikovetsky et al., 2011). If the attached concentration exceeds this maximum value, particle detachment occurs and the detached particles follow the classical filtration equation (3); otherwise the

maximum attached concentration holds. The dependency $\sigma_a = \sigma_{cr}(U)$ is called the maximum retention function. The above attachment-detachment scenario is described by the following set of equations:

$$\begin{aligned} \frac{\partial \sigma_a}{\partial t} &= \lambda_a U c, & \sigma_a < \sigma_{cr}(U) \\ \sigma_a &= \sigma_{cr}(U) \end{aligned} \quad (5)$$

The maximum retention function decreases as the flow velocity increases. Therefore, the velocity increase causes instant release of the attached fine-particle excess.

The maximum retention function $\sigma_{cr}(U)$ is a phenomenological function of the model and can be determined only by the inverse-problem approach applied to fines migration tests (Figs. 4 and 5). However, it can be calculated theoretically for a simplified geometry of porous space, using the conditions of mechanical equilibrium of particles attached to the rock surface. Freitas and Sharma (2001), Bergendahl and Grasso (2003), and Bradford et al. (2013) discuss the torque balance of attaching and detaching forces exerting on a particle situated at the rock or internal cake surface (Fig. 6):

$$F_d(U, r_{scr})l(r_{scr}) = F_e(r_{scr}) - F_l(U, r_{scr}) + F_g(r_{scr}), \quad l = l_d / l_n. \quad (6)$$

Here F_d , F_e , F_l , and F_g represent drag, electrostatic, lift, and gravitational forces, respectively; l_d and l_n are the lever arms for drag and normal forces, respectively.

Substitution of the expressions for drag, electrostatic, lift, and gravitational forces into the torque balance equation (6) yields the expression of the maximum retention function (Bedrikovetsky et al., 2011). The maximum retention function (5) for the case of poly-layer attachment of single-radius particles in rock having mono-sized cylindrical capillaries is a quadratic polynomial with flow velocity as the variable. The maximum retention function for a monolayer of poly-dispersed particles is expressed via size-distribution for fine particles (You et al., 2015).

Expression (5) substitutes the equation for simultaneous attachment and detachment (2) in the mathematical model for colloidal-suspension transport (1-4). The modified model consists of three equations (1, 3, 5) for three unknown concentrations c , σ_a , and σ_s . Eq. (4) for pressure can be separated from the system (1, 3, 5). The one-dimensional flow problem with attachment and detachment allows for exact solution, yielding suspended, attached, and strained concentrations and pressure drop across the core. The laboratory- and theoretically determined maximum retention functions are in good agreement, which validates the maximum retention function as a mathematical model for particle detachment (Zeinijahromi et al., 2012; Nguyen et al., 2013).

Nevertheless, the exact solution of the system (1, 3, 4, 5) shows complete pressure drop stabilisation after injection of one pore volume (Bedrikovetsky et al., 2011), whereas numerous laboratory studies exhibit 30–500 PVI (pore volume injected) periods of stabilisation (Ochi and Vernoux, 1998, 1999; Oliveira et al., 2014). Fig. 3a shows the permeability stabilisation times 70–3000 PVI for different injection velocities (Ochi and Vernoux, 1998). The stabilisation times for flow exhibited in Fig. 3e vary from 300 to 1200 PVI. Therefore, the modified model for colloidal suspension transport in porous media (1, 3, 5) allows for good matching of stabilised permeability and fails to predict the long stabilisation period.

Several works have claimed slow surface motion of the mobilised particles, and simultaneous fast particle transport in the bulk of the aqueous suspension. Li et al. (2006) attributed the slow surface motion to particles in the secondary energy minimum. Yuan and Shapiro (2011a) and Bradford et al. (2012) introduced slow particle velocity in the classical suspension flow model, resulting in a two-speed model that successfully matched their laboratory data on breakthrough concentration. Navier-Stokes-based simulation of colloids' behaviour at the pore scale, performed by Sefrioui et al. (2013), also exhibited particle transport speeds significantly lower than the water velocity. However, classical filtration theory along with the modified particle detachment model assumes that particle transport is at carrier fluid velocity (Tufenkji, 2007; Civan, 2014).

Oliveira et al. (2014) attributed long stabilisation periods to slow drift of fine particles near the rock surface in the porous space. However, a mathematical model for slow particle migration and corresponding match of the stabilisation periods is unavailable in the literature.

Mahani et al. (2014, 2015) observed delay between salinity alteration and corresponding surface change. This delay is attributed to saline water diffusion from the contact area between the deformed particle and rock surface. The so-called Nernst-Planck diffusion in the thin slot between two plates subject to molecular-force action is significantly slower than the Brownian diffusion, which can bring about significant delay. The diffusive delay in particle mobilisation due to water salinity decrease can serve as another explanation for the long stabilisation period. Yet, a mathematical model that accounts for delay in particle mobilisation also seems absent from the literature.

In the current work, the long times for permeability stabilisation are attributed to slow surface motion of mobilised fine particles. The governing system Eqs. (1, 3, 5) is modified further by replacing the water flow velocity U by the particle velocity $U_s < U$ (Fig. 1). We also introduced a maximum retention function with delay, which corresponds to the Nernst-Planck diffusion from the grain-particle contact area into the bulk of the fluid. We derived the form for the maximum retention function for a monolayer of size-distributed fines, which accounts for its non-convex form. It was found that during continuous velocity/pH/temperature increase or salinity decrease, the largest particles were released first. The obtained system with slow fines migration and delayed maximum

retention function allows for exact solution for cases of piecewise-constant velocity/pH/temperature increase or salinity. Good agreement between the laboratory and modelling data allows validating the proposed model for slow surface motion of released fine particles in porous media.

The remainder of the text is as follows. Section 2 presents the laboratory study of fines migration due to high velocities and presents the mathematical model for slow particle migration that explains the long stabilization periods. The analytical model is derived, providing explicit formulae for concentration profiles and histories, and also for the pressure drop. Section 3 presents the laboratory study of fines migration due to low salinities, and derives the mathematical model that accounts for slow particle migration and for delayed fines mobilisation. The analytical model is also derived. Section 4 presents the analytical model for fines mobilisation at high temperature. The recalculation method for varying salinity, temperature, pH, or velocity is developed. Section 5 presents the conclusion.

2. Fine particles mobilisation, migration, and straining under high velocities

This section presents the modelling and laboratory study for fine particles migration, detached by drag and lifting forces at increased velocities. Section 2.1 presents a brief physical description of fines detachment in porous media and introduces the maximum retention function for a mono-layer of size-distributed particles. The qualitative analysis of the laboratory results on long-period stabilization, presented in this section yields the slow-particle modification of the mathematical model for fines migration in porous media. Section 2.2 presents those basic transport equations. Section 2.3 derives the analytical model for one-dimensional flow under piecewise increasing flow velocity with consequent fines release and permeability impairment. Section 2.4 describes the laboratory coreflood tests with fines mobilization along with the successful experimental-data matching by the analytical model. Section 2.5 discusses the model validity, following the results of the laboratory and analytical modelling.

2.1. Physics of fines detachment, transport, and straining in porous media

The physics of fines detachment/mobilization on a microscale is discussed in this section. In the presence of low ionic strength or high flow velocity, reservoir fines detach from the rock surface, mobilize, and flow through the porous media as shown in Figs. 1 and 6. Four forces act on a fine particle attached to the surface of the grain: drag, lift, electrostatic, and gravity forces. For calculation of drag force, we use the expression proposed by Bergendahl and Grasso (2003) and Bradford et al. (2013); lift force is calculated using the formula of Leighton and Acrivos (1985) and Akhatov et al. (2008); and the DLVO (Derjagin-Landau-Verwey-Overbeek) theory is used for calculating the

electrostatic forces (Derjagin and Landau, 1941; Elimelech et al., 1995; Khilar and Fogler, 1998; Israelachvili, 2011).

Elastic particles located on the grain surface undergo deformation due to gravitational, lift, and electrostatic forces acting normal to the grain surface. The resultant of these forces (normal force) is shown on the right side of Eq. (6). We assume that at the mobilization moment, a particle rotates around the rotation-touching point in the boundary of the particle-grain contact area. Also assumes is that the lever arm is equal to the radius of the contact area of particle deformation subject to the normal force (Derjaguin et al., 1975; Freitas and Sharma, 2001; Schechter, 1992; Bradford et al., 2013). The contact area radius is equal to the lever arm l_n and is calculated using Hertz's theory of mutual grain-particle deformation:

$$l_n^3 = \frac{F_n r_s}{4K} \quad l_d = \sqrt{r_s^2 - l_n^2} \quad K \equiv \frac{4}{3 \left(\frac{1-\nu_1^2}{E_1} + \frac{1-\nu_2^2}{E_2} \right)}. \quad (7)$$

Here K is the composite Young modulus that depends on Poisson's ratio ν and Young's elasticity modulus E of the particle and of the surface. Indices 1 and 2 refer to the particle and solid matrix surfaces, respectively.

Fig. 6b depicts the scenario in which particle mobilisation revolves around the contacting roughness (asperity) on the surface of a grain. The value of l_n in the first scenario was determined by the elastic properties of rock and particle, and in the second scenario by the surface roughness.

Two coreflood tests (I and II) at increased fluid velocity on Berea sandstone cores were carried out by Ochi and Vernoux (1998) and resulted in mobilization of kaolinite particles (Fig. 3). The following electrostatic constants and parameters for quartz and kaolinite were used to calculate F_e in Eq. (6): surface potentials ψ_{01} and ψ_{02} are (-55 mV, -50 mV) for test I and (-70 mV, -80 mV) for test II (Ochi and Vernoux, 1998); the Hamaker constant is $2.6 \times 10^{-20} J$ (Welzen et al., 1981; Kia et al., 1987); atomic collision diameter is $0.4 \times 10^{-9} m$ (Das et al., 1994); and salinities are 0.1 mol/L for test I and 0.01 mol/L for test II. The Hamaker constant was calculated using dielectric constant for water $D = 78.0$ and permittivity of free space (vacuum) $\epsilon_0 = 8.854 \times 10^{-12} C^2 J^{-1} m^{-1}$ (Israelachvili, 2011; Khilar and Fogler, 1998). Electron charge was $e = 1.6 \times 10^{-19} C$, Boltzmann's constant was $k_B = 1.3806504 \times 10^{-23} J/K$, and temperature was $T = 25 ^\circ C$. Young's modulus for kaolinite was 6.2 GPa and for quartz was 12 GPa (Prasad, 2002), and Poisson's ratios were equal to 0.281 and 0.241 (Gercek, 2006) and were used to evaluate the lever arm ratio according to Eq. (7). The above parameters were used to construct graphs for electrostatic potential and force versus separation particle-grain distance (Figs. 7(a) and (b)).

The total potential of interaction V determines electrostatic force F_e . Zero-values for F_e correspond to energy extremes V_{max} and V_{min} , and the minimum value of electrostatic force is obtained from the

inflection point of the total potential of interaction curve. The first test of Ochi and Vernoux (Fig. 3a, b, c, d) was favourable for attachment of kaolinite particles to the grain surface, which resulted in the absence of the secondary minimum on the total potential of interaction curve. For the second test (Figs. 3 e, f, g, h), the values of the primary and secondary energy minima equalled $550 kT$ and $19 kT$, respectively. The energy barrier was $87 kT$, exceeding the values of the secondary minimum and allowing a particle to jump from secondary minimum to primary minimum (Elimelech et al., 1995). Therefore, the second test was unfavourable for kaolinite particle attachment to the grain surface.

Fluid flow velocity affects lifting and drag forces, whereas particle size determines the magnitudes of all forces in Eq. (6) under mechanical equilibrium. Therefore, the critical radius of the particle mobilized by fluid flow with velocity U can be determined as follows: $r_{scr} = r_{scr}(U)$ is an implicit function from Eq. (6), i.e., Eq. (6) is a transcendent equation for implicit dependency $r_{scr} = r_{scr}(U)$. The stationary iterative numerical procedure can be used to solve Eq. (6) (Varga, 1962). The graph of the function $r_{scr} = r_{scr}(U)$ obtained using the above parameters shows that the size of each mobilised particle $r_{scr}(U)$ decreases monotonically as fluid velocity increases. Therefore, those particles which remained immobilised on the grain surface at fluid velocity U have sizes $r < r_{scr}(U)$. The magnitude of F_e increases as the Hamaker constant increases (see Fig. 8), resulting in the right-shift of the $r_{scr}(U)$ -curve.

Let us assume that the attached particles form a mono-layer on the rock surface. The initial concentration distribution of attached particle sizes is denoted as $\Sigma_a(r_s)$. Particles are mobilised by descending size as mentioned above. Thus, the critical retention concentration in Eq. (5) includes all particles with radii smaller than $r_{scr}(U)$:

$$\sigma_{cr}(U) = \sigma_{a0} \int_0^{r_{scr}(U)} \Sigma_a(r_s) dr_s. \quad (8)$$

Now we assume that the attached particles are size-distributed according to the breakage algorithm (i.e., log-normal distribution for attached particle sizes $\Sigma_a(r_s)$ holds (Jensen et al., 2000)). The forms of the maximum retention function as calculated by Eq. (8) for different size distributions of the attached particles, using the above values for electrostatic and elastic constants, are shown in Fig. 9.

Bedrikovetsky et al. (2011) found that $\sigma_{cr}(U)$ for uniformly-sized particles that form the poly-layer coating on the surface of cylindrical pores is a quadratic polynomial. The corresponding curves $\sigma_{cr}(U)$ are convex. The model for the poly-layer coating can be modified by the introduction of size distributions for spherical particles and cylindrical pores; the resulting maximum retention curves can contain the concave parts (Fig. 9).

Fig. 9 indicates that the maximum retention function for monolayer fines is not convex. The calculated $\sigma_{cr}(U)$ -curves for three particle-size distributions characterised by equal variance coefficients support the above observation that the larger the particle, the higher the drag force on the particle and the less the remaining particles (Fig. 9a). Similar calculations for lognormal distributions with the same average particle size and different variance coefficients result in the $\sigma_{cr}(U)$ -curves shown in Fig. 9b. The higher fraction of mobilised large particles corresponds to larger coefficient of variation C_v . For the low velocity range, $\sigma_{cr}(U)$ -curves for high values of standard deviation lie lower; whereas with the increase of fluid velocity, $\sigma_{cr}(U)$ -curves shift to higher σ_{cr} -values. Eq. (8) shows that the $\sigma_{cr}(U)$ -curve has a step-shape for mono-sized particles ($C_v \rightarrow 0$), meaning that the maximum retention function is a step-function. The wider the attached particle-size distribution, the wider the transitional spread of the $\sigma_{cr}(U)$ -curves. The phenomenological model for fines detachment in porous media (1, 3–5) assumes the existence of a maximum retention function without any constraint on its form.

Now we consider particle-free water being injected with increasing piecewise-constant velocity into a core. The movable attached fines concentration is σ_{a0} . There is no particle mobilisation at low fluid velocities (see Fig. 9c), because the attaching torque (6) exceeds the detaching torque for all size particles: point (U, σ_{a0}) is located below the maximum retention curve. Concentration of attached particles remains constant along the horizontal arrow directed from the point $U = 0$ up to critical velocity $U = U_0$. Value U_0 corresponds to the minimum velocity that results in mobilisation of particles and the consequent first fine appearance in the core effluent.

The critical velocity U_0 is determined by value σ_{a0} as follows:

$$\sigma_{a0} = \sigma_{cr}(U_0). \quad (9)$$

Movement along the $\sigma_{cr}(U)$ -curve to the right and down corresponds to velocity increase above the critical value $U > U_0$. An instant rate change from U_1 to U_2 is accompanied by instant particle mobilisation with concentration $\Delta\sigma_{a1} = \sigma_{cr}(U_1) - \sigma_{cr}(U_2)$ and increase in suspended concentration by $[\sigma_{cr}(U_1) - \sigma_{cr}(U_2)]/\phi$. The mobilised particle moves along the rock surface with velocity $U_s < U$ until it is strained by a pore throat smaller than the particle size. This results in rock permeability decline due to plugging of the conductive pores. The increased strained particle concentration yields the permeability decline according to Eq. (4). Decline in stabilised permeability values at various fluid velocities, due to increasing strained particle concentration for tests I and II, is presented in Figs. 10(a) and (b).

Let us introduce the non-dimensional pressure drop across the core, normalised by the initial pressure drop. This is denoted as the impedance J :

$$J(T) = \frac{\Delta P(T)U(0)}{U(T)\Delta P(0)} = \frac{k_0}{\langle k \rangle(T)}, \quad (10)$$

where $\langle k \rangle(T)$ is the average core permeability. The permeability decline curves in Figs. 3a and 3e are recalculated to yield the impedance growth curves in Figs. 11a and 11b, respectively.

The increase in pressure drop across the core from Δp_{n-1} to Δp_n , or permeability decline from k_{n-1} to k_n is caused by increasing fluid velocity U_n , $n=1,2,3\dots$ which leads to particle mobilisation. Permeability decline during the increase in fluid velocity is shown in Fig. 3.

According to the data from test I (Fig. 3a) and II (Fig. 3b), rock permeabilities stabilise after many pore volumes have been injected. However, classical filtration theory says that for a mobilised particle to appear at the end of the core requires a flight time along the overall core. Each fine particle is transported by the carrier fluid; it is strained in the core or arrives at the outlet after injection of one pore volume. According to Figs. 3a and 3e, permeability stabilisation times are significantly higher than 1 PVI. This is explained by slow particle drift along the rock surface: the mobilised particles move along the rock with velocity $U_s < U$ that is significantly lower than the carrier fluid velocity.

The next section introduces the basic governing equations for the transport of suspended colloids in porous media; the basic system includes the maximum retention function σ_{cr} that models particles' detachment and their slow drift along the porous medium with low velocity $U_s < U$.

2.2. Governing system for suspension-colloidal transport and detachment in porous media

The following assumptions are introduced for the development of the mathematical model for detachment/mobilisation of particles and transport of suspended colloids in porous media (Yuan and Shapiro, 2011a; Yuan et al., 2012):

- the mobilised fine particles cannot reattach to the rock surface;
- the mobilised particles do not diffuse in long micro-homogeneous cores;
- the carrier fluid is incompressible;
- presence of low-concentrated particles in flowing fluid does not change density or viscosity of suspension, which are equal to those of injected water;
- there exists a phenomenological maximum retention function for particles attached to the rock surface;
- volume balance of the incompressible carrier fluid is not affected by the presence of small concentrations of suspended, attached, or strained particles;
- the mobilised particles move with velocity $U_s < U$.

Mobilised particles move along the surface of grains with velocity $U_s < U$, meaning that the drifted particle concentration is significantly higher than the suspended concentration of fine particles carried by water stream (see Fig. 1). The drift speed U_s is a phenomenological constant of the model.

The slow fines-drift assumption $U_s < U$ determines the difference between the above formulated assumptions and those for the modified model (1, 3–5). Thus, the system of governing equations includes a mass balance equation for suspended, attached, and strained fines where the suspended particles are transported by water flux with reduced velocity U_s :

$$\frac{\partial(\phi c + \sigma_s + \sigma_a)}{\partial t} + U_s \frac{\partial c}{\partial x} = 0. \quad (11)$$

The straining rate is assumed to be proportional to particle advection flux, cU_s (Herzig et al., 1970):

$$\frac{\partial \sigma_s}{\partial t} = \lambda(\sigma_s) U_s c. \quad (12)$$

If the maximum retention concentration is greater than attached concentration, the particle attachment rate (5) is also assumed to be proportional to the particle advection flux cU_s :

$$\begin{aligned} \frac{\partial \sigma_a}{\partial t} &= \lambda_a U_s c, & \sigma_a < \sigma_{cr}(U) \\ \sigma_a &= \sigma_{cr}(U) \end{aligned} \quad (13)$$

Otherwise, the attached particle concentration is expressed by the maximum retention function given by Eq. (8).

Four equations (4, 11, 12, 13) with four unknowns c , σ_a , σ_s , and p constitute a closed system and a mathematical model for fine-particle migration in porous media.

Now we introduce the following dimensionless parameters:

$$S_a = \frac{\sigma_a}{\sigma_{a0}}, S_s = \frac{\sigma_s}{\sigma_{s0}}, C = \frac{c\phi}{\sigma_{a0}}, \Lambda_a = \lambda_a L, \Lambda_s = \lambda_s L, T = \frac{\int_0^t U(y) dy}{\phi L}, X = \frac{x}{L}, \alpha_n = \frac{U_{sn}}{U_n}, P = \frac{kp}{\mu LU} \quad (14)$$

Here, the particle drift velocities U_{sn} and delay factors α_n , $n=1,2,3\dots$ correspond to flow velocities U_n ; T is the accumulated non-dimensional volume of injected water. For the case of piecewise constant flow velocity $U(t)$, the dimensionless accumulated injected volume $T(t)$ is piecewise linear.

Substitution of dimensionless parameters (14) into governing equations (4, 11–13) yields the following dimensionless system which consists of the particle balance

$$\frac{\partial(C + S_s + S_a)}{\partial T} + \alpha_n \frac{\partial C}{\partial X} = 0, \quad (15)$$

particle straining kinetics

$$\frac{\partial S_s}{\partial t} = \Lambda_s \alpha_n C, \quad (16)$$

particle attachment-detachment kinetics

$$\begin{aligned} \frac{\partial S_a}{\partial T} &= \Lambda_a \alpha_n C, & S_a < S_{cr}(U) \\ S_a &= S_{cr}(U) \end{aligned} \quad (17)$$

and the modified Darcy's law that accounts for permeability damage due to fines retention

$$1 = -\frac{1}{1 + \beta_s \sigma_{a0} S_s} \frac{\partial P}{\partial X}. \quad (18)$$

In the next section, we solve the non-dimensional governing system (15–18) for the conditions of laboratory tests with piecewise increasing velocity.

2.3. Analytical model for one-dimensional suspension-colloidal flow with fines mobilisation and straining

During coreflood when velocity U_1 is higher than U_0 , i.e., $\sigma_{a0} > \sigma_{cr}(U_1)$, the excess of the attached concentration is instantly released into the colloidal suspension. Particle straining in the proposed model is irreversible; therefore, it is assumed that initial porosity and permeability already account for the strained-particle initial concentration. Coreflood with constant fluid velocity results in a constant attached concentration S_a given by the maximum retention function. Thus, the initial conditions are

$$T = 0: C = \Delta S_{a1} = S_{a0} - S_{cr}(U_1), S_s = 0, S_a = S_{cr}(U_1). \quad (19)$$

The inlet boundary condition corresponds to injection of water without particles:

$$X = 0: c = 0. \quad (20)$$

Substitution of the expression for straining rate (16) into mass balance equation (15) and accounting for steady-state distribution of attached particles S_a yields the linear first-order hyperbolic equation

$$\frac{\partial C}{\partial T} + \alpha_1 \frac{\partial C}{\partial X} = -\Lambda_s \alpha_1 C. \quad (21)$$

The next section uses the method of characteristics to solve Eq. (21).

2.3.1 Exact analytical solution for injection at constant rate

The characteristic velocity in Eq. (21) equals α_I . The solution $C(X,T)$ is presented in Table 1, and integration of Eq. (16) over T determines the strained concentration $S_s(X,T)$.

According to Fig. 12a, the concentration front of the injected particle-free fluid moves along the path $X = \alpha_I T$. Behind the concentration front, particle concentration equals zero. The “last” mobilised particle arrives at the core outlet when $T = 1/\alpha_I$. The mobilised particles are uniformly distributed; they move with the same velocity and have the same probability of capture by smaller vacant pore throats. Therefore, the profile of suspended particle concentration is uniform during fluid flow, and concentration of suspension in zone I is independent of X (see the second line in Table 1). This leads to the conclusion that the concentration of particles strained in thin pores is independent of X ahead of the concentration front. Particle straining occurs for non-zero concentration of suspended particles. Therefore, the strained particles accumulate at a reservoir point X until the arrival of the concentration front; afterwards, the concentration of suspended particles remains unchanged. Therefore, the concentration of strained particles behind the concentration front is steady-state.

The profiles of suspended particle concentration at $T = 0$, T_a (before the arrival of the concentration front at the outlet of the core), and T_b (after the arrival of the concentration front) are shown in Fig. 12b. We denote ΔS_{a1} as the initial concentration of the released suspended particles. The profile of the concentration of suspended particles equals zero behind the concentration front and is constant ahead of the front. After the front's arrival, the breakthrough concentration of suspended particles equals zero because all mobilised particles are either strained in thin pore throats or emerge at the rock effluent.

Three profiles of concentration of strained particles, for times 0, T_a , and T_b , are shown in Fig. 12(c). No strained particles are present in the rock before particle mobilisation. The concentration of strained particles continues to grow until the front arrival, and it then remains unchanged. The duration of particle straining during the flow becomes longer, and the maximum concentration of accumulated strained particles grows with X . Therefore, the profiles of strained particle concentration grow as X increases. The probability of particle capture ahead of the front remains constant. Thus, the strained profile is uniform, because the particle advective flux is uniform.

Fig. 13 shows the history of particle breakthrough concentration. The later the arrival, the higher the particle capture probability. According to Herzig et al. (1970), the coefficient of filtration λ_s equals the probability of particle straining per unit length of the particle trajectory. Therefore, the number of particles captured by thin pore throats increases with time, and breakthrough concentration $C(I,T)$

decreases with time. All mobilised fine particles either are strained or exit the core at time $T_{st,1}$, i.e., concentration of suspended particles becomes zero:

$$T_{st,1} = \frac{1}{\alpha_1}. \quad (22)$$

The rock permeability stabilises at time $T_{st,1}$.

Core impedance can be calculated directly from Eq. (10). Impedance for the time interval with the constant fluid velocity from Eq. (18) equals

$$J(T) = \int_0^1 \left(-\frac{\partial P}{\partial X} \right) dX = 1 + \beta_s \sigma_{a0} \int_0^1 S_s(X, T) dX. \quad (23)$$

Substituting the solution for the concentration of the retained particles (rows 4 and 5 in Table 1) into Eq. (23) and integrating over X results in the following explicit formula for impedance increase during the injection:

$$J(T) = 1 + \beta_s \sigma_{a0} \Delta S_{a1} \left[1 - \frac{1}{\Lambda_s} - \left(1 - \frac{1}{\Lambda_s} - \alpha_1 T \right) e^{-\alpha_1 \Lambda_s T} \right], \quad T < \alpha_1^{-1}. \quad (24)$$

Substituting the expression for stabilisation time (22) into Eq. (24) yields the stabilised impedance value

$$J(T_{st1}) = 1 + \beta_s \sigma_{a0} \Delta S_{a1} \left(1 - \frac{1}{\Lambda_s} + \frac{e^{-\Lambda_s}}{\Lambda_s} \right), \quad T \geq \alpha_1^{-1}. \quad (25)$$

Monotonic increase in dimensionless pressure drop across the core from one to the maximum value is achieved at time $1/\alpha_1$, coinciding with the arrival of the “last” mobilised particle at the core outlet. After that, the pressure drop remains unchanged.

2.3.2 Analytical solution for multiple injections

The solution of the problem (15–18) where fluid velocity has changed from U_{n-1} to U_n is similar to that of the first stage under U_1 . The only difference is that the concentration of strained particles for $T > T_n$ equals the total concentration of strained particles before the fluid velocity alteration at time $T = T_n - 0$ and the concentration of particles that have been strained during time $T > T_n$. We discuss the case where the change of fluid velocity occurs after permeability stabilisation.

Following the fluid velocity change from U_{n-1} to U_n , the attached particles immediately detach. Detached particle concentration is $\Delta\sigma_{an} = \sigma_{cr}(U_{n-1}) - \sigma_{cr}(U_n)$. The fines detached add to the strained particle concentration that remains after the previous fluid injection with velocity U_{n-1} :

$$T = T_n : C = \Delta S_{an} = S_{cr}(U_{n-1}) - S_{cr}(U_n), S_s = S_s(X, T_n - 0), S_a = S_{cr}(U_n). \quad (26)$$

Substituting strained concentration (see Table 1) into Darcy's law (18) and integrating for pressure gradient over X along the core yields the impedance for $T > T_n$:

$$T < T_n + \alpha_n^{-1} : \quad J(T) = J_{0n} + \beta_s \sigma_{a0} \Delta S_{an} \left[1 - \frac{1}{\Lambda_s} - \left(1 - \frac{1}{\Lambda_s} - \alpha_n (T - T_n) \right) e^{-\alpha_n \Lambda_s (T - T_n)} \right]. \quad (27)$$

Substituting stabilised time $T = T_n + 1/\alpha_n$ into Eq. (27) gives the stabilised impedance after the n -th injection with velocity U_n .

The analytical model-based formulae for impedance (rows 12 and 13 in Table 1) will be used to match the laboratory tests in the next section.

2.4. Adjustment of the analytical model from the laboratory experiments

In order to replicate water injection in a well, Ochi and Vernoux (1998) performed two laboratory corefloods. Their tests were performed with Berea cores to provide real-world bottom-hole pressures and temperatures. Experiments were carried out at different fluid velocities. For test I, Fig. 3a graphs permeability and Fig. 3b graphs flow velocity. Permeability and velocity during test II are shown in Fig. 3. Initial and boundary conditions (19, 20) correspond to injection of clean particle-free water with piecewise increasing velocity. Pressure drop along the core was measured. Both tests used Berea sandstone cores prepared from the same block, so that the rock properties for both cores would be similar. As fluid velocity increased, kaolinite particles detached from the grain surface. The mobilised fines migrated and were strained by the rock. We used the analytical model proposed in Section 2.3 for matching the pressure drop across the sandstone cores during the tests. Minimisation of the difference between the modelled and measured pressure drop across the cores was used to adjust the phenomenological constants of the model: α , $\Delta\sigma$, λL , and β .

2.4.1 Tuning the rheological model parameters from laboratory coreflooding data

The following assumptions are adopted in this study. Formation damage and filtration coefficients remain constant for the duration of the experiment; therefore, these parameters are independent of fluid velocity and concentration of the retained particles. The drift delay factor was assumed to vary, i.e., the alteration of rock surface during detachment/mobilisation of particles affects drift velocity.

For stabilised permeability, according to Eq. (4), the permeability values k_n fulfil the following relationship:

$$\beta[\sigma_{cr}(U_{n-1})]\Delta\sigma_{an} = \frac{k_{n-1}}{k_n} - 1. \quad (28)$$

Pressure drops along the core, which define the permeabilities k_i , were measured during coreflood tests with varying fluid velocities U_i . We applied the least square method to tune the above experimental pressure drop data and obtained filtration coefficient λ_s , the products $\beta_s\Delta\sigma_{cr}(U_n)$, $n=1,2,\dots$, and the drift delay factors α_n for different fluid velocities U_n . The optimisation problem (Coleman et al., 1996) was solved using the reflective trust region algorithm in Matlab (Mathworks, 2010).

The average core permeabilities, evaluated from pressure drop data across the cores (Ochi and Vernoux, 1998) and presented in Figs. 3a and 3e, were used to calculate the rock impedances, which are shown by circles in Fig. 11.

For Berea sandstone, we assumed typical porosity 0.2 and typical concentration of kaolinite particles that can be mobilised is 0.06 (Khilar and Fogler, 1998). The attached volumetric concentration is equal to $\sigma_{a0}=0.06\times 0.8=0.048$, which is equal to the σ_{cr} that corresponds to $U_0 < U_I$ (see Eq. (9)). We calculated the formation damage coefficient for the condition of total removal of all kaolinite particles at maximum fluid velocity, during the last fluid injection, and straining of fraction of these particles in thin pore throats:

$$\beta_s = \frac{\sum_{n=1}^N (\beta_s \Delta\sigma_{an})}{\sigma_{a0}}. \quad (29)$$

The tuning procedure results in groups $\beta_s\Delta\sigma_{an}$. Using the values of released concentrations $\Delta\sigma_{an}$, $\sigma_{cr}(U)$ is calculated as follows:

$$\sigma_{cr}(U_n) = \sigma_{a0} - \sum_{n=1}^N \Delta\sigma(U_n). \quad (30)$$

2.4.2 Results

Table 2 shows results for history matching of impedance for the two cores. Results for prediction by the adjusted model are presented in Fig. 11 in the form of continuous impedance curves. Tuning of the model parameters resulted in monotonically decreasing dependency of the drift delay factor $\alpha=\alpha(S)$ for corefloods in cores I and II (Figs. 3d and 3h, respectively). The higher the strained concentration,

the higher the rock tortuosity, which decelerates particle drift. Also, the higher the strained concentration, the smaller the mobilised particles, which drifted at lower velocity.

The experimental data closely matched the model (R^2 values were 0.99 and 0.98 for cores I and II, respectively). Fixing the drift delay factor for the overall period of fluid injection and matching the impedance data resulted in significantly lower R^2 values during adjustment of the proposed model.

Using Eq. (30) to tune the model for two cores yielded the maximum retention function shown in Fig. 14. The increase in fluid velocity resulted in the increase of drag and lifting forces, which detached the kaolinite particles from the surface of the rock grains and reduced concentration of kaolinite particles remaining immobilised on the rock grain surface. If a mono-layer of poly-sized kaolinite particles is attached to the surface of rock grains, the mechanical equilibrium model (6, 8) indicates that the obtained σ_{cr} -curves are not convex.

The proposed model can be used to calculate the size distribution of attached fine particles $\Sigma_a(r_s)$ from the maximum retention function $\sigma_{cr}(U)$: the minimum mobilized size $r_{scr}(U)$ is determined from Eq. (6), and size distribution function $\Sigma_a(r_s)$ is calculated from Eq. (8) by regularized numerical differentiation (Coleman and Li, 1996).

Because the fluid velocity was changing step-wise during coreflood tests (seven velocities for test I, and four velocities for test II), the calculated kaolinite particle distributions are given in the form of a histogram (Fig. 15). As follows from Figs. 3c and 3g, the minimum radius of detached particles decreases as fluid velocity increases. This observation agrees with the shape of the velocity-dependency of the critical radius exhibited in Fig. 8.

Figs. 16a and 16b compare the various forces acting on a particle at the critical moment of its mobilisation. According to Fig. 15, the ranges of particle radii cover the ranges of size distributions for particles attached to the surface of rock grains. The drag force was two orders of magnitude smaller than the electrostatic force. The drag force was significantly larger than the gravitational and lifting forces. Because lever arm ratio l significantly exceeded one, the small drag torque exceeded the torque developed by electrostatic force.

The maximum retention function can be parameterised by the critical particle radius $\sigma_{cr}(U) = \sigma_{cr}(r_{scr}(U))$. Considering the value $\sigma_{cr}(r_{scr}(U))$ as an accumulation function of retained concentration for all particles with radius smaller than r_{scr} , yields the corresponding histogram (Fig. 15) representing the concentration distribution of initial reservoir fines for various radii. Thus, we can explain the maximum retention function, σ_{cr} , for various sized particles attached to the grain surface: if particles attached to the grain surface cannot be mobilised by fluid flowing with velocity U , then their radii are

smaller than $r_{scr}(U)$ and their concentration is expressed as $\sigma_{cr}(U)$. Increasing fluid velocity U results in the decrease of minimum radius of particles detached by flow with velocity U .

The calculated values of filtration and formation damage coefficients (Table 2) fall within the common ranges of these coefficients reported by Pang and Sharma (1997). The orders of magnitude of drift delay factor, which vary between 10^{-3} and 10^{-4} in the present work, are the same as those reported by Oliveira et al. (2014).

2.5. Summary and discussion

According to mathematical model (1, 3, 5), which accounts for the maximum retention function for detachment and migration of particles with the velocity of a carrier fluid, rock permeability should stabilise after 1 PVI. However, the experimental data showed that the permeability stabilisation periods are significantly greater than 1 PVI. Such behaviour can be explained only if a mobilised particle moves significantly slower than the flowing fluid. This behaviour could be described by a two-speed model containing six constants of mass exchange between particles moving slow and fast, two detachment and two filtration coefficients for fast and slow particles, and slow moving particle (Yuan and Shapiro, 2011; Bradford et al., 2012); the model tuning for the experimental breakthrough curves is not unique. Complete characterisation of the two-speed model would entail complex experiments in which pressure drop is measured along a core, obtaining the breakthrough curve and calculation of the retained particle concentration. Yet, most coreflood studies have reported data for pressure drop along the core only. For this reason, the present study considers a rapid exchange between populations of particles migrating with fast and slow velocities along each rock pore, yielding a unique particle drift velocity. We also assume that this exchange occurs significantly faster than the capture of particles by the rock after free run in numerous pore lengths, resulting in equal concentrations of particles moving with fast and slow velocities. The above assumptions translate to a single-velocity model.

The proposed model (15-18) is applied to the data treatment of laboratory tests. The modelling results show that the migrating particles move significantly slower than the carrier fluid. Hence, there is a delay in the permeability stabilisation due to fines migration. The delay time is in the range of 500-1250 PVIs, which corresponds to the drift delay factor α_n varying between 0.0008-0.002.

Migration of mobilised particles in a porous medium occurs in two simultaneous ways: one fraction moves with a carrier fluid, whereas another part of particles drifts along grain surface with significantly lower velocity. Particle size distribution, velocity of a carrier fluid and the magnitude and sign of electrostatic forces between the particle and grain determine the fraction of those particles. According to Li et al. (2006), Yuan and Shapiro (2011b) and Sefrioui et al. (2013), such slow particle movement along the rock grain surface occurs via sliding, rolling, temporary detachment from grain

surface to a carrier fluid and return back to the grain surface when particle meets and collides with the grain surface asperities.

Consider an immobile particle attached to a grain surface. By application of torque balance equation, we prove that for each fluid velocity there does exist such a critical particle radius that all particles with larger sizes are removed from the grain surface: $r_{scr}=r_{scr}(U)$ (see Fig. 6).

Thus we can define σ_{cr} for a monolayer of attached particles of different sizes as the concentration of attached particles with $r < r_{scr}$. Therefore, it is possible to calculate the maximum retention function σ_{cr} from the size distribution of the attached particles that can be mobilised by fluid velocity.

Electrostatic constants of the particle-rock interaction, attached fines radius histogram, and the Young's moduli and Poisson's ratios for particle and rock determine σ_{cr} for poly-size particles attached to the pore surface.

The maximum retention function is a monotonically decreasing function of the particle size. The wider is the particle size distribution (or the higher is the variance coefficient for particle size distribution), the lower is the σ_{cr} for low fluid velocities, and the higher is the σ_{cr} for high fluid velocities.

For the case of a poly-layer of mono-sized attached particles, the shape of σ_{cr} -curve is convex; whereas for a monolayer of dispersed attached particles, it has the shape of an arbitrary monotonically decreasing curve. σ_{cr} -curve changes its shape from convex to concave when a monolayer of log-normal distributed attached particles are under the action of small and high fluid velocities, respectively (see Fig.9).

The exact analytical solution can be obtained for 1d problem for suspension flow with piecewise increasing fluid velocity causing particle straining in thin pore throats. At the moment of velocity change, the concentration front starts moving from the inlet of the core, coincides with the trajectory of the drifting particle and separates the particle-free region behind the front and the area ahead of the front. The suspended and strained concentration profiles ahead of the front are uniform.

The drift delay factor is a function of the particle size and the geometry of the porous media undergoing continuous changes during straining of particles in thin pore throats. Smaller particles move with lower velocities along the pore surface; the drift delay factor is lower too. With increasing fluid velocity during coreflood tests, the size of the released particle decrease; this explains why the drift delay factor decreases (see Figs. 3d and 3h). The proposed model for colloidal-suspension transport in porous media with instant particle release and slow drift, given by Eqs. (15-18), can be further developed by introduction of the phenomenological function in the form $\alpha=\alpha(r_s,\sigma_s)$.

Validation of the proposed mathematical model is supported by a good agreement between the experimental data for pressure drop across the core during corefloods with piecewise increasing velocity with those calculated by the above model. The close match between experimental data and the matched modelling results can only be regarded as a preliminary model validation. Therefore, additional experiments should be carried out with the following measurable parameters: retention profiles, breakthrough particle concentrations and their size distribution. The above measured experimental parameters should be matched by the analytical solutions presented in Table 1. This will lead to the validation of the proposed model, which describes experimental conditions when velocity of the moving particles significantly differs from the velocity of the carrier fluid. Analysis of the available literature shows that such tests are not available.

3. Fines detachment and migration at low salinities

Salinity variation has significant effect on fines detachment, by affecting the electrostatic force between particles and rock surface. The lower the salinity, the weaker is the attraction between particles and rock, and thus the more particles are released. The detached particles migrate with carrier fluid and plug the smaller pores downstream, leading to significant permeability reduction. This section starts from laboratory coreflood test with piecewise decreasing salinity (section 3.1). The measured permeability history curves, outlet particle concentration and effluent ionic strength are presented in section 3.2. It is followed by the derivation of mathematical model for fines detachment and migration in porous media accounting for both effects of slow particle migration and delayed release, under salinity variations (section 3.3). In section 3.4, two particular models which account for slow migration and release delay effects respectively are applied to the experimental data treatment, and the quality of matching by two models is compared. Afterwards, the same data are treated using the general model developed in section 3.3.

3.1. Laboratory study

Section 3.1.1 describes the laboratory setup. Section 3.1.2 presents characteristics of rock and fluids used in the tests. Section 3.1.3 describes the experimental procedure. Section 3.1.4 presents characterisation technique of the effluent liquids.

3.1.1 Experimental setup

In this study, we developed and assembled an experimental setup for suspension-colloidal flow in natural rocks with permeability and breakthrough fines concentration measurements. The distinguished feature of the set-up is pressure measurements at the intermediate core point, which supplement the routine pressure measurements at the core inlet and outlet. This apparatus is schematically shown in Fig. 17 and its photo is presented in Fig. 18.

High-pressure coreholder 1 (model DHCH, CoreLab, USA) contains sandstone core plug 2 inserted inside a Viton sleeve 3. The Viton sleeve transfers overburden pressure from manual pressure generator 4 (model 87-6-5, HiP Equipment Company, USA) to the sandstone core. The overburden, core inlet, core middle and core outlet pressures are measured by absolute pressure transmitters 5-8 (model PA-33X, KELLER AG für Druckmesstechnik, Switzerland), respectively. High-pressure liquid chromatography pump (HPLC) 9 (Scientific Systems, Inc., USA) pumps artificial formation fluid (AFF) 10 through the sandstone core plug. A back-pressure regulator 11 (BP-series, CoreLab, USA) maintains constant core outlet pressure and smooth HPLC pump operation. Differential pressure between core inlet and middle point of the core is measured by differential pressure transmitter 12 (model EJX-110, Yokogawa[®], Japan) with maximum differential pressure ranged from zero to 140 kPa. When differential pressure exceeds this range, it is determined by the difference between readings of the two absolute pressure transmitters 6 and 7. Difference between the readings of two absolute pressure transmitters 8 and 6 determines pressure drop across the whole sandstone core plug. Swagelok[®] two-way valves perform the following operations: valve 13 connects manual pressure regulator to coreholder, valve 14 connects HPLC pump to the inlet of the coreholder, valves 15 and 16 connect the differential pressure transmitter to the inlet and middle point of the coreholder, and valve 17 is used for re-zeroing the differential pressure transmitter. Concentration of suspended particles in effluent samples 18 is measured by PAMAS S4031 GO portable particle counter 19 (PAMAS GmbH, Germany). A standalone computer 20, data acquisition module 21 (model ADAM-4019+, ADVANTECH[™], Taiwan), ADAM-4561 RS-232/422/485 signal converter 22 (ADVANTECH[™], Taiwan) perform the test data processing. Signals from differential pressure and absolute pressure transmitters are fed into ADAM-4019+ module, and are converted to pressure/differential pressure readings and transferred to Microsoft Excel spreadsheet in real-time via custom-built software (ADVANTECH ADAMView Ver. 4.25 platform). As the result, calculated core permeability values are recorded and monitored in graphical form in real-time.

3.1.2 Characterisation of cores and fluids

The sandstone core plug originated from depth 1875 m from the Birkhead Formation (Eromanga Basin, Australia) has a mean diameter of 37.82 mm, total length 49.21 mm and intermediate point length 25.10 mm. The core plug contains 9.2 % of kaolinite (see Table 3).

The major ionic components of formation fluid (FF) for the studied well supplied by Amdel Laboratories (Adelaide, Australia) are listed in Table 4. We converted these ionic compositions into molecular concentrations of an artificial formation fluid (AFF). According to total dissolved solids and electrolytic conductivity data presented in Table 4, we successfully matched the composition of AFF to the original FF. These two fluids (FF and AFF) are potassium-chloride driven (67.1% KCl). According to the composition data from Table 4 we prepared AFF using deionized ultrapure water

(Millipore Corporation, USA; later in the text it is called the DI water). The ionic strength of prepared AFF is boosted to 0.6 M by addition of NaCl to match its ionic strength with that of completion fluid. Lower ionic strength AFFs (0.6; 0.4; 0.2; 0.1; 0.05; 0.025; 0.01; 0.005; 0.001 M) are obtained by dilution of 0.6 M AFF with DI water.

3.1.3 Methodology of laboratory study

Drying of the core plug in the atmospheric oven at 60 °C for 24 hours is followed by its placement into a vacuum desiccator and saturation with 0.6 M AFF.

At the beginning of the experiment, the core plug is installed inside the Viton sleeve and placed in the stainless steel coreholder. An overburden pressure of 1000 *psi* is developed by the pressure generator and maintained at this level during the experiment. Artificial formation fluid with 0.6 M NaCl ionic strength is pumped by HPLC through the core plug at volumetric flowrate of 1.0 *mL/min* (superficial velocity 1.483×10^{-5} *m/s*). Pumping of this fluid continued until stabilization of permeability. The permeability stabilization is achieved within experimental uncertainty of 3.2% (Badalyan et al. 2012). Differential pressures across the whole core plug and between inlet and the middle point of the core are recorded by the data acquisition system. Automatic fraction collector collected effluent samples at 0.17 and 0.86 PVI, respectively. The bulk effluent sample of 114 PVI corresponded to the last stage of injection of the fluid with chosen ionic strength; this sample was collected over the 16-hour period.

Experiments with different ionic-strength corefloods are carried out using the same methodology.

3.1.4 Characterisation of effluent fluids

Particle concentration in effluent suspensions is measured by the particle counter PAMAS. Calibration of the particle counter/sizer is carried according to ISO Standard 21501-2:2007 (International organisation for Standardisation 2007). This unit measures the number of particles in the particle size range 0.5 to 5.0 μm , which is further converted into particle concentration expressed in m^3/mL or ppm (*vol/vol*) and particle size distribution. Multiplying the obtained particle concentration (m^3/mL) by the volume of respected effluent sample, we obtain the total volume of particles collected in each sample; the summation of the above volumes gives the total volume of particles collected during coreflood with fluid of fixed ionic strength.

Monitoring of ionic strength of effluent streams is carried out through measurement of their electrolytic conductivity using Mettler Toledo conductivity meter (Model S230 SevenCompact, Mettler-Toledo AG Analytical, Germany). The conductivity meter is calibrated using the following electrolytic conductivity standards covering the entire fluid ionic strength range used in the present study: 63.62 *mS/cm* (custom made solution), 12.88 *mS/cm*, 1413 $\mu\text{S/cm}$, 500 $\mu\text{S/cm}$, 84 $\mu\text{S/cm}$, and 10 $\mu\text{S/cm}$.

3.2. Analysis of experimental data

In this section, the experimental results of permeability and outlet particle size distribution versus time, measured using the laboratory procedure presented in section 3.1, are analyzed.

Initial (undamaged) core permeability measured during initial stage of coreflood with 0.6 *M* AFF is equal to $k=34.64$ *mD*. Mean pore-throat radius is calculated according to equation proposed by Katz and Thompson 1986: $r_p = (k/(4.48\phi^2))^{0.5}$, where k is in *mD*; the result is: $r_p=6.62$ μm . Mean-volume half-size of particles collected in effluent suspensions is measured by PAMAS and results in 1.47 μm . The so-called jamming ratio factor is determined by the ratio of mean-volume half-size of particles to mean pore-throat radius and is equal to 0.22. Earlier, (van Oort et al. 1993) proposed a “golden 1/7-1/3 rule of filtration”: if jamming ratio factor is less than 1/7 particles move through the porous medium and not captures; if this factor is between 1/7 and 1/3, then particles are strained in pore throats and cause rock permeability decline; if jamming ratio factor is greater than 1/3, then particles are captured at the entrance of a porous medium. Value of jamming ratio in the present study falls in between 1/7 and 1/3 suggesting that some of mobilised particles are captured in pore-throats causing permeability decline which happens during deep bed filtration.

The cumulative produced-particle volume and effluent fluid ionic strength versus PVI for the coreflood test are shown in Figs. 19a,b,c. Volume of produced fines increases when effluent ionic strength declines. In average, it takes about 1.0-1.5 PVI before effluent ionic strength starts to decrease for a newly-injected lower ionic-strength fluid. Rock impedance rapidly rises after this delay, suggesting that lower ionic strength fluid detach and mobilize the fine particles, causing pore blockage and increase of core impedance (permeability decline). Appreciable volume of fines was collected during coreflood with DI water suggesting that very low ionic strength AFF (0.001 *M*) was not able to remove all fines.

The measured average permeability along the core $\langle k \rangle(T)$ under piecewise decrease of salinity, scaled by the initial core permeability k_0 , is presented in Figs. 20a and 23a. The permeability history curves show that it takes much longer than one PVI for the permeability reaching stable values. The delay in permeability stabilization suggests that certain amount of particles is released with delay, if compared to the instantly released particles after salinity variation. The long-term permeability stabilization may also be caused by the slow migration of released particles drifting along the rock surface (Yuan and Shapiro 2011a; You et al. 2015). Slow migration model has been discussed in Section 2. The next section presents the model with delay.

3.3. Analytical model with slow migration and delay particle release

The permeability history curves presented in section 3.2 show that the steady state is reached after tens to hundreds PVIs of water injection. This delay phenomenon can be explained by the Nernst-Planck diffusion of ions between the bulk of the fluid in the pore and the contact particle-grain area of the mutual deformation (Mahani et al. 2015, 2016), which has not been considered in the slow-migration model (15-18) presented in section 2. In this section, we generalize the previous model by accounting for both slow migration of particles and their delayed release.

Consider a delay τ in fines detachment if compared with the moment, when water salinity is equal to $\gamma(x,t)$. Introducing delay into the expression of maximum retention function yields: $\sigma_a(x,t+\tau) = \sigma_{cr}(\gamma(x,t))$. Keeping two first terms of Taylor's expansion over small delay τ results in:

$$\tau \frac{\partial \sigma_a}{\partial t} = \sigma_{cr}(\gamma_1) - \sigma_a \quad (31)$$

System of three equations (11, 12) and (31) describes the suspension-colloidal transport in porous media with delayed release of the reservoir fines due to salinity decrease. The kinetic equation (31) substitutes equation (31) for maximum retention function. System of three equations (11, 12, 31) defines the same three unknowns: c , σ_a , and σ_s .

Introduction of dimensionless group for delay

$$\varepsilon = \frac{U\tau}{\phi L}$$

and using concentration of released particles $\Delta\sigma_{cr}$ in dimensionless variables (14) instead of σ_{a0} yields the following dimensionless system:

$$\frac{\partial(C + S_s + S_a)}{\partial T} + \alpha \frac{\partial C}{\partial X} = 0 \quad (32)$$

$$\varepsilon \frac{\partial S_a}{\partial T} = S_{cr}(\gamma_1) - S_a \quad (33)$$

$$\frac{\partial S_s}{\partial T} = \alpha \Lambda C \quad (34)$$

We assume that the time of mobilized particle arrival at the core outlet $1/\alpha$ is significantly higher than 1 PVI, i.e. $\alpha \ll 1$. Therefore, the initial conditions at $T=0$ correspond to injected salinity γ_1 . The initial concentration of attached particles corresponds to the critical value $\sigma_{a0} = \sigma_{cr}(\gamma_0)$, where $\gamma_0 > \gamma_1$. Boundary conditions correspond to injection of particle-free water with salinity γ_1 :

$$C(X,0) = 0, \gamma(X,0) = \gamma_1, S_s(X,0) = 0, S_a(X,0) = S_{a0} = \frac{\sigma_{a0}}{\Delta\sigma_a} \quad (35)$$

$$C(0,T) = 0, \gamma(0,T) = \gamma_1$$

The solution of linear ordinary differential equation (33) with initial condition (35) is

$$S_a = S_{acr}(\gamma_1) - [S_{acr}(\gamma_1) - S_{a0}] \exp\left(-\frac{T}{\varepsilon}\right) \quad (36)$$

It allows for explicit expression for the detaching rate:

$$\frac{\partial S_a}{\partial T} = \frac{1}{\varepsilon} [S_{acr}(\gamma_1) - S_{a0}] \exp\left(-\frac{T}{\varepsilon}\right) \quad (37)$$

Substitution of expressions for the detaching and straining rates, given by Eqs. (37) and (34), respectively, into the overall particle balance Eq. (32) yields

$$\frac{\partial C}{\partial T} + \alpha \frac{\partial C}{\partial X} = -\alpha\Lambda C + \frac{1}{\varepsilon} [S_{a0} - S_{acr}(\gamma_1)] \exp\left(-\frac{T}{\varepsilon}\right) \quad (38)$$

Introduction of constant

$$y = \frac{1}{\varepsilon} [S_{a0} - S_{acr}(\gamma_1)], \quad b = 1/\varepsilon \quad (39)$$

simplifies Eq. (38):

$$\frac{\partial C}{\partial T} + \alpha \frac{\partial C}{\partial X} = -\alpha\Lambda C + y \exp(-bT) \quad (40)$$

First, discuss the flow ahead of the mobilised fine front for $T \leq X/\alpha$. The characteristic form of the linear hyperbolic equation (40) is

$$\frac{dx}{dT} = \alpha \quad (41)$$

$$\frac{dC}{dT} = -\alpha\Lambda C + y \exp(-bT), \quad C(X,0) = 0 \quad (42)$$

For the case of $\alpha\Lambda \neq b$ the solution of linear ordinary differential equation (42) is:

$$C(T) = \frac{y}{\alpha\Lambda - b} (e^{-bT} - e^{-\alpha\Lambda T}) \quad (43)$$

For the case of $\alpha\Lambda = b$ the solution of Eq. (42) is

$$C(T) = yTe^{-bT} \quad (44)$$

Like in the case of fines migration after abrupt velocity increase (row 3 in Table 1), initial uniform suspended profile moves with equal capture probability for all particles. Thus, the suspended profile remains constant, and suspension concentration is only time-dependent.

Now consider the solution behind the mobilized fines front for $T > X / \alpha$. The characteristic form of Eq. (40) with zero boundary condition is

$$\frac{dT}{dX} = \frac{1}{\alpha}, T(0) = \eta \quad (45)$$

$$\frac{dC}{dX} = -\Lambda C + \frac{y}{\alpha} e^{-bT}, C(0) = 0 \quad (46)$$

For the case of $\alpha\Lambda \neq b$ the solution of linear ordinary differential equation (53) is:

$$C(X) = \frac{m}{\Lambda - \frac{b}{\alpha}} \left(e^{\frac{b}{\alpha}X} - e^{-\Lambda X} \right), \quad m = \frac{y}{\alpha} e^{(-b\eta)} \quad (47)$$

Substituting the constant along the characteristic line

$$\eta = T - \frac{x}{\alpha} \quad (48)$$

into solution (47) yields the suspended concentration behind the front

$$C(X, T) = \frac{y}{\alpha\Lambda - b} e^{-bT} \left(1 - e^{\left(\frac{b}{\alpha} - \Lambda\right)X} \right) \quad (49)$$

For the case of $\alpha\Lambda = b$ the solution of Eq. (46) is

$$C(X) = mXe^{-\Lambda X} \quad (50)$$

Substituting the constant along the characteristic line

$$\eta = T - \frac{x}{\alpha}$$

into solution (50) yields the suspended concentration behind the front

$$C(X,T) = \frac{y}{\alpha} e^{-bT} X e^{\left(\frac{b-\Lambda}{\alpha}\right)X} \quad (51)$$

Formulae for strained concentration S_s are obtained by substitution of the suspended concentration $C(X,T)$ in straining rate equation (34) and integration in T. The solution is given in Table 5 for the case $\alpha\Lambda \neq b$ and in Table 6 for the case $\alpha\Lambda = b$.

3.4. Experimental data treatment and model validation

In this section, we treat the experimental data using three simplified models: slow-particle migration model, delay-particle release model, and the general model that accounts for both effects. The histories of impedance across the half-core and whole core, and the accumulative outlet concentration of particles are matched by each model. The reflective trust region algorithm is applied for solution of the optimization problem (Coleman et al. 1996) using the software Matlab (Mathworks 2010).

The results of matching by the slow-particle migration model are presented in Fig. 21a for impedance, and in Fig. 21b for accumulated particle concentration. The coefficient of determination is equal to $R^2=0.9902$. The tuning parameter values are shown in Table 7 and in Fig. 22.

The piecewise-constant salinity decrease in the test and consequent fines particle release corresponds to increasing of strained particle concentration. This changes the pore space geometry and values of the tuned parameters.

The drift delay factor α decreases as permeability decreases (Fig. 22a). It can be explained by the decreasing size of released particles during the salinity decrease. Smaller particles are exerted by lower drag force and they move slowly. Also, the rock tortuosity increases due to straining, so the fines move slowly. Regarding formation damage coefficient β , two factors compete during the salinity decrease. The lower is the permeability the higher is the formation damage coefficient. Yet, the smaller are the particles the lower is the formation damage coefficient. The retained-concentration-dependency for the formation damage coefficient, shown in Fig. 22b is attributed to the dominant effect of the particle size over the permeability effect. The filtration coefficient for straining λ increases during rock tortuosity increase during salinity decreasing (Fig. 22c). Yet, it should decrease due to decrease of the released particle size. Fig. 22d presents the salinity-dependency of the maximum retention function, which exhibits a typical form (Bedrikovetsky et al., 2012; Zeinijahromi et al., 2012).

The results of matching by the delay-particle release model are presented in Fig. 23a for impedance, and in Fig. 23b for accumulated particle concentration. The tuning parameter values are shown in Table 8. The coefficient of determination is equal to $R^2=0.9874$ and is slightly lower than that for the slow-particle model.

The formation damage coefficient β increases as salinity declines (Fig. 24a), which is different from the slow-particle model; the effect can be explained by the dominant role of permeability decline on the formation damage coefficient. Yet, this explanation contradicts to the conclusion made above for the slow-particle model. The filtration coefficient λ decreases during salinity decrease (Fig. 24b), which also contradicts to the conclusion made above for the slow-particle model. The effect can be explained by the blocking filtration function, where λ is proportional to the vacancy concentration; it tends to zero when the number of pores larger than particle tends to zero. The delay time τ decreases with increase of strained concentration (Fig. 24c); this is attributed to more confined porous space and smaller diffusive path. The maximum retention function hasn't got a typical form (Fig. 24d); usually bulk of fines is released by low-salinity and fresh water. Low fines release by low-salinity water can be explained by low concentration of small particles, which is usually not the case.

H Mahani 2015a, b measured the delay period, which is significantly (10-20 times) longer than expected by diffusion alone and is explained by slow electro-kinetic Nernst-Planck ion-diffusion in the field of electrostatic DLVO forces. The delay time τ varies from 10800 to 363600 s, which corresponds to dimensionless time in PVI that is equal $\varepsilon=U\tau/\phi L$ and varies from 15.49 to 521.62 PVI for conditions of the test presented in section 3.1 ($\phi=0.21$, $U=1.48\times 10^{-5}$ m/s). The obtained values have the same order of magnitude as those obtained by tuning the parameter ε from laboratory tests (Tables 8 and 9).

The results of matching by the general model that accounts for both slow-particle migration and delay-particle release effects are presented in Fig. 25a for impedance, and in Fig. 25b for accumulated particle concentration. The tuning parameter values are shown in Table 9. The coefficient of determination is equal to $R^2=0.9899$. The stained-concentration dependencies for α , β , λ , and σ_{er} (Figs. 26 a, b, c and e, respectively) follow the same tendencies as those exhibited by the slow-particle model. The delay time τ (Fig. 26 d) has the same form as that for the delay-particle model. The coefficient of determination is equal to $R^2=0.9899$.

3.5. Summary and discussion

The laboratory study of fines migration mobilized by decreasing brine salinity, provide three measurement histories during injections with constant salinity: impedance across the half-core and whole core, and the outlet concentration of fine particles. Each pressure curve and each concentration curve has at least two degrees of freedom, so three measurement data for constant salinity period has 6 degrees of freedom.

The slow-particle migration and delay-particle release models have four independent coefficients separately. Thus, 6-dimensional data-set was matched by four model coefficients with high accuracy.

The strained-saturation dependencies of the tuned parameters have been explained. The close agreement between the experimental data and the models allows concluding the validity of both the slow-particle migration model and the delay-particle release model.

The general model has five independent coefficients. This is higher than those for the slow-particle migration and delay-particle release models, but still lower than the number of degree of freedom of the laboratory data-set (6). The agreement coefficient is also very high. The obtained delay periods have the same order of magnitude with those observed in laboratory tests (Mahani et al., 2015a, b). However, the model does not exhibit a common form of the maximum retention function.

4. Fines detachment and migration at high temperatures

This section discusses temperature-dependency of particle detachment and fines migration with applications to geothermal reservoirs.

4.1 Materials and preparation

Availability of cuttings and the absence of cores from geothermal well Salamander-1 (Pretty Hill Formation, Otway Basin, South Australia, Australia) make it difficult to experimentally study formation damage exhibited in this well during production. To circumvent this problem we studied formation damage on a core with analogous mineral characteristics obtained from the nearby Ladbroke Grove-1 well from the same formation and basin. This core came from depth 2557.12 *m*. It is 3.92 *cm* in diameter and 6.33 *cm* in length. Core imbibition procedure, described in section 3.1.3, results in 17.2 % porosity.

4.2 SEM-EDAX analyses for released fines

The results of SEM-EDX analyses for the fines filtered from the effluent suspensions fines are shown in Fig. 27. Plate-like “booklets” characteristic of kaolinite is shown on SEM image (see Fig. 27a). The so-called “peak height ratio” equivalent to the ratio of relative molar proportions of Al and Si shown on EDX spectrum (see Fig. 27b) is approximately equal to unity. This suggests that the above “booklets” are identified as kaolinite, $\text{Al}_2(\text{Si}_2\text{O}_5)(\text{OH})_4$. The amount of fines from effluent stream collected by filtering through 0.45 μm Nylon filter is insufficient to perform XRD analysis which may give additional information about mineralogy of these fines.

4.3 Analysis of temperature effect on physical parameters

Several Derjaguin-Landau-Verwey-Overbeek (DLVO) parameters listed in Table 10 are temperature-dependent. Studying their sensitivity to temperature variation helps to predict the effect of temperature on fines mobilisation. Since the most abundant minerals in the studied sandstone core are quartz and kaolinite we use the following DLVO parameters for calculations: the refractive index of

kaolinite $n_1 = 1.502$ is adopted from (Egan and Hilgeman, 1979); the temperature dependences of refractive index of quartz n_2 and brine n_3 as functions of temperature are provided by Leviton and Frey (2006) and Aly and Esmail (1993), respectively; dielectric constant of quartz $\epsilon_2 = 4.65$ is adopted from (Stuart, 1955); dielectric constant of kaolinite $\epsilon_1 = 6.65$ and 6.35 at $T = 25^\circ\text{C}$ and 80°C , respectively, are adopted from (Leluk et al., 2010; see Table. 10); dielectric constant of brine ϵ_3 at various ionic strengths and temperatures is presented in Table. 11; zeta potentials for fines and porous matrix are calculated according to Schembre and Kavscek (2005). Variation of water viscosity is adopted from Al-Shemmeri (2012) in the form $\mu(T) = 2.414 \times 10^{-5} \times 10^{247.8/(T-140)}$. The data on temperature dependences of the characteristic wavelength of interaction λ , refractive index of clay n_1 and collision diameter σ_c are unavailable in the literature. Therefore, following Schembre and Kavscek, 2005, Schembre et al., 2006a, 2006b and Lagasca and Kavscek, 2014, we assume the above mentioned parameters to be constant. The values of constants are taken from works by Gregory (1981), Egan (1979) and Elimelech et al. (2013).

The above mentioned parameters have been used in order to calculate the critical particle size versus velocity by Eq. (6). Fig. 28 presents the results of these calculations. The higher is the temperature the lower is the electrostatic attraction. Thus, a particle is detached at lower velocity where the temperature increases; so curve 3 is located below the curve 1. Salinity increase yields the increase of electrostatic force, so curve 2 is located above the curve 1. During temperature increase under constant velocity, the drag force detaches the particles in order of their size decreasing, i.e. first large particle are mobilised.

4.4 Experimental results and model prediction at geothermal conditions

The corefloods using the Ladbroke Grove-1 core have been performed using the methodology of piecewise-constant salinity decrease described in Section 3. The experimental data of permeability variation with PVI are shown by black circles in Fig. 29a. Variation of effluent particle concentration as a function of fluid ionic strength is shown by black points in Fig. 29b. These graphs show the same trend as those presented in Figs. 3, 19, 20, 23, and 25. Permeability variation during corefloods with piecewise-constant salinity decrease shows almost instant decline when salinity of injected fluid drops abruptly. Such permeability behaviour suggests that the significant fraction of attached fine particles is mobilised instantly and then is size excluded gradually with time.

The analytical model presented in Section 2.3 (rows 12 and 13 in Table 1) is used to treat experimental data. Typical log-normal size distribution is assumed for fines of the Ladbroke Grove-1 core.

We choose the following parameters for tuning the analytical model: filtration and formation damage coefficients, λ and β , respectively; drift delay factor α ; variance coefficient for particle size

distribution C_v ; and mean particle size $\langle r_s \rangle$. Smaller particles are mobilised when ionic strength of injected fluid decreases. It is assumed, that at each injected-fluid ionic strength the particles with constant radius are mobilised. For this reason, the following parameters remain unchanged for each injected-fluid ionic strength: the filtration and formation damage coefficients and drift delay factor. The tuning procedure for the analytical model include the so-called least square goal function of the difference between model predicted results and measured data. Minimisation of this difference is carried out using the Levenburg-Marquardt minimisation algorithm (Marquardt, 1963). Values of tuning parameters obtained by application of the above minimisation algorithm are presented in Table 12. Results of modelling are shown in Figs. 29a and 29b as red curves for optimised permeability as function of PVI, and effluent concentration as function of fluid ionic strength. There is a very good agreement between model-predicted results and measured data for both core permeability and outlet particle concentration. This is supported with coefficients of determination being close to one as follows: $R^2=0.997$ and $R^2=0.943$, respectively.

Let us calculate the number of the degree of freedom for the experimental data set. Assuming the exponential pressure drop variation, we obtain three degrees of freedom for each time interval in Fig. 29a. The initial permeability is given, which results in $3 \times 4 - 1 = 11$ degrees of freedom of the pressure drop measurements. Four independent breakthrough particle concentrations, averaged over the constant-salinity injection periods, add 4 degrees of freedom, making the total 15. Table 12 shows 15 independent constants tuned from the experimental data. There is a good agreement between the experimental and modelling data. We conclude that the model perfectly describes the laboratory results.

Yet, the validation of the proposed model would require measurements of the breakthrough particle concentrations with time. It would allow enhancing the number of the degree of freedom for the experimental data set.

We performed sensitivity analysis using the following main parameters: the drift delay factor, formation damage and filtration coefficients with results given in Figs. 29a and 29b. As follows from blue curve in Fig. 29a, when α increases the stabilisation time decreases since particles start to move faster. Lower probability of particle capture by thin pores translates to lower values of λ leading to higher values for permeability stabilisation period according to light blue curve in Fig. 29a. Small values of β correspond to permeability damage with time according to Fig. 29a (green curve). The only one modelling parameter, λ , has significant effect on breakthrough concentration of mobilised particles since it describes the probability of mobilised particle capture by thin pore throats. As follows from Fig. 29a (light blue curve) lower values of λ correspond to higher breakthrough particle concentrations. Experimental results show that effluent (breakthrough) particle concentration is significantly lower than concentration of mobilised particles $\Delta\sigma_i$. Therefore, the breakthrough particle

concentration is insensitive to drift delay factor as shown by blue curve in Fig. 29a. As shown by green curve in Fig. 29a the breakthrough concentration is insensitive to β . The obtained values of λ and β presented in Table 12 along with concentration of strained particles fall within their common intervals according to (Nabzar and Chauveteau, 1997; Pang and Sharma, 1997; Civan, 2007, 2016).

The tuned data allows predicting the maximum retention function by Eq. (8). Maximum retention function for monolayer of multi-sized particles versus fluid velocity and fluid ionic strength are shown in Fig. 30a and 30b, respectively. According to Fig. 30a, initial attached particle concentration is shown by point I . When fluid velocity increases from 0 to U_A , the state point moves along the path $I \rightarrow A$ without particle mobilisation. Increasing fluid velocity from U_A to U_B (movement from point A to point B) leads to the start of particle mobilisation at critical fluid velocity $U=U_B$. If we continue increase fluid velocity from U_B to U_C the state point moves down along the maximum retention curve from point B to C . If we compare Figs. 30a and 30b, we observe similar typical shape of the maximum retention function with gradual decrease of fluid ionic strength corresponding to increase of fluid velocity. This results in similarity between the critical ionic strength γ_B and critical fluid velocity U_B . According to (Miranda and Underdown, 1993; Khilar and Fogler, 1998), the notions of critical velocity and critical ionic strength correspond to the first particle release when fluid velocity increases and fluid ionic strength decreases, respectively. If we introduce the maximum retention function it is possible to predict the amount of the released fines as a result of changing the critical parameters. The amount of mobilised particles during fluid velocity and/or salinity alteration are denoted as $\Delta\sigma$ in Figs. 30a and 30b.

Electrostatic attaching force decreases with temperature leading to the drop of maximum retention function. From another side, reduction of water viscosity with temperature results in decrease of both lifting force and detaching drag force. These changes translate to the rise of maximum retention function. Therefore, the above two competitive effects determine if maximum retention function increases or decreases.

According to Figs. 30a and 30b, the dominance of temperature influence on electrostatic attaching forces leads to decrease of maximum retention function and resultant permeability decline with temperature rise. We calculated and plotted σ_{cr} -curves for the following temperatures (see Fig. 30a and 30b): room temperature, 80°C, 100°C and 129°C (curves 1-4, respectively). Comparison of these curves shows the decline of the maximum retention function with temperature increase. Salamander-1 geothermal well is characterised by a reasonably moderate temperature of $T=129^\circ\text{C}$ and ionic strength equivalent to 0.2 M NaCl. At these field conditions, according to curve 4 (see Fig. 30b) almost all fines are mobilised with the decrease of the maximum retention function down to zero.

Apart from high temperature, fluid velocity alteration also effects particle mobilisation within a porous medium. We calculated and plotted σ_{cr} -curves for the following fluid velocities (see Fig. 30c): at wellbore velocity r_w , at $50 r_w$ and $100 r_w$ (curves 1-3, respectively). If one decreases fluid velocity the maximum retention concentration will rise due to reduced detaching drag force acting on the attached particles.

4.5 Using ionic strength sensitivity to characterise fines mobilisation system

Consider inflow performance in geothermal production wells. The well rate per unit of the reservoir thickness is $q = 2\pi rU$. During production one observes two or more orders of magnitude decrease of fluid velocity in the direction from well bore towards the drainage contour. The magnitude of this decrease is the function of the distance from the well. Variation of fluid viscosity with temperature affects detaching drag force which is a function of fluid velocity. Therefore, such rheological dependence of σ_{cr} should be studied in a wide range of fluid velocities. Having studied this relationship, one can reliably estimate well productivity index. However, the maximum available capacity of commercially available pumps limits the above studies at high fluid velocity variations.

Coreflood with lower ionic strength fluid also leads to particle mobilisation. Therefore, it is much easier to run such tests with significant variation of fluid ionic strength in laboratory. The torque balance equation (6) has the following two solutions: $\sigma_{cr} = \sigma_{cr}(\gamma)$ and $\sigma_{cr} = \sigma_{cr}(U)$. Since $\sigma_{cr}(\gamma_0) = \sigma_{cr}(U_0)$, then we get the following translation formula:

$$\sigma_{cr}(U, \gamma_0) = \sigma_{cr}(U_0, \gamma). \quad (52)$$

This formula translates $\sigma_{cr} = \sigma_{cr}(\gamma)$ to $\sigma_{cr} = \sigma_{cr}(U)$ and vice versa.

Below we describe such translation for a monolayer of multi-sized particles attached to the wall of pores (see Eq. (8)). Let after running of coreflood tests with varying fluid ionic strength one obtains $\sigma_{cr}(U_0, \gamma)$ relationship. Equation (6) determines critical particle radius as $r_{scr}(U, \gamma)$. It is possible to calculate $r_{scr}(U_0, \gamma) = r_{scr}(U, \gamma_0)$ corresponded to each value of γ , and corresponding velocity for fixed ionic strength γ_0 . Therefore, the experimentally obtained relationship $\sigma_{cr}(U_0, \gamma)$ can be recalculated into $\sigma_{cr}(U, \gamma_0)$ relationship.

Curve 1 in Fig. 30b corresponds to $\sigma_{cr}(U_0, \gamma)$ at constant fluid velocity and ambient temperature. The translation curve 1 in Fig. 30a represents $\sigma_{cr}(U, \gamma_0)$ at constant fluid ionic strength and ambient temperature.

According to Fig. 30b, permeability decline during low ionic strength coreflood is defined by the form of the maximum retention curve. Very low cumulative breakthrough concentration at high fluid ionic strength at point *I* (see Fig. 29b) corresponds to point *I* in Fig. 30b on a flat part of maximum retention

curve. With increase of fluid ionic strength from state *I* to *III* through point *II* one observes an increase of cumulative breakthrough concentration (or the amount of mobilised and produced fines) according to Fig. 29b. This corresponds to downward movement along the critical retention curve. The slope of this curve increases towards point *III* (see Fig. 30b). Further decrease of fluid ionic strength towards point *IV* is accompanied by less increase of released and produced fines (see Fig. 29b). This is accompanied by inflection of maximum retention curve with decrease of its slope according to Fig. 30b.

4.6. Summary and discussion

Laboratory study on fines migration and micro scale modelling of fines mobilisation allow drawing the following conclusions:

Mechanical equilibrium of attached fines is determined mostly by drag and electrostatic forces; neglecting lifting and gravitational forces allows for reduction of the number of tuning parameters in torque balance equation by two.

Maximum retention function for monolayer deposit of size-distributed particles is expressed by explicit formula.

The effect of electrostatic attraction weakening with temperature rise dominates over the effect of detaching drag force reduction at ambient and field conditions. It yields decrease of the maximum retention concentration with temperature. Consequently, geothermal reservoirs are more susceptible to fines migration than conventional aquifers or oilfields.

The laboratory “velocity-ionic strength” translation procedure along with the mechanical equilibrium model allows determining velocity dependency of the maximum retention function from tests with varying ionic strength.

Experiment-based estimation of dependency of the maximum retention function on velocity and temperature is obtained for specific conditions of geothermal reservoirs.

Kaolinite and illite/chlorite, as main clay minerals presented in released fines from coreflood in the present study, are responsible for formation damage.

Coreflood exhibits almost instant permeability response to abrupt salinity change, suggesting that the significant fraction of attached fine particles is mobilised instantly and then is size excluded gradually with time.

Stabilisation time highly exceeds one pore volume, indicating that the fine particles migrate with the velocity significantly lower than the carrier water velocity.

5. Conclusions

The analytical modelling and laboratory study of fines migration due to velocity/salinity/temperature/*pH* alternations during coreflooding allow drawing the following conclusions:

1. Mechanical equilibrium of attached fines is determined mostly by drag and electrostatic forces; neglecting lifting and gravitational forces allows for reduction of the number of tuning parameters in torque balance equation by two.
2. Low-velocity fines drift along rock surface (rolling, sliding) explains the long permeability-stabilization periods. Stabilisation time highly exceeds one pore volume, suggesting that the fine particles migrate with the velocity that is significantly (two-three orders of magnitude) lower than the carrier water velocity.
3. Another explanation of long permeability-stabilization periods is the delay in particle release due to slow diffusion of salt from the grain-particle deformation-caused contact area into the bulk of the fluid.
4. One-dimensional problem of slow fines migration with delayed particle release after velocity/salinity/*pH* altering allows for exact solution. The analytical model contains explicit formulae for breakthrough and retained concentrations and pressure drop history.
5. Matching the measured permeability and accumulative outlet particle concentration by the analytical model accounting for both slow fines migration and delayed release shows high agreement between measured data and modelling results.
6. Slow-particle model matches the experimental data with higher accuracy than the delay-release model. The straining-concentration and salinity dependencies for model parameters obtained from tuning by the slow-particle model have typical forms observed in other studies, whereas those obtained using the delay-release model reveal the untypical form of the maximum retention function.
7. Fine particles are mobilised during velocity, temperature, and *pH* increase, or salinity decrease in the order of decreasing of their sizes.
8. The maximum retention function for size-distributed fine particles attached to pore walls in a mono-layer is expressed by an explicit formula that includes the size distribution of attached particles and the critical detached size curve. This function is equal to accumulated concentration of particles smaller than that mobilized by the flux with a given flow with velocity U .
9. Size distribution of the attached movable particles can be determined from the maximum retention function and the critical detached size curve.
10. The laboratory “velocity-ionic strength” and “temperature-ionic strength” translation procedures along with the mechanical equilibrium modelling allows determining velocity-

and temperature- dependencies of the maximum retention concentration from tests with varying ionic strength.

11. The effect of electrostatic attraction weakening with temperature on the maximum retention function dominates over that of the water viscosity decrease with temperature in this study. It results in the maximum retention function decrease with temperature. Therefore, geothermal reservoirs are more susceptible to fines migration than conventional aquifers or oilfields.

Acknowledgements

The authors are grateful to numerous researchers with whom they were working jointly on colloidal-suspension transport in porous media: Prof. A Shapiro and Dr. H. Yuan (Denmark Technical University), Dr. R. Farajzadeh and Profs. P. Zitha and H. Bruining (Delft University of Technology), Prof. A. Polyaniin (Russian Academy of Sciences), Prof. Y. Osipov (Moscow University of Civil Engineering) and L. Kuzmina (National Research University, Russia).

Nomenclature

A_{132}	Hamaker constant for interaction between material 1 and 2 in medium 3, ML^2T^{-2}
c	Suspended particle concentration, L^{-3}
C	Dimensionless suspended particle concentration
C_{mi}	Molar concentration of i -th ion, L^{-3}
D	Dispersion coefficient
D_e	Dielectric constant
e	electron charge, C
E	Young's modulus, $ML^{-1}T^{-2}$
F	Force, MLT^{-2}
h	Particle-surface separation distance, L
H	Half width of the channel, L
J	Impedance (normalized reciprocal of mean permeability)
k	Permeability, L^2
k_{det}	Detachment coefficient
$\langle k \rangle$	Mean permeability, L^2

k_B	Boltzmann constant, $ML^2T^{-2}K^{-1}$
k_n	Number of data points in each stage
K	Composite Young's modulus, $ML^{-1}T^{-2}$
l	Lever arm ratio
l_n	Normal lever, L
l_d	Tangential (drag) lever, L
L	Core length, L
p	Pressure, $MT^{-2}L^{-1}$
P	Dimensionless pressure
n	Serial number of variant velocities
N	Serial number of final velocities
r_s	Radius of a particle, L
r_{scr}	Critical radius of a particle can be removed at certain velocity, L
S_a	Dimensionless attached particle concentration
S_s	Dimensionless Strained particle concentration
ΔS_a	Dimensionless mobilized concentration of detached particles with velocity alternation
t	Time, T
T	Dimensionless time
$t_{st,n}$	Stabilization time for n^{th} flow rate, T
$T_{st,n}$	Dimensionless stabilization time for n^{th} flow rate
t_n	Initial time of n^{th} flow rate, T
T_n	Dimensionless initial time of n^{th} flow rate
\bar{u}	Average velocity through a slot
u_t	The tangential cross flow velocity of fluid in the center of the particle
U	Darcy's velocity, LT^{-1}
U_s	Particle's seepage velocity, LT^{-1}

V	Potential energy, ML^2T^{-2}
x	Linear coordinate, L
X	Dimensionless linear coordinate
z_i	Electrolyte valence of the i -th ion

Greek symbols

α	Drift delay factor
β	Formation damage coefficient
Y	Salinity
ε	Dimensionless delay time
ε_0	Free space permittivity, $C^{-2}J^{-1}m^{-1}$
η	intersection of characteristic line and the T axis
κ	Debye length, L^{-1}
λ_a	Filtration coefficient for attachment mechanism, L^{-1}
λ_s	Filtration coefficient for straining mechanism, L^{-1}
A_a	Dimensionless filtration coefficient for attachment mechanism
A_s	Dimensionless filtration coefficient for straining mechanism
μ	Dynamic viscosity, $ML^{-1}T^{-1}$
ν	Poisson's ratio
ρ	Fluid density, ML^{-3}
ρ_s	Particle density, ML^{-3}
σ_{cr}	Critical retention function, L^{-3}
$\Sigma_a(r_s)$	Size distribution of attached particles, L^{-3}
σ	Concentration of retained particles, L^{-3}
$\Delta\sigma_n$	Mobilized concentration of detached particles with velocity switch from U_{n-1} to U_n

σ_{LJ}	Atomic collision diameter, L
τ	Delay time of particle release, T
ν_i	The number of ions per unit volume
ω	Dimensionless coordinate of an immediate core point
χ	Lifting factor
ϕ	Porosity
Ψ_{01}	Particle surface potential
Ψ_{02}	Collector surface potential
ω	Drag factor
<i>Subscripts</i>	
a	Attached (for fine particles)
d	Drag (for force)
g	Gravitational (for force)
$iiion$	Injected ions
$Oion$	Initial ions
l	Lifting (for force)
e	Electrostatic (for force)
max	Maximum
n	Normal (for force), flow rate number (for velocities, inherited retained concentrations, particle – fluid velocity ratios, inherited impedances)
BR	Born repulsion (for potential energy)
DLR	Electrostatic double layer (for potential energy)
LVA	London-van der Waal (for potential energy)
0	Initial value or condition (for permeability, retained concentrations)

References

Akhatov IS, Hoey JM, Swenson OF et al (2008) Aerosol focusing in micro-capillaries: Theory and experiment. *Journal of aerosol science* 39(8): 691-709.

Al-Shemmeri T (2012) *Engineering Fluid Mechanics*. Bookboon.

Aly KM, Esmail E (1993) Refractive index of salt water: effect of temperature. *Optical Materials* 2(3): 195-199.

Amix B, Bass R, Whiting A (1964) *Applied Reservoir Engineering*.

Arab D, Pourafshary P, Ayatollahi et al (2014) Remediation of colloid-facilitated contaminant transport in saturated porous media treated by nanoparticles. *International Journal of Environmental Science and Technology* 11(1): 207-216.

Badalyan A, Carageorgos T, Bedrikovetsky P et al (2012) Critical analysis of uncertainties during particle filtration. *Review of Scientific Instruments* 83(9): p.095106.

Bai T, Chen Z, Aminossadati SM et al (2015) Characterization of coal fines generation: A micro-scale investigation. *Journal of Natural Gas Science and Engineering*, 27: 862-875.

Bedrikovetsky P.G., 1993, *Mathematical Theory of Oil & Gas Recovery (With applications to ex-USSR oil & gas condensate fields)*, Kluwer Academic Publishers, London-Boston-Dordrecht, 600 p.

Bedrikovetsky P, Siqueira FD, Furtado CA et al (2011a) Modified particle detachment model for colloidal transport in porous media. *Transport in porous media* 86(2): 353-383.

Bedrikovetsky P, Vaz AS, Furtado CJ et al (2011b) Formation-damage evaluation from nonlinear skin growth during coreflooding. *SPE Reservoir Evaluation & Engineering* 14(02): 193-203.

Bedrikovetsky P, Zeinijahromi A, Siqueira FD et al (2012) Particle detachment under velocity alternation during suspension transport in porous media. *Transport in porous media* 91(1): 173-197.

Bedrikovetsky P, Vaz A, Machado F et al (2012), Skin due to Fines Mobilisation, Migration and Straining during Steady State Oil Production, *J Petrol Sci Tech* 30(15): 1539-1547

Bergendahl JA, Grasso D (2003) Mechanistic basis for particle detachment from granular media. *Environmental science & technology* 37(10): 2317-2322.

Bradford SA, Bettahar M (2005) Straining, attachment, and detachment of oocysts in saturated porous media. *Journal of Environmental Quality* 34(2): 469-478.

Bradford SA, Torkzaban S, Kim H et al (2012) Modeling colloid and microorganism transport and release with transients in solution ionic strength. *Water Resources Research* 48(9): .

Bradford SA, Torkzaban S, Shapiro A (2013) A theoretical analysis of colloid attachment and straining in chemically heterogeneous porous media. *Langmuir* 29(23): 6944-6952.

Byrne MT, Waggoner SM (2009) Fines migration in a high temperature gas reservoir-laboratory simulation and implications for completion design. In 8th European Formation Damage Conference. Society of Petroleum Engineers.

Byrne M, Rojas E, Kandasamy R et al (2014) Fines Migration in Oil and Gas Reservoirs: Quantification and Qualification Through Detailed Study. In SPE International Symposium and Exhibition on Formation Damage Control. Society of Petroleum Engineers.

Civan, F., 2014. Reservoir Formation Damage, 3rd ed. Gulf Professional Publishing: Burlington, MA, USA.

Civan, F., 2016. Modified Formulations of Particle Deposition and Removal Kinetics in Saturated Porous Media. *Transp. Porous Med.* 111:381-410.

Coleman TF, Li Y (1996) An interior trust region approach for nonlinear minimization subject to bounds. *SIAM Journal on optimization* 6(2): 418-445.

Das SK, Schechter RS, Sharma MM (1994) The role of surface roughness and contact deformation on the hydrodynamic detachment of particles from surfaces. *Journal of colloid and interface science* 164(1): 63-77.

Derjaguin BV, Landau L (1941) Theory of the stability of strongly charged lyophobic sols and of the adhesion of strongly charged particles in solutions of electrolytes. *Acta physicochim. URSS* 14(6): 633-662.

Derjaguin BV, Muller VM, Toporov YP (1975) Effect of contact deformations on the adhesion of particles. *Journal of Colloid and interface science* 53(2): 314-326.

Egan W (2012) *Optical properties of inhomogeneous materials: Applications to geology, astronomy chemistry, and engineering.* Elsevier.

Elimelech M, Gregory J, Jia X (2013) *Particle deposition and aggregation: measurement, modelling and simulation.* Butterworth-Heinemann.

Fleming N, Mathisen AM, Eriksen SH et al (2007) Productivity Impairment due to Kaolinite Mobilization: Laboratory & Field Experience, Oseberg Sor. In European Formation Damage Conference. Society of Petroleum Engineers.

Fleming N, Ramstad K, Kidd S et al (2010a) Impact of Successive Squeezes on Treatment Lifetime and Well Productivity: Comparative Assessment of Viscosified and Nonviscosified Treatments. *SPE Production & Operations* 25(01): 99-110.

Fleming N, Ramstad K, Mathisen AM et al (2010b) Squeeze Related Well Productivity Impairment Mechanisms & Preventative/Remedial Measures Utilised. In SPE International Conference on Oilfield Scale. Society of Petroleum Engineers.

Freitas AM, Sharma MM (2001) Detachment of particles from surfaces: an AFM study. *Journal of colloid and interface science* 233(1): 73-82.

- Gercek H (2007) Poisson's ratio values for rocks. *International Journal of Rock Mechanics and Mining Sciences* 44(1): 1-13.
- Gregory J (1981) Approximate expressions for retarded van der Waals interaction. *Journal of Colloid and Interface Science* 83(1): 138-145.
- Guo Z, Hussain F, Cinar Y (2015) Permeability variation associated with fines production from anthracite coal during water injection. *International Journal of Coal Geology* 147: 46-57.
- Han G, Ling K, Wu H et al (2015) An experimental study of coal-fines migration in Coalbed-methane production wells. *Journal of Natural Gas Science and Engineering* 26: 1542-1548.
- Herzig JP, Leclerc DM., Goff PL. (1970) Flow of suspensions through porous media—application to deep filtration. *Industrial & Engineering Chemistry* 62(5): 8-35.
- International Organisation for Standardisation (2007) Determination of particle size distribution - Single particle light interaction methods - Part 2: Light scattering liquid-borne particle counter, ISO Standard 21501-2:2007, International Organization for Standardization, Geneva.
- Israelachvili JN (2011) *Intermolecular and surface forces: revised third edition*. Academic press.
- Jaiswal DK, Kumar A, Yadav RR (2011) Analytical solution to the one-dimensional advection-diffusion equation with temporally dependent coefficients. *Journal of Water Resource and Protection* 3(01): 76.
- Jensen JL (2000) *Statistics for petroleum engineers and geoscientists (Vol. 2)*. Gulf Professional Publishing.
- Kia SF, Fogler HS, Reed MG (1987) Effect of salt composition on clay release in Berea sandstones. In *SPE International Symposium on Oilfield Chemistry*. Society of Petroleum Engineers.
- Khilar KC, Fogler HS (1998) *Migrations of fines in porous media (Vol. 12)*. Springer Science & Business Media.
- Lagasca, JRP, Kovscek AR (2014) Fines migration and compaction in diatomaceous rocks. *Journal of Petroleum Science and Engineering* 122: 108-118.
- Leighton D, Acrivos A (1985) The lift on a small sphere touching a plane in the presence of a simple shear flow. *Zeitschrift für angewandte Mathematik und Physik ZAMP* 36(1): 174-178.
- Leluk K, Orzechowski K, Jerie, K (2010) Dielectric permittivity of kaolinite heated to high temperatures. *Journal of Physics and Chemistry of Solids* 71(5): 827-831.
- Lever A, Dawe RA (1984) Water-Sensitivity and Migration of Fines in the Hopeman Sandstone. *Journal of Petroleum Geology* 7(1): 97-107.
- Leviton DB, Frey BJ (2006) Temperature-dependent absolute refractive index measurements of synthetic fused silica. In *SPIE Astronomical Telescopes and Instrumentation (pp. 62732K-62732K)*. International Society for Optics and Photonics.

- Li X, Lin CL, Miller JD et al (2006) Role of grain-to-grain contacts on profiles of retained colloids in porous media in the presence of an energy barrier to deposition. *Environmental science & technology* 40(12): 3769-3774.
- Mahani H, Berg S, Ilic D et al (2015a) Kinetics of low-salinity-flooding effect. *SPE Journal* 20(01): 8-20.
- Mahani H, Keya AL, Berg S et al (2015b) Insights into the Mechanism of Wettability Alteration by Low-Salinity Flooding (LSF) in Carbonates, *Energy Fuels* 29: 1352–1367.
- Marques M, Williams W, Knobles M et al 2014, Fines migration in fractured wells: integrating modeling, field and laboratory data. *J SPE Production & Operations* 29: 309-322.
- Marshall WL (2008) Dielectric Constant of Water Discovered to be Simple Function of Density over Extreme Ranges from -35 to + 600 °C and to 1200 MP_a (12000 Atm.), Believed Universal. *Nature Proceedings*: doi, 10, 1-40.
- MATLAB and Optimization Toolbox (R2010b) The MathWorks, Inc., Natick, Massachusetts, United States.
- Miranda R, Underdown D, (1993) Laboratory measurement of critical rate: A novel approach for quantifying fines migration problems. In: *SPE Production Operations Symposium*, 21-23 March, Oklahoma City, Oklahoma, Society of Petroleum Engineers.
- Muecke TW (1979) Formation fines and factors controlling their movement in porous media. *J.Pet.Technol.* 31(2): 144–150,
- Nabzar L, Chauveteau G, Roque C (1996) A new model for formation damage by particle retention. In *SPE Formation Damage Control Symposium*. Society of Petroleum Engineers.
- Nguyen TKP, Zeinijahromi A, Bedrikovetsky P (2013) Fines-migration-assisted improved gas recovery during gas field depletion. *Journal of Petroleum Science and Engineering* 109: 26-37.
- Ochi J, Vernoux JF (1998) Permeability decrease in sandstone reservoirs by fluid injection: hydrodynamic and chemical effects. *Journal of Hydrology* 208(3): 237-248.
- Ochi J, Vernoux JF (1999) A two-dimensional network model to simulate permeability decrease under hydrodynamic effect of particle release and capture. *Transport in porous media* 37(3): 303-325.
- Oliveira M, Vaz A, Siqueira F et al (2014) Slow migration of mobilised fines during flow in reservoir rocks: Laboratory study. *Journal of Petroleum Science and Engineering* 122: 534-541.
- Pang S, Sharma MM (1997) A Model for Predicting Injectivity Decline in Water-Injection Wells. *SPEFE* 12 (3): 194-201. SPE-28489-PA. DOI: 10.2118/28489-PA.
- Prasad M, Kopycinska M, Rabe U et al (2002) Measurement of Young's modulus of clay minerals using atomic force acoustic microscopy. *Geophysical Research Letters* 29(8).
- Sarkar A, Sharma M (1990). Fines migration in two-phase flow. *J.Pet.Technol.* 42 (5): 646–652

Schembre JM, Kovscek AR (2005) Mechanism of formation damage at elevated temperature. *Journal of Energy Resources Technology*, 127(3), 171-180.

Schembre JM, Tang GQ, Kovscek AR (2006a) Wettability alteration and oil recovery by water imbibition at elevated temperatures. *Journal of Petroleum Science and Engineering*, 52(1), 131-148.

Schembre JM, Tang GQ, Kovscek AR (2006b) Interrelationship of Temperature and Wettability on the Relative Permeability of Heavy Oil in Diatomaceous Rocks (includes associated discussion and reply). *SPE Reservoir Evaluation & Engineering* 9(03): 239-250.

Sefrioui N, Ahmadi A, Omari A et al (2013) Numerical simulation of retention and release of colloids in porous media at the pore scale. *Colloids and Surfaces A: Physicochemical and Engineering Aspects* 427: 33-40.

Schechter RS (1992) Oil well stimulation.

Stuart MR (1955) Dielectric constant of quartz as a function of frequency and temperature. *Journal of Applied Physics* 26(12): 1399-1404.

Tufenkji N (2007) Colloid and microbe migration in granular environments: a discussion of modelling methods. In *Colloidal Transport in Porous Media* (pp. 119-142). Springer Berlin Heidelberg.

Van Oort E, Van Velzen JFG, Leerlooijer K (1993) Impairment by suspended solids invasion: testing and prediction. *SPE Production & Facilities* 8(03): 178-184.

Varga RS (2009) Matrix iterative analysis (Vol. 27). Springer Science & Business Media.

Vortisch W, Harding D, Morgan J (2003) Petrographic analysis using cathodoluminescence microscopy with simultaneous energy-dispersive X-ray spectroscopy. *Mineralogy and Petrology* 79(3-4): 193-202.

Watson RB, Viste P, Kageson-Loe NM et al (2008) Smart Mud Filtrate: An Engineered Solution To Minimize Near-Wellbore Formation Damage Due to Kaolinite Mobilization: Laboratory and Field Experience, Oseberg Sør. In *SPE International Symposium and Exhibition on Formation Damage Control*. Society of Petroleum Engineers.

Welzen JTAM, Stein HN, Stevels JM et al (1981) The influence of surface-active agents on kaolinite. *Journal of Colloid and Interface Science* 81(2): 455-467.

You Z, Bedrikovetsky P, Badalyan A (2015) Particle mobilization in porous media: Temperature effects on competing electrostatic and drag forces. *Geophysical Research Letters* 42(8): 2852-2860.

You Z, Yang Y, Badalyan A et al (2016). Mathematical modelling of fines migration in geothermal reservoirs. *J Geothermics* 59: 123–133.

Yuan H, Shapiro AA (2011a) A mathematical model for non-monotonic deposition profiles in deep bed filtration systems. *Chemical Engineering Journal* 166(1): 105-115.

Yuan H, Shapiro AA (2011b) Induced migration of fines during waterflooding in communicating layer-cake reservoirs. *Journal of Petroleum Science and Engineering* 78(3): 618-626.

Yuan H, Shapiro A, You Z et al (2012) Estimating filtration coefficients for straining from percolation and random walk theories. *Chemical engineering journal* 210: 63-73.

Zeinijahromi A, Vaz A, Bedrikovetsky P et al (2012) Effects of fines migration on well productivity during steady state production. *Journal of Porous Media* 15(7).

Zeinijahromi A, Vaz A, Bedrikovetsky P (2012) Well impairment by fines production in gas fields, *Journal of Petrol Sci Eng* 88-89: 125-135

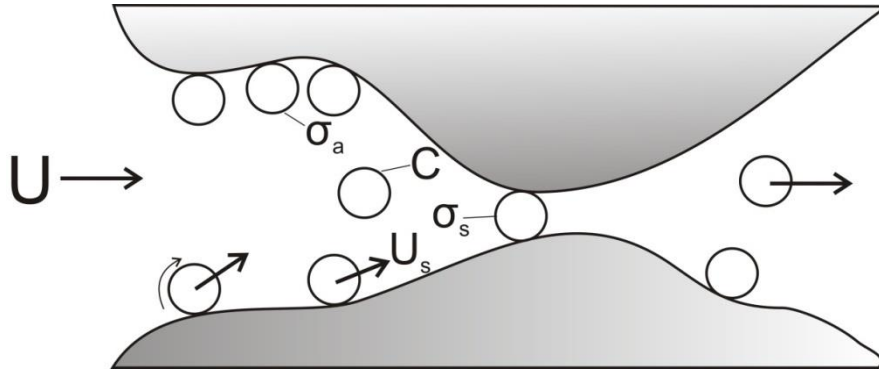


Fig. 1. Schematic for fines detachment, migration, and straining with consequent permeability decline.

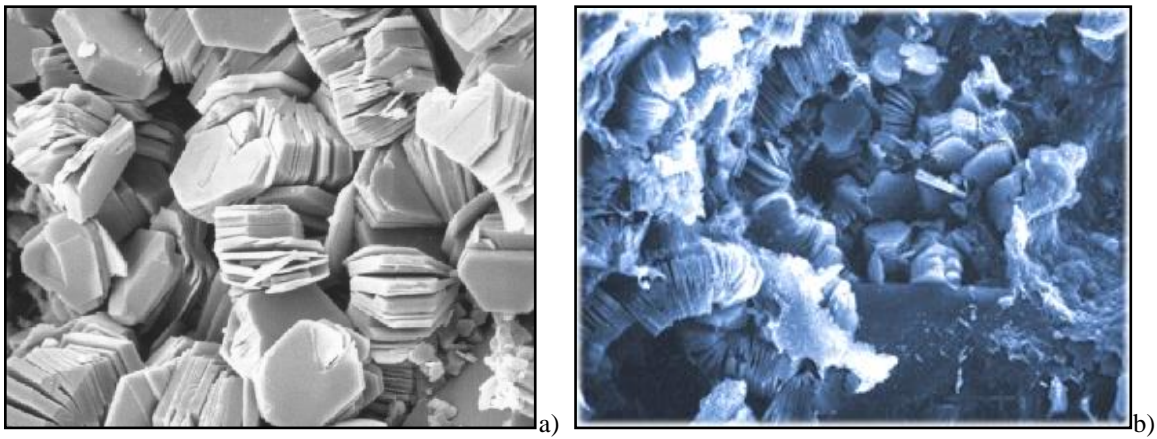


Fig. 2. Kaolinite particles attached to the grain surface (SEM image): a) leaflet shape; b) leaflets in the pore space.

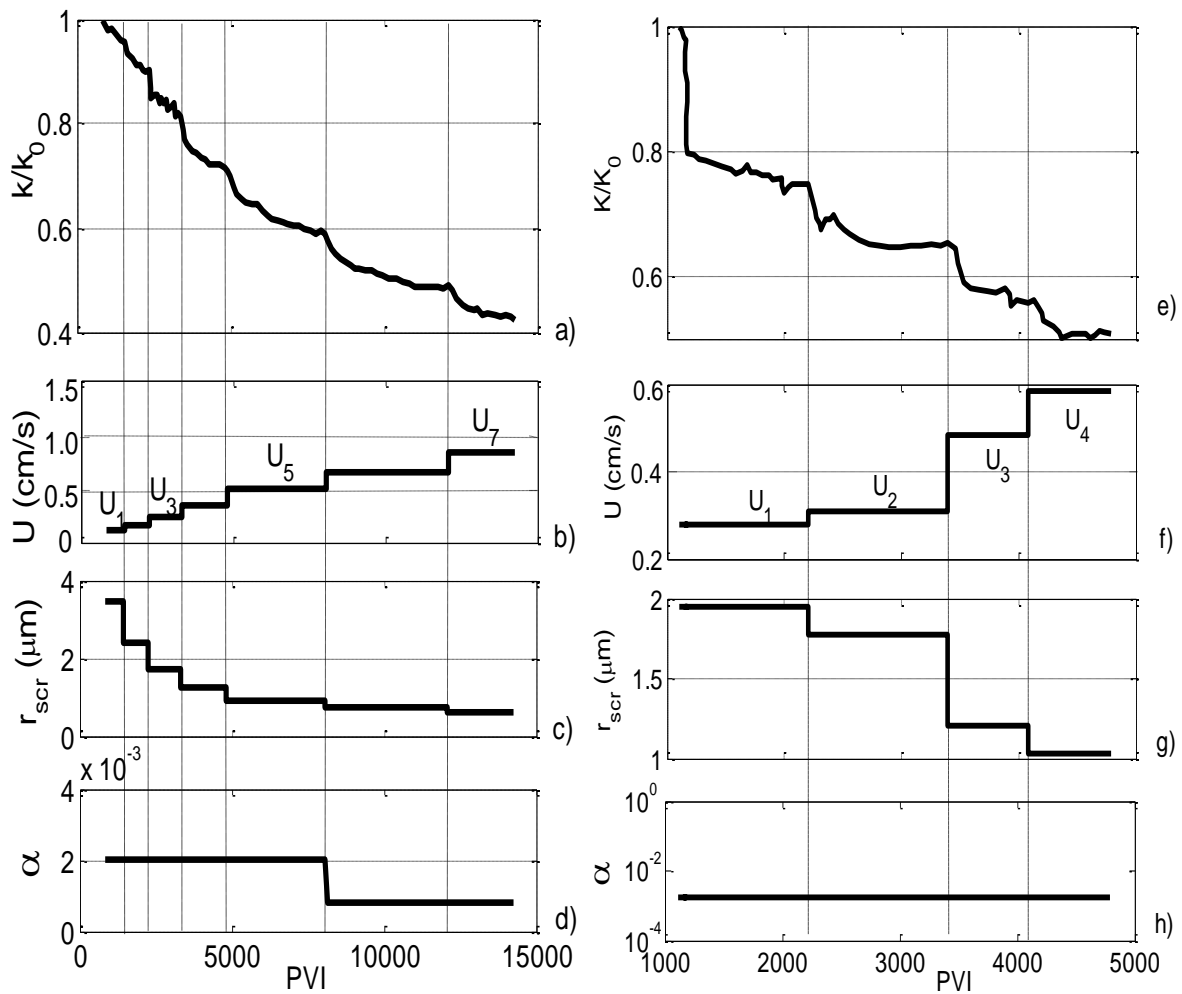


Fig. 3. Variation of normalized permeability, rate, critical fine radius and drift delay factor with time during coreflood with piecewise increasing velocity during test *I* (a,b,c, and d) and test *II* (e,f,g, and h): a,e) experimentally determined permeability decline with time; b, f) increasing velocity during the test; c, g) decrease of the mobilised fines radius as velocity increases as calculated from torque balance; d, h) delay drift factor from the model adjustment.

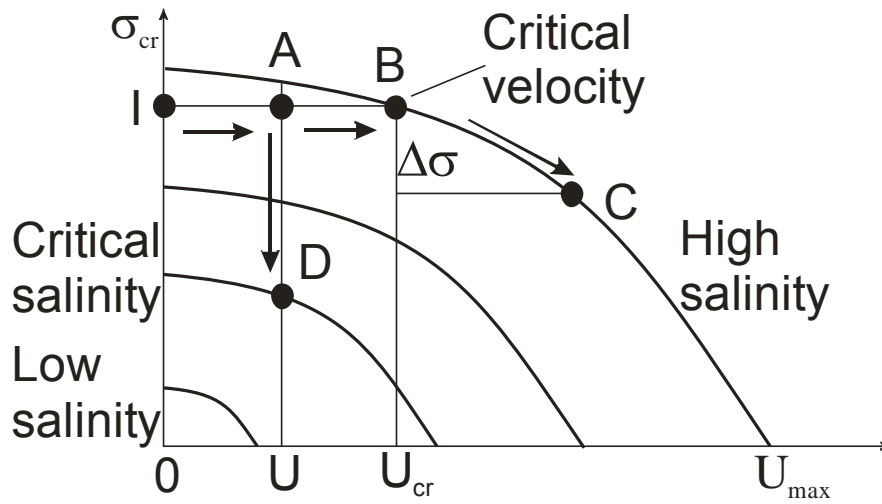


Figure 4. Velocity- and salinity-dependencies of maximum retention function with introduction of critical velocity and salinity.

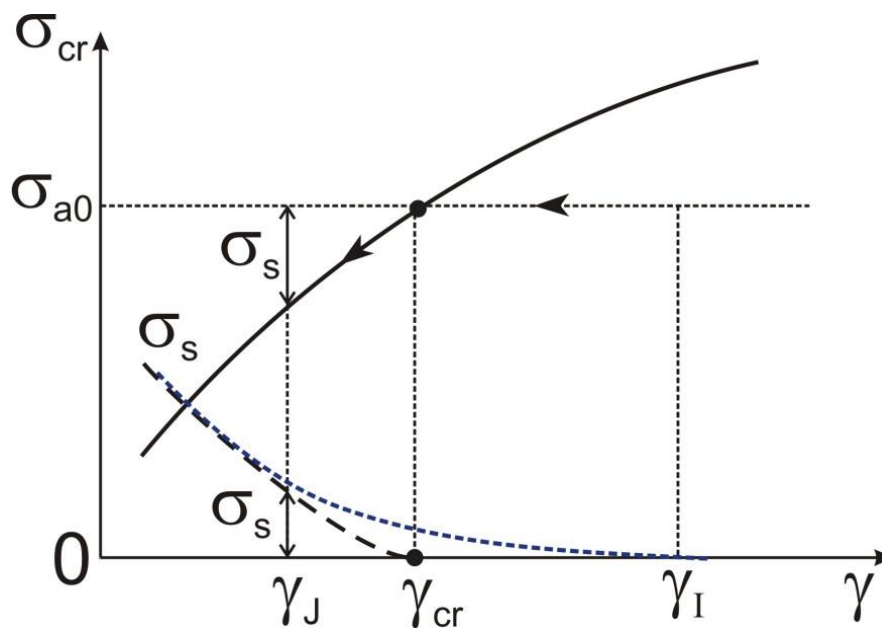


Figure 5. Strained concentration σ_s in large scale approximation is determined by the maximum retention function $\sigma_{cr}(\gamma)$; here concentrations σ_s and $\sigma_{cr}(\gamma)$ are extrapolated by the vanishing function into the domain $\sigma < \sigma_{cr}(\gamma)$ where no particles are mobilised.

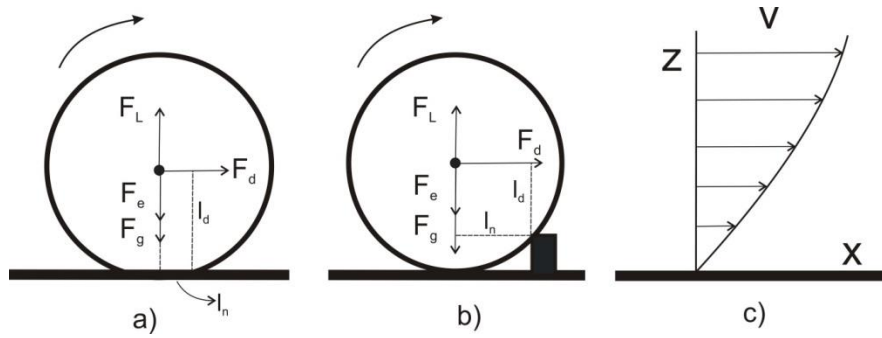


Fig. 6. Different scenarios for particle detachment in mono-layer on the grain surface and forces exerting the particles; torque and force balance on a fine particle attached to the pore wall: a) the lever arm is equal to the contact area radius, deformation due to attracting electrostatic force; b) the lever arm is determined by the asperity size; c) velocity distribution in Hele-Shaw flow in a pore.

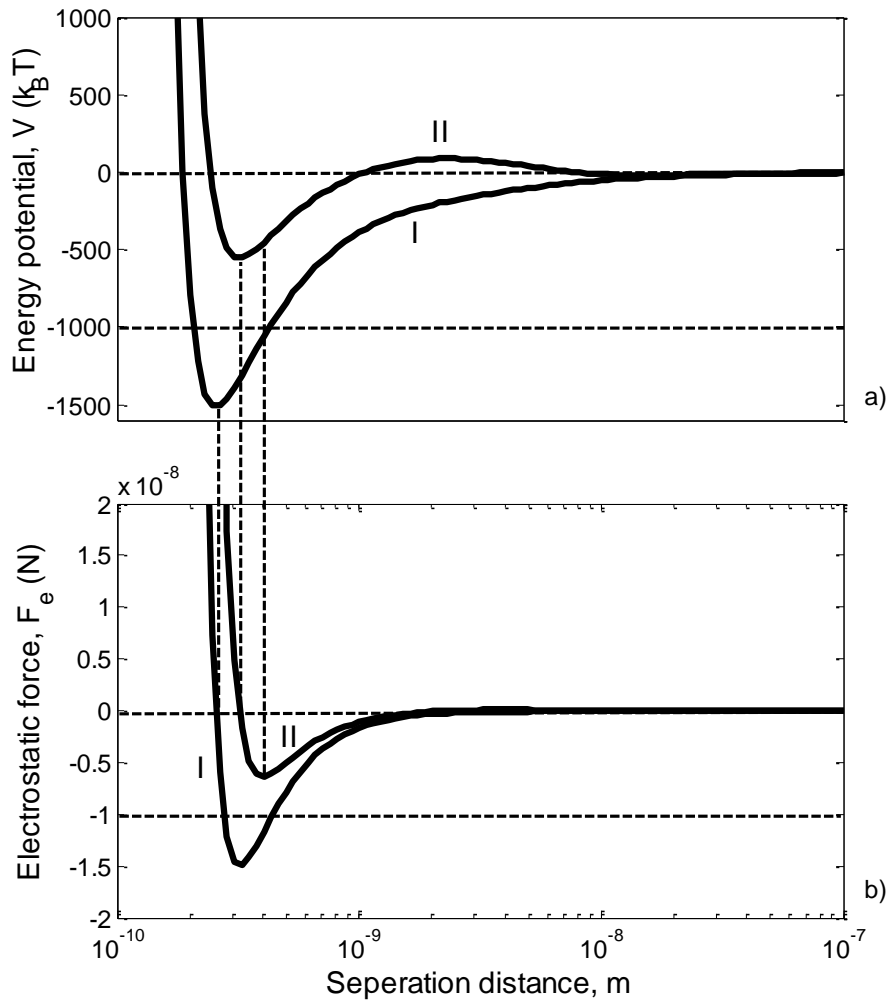


Fig. 7. Energy potential and electrostatic force for tests *I* and *II*: a) energy potential; b) electrostatic force.

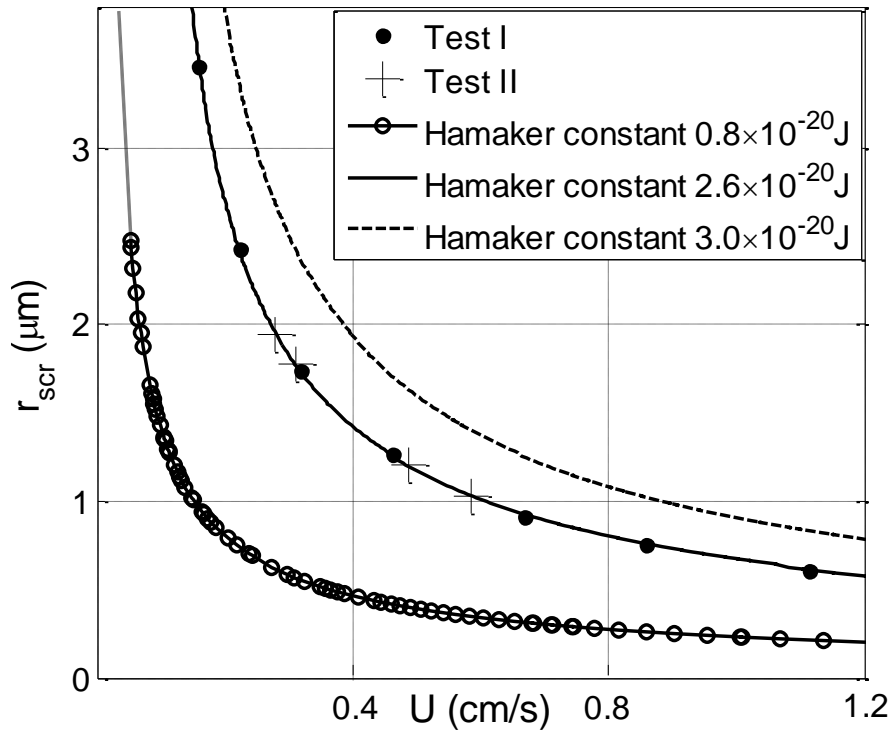
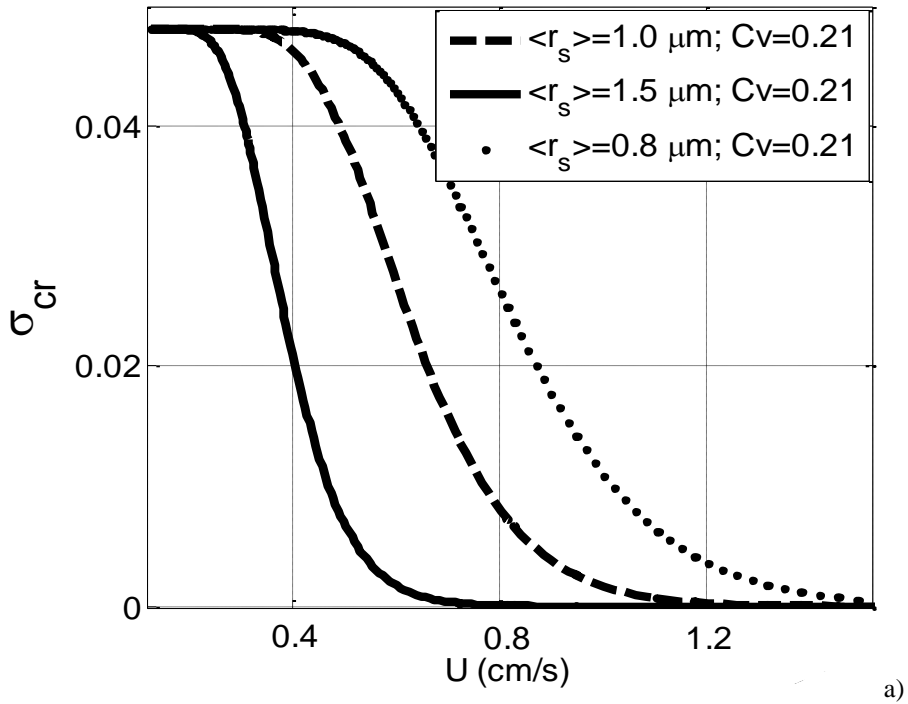
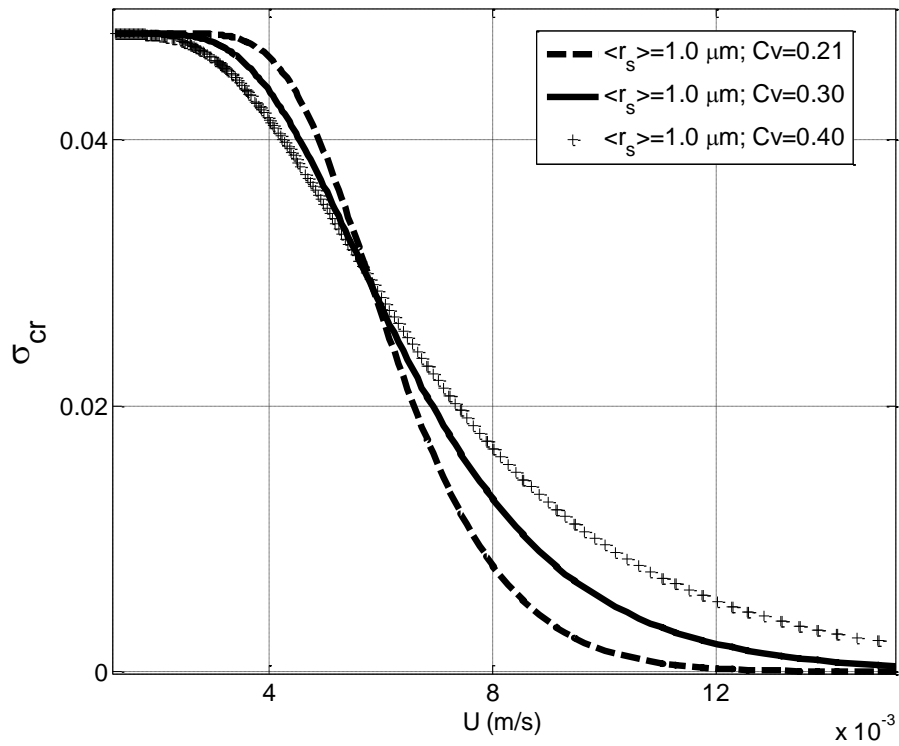
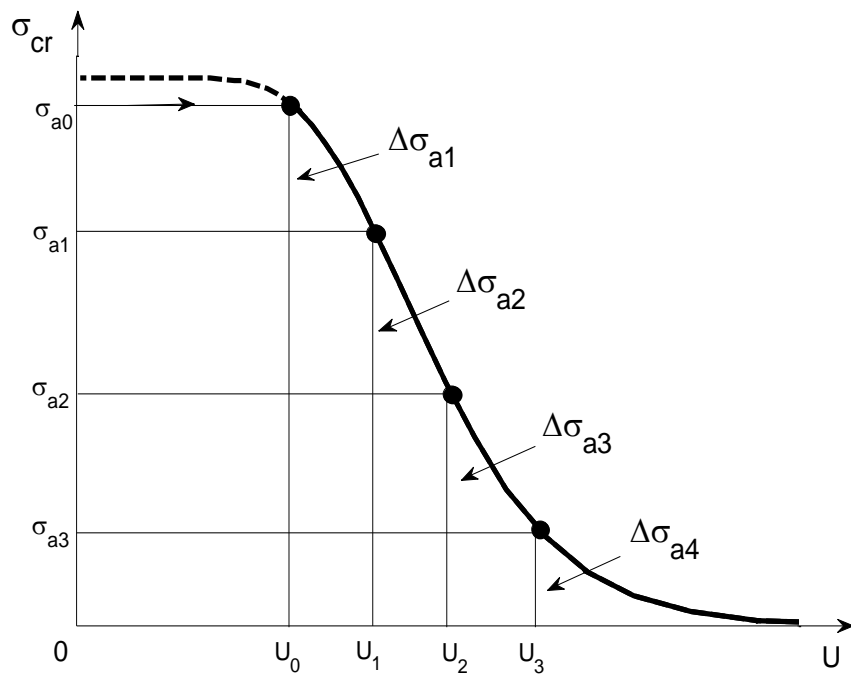


Fig. 8. Critical particle size (minimum size of the fine particles lifted by the flux with velocity U).





b)



c)

Fig. 9. Maximum retention function for the attached fines forming a mono-layer on the pore surface: a) for log-normal particle size distributions with varying mean particle size; b) for log-normal particle size distributions with varying variance coefficient; c) determining the maximum retention function from the amount of particles released at each abrupt velocity alternation.

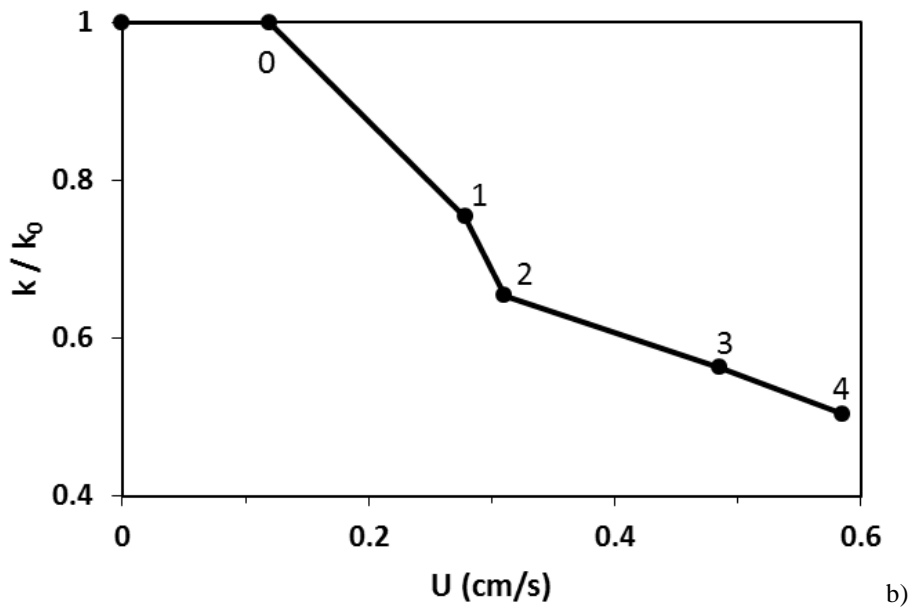
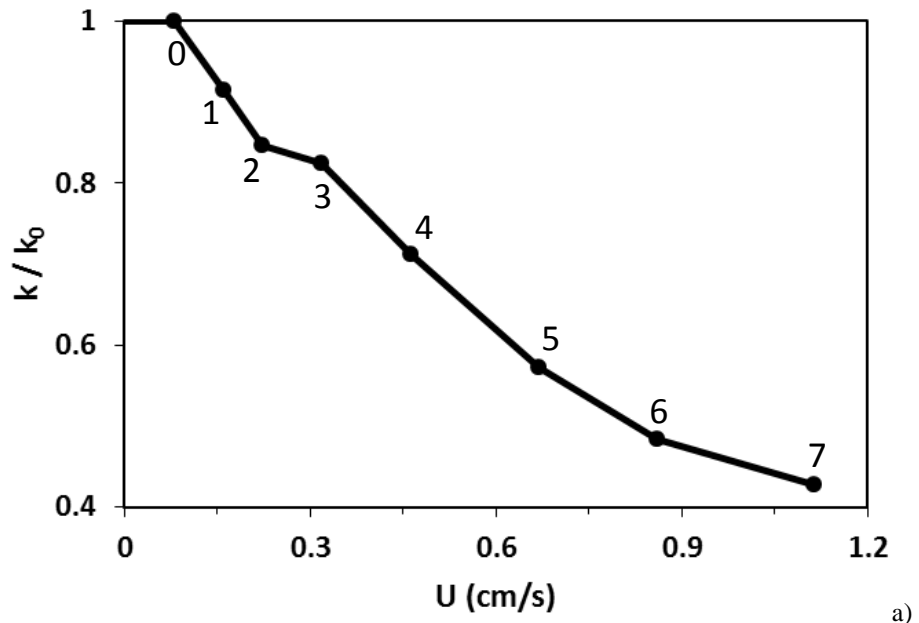


Fig. 10. Stabilised normalized permeability versus velocity: a) test I; b) test II.

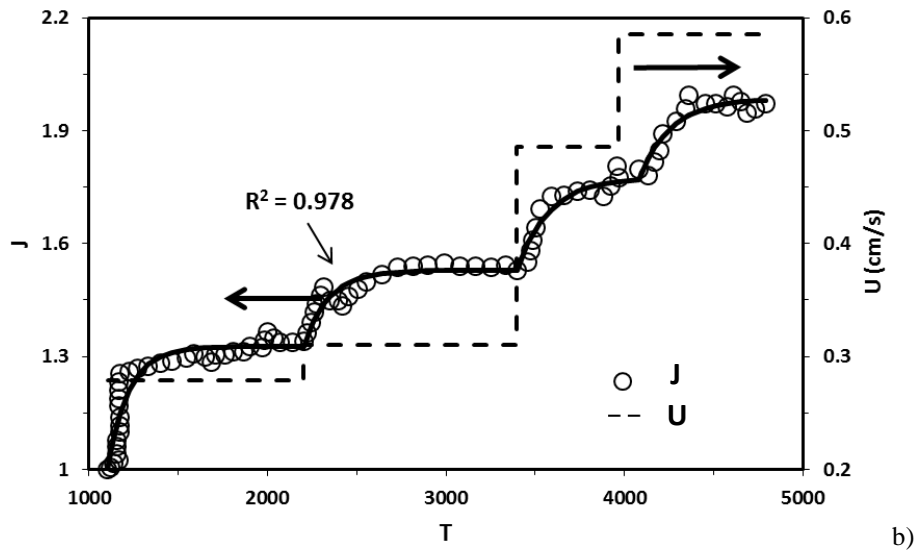
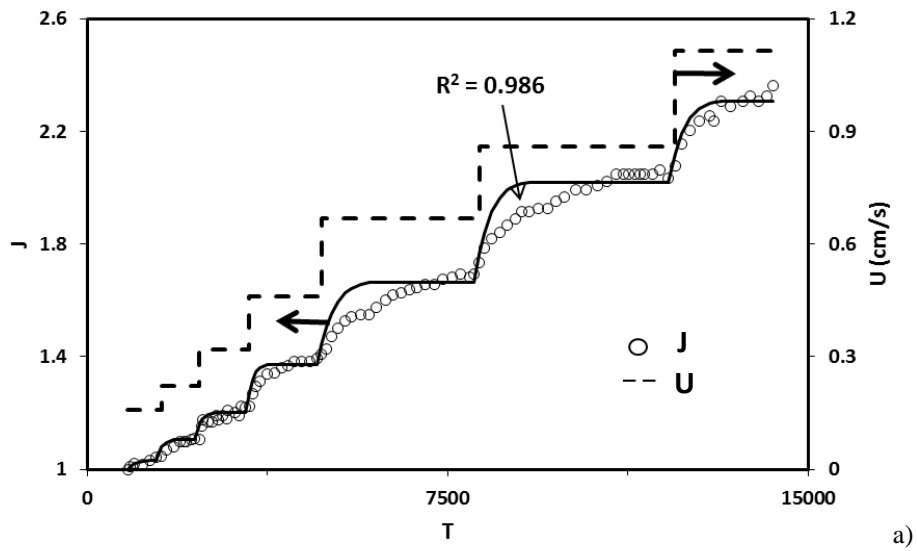


Fig. 11. Matching the pressure drop across the core as obtained from coreflow by the mathematical model: a) test I; b) test II.

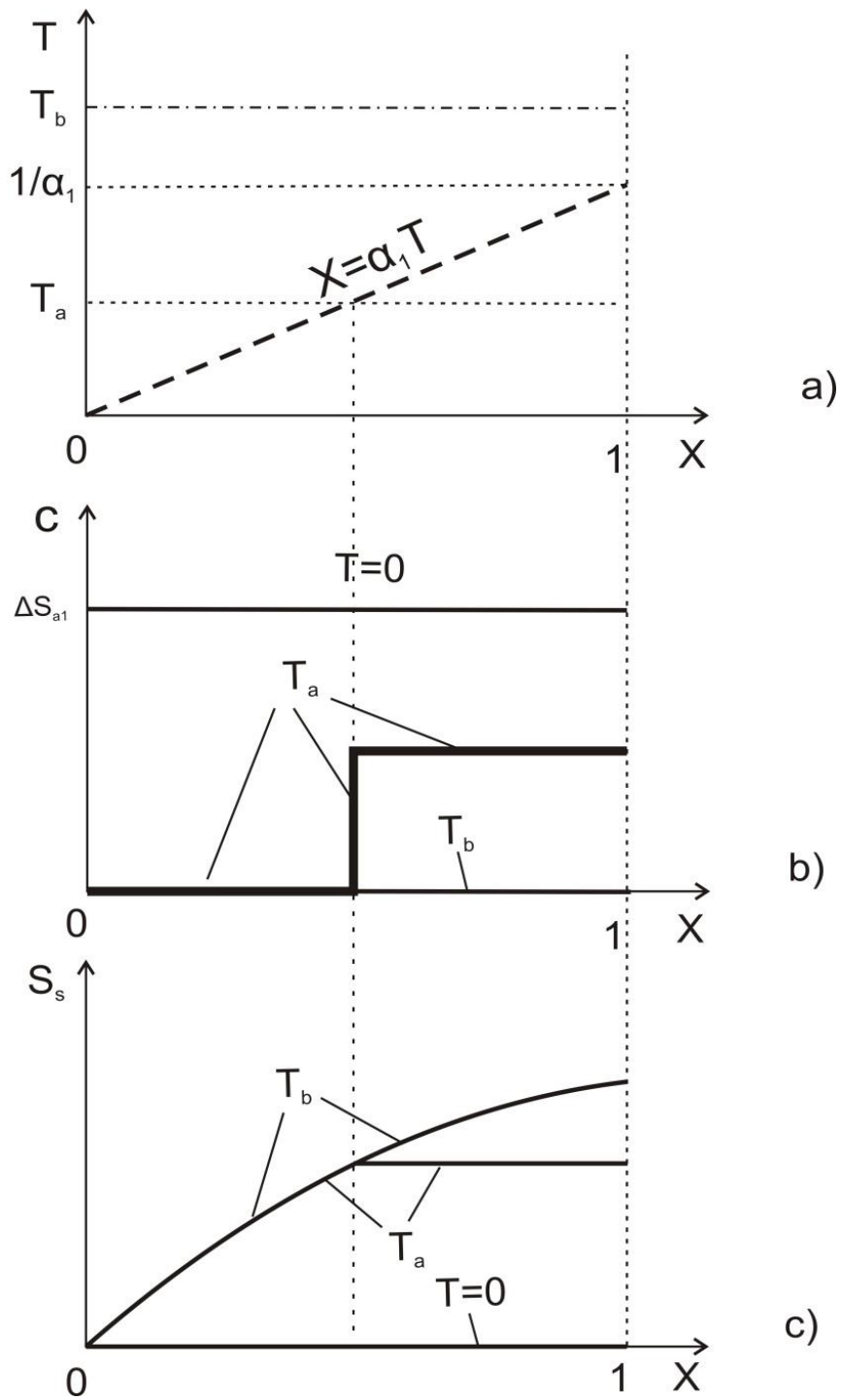


Fig. 12. Schematic for the analytical solution of 1d fines migration under piecewise increasing velocity at times before and after the breakthrough (moments T_a and T_b , respectively): a) trajectory of fronts and characteristic lines in (X, T) -plane; b) suspended concentration profiles in three moments $T=0$, T_a and T_b ; c) strained concentration profiles in three moments.

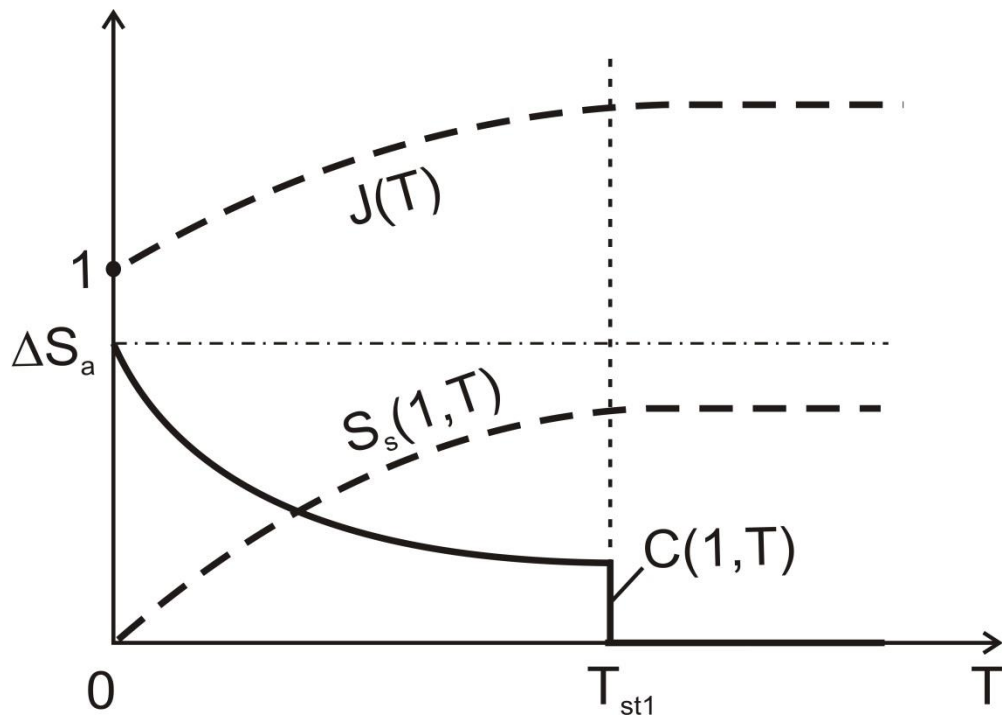
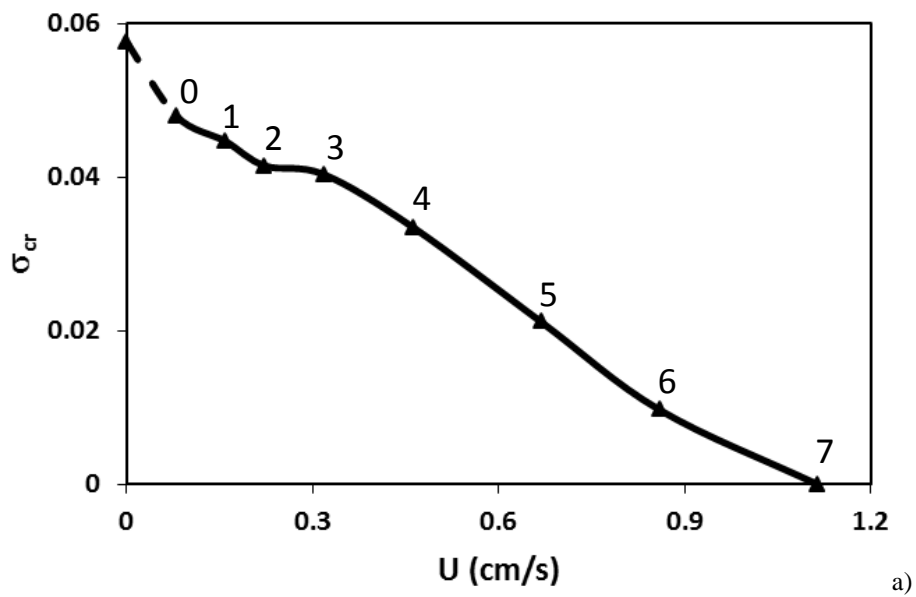


Fig. 13. Histories for dimensionless pressure drop across the core J and breakthrough concentration C , strained concentration S_s at the outlet.



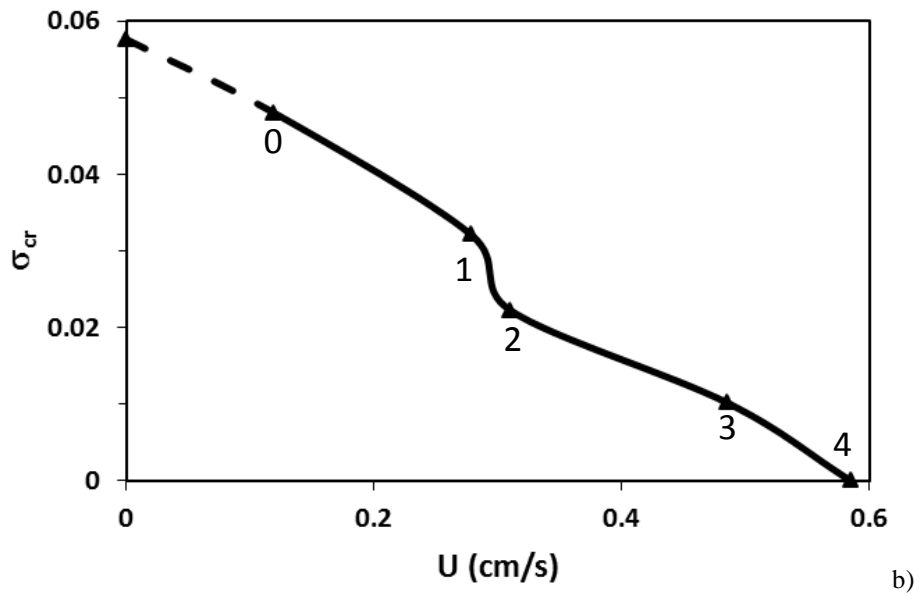
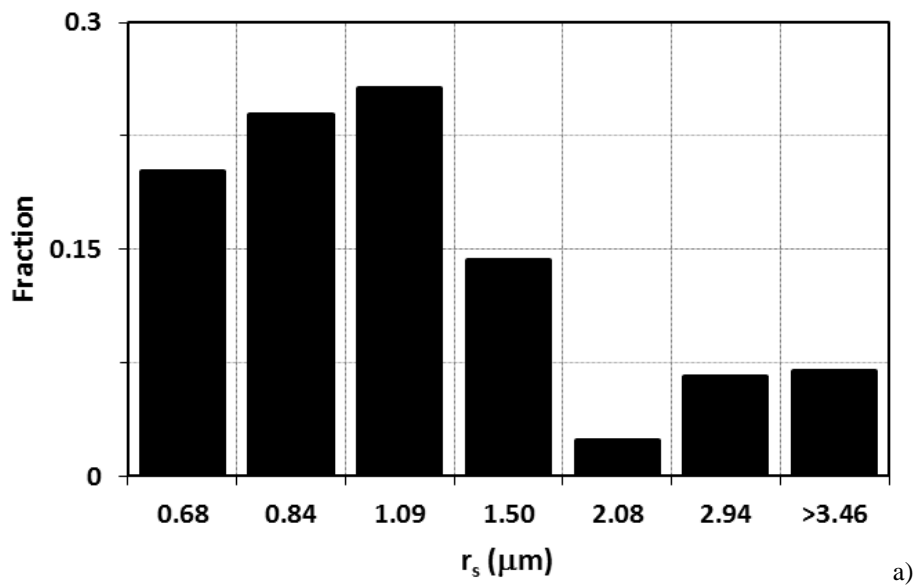


Fig. 14. Maximum retention curves $\sigma_{cr}(U)$ as obtained from tests data: a) test I; b) test II.



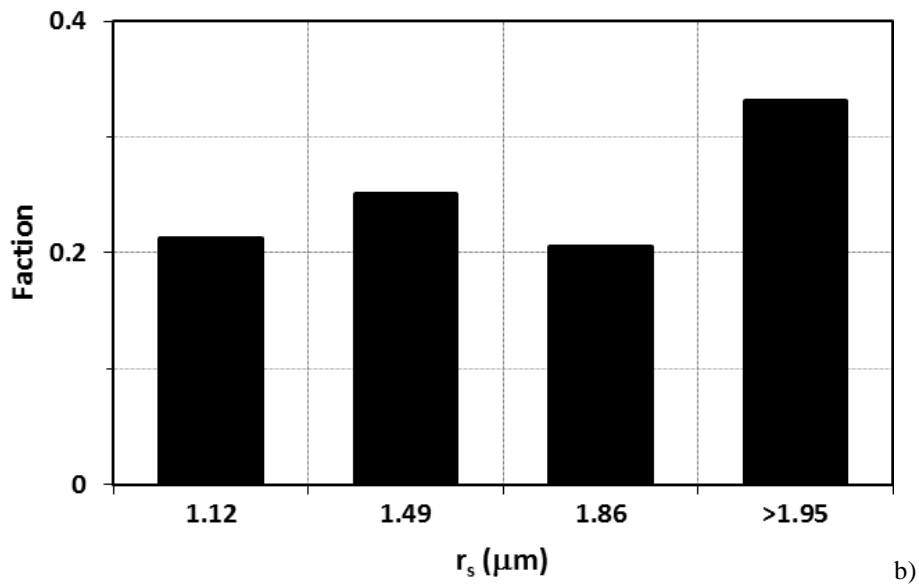


Fig. 15. Size distributions of movable fine particles on the matrix surface: a) test I; b) test II.

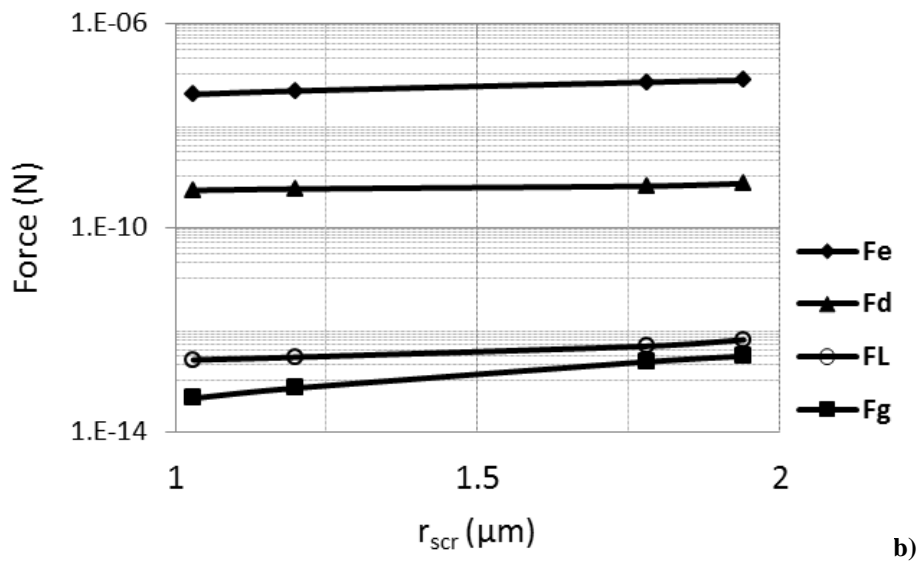
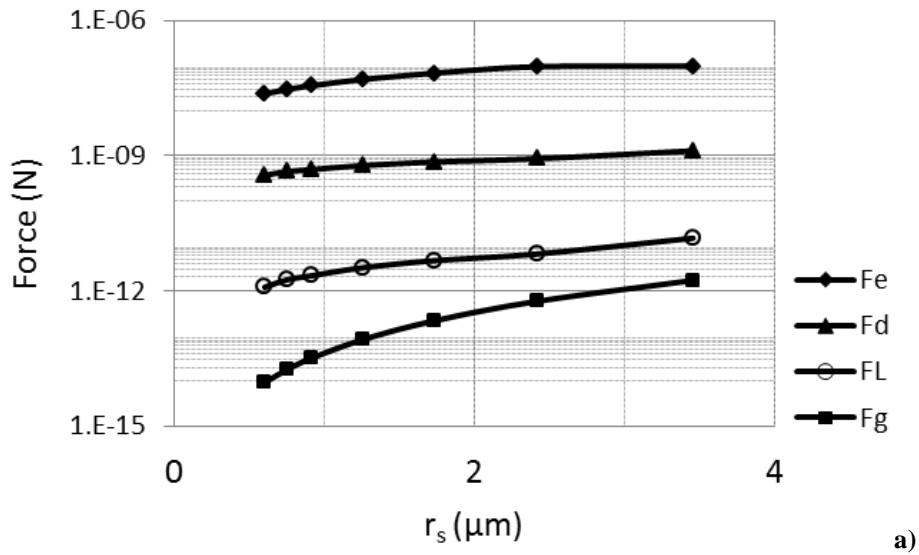


Fig. 16. Forces exerting on the attached particles: a) for coreflood test *I*; b) for test *II*.

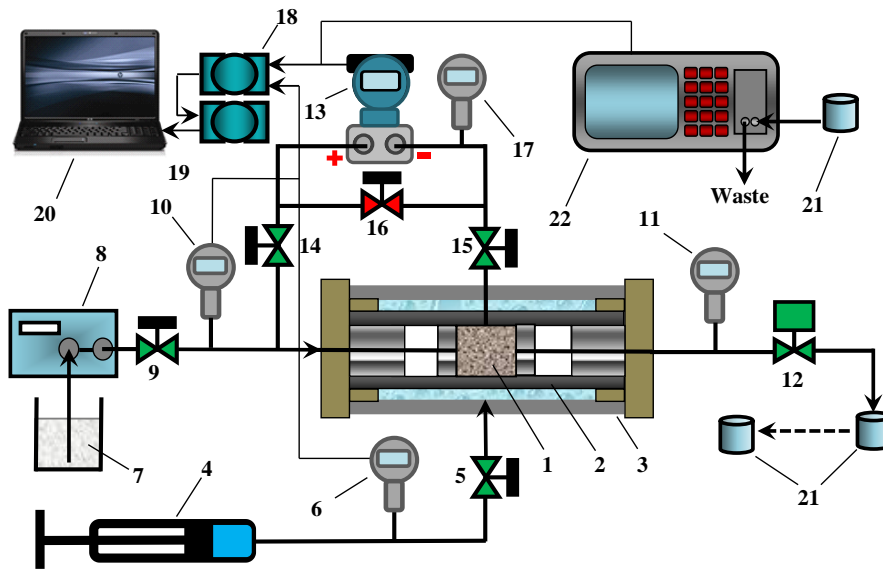


Fig. 17. Schematic of laboratory setup for fines migration in porous media: 1 -Core plug; 2- Viton sleeve; 3- Core-holder; 4- Pressure generator; 5,9,14-16- Manual valves; 6,10,11,17- Pressure transmitters; 7- Suspension; 8- HPLC pump; 12- Back-pressure regulator; 13- Differential pressure transmitter; 18- Data acquisition module; 19- Signal converter; 20- Computer; 21- Beakers; 22- PAMAS particle computer/sizer.

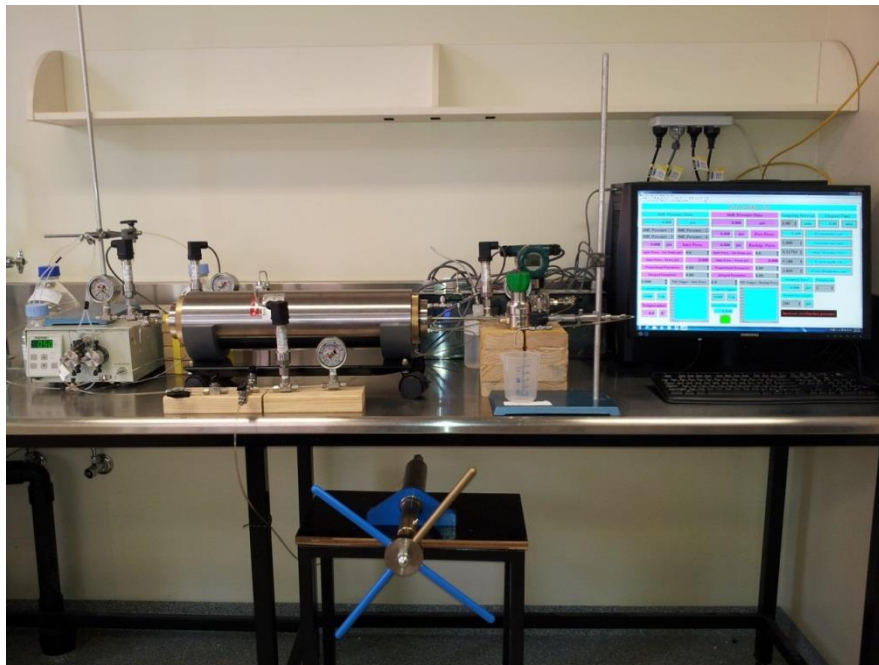


Fig. 18. Photo of laboratory setup for fines migration in porous media.

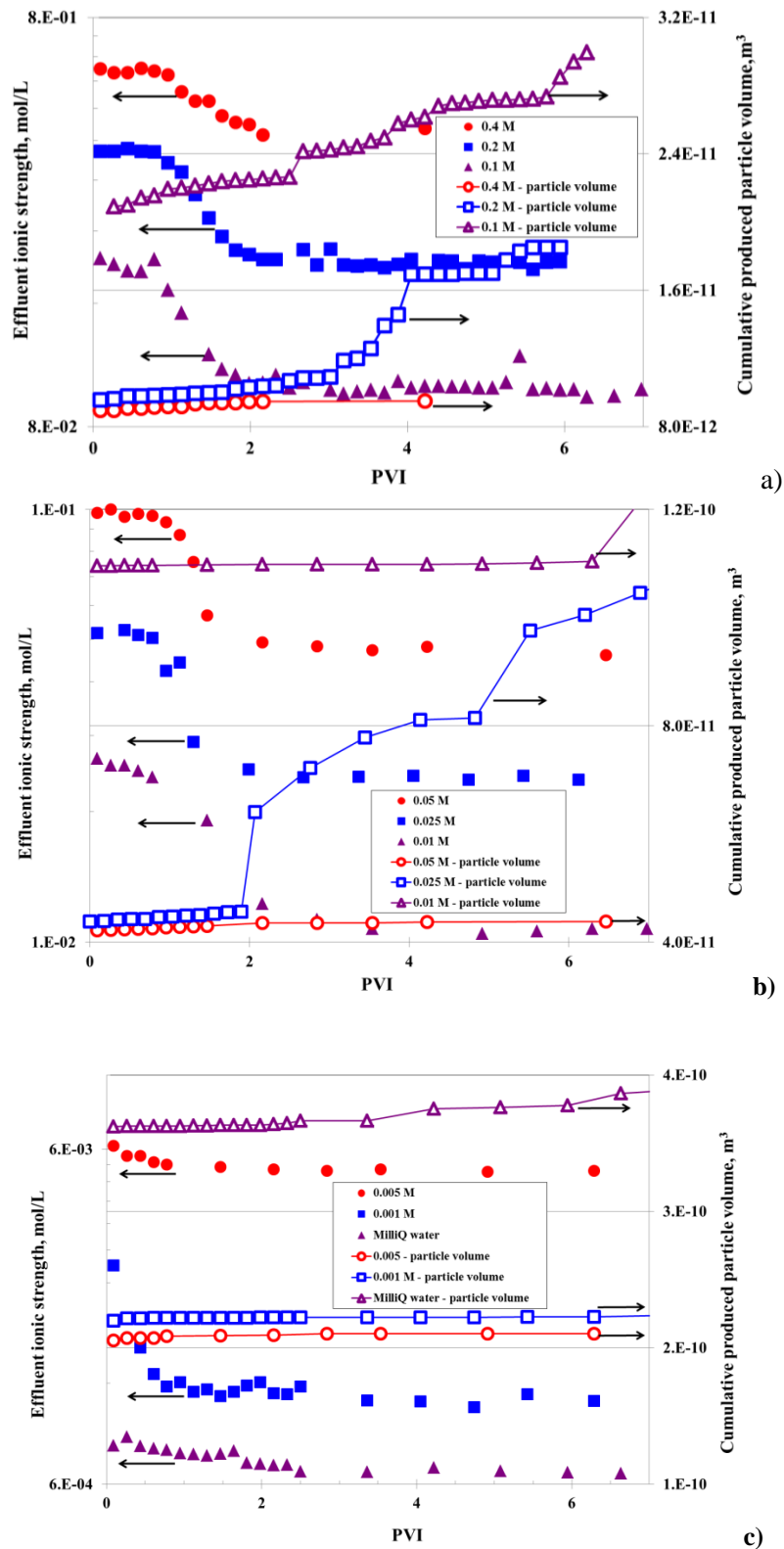


Fig. 19. Variation of effluent ionic strength and cumulative produced-particle volume vs PVI during injection of water with piecewise-constant decreasing salinity: (a) for salinities 0.4 M, 0.2 M, and 0.1 M; (b) for salinities 0.05 M, 0.025 M, and 0.01 M; (c) for salinities 0.005 M, 0.001 M, and MilliQ water.

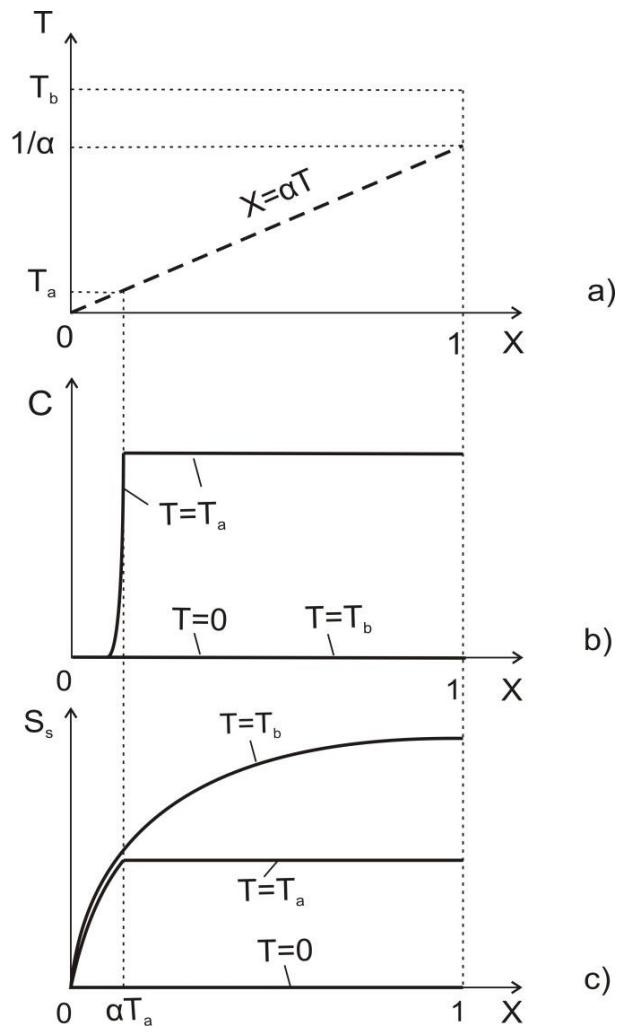


Fig. 20. Analytical slow-fines delay-release model: (a) trajectory of fronts and characteristic lines in (X, T) plane; (b) suspended concentration profiles in three moments; (c) strained concentration profiles in three moments.

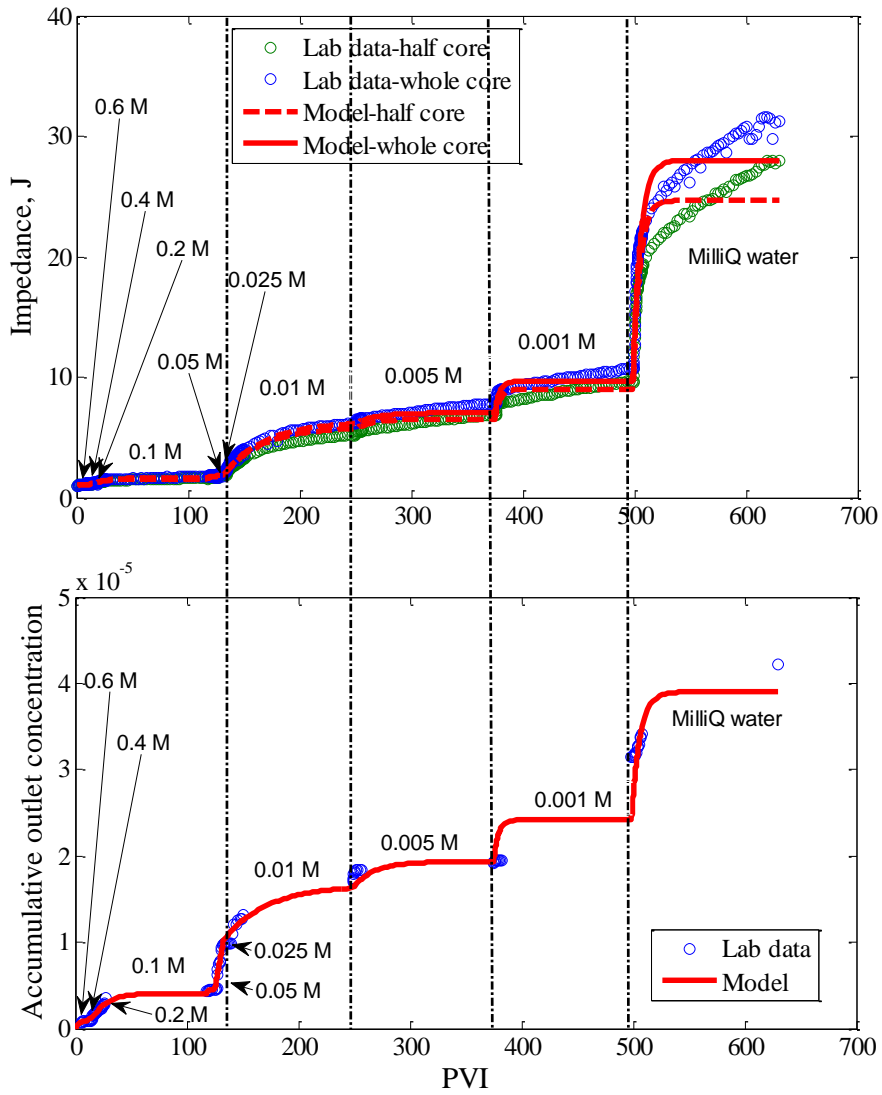
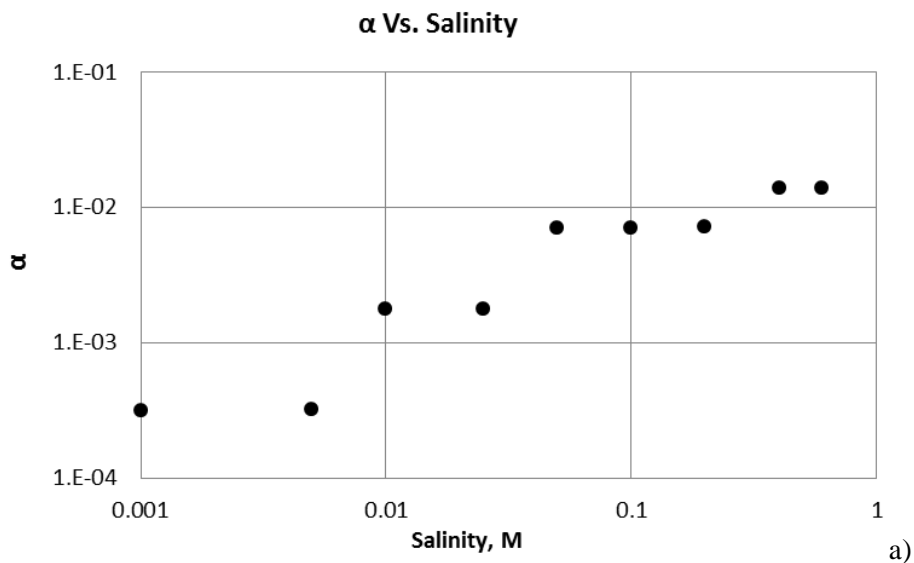


Fig. 21. Matching the coreflood data by the slow-particle model: (a) dimensionless pressure drop across the overall core; (b) dimensionless pressure drop across the first core section; (c) accumulated fine-particle production.



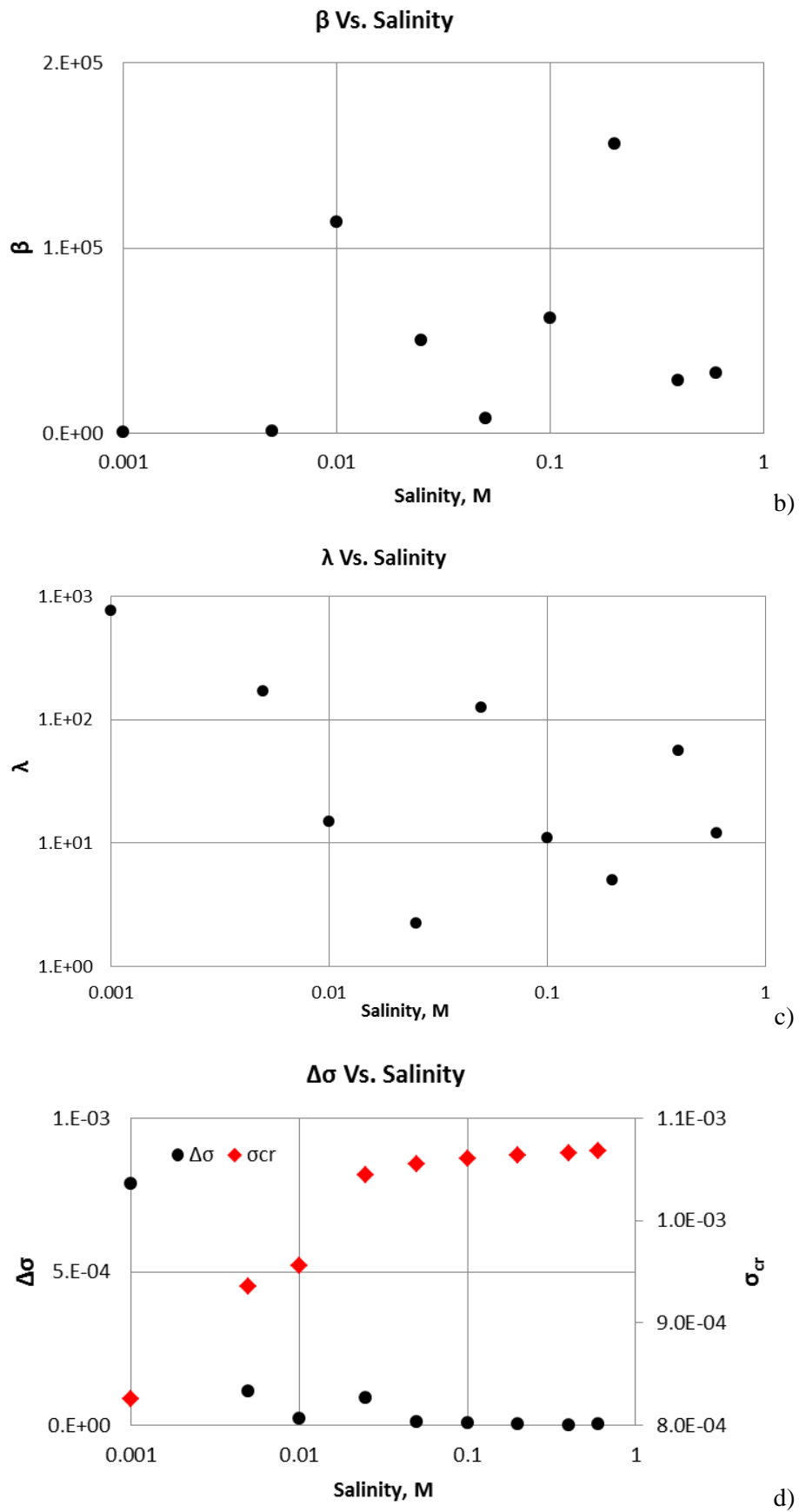


Fig. 22. Tuned values of the slow-particle model parameters: (a) drift delay factor; (b) formation damage coefficient; (c) filtration coefficient; (d) maximum retention function.

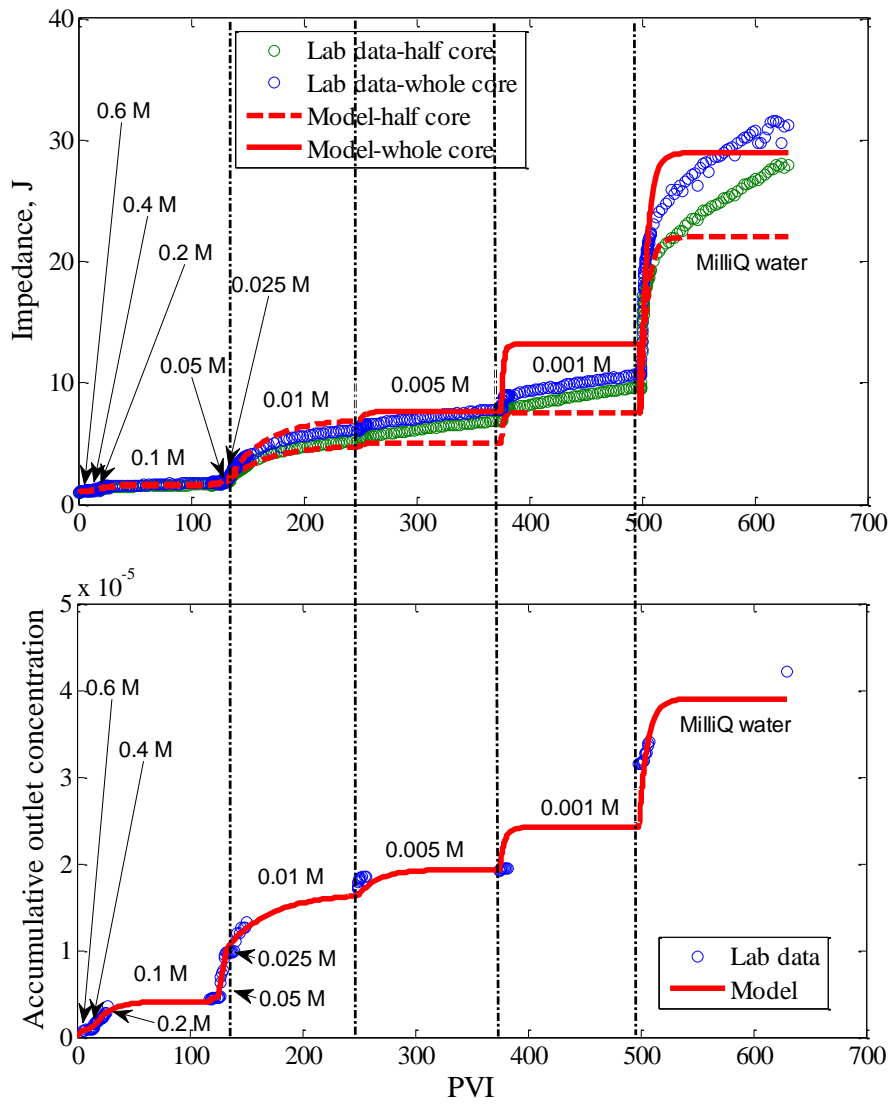
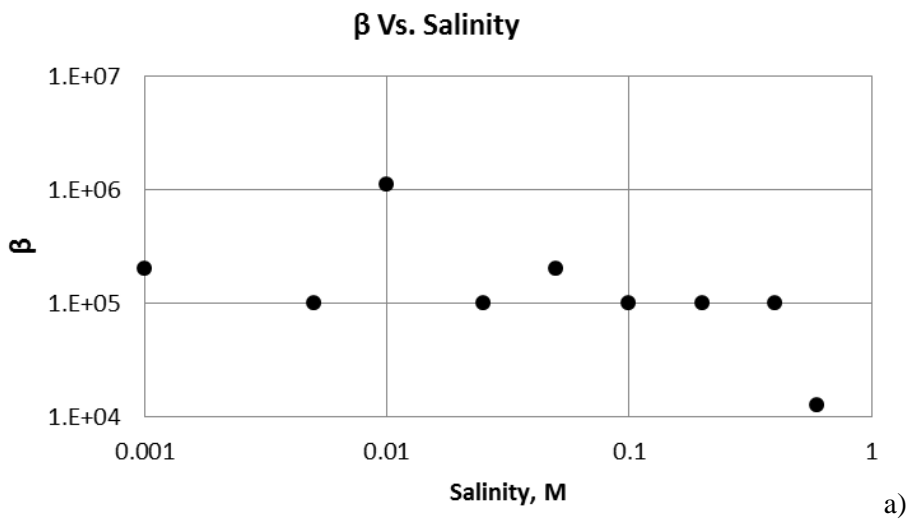


Fig. 23. Matching the coreflood data by the delayed-particle-release model: (a) dimensionless pressure drop across the overall core; (b) dimensionless pressure drop across the first core section; (c) accumulated fine-particle production.



a)

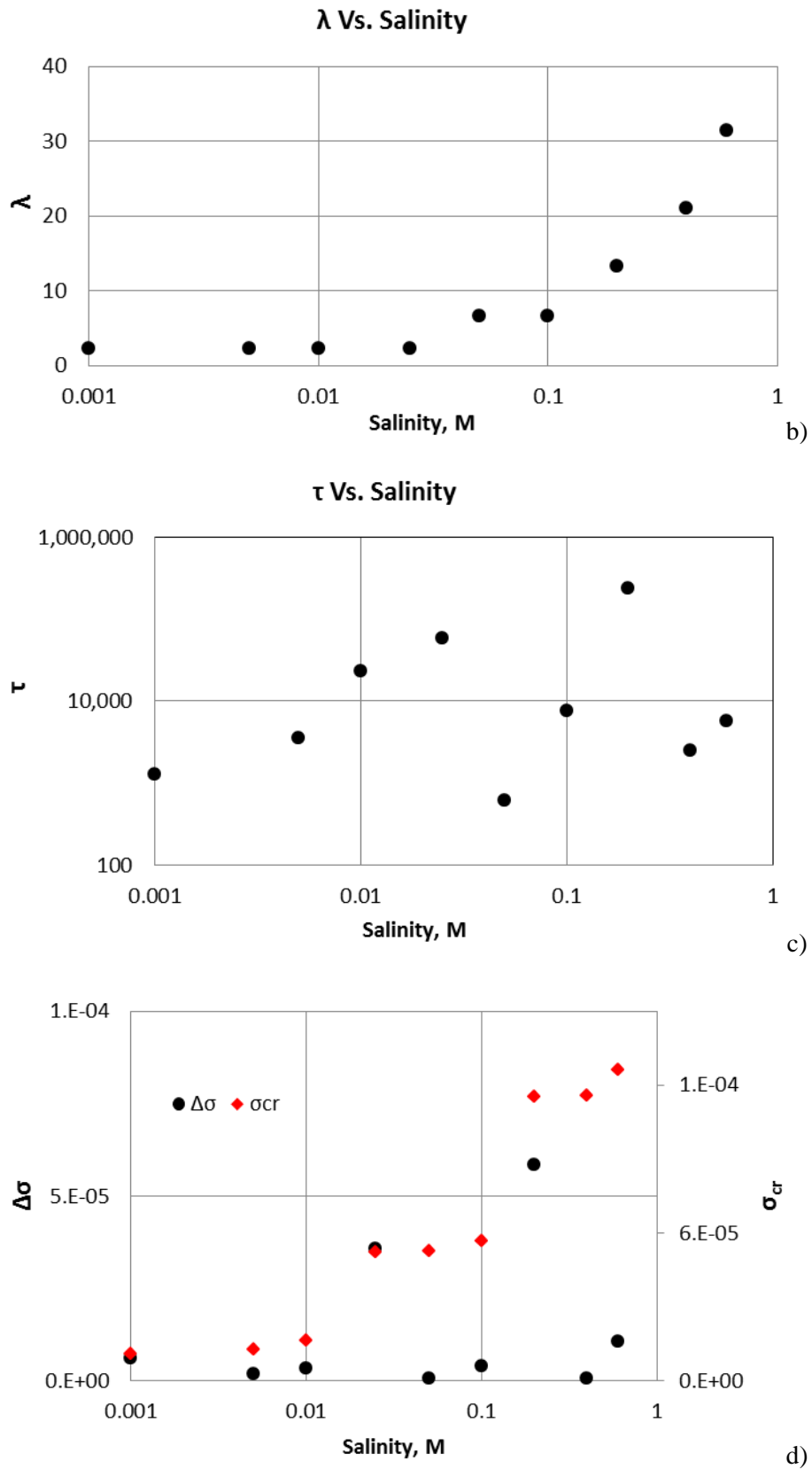


Fig. 24. Tuned values of the delayed-particle-release model parameters for 10 different-salinity stages: (a) formation damage coefficient; (b) filtration coefficient; (c) dimensionless delay; (d) concentration of detached fines.

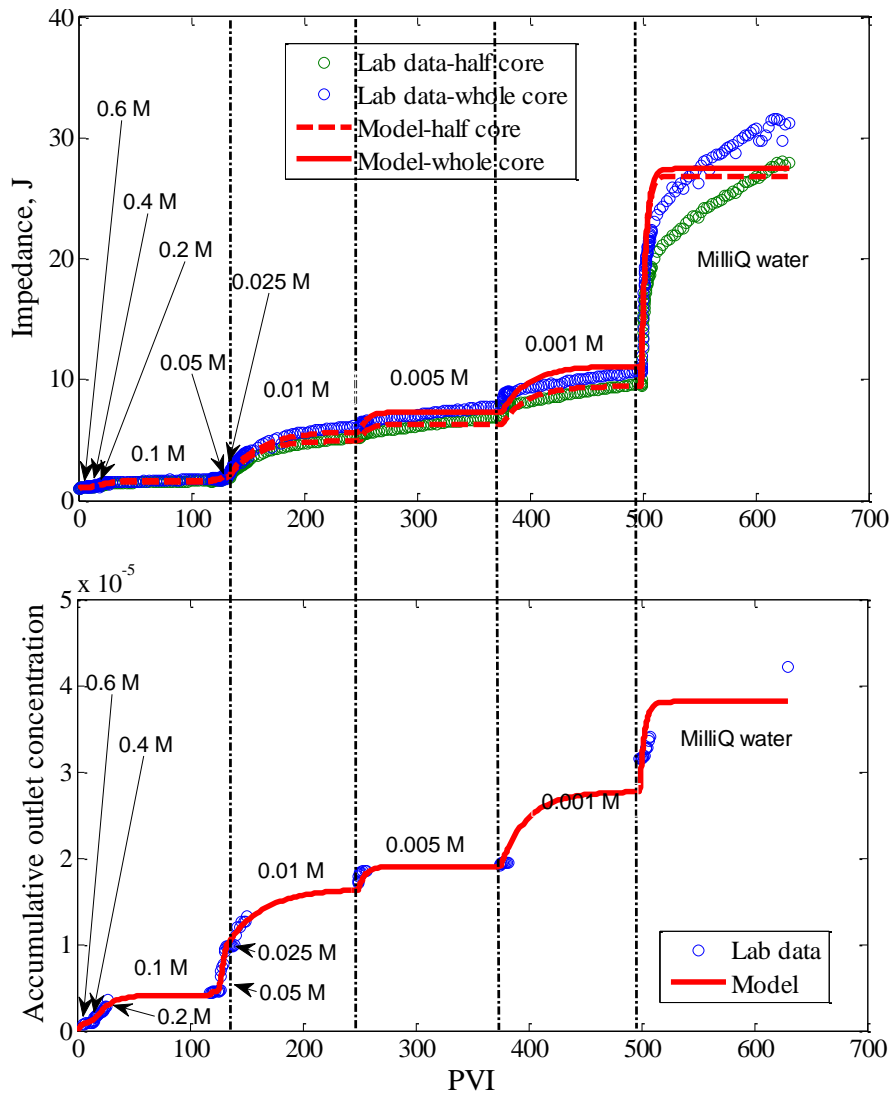
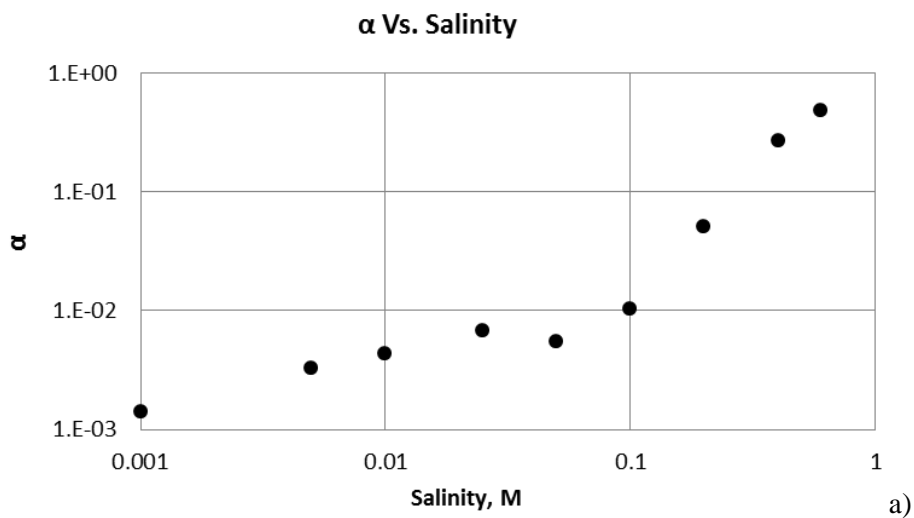
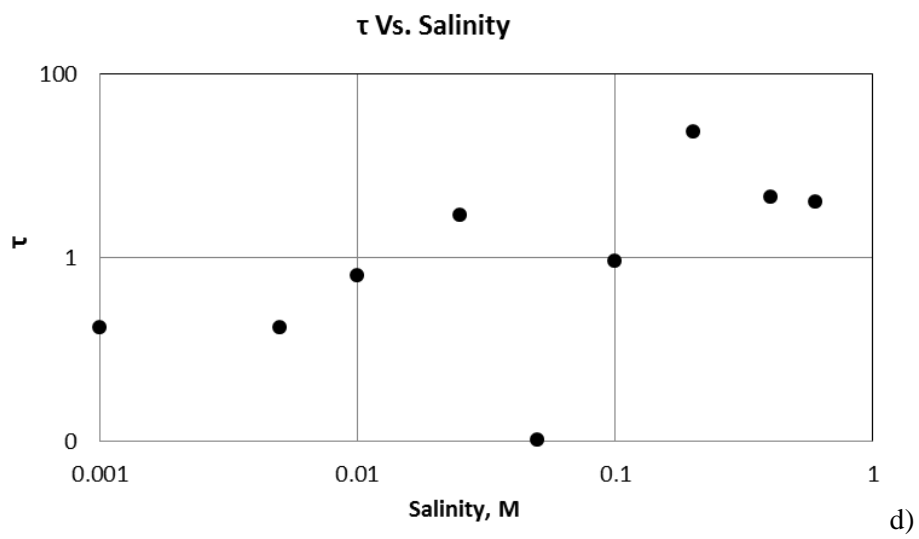
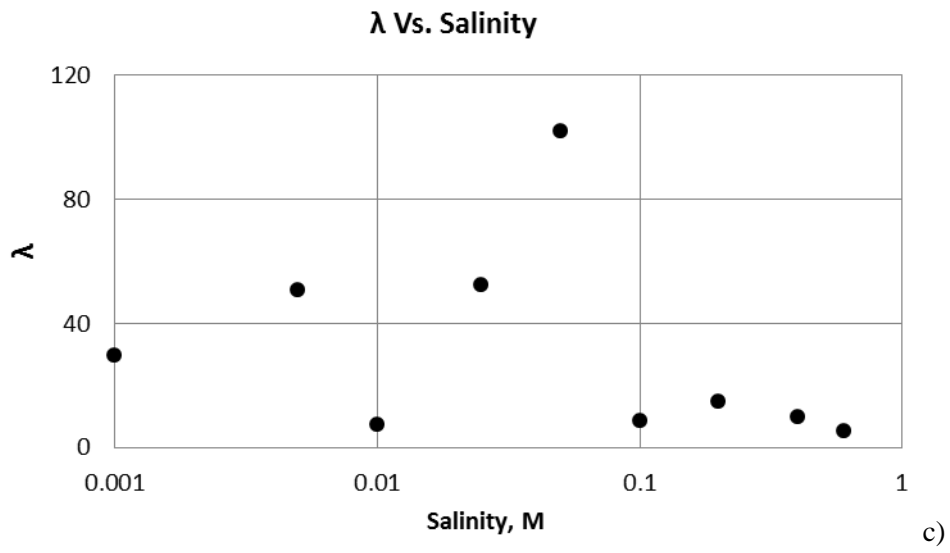
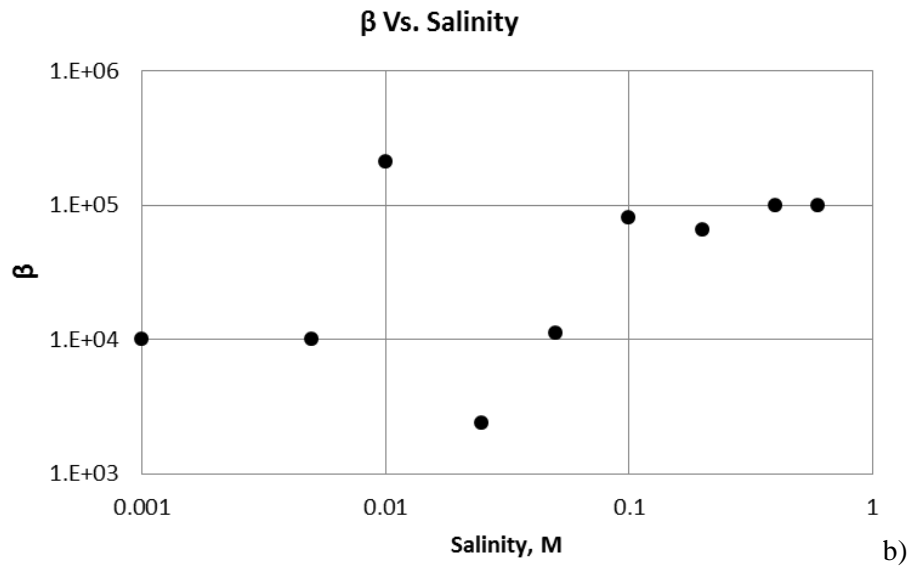


Fig. 25. Matching the coreflood data by the slow-particle delayed -release model: (a) dimensionless pressure drop across the overall core; (b) dimensionless pressure drop across the first core section; (c) accumulated fine-particle production.



a)



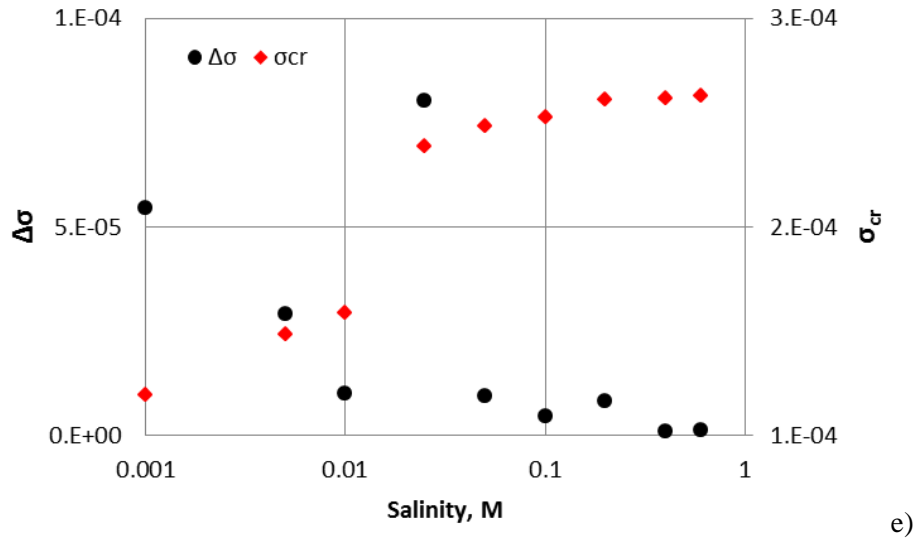


Fig. 26. Tuned values of the slow-particle delayed-release model parameters for 10 different-salinity stages: (a) drift delay factor; (b) formation damage coefficient; (c) filtration coefficient; (d) dimensionless delay; (e) concentration of detached fines.

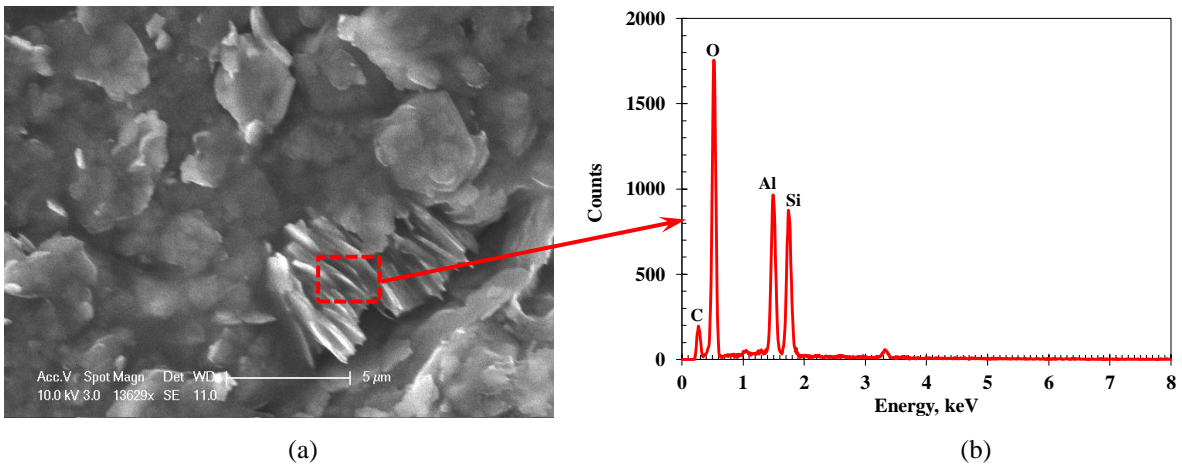


Fig. 27. SEM-EDX results for the core sample (Ladbroke Grove-1 well): (a) SEM image; (b) EDX spectra for kaolinite.

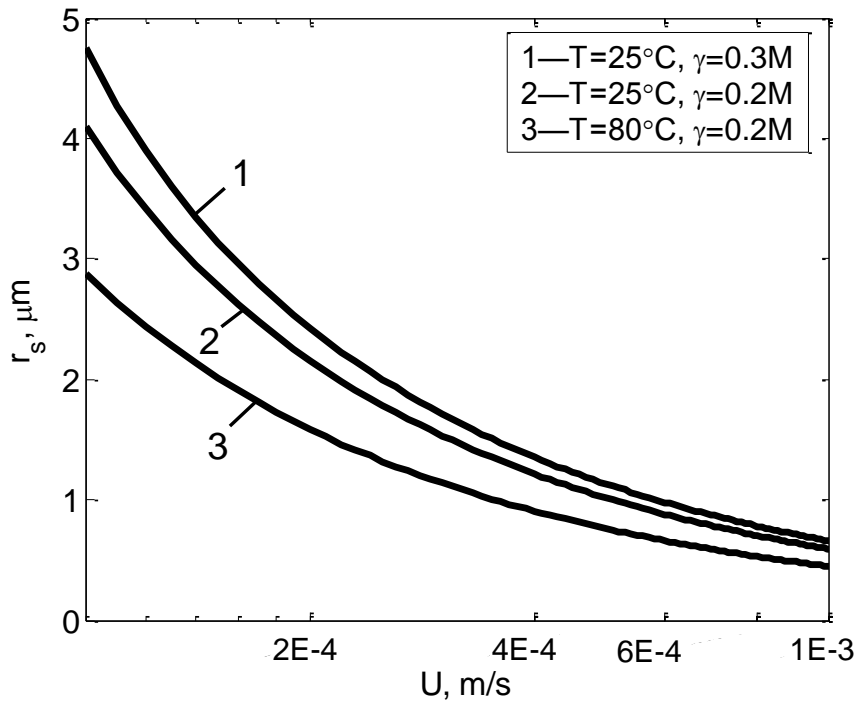
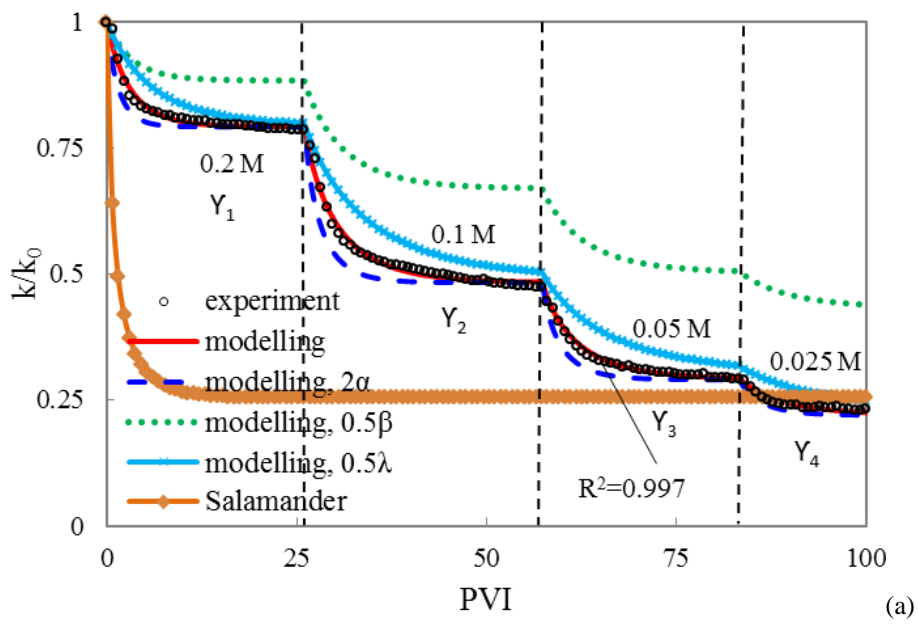


Fig. 28. Maximum retention function for monolayer of size distributed particles mobilised by the fluid flow with various velocities.



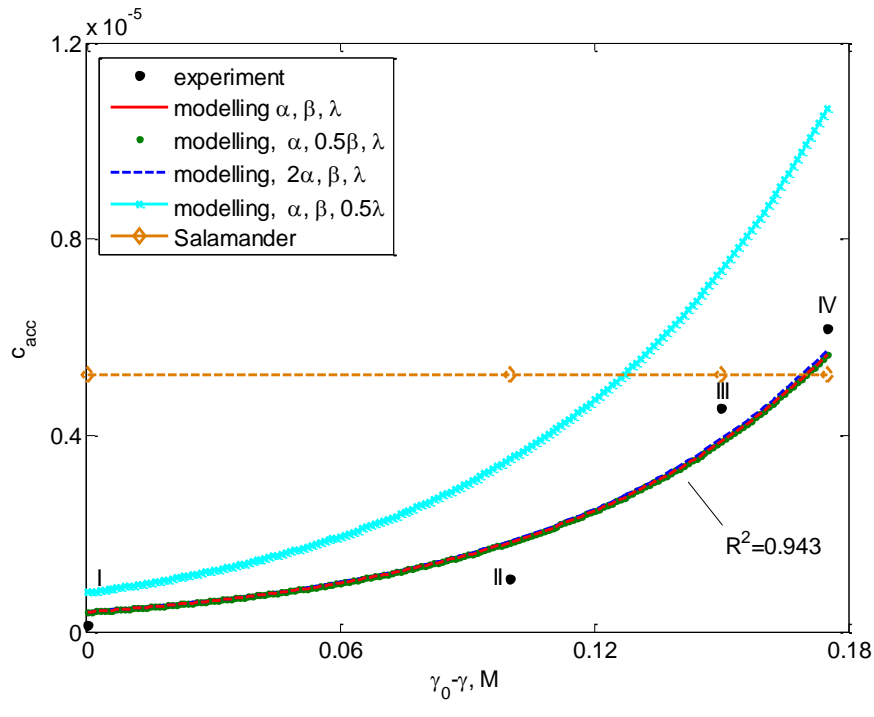
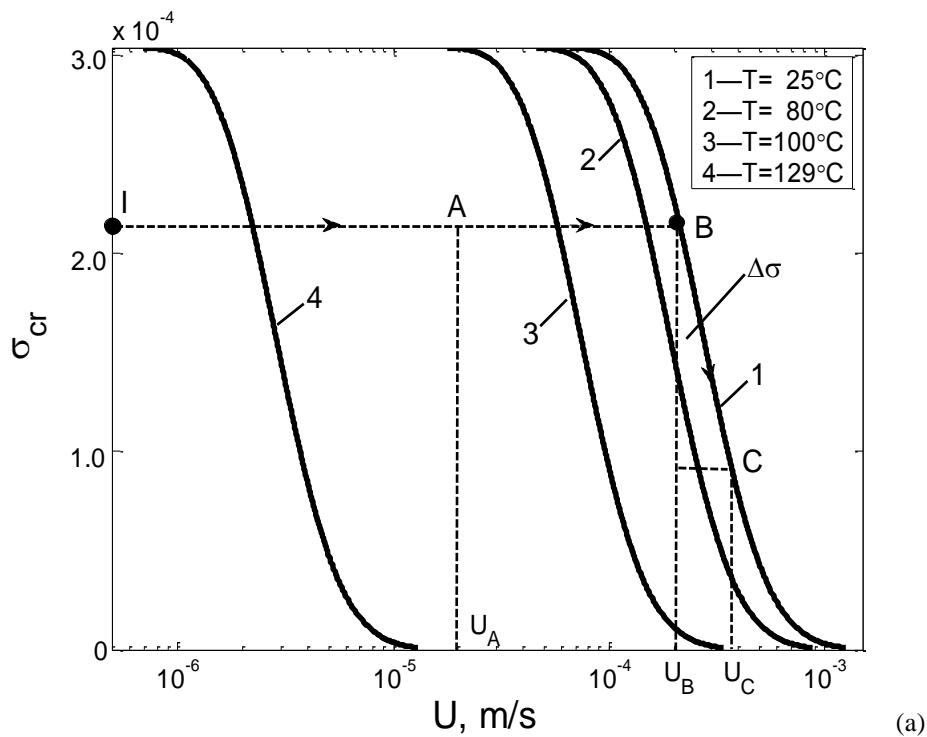
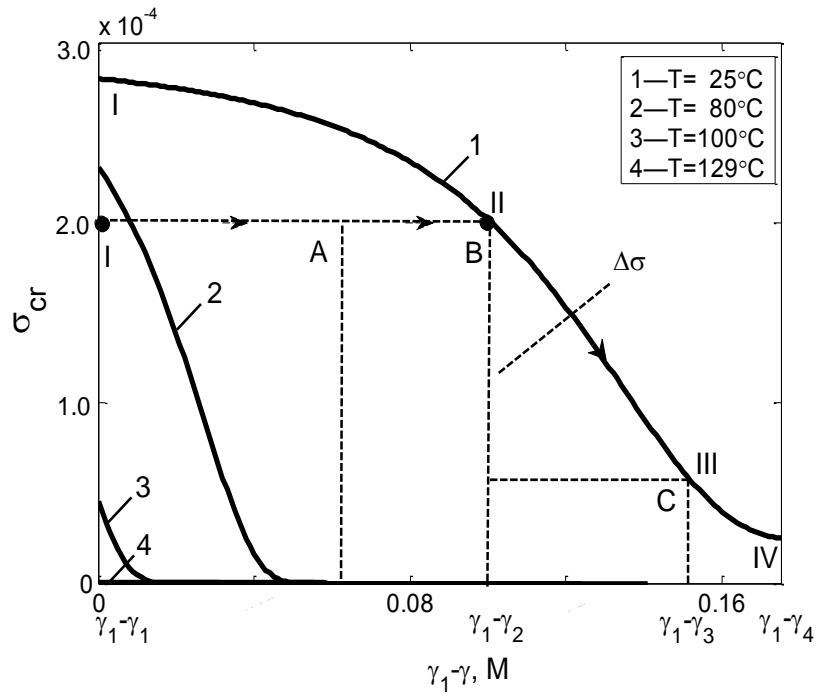
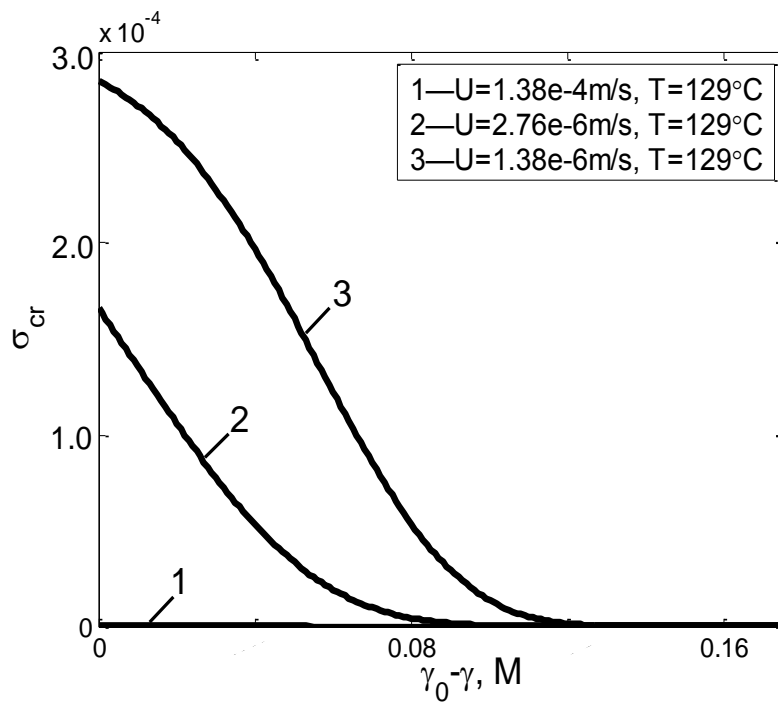


Fig. 29. Results of tuning the laboratory data from corefloods with varying fluid ionic strength at $T=25^{\circ}\text{C}$ using the analytical model and prediction for Salamander geothermal field ($T=129^{\circ}\text{C}$): (a) decrease of core permeability during tests with piecewise decreasing ionic strength; (b) cumulative breakthrough concentration at different fluid ionic strengths.





(b)



(c)

Fig. 30. Temperature-, velocity-, and salinity-dependence of maximum retention function: (a) maximum retention concentration vs velocity at different temperatures; (b) ionic strength dependency of maximum retention concentration ($\gamma_0 = 0.2M$ NaCl) at different temperatures; (c) ionic strength dependency at geothermal reservoir temperature and different velocities.

Table 1. Exact analytical solution for 1d fines migration during the increase of piece-wise constant velocity

Term	Explicit formulae for 1d solution	(X,T) -domain
Suspension concentration during stage 1	$C = 0$	$X \leq \alpha_1 T$
	$C = \Delta S_{a1} e^{-\alpha_1 \Lambda_s T}$	$X > \alpha_1 T$
Retention concentration during stage 1	$S_s = \Delta S_{a1} (1 - e^{-\Lambda_s X})$	$X \leq \alpha_1 T$
	$S_s = \Delta S_{a1} (1 - e^{-\alpha_1 \Lambda_s T})$	$X > \alpha_1 T$
Impedance during stage 1	$J(T) = 1 + \beta_s \sigma_{a0} \Delta S_{a1} \left[1 - \frac{1}{\Lambda_s} - \left(1 - \frac{1}{\Lambda_s} - \alpha_1 T \right) e^{-\alpha_1 \Lambda_s T} \right]$	$T < \alpha_1^{-1}$
	$J(T) = 1 + \beta_s \sigma_{a0} \Delta S_{a1} \left[1 - \frac{1}{\Lambda_s} - \frac{e^{-\Lambda_s}}{\Lambda_s} \right]$	$T \geq \alpha_1^{-1}$
Suspension concentration during stage n	$C = 0$	$X \leq \alpha_1 T$
	$C = \Delta S_{an} e^{-\alpha_n \Lambda_s (T - T_n)}$	$X > \alpha_1 T$
Retention concentration during stage n	$S_s - S_{sn} = \Delta S_{an} (1 - e^{-\Lambda_s X})$	$X < \alpha_n (T - T_n)$
	$S_s - S_{sn} = \Delta S_{an} \left[1 - e^{-\alpha_n \Lambda_s (T - T_n)} \right]$	$X \geq \alpha_n (T - T_n)$
Impedance during stage n	$J(T) = J_{0n} + \beta_s \sigma_{a0} \Delta S_{an} \left[1 - \frac{1}{\Lambda_s} - \left(1 - \frac{1}{\Lambda_s} - \alpha_1 (T - T_n) \right) e^{-\alpha_n \Lambda_s (T - T_n)} \right]$	$T < T_n + \alpha_1^{-1}$
	$J(T) = J_{0n} + \beta_s \sigma_{a0} \Delta S_{an} \left[1 - \frac{1}{\Lambda_s} - \frac{e^{-\Lambda_s}}{\Lambda_s} \right]$	$T \geq T_n + \alpha_1^{-1}$

Table 2. Tuned values of the model parameters

Model parameter	Test I	Test II
α_1	0.0020	0.0018
α_2	0.0020	0.0018
α_3	0.0020	0.0018
α_4	0.0020	0.0018
α_5	0.0020	-
α_6	0.0008	-
α_7	0.0008	-
$\Delta\sigma_{a1}$	0.0017	0.0206
$\Delta\sigma_{a2}$	0.0039	0.0102
$\Delta\sigma_{a3}$	0.0045	0.0086
$\Delta\sigma_{a4}$	0.0076	0.0086
$\Delta\sigma_{a5}$	0.0114	-
$\Delta\sigma_{a6}$	0.0114	-
$\Delta\sigma_{a7}$	0.0076	-
λL	2.2869	3.0069
β	30.9328	22.9161

Table 3. Mineralogical composition of the rock

Mineralogy	A1 core
	% (w/w)
Quartz	59.9
K-feldspar	2.3
Plagioclase	1.0
Kaolinite	9.2
Illite/mica	18.6
Illite/smectite	2.0
Chlorite	5.1
Siderite	1.9
Total	100.00

Table 4. Ionic compositions for formation and artificial formation fluids

Parameter/ Ion	Units	FF	Parameter/ Ion	Units	AFF	AFF (NaCl)
Electrical conductivity	μS/c	24000	Electrical	μS/c	25257	49200
pH	N/A	7.6	pH	N/A	7.9	8.1
Total dissolved solids	mg/L	15000	Total dissolved solids	mg/L	15275	36851
Ionic strength	mol/L	0.231	Ionic strength	mol/L	0.230	0.601
Chloride	mg/L	7300	NaCl	mg/L	3118	24693
Sulphate as SO ₄ ²⁻	mg/L	350	MgCl ₂	mg/L	70.5	70.5
Bicarbonate as HCO ₃ ⁻	mg/L	450	Na ₂ SO ₄	mg/L	517.5	517.5
Calcium	mg/L	260	CaCl ₂	mg/L	720.0	720.0
Magnesium	mg/L	18	NaHCO ₃	mg/L	553.4	553.4
Sodium	mg/L	1600	KCl	mg/L	10296	10296
Potassium	mg/L	5400				

Table 5 Analytical model for fines mobilisation, migration and suspension ($\alpha\Lambda \neq b$).

Term	Notation	Zones	Expression
Suspended concentration	$C(X,T)$	$T \leq X / \alpha$	$\frac{y}{\alpha\Lambda - b} (e^{-bT} - e^{-\alpha\Lambda T})$
		$T > X / \alpha$	$\frac{y}{\alpha\Lambda - b} e^{-bT} \left(1 - e^{\left(\frac{b}{\alpha} - \Lambda\right)X} \right)$
Strained concentration	$S_s(X,T)$	$T \leq X / \alpha$	$\alpha\Lambda \left[\frac{y}{\alpha\Lambda(\alpha\Lambda - b)} e^{-\alpha\Lambda T} - \frac{y}{b(\alpha\Lambda - b)} e^{-bT} \right] - \alpha\Lambda \left[\frac{y}{\alpha\Lambda(\alpha\Lambda - b)} - \frac{y}{b(\alpha\Lambda - b)} \right]$
		$T > X / \alpha$	$\alpha\Lambda \left[\frac{y}{\alpha\Lambda(\alpha\Lambda - b)} e^{-\alpha\Lambda X} - \frac{y}{b(\alpha\Lambda - b)} e^{-\frac{bX}{\alpha}} \right] - \alpha\Lambda \left[\frac{y}{\alpha\Lambda(\alpha\Lambda - b)} - \frac{y}{b(\alpha\Lambda - b)} \right] \dots$ $+ \alpha\Lambda \left[-\frac{y}{b(\alpha\Lambda - b)} \left(1 - e^{\left(\frac{b}{\alpha} - \Lambda\right)X} \right) e^{-bT} \right] + \alpha\Lambda \left[\frac{y}{b(\alpha\Lambda - b)} \left(1 - e^{\left(\frac{b}{\alpha} - \Lambda\right)X} \right) e^{-\frac{bX}{\alpha}} \right]$
Permeability	$k(t_D)$		$k_0 \left(1 + \frac{\beta\phi}{\omega} \int_0^\omega S_s(x_D, t_D) dx_D \right)^{-1}$

Table 6 Analytical model for fines mobilisation, migration and suspension($\alpha\Lambda = b$).

Term	Notation	Zones	Expression
Suspended concentration	$C(X,T)$	$T \leq X/\alpha$	yTe^{-bT}
		$T > X/\alpha$	$\frac{y}{\alpha}e^{-bT} X$
Strained concentration	$S_s(X,T)$	$T \leq X/\alpha$	$-ye^{-bT}T + \frac{y}{b}(1 - e^{-bT})$
		$T > X/\alpha$	$\frac{y}{b}\left(1 - e^{-\frac{bX}{\alpha}}\right) - \frac{y}{\alpha}Xe^{-bT}$
Permeability	$k(t_D)$		$k_0\left(1 + \frac{\beta\phi}{\omega} \int_0^\omega S_s(x_D, t_D) dx_D\right)^{-1}$

Table 7. Fitted parameters for the slow-particle model

Salinity	β	$\Delta\sigma$	α	λ	ϵ
0.6M	32803	3.17E-06	0.0138	12.06	0
0.4M	93310	4.35E-07	0.0439	17.78	0
0.2M	916406	3.72E-07	0.0628	1.14	0
0.1M	89189	4.63E-06	0.0094	8.28	0
0.05M	100070	1.04E-06	0.0500	9.99	0
0.025M	41985	1.30E-05	0.0128	2.81	0
0.01M	99875	2.15E-05	0.0019	15.78	0
0.005M	2928	6.27E-05	0.0010	99.87	0
0.001M	4451	8.87E-05	0.0030	84.44	0
0M	8879	2.10E-04	0.0022	69.37	0

Table 8. Fitted parameters for the delayed-particle-release model

Salinity	β	$\Delta\sigma$	α	λ	ϵ
0.6M	12876	1.07E-05	1.0000	31.40	8
0.4M	99876	6.09E-07	1.0000	21.07	4
0.2M	99976	5.86E-05	1.0000	13.27	338
0.1M	99973	3.97E-06	1.0000	6.65	11
0.05M	199985	5.60E-07	1.0000	6.65	1
0.025M	99990	3.56E-05	1.0000	2.23	84
0.01M	1100000	3.51E-06	1.0000	2.23	33
0.005M	100000	1.77E-06	1.0000	2.23	5
0.001M	200000	6.02E-06	1.0000	2.23	2
0M	900000	5.14E-06	1.0000	2.34	6

Table 9. Fitted parameters for the slow-particle delayed-release model

Salinity	β	$\Delta\sigma$	α	λ	ϵ
0.6M	99998	1.14E-06	0.4835	5.14	3.99
0.4M	99998	8.06E-07	0.2682	10.00	4.59
0.2M	64851	8.21E-06	0.0503	14.85	23.64
0.1M	80078	4.63E-06	0.0103	8.54	0.91
0.05M	11084	9.38E-06	0.0055	101.73	0.01
0.025M	2370	8.02E-05	0.0067	52.28	2.94
0.01M	208613	9.90E-06	0.0043	7.30	0.63
0.005M	9963	2.91E-05	0.0033	50.65	0.17
0.001M	10070	5.44E-05	0.0014	29.74	0.17
0M	30211	6.52E-05	0.0084	29.74	0.17

Table 10. Temperature effects on the parameters in DLVO interaction energy model

Parameter	Temperature effect	References
λ	N/A	Gregory (1981)
ε_1	Table 2 below	Leluk et al. (2010)
ε_2	Negligible if $T < 170^\circ\text{C}$ (Fig. 1 in Ref)	Stuart (1955)
ε_3	Table 3 below	Marshall (2008)
n_1	N/A	Egan and Hilgeman (1979)
n_2	Interpolation from Fig. 1 in Ref	Leviton and Frey (2006)
n_3	Eq. (8) in Ref	Aly and Esmail (1993)
ζ_s	Eq. (9) in Ref	Schembre and Kavscek (2005)
ζ_{pm}	Eq. (9) in Ref	Schembre and Kavscek (2005)
σ_c	N/A	Elimelech et al. (2013)

Table 11. Dielectric constant of kaolinite ε_1 (interpolated from data in Leluk et al. (2010))

$T, ^\circ\text{C}$	ε_1
25	6.65
80	6.35
130	6.11
180	5.89

Table 12. Dielectric constant of brine ϵ_3 *

	0.6M	0.4M	0.2M	0.1M	0.05M	0.025M	0.01M	0.005M	0.001M	0.00013M
25°C	72.767	74.995	77.222	78.336	78.893	79.172	79.339	79.395	79.439	79.449
100°C	50.711	52.263	53.816	54.592	54.980	55.174	55.291	55.329	55.361	55.367
129°C	44.191	45.544	46.897	47.574	47.912	48.081	48.183	48.216	48.243	48.249
200°C	31.589	32.556	33.524	34.007	34.249	34.370	34.442	34.466	34.486	34.490
300°C	18.744	19.318	19.892	20.179	20.323	20.394	20.437	20.452	20.463	20.466

*Values in Table 3 are calculated from formula $\epsilon_3(T)$ given by Marshall (2008) based on laboratory measured ϵ_3 values with different ionic strength at ambient condition.

Table 13. Values of the model tuning parameters in the coreflood test.

Parameter	Value
$r_s, \mu m$	1.80
C_v	0.66
σ_0	3.04e-4
α_1	4.10e-3
α_2	2.96e-3
α_3	2.81e-3
α_4	2.74e-3
β_1	9793
β_2	7631
β_3	7391
β_4	7158
λ_{D1}	67.14
λ_{D2}	53.79
λ_{D3}	51.11
λ_{D4}	50.13

4 Mathematical modelling of fines migration in geothermal reservoirs

You, Z., **Yang, Y.**, Badalyan, A., Bedrikovetsky, P. and Hand, M.

Geothermics, 59, (2016)123-133

Statement of Authorship

Title of Paper	Mathematical modelling of fines migration in geothermal reservoirs
Publication Status	<input checked="" type="checkbox"/> Published <input type="checkbox"/> Accepted for Publication <input type="checkbox"/> Submitted for Publication <input type="checkbox"/> Unpublished and Unsubmitted work written in manuscript style
Publication Details	You, Z., Yang, Y., Badalyan, A., Bedrikovetsky, P. and Hand, M., 2016. Mathematical modelling of fines migration in geothermal reservoirs. Geothermics, 59, pp.123-133.

Author Contributions

By signing the Statement of Authorship, each author certifies that:

- i. the candidate's stated contribution to the publication is accurate (as detailed above);
- ii. permission is granted for the candidate to include the publication in the thesis; and
- iii. the sum of all co-author contributions is equal to 100% less the candidate's stated contribution

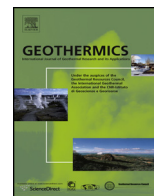
Name of Principal Author	Zhenjiang You		
Contribution to the Paper	Supervised development of work, helped in data interpretation and manuscript evaluation		
Signature	<table border="1" style="float: right;"> <tr> <td>Date</td> <td>20/7/16</td> </tr> </table>	Date	20/7/16
Date	20/7/16		

Name of Co-Author (Candidate)	Yulong Yang		
Contribution to the Paper	Derived analytical solution and performed data treatment		
Overall percentage (%)	50%		
Signature	<table border="1" style="float: right;"> <tr> <td>Date</td> <td>20/07/2016</td> </tr> </table>	Date	20/07/2016
Date	20/07/2016		

Name of Co-Author	Alex Badalyan		
Contribution to the Paper	Performed laboratory work, helped in data interpretation		
Signature	<table border="1" style="float: right;"> <tr> <td>Date</td> <td>20.07.2016</td> </tr> </table>	Date	20.07.2016
Date	20.07.2016		

Name of Co-Author	Pavel Bedrikovetsky		
Contribution to the Paper	Supervised development of work, helped in data interpretation and manuscript evaluation		
Signature	<table border="1" style="float: right;"> <tr> <td>Date</td> <td>21/07/2016</td> </tr> </table>	Date	21/07/2016
Date	21/07/2016		

Name of Co-Author	Martin Hand
Contribution to the Paper	Supervised development of work and manuscript evaluation
Signature	
	Date 17-7-2016



Mathematical modelling of fines migration in geothermal reservoirs



Zhenjiang You^{a,*}, Yulong Yang^a, Alexander Badalyan^a, Pavel Bedrikovetsky^a,
Martin Hand^b

^a Australian School of Petroleum, The University of Adelaide, Adelaide, SA 5005, Australia

^b South Australian Centre for Geothermal Energy Research, Institute of Mineral and Energy Resources, The University of Adelaide, Adelaide, SA 5005, Australia

ARTICLE INFO

Article history:

Received 4 September 2014

Accepted 25 May 2015

Available online 29 June 2015

Keywords:

Permeability reduction

Formation damage

Fines migration

Mathematical model

Slow particle motion

ABSTRACT

Laboratory-based mathematical modelling of fines migration allows predicting well productivity reduction during the geothermal reservoir exploitation. The analytical model for one-dimensional flow with ionic strength alteration has been derived. Good adjustment of the permeability and breakthrough concentration data from coreflood test by the analytical model has been achieved, and the tuned model coefficients fall in the common ranges. The obtained maximum retention function of multi-sized fines allows calculating their size distribution. During the temperature rise, weakening of electrostatic attraction on fines attached to rock surface overwhelms the reduction of detaching drag force due to water viscosity decrease. It leads to increased fines detachment and more severe permeability decline at elevated temperatures, typical for geothermal fields.

© 2015 Elsevier Ltd. All rights reserved.

1. Introduction

Transport of suspensions and colloids in porous media with particle capture and permeability decline occurs in several processes of geothermal reservoir and production engineering, such as production of hot water from geothermal wells, enhanced geothermal systems with cold water injection and hot water/steam production, seasonal hot water storage in aquifers, etc. (Priisholm et al., 1987; Baudracco, 1990; Baudracco and Aoubouazza, 1995; Ghassemi and Zhou, 2011; Aragón-Aguilar et al., 2013; Rosenbrand et al., 2012, 2013, 2014, , 2015). The mathematical modelling of deep bed filtration accounting for particle capture, detachment and rock clogging is an essential part of the planning and design of the above-mentioned processes.

Since the particle capture by straining is the main physical mechanism of permeability damage during fines migration, and size exclusion is defined by pore and particle sizes, the micro scale models accounting for pore and particle size distributions are adequate for fines migration prediction (see micro scale schematic of fines mobilisation, migration and straining in Fig. 1). The detailed description of fines migration accounting for pore and particle size distributions can be performed by using the micro scale models of random walks (Cortis et al., 2006; Shapiro, 2007; Yuan and Shapiro, 2011), population balance models (Sharma and Yortsos, 1987a,b; You et al., 2013) and Boltzmann's physical kinetics

equation (Shapiro and Wesselingh, 2008). However, to the best of our knowledge, the data on particle and pore size distributions during fines migration are not available in the literature. Therefore, the averaged equations operating with overall suspended, retained and attached particle concentrations are used in the current work for fines migration prediction and assessment.

Other temperature-sensitive rock parameters affecting geothermal exploration and production are porosity, electrical conductivity and seismic properties (Jaya et al., 2010; Kristinsdottir et al., 2010; Milsch et al., 2010; Rosenbrand et al., 2015).

The most commonly used approach for evaluating fines migration, retention and detachment in laboratory and field-scale studies is to apply the mass balance equation for solute transport with the sink term for particle retention and the source term for particle dislodging (Schijven and Hassanizadeh, 2000; Logan, 2001; Cortis et al., 2006; Tufenkji, 2007; Shapiro and Yuan, 2013):

$$\frac{\partial}{\partial t}(\phi c + \sigma) + U \frac{\partial c}{\partial x} = D \frac{\partial^2 c}{\partial x^2} \quad (1)$$

$$\frac{\partial \sigma}{\partial t} = \lambda(\sigma)cU - k_{\text{det}}\sigma \quad (2)$$

where c and σ are dimensionless volumetric concentrations of suspended and strained particles, respectively; U is the flow velocity and D is the diffusion coefficient.

The capture term in Eq. (2) is proportional to the advective particle flux; the proportionality coefficient λ is called the filtration coefficient. The detachment term is proportional to the retained concentration; the proportionality coefficient k_{det} is called the

* Corresponding author.

E-mail address: zyou@asp.adelaide.edu.au (Z. You).

Nomenclature

C_v	coefficient of variance
c	volumetric concentration of suspended particles
D	diffusion coefficient ($L^2 T^{-1}$)
F	force (MLT^{-2})
i	index
j	index
k	permeability (L^2)
k_{det}	detachment rate coefficient (T^{-1})
L	length of core (L)
l	lever (L)
n	index
p	pressure ($MT^{-2}L^{-1}$)
Q	intermediate function
r	radius (L)
S	dimensionless concentration of retained particles
T	temperature (K)
t	time (T)
U	Darcy velocity (LT^{-1})
x	distance (L)

Greek letters

α	drift delay factor
β	formation damage coefficient
γ	ionic strength
ε	erosion ratio (ratio between the torques of detaching and attaching forces)
λ	filtration coefficient (L^{-1})
μ	dynamic viscosity ($ML^{-1}T^{-1}$)
Σ	concentration distribution of captured particles (L^{-1})
σ	volumetric concentration of captured particles
ϕ	porosity

Subscripts

a	attachment
cr	critical (for the maximum retention function)
D	dimensionless
d	drag
e	drainage (for reservoir radius), electrostatic (for force)
g	gravitational
l	lifting
s	straining (for retained concentration), radius (for particles)
scr	critical radius (for retained particles)
0	initial value

detachment rate coefficient. System of Eqs. (1) and (2) together with the micro-scale-modelling-based formula for coefficient λ is called the classical filtration theory in the above references. The advanced theory for the filtration coefficient dependency on particle–grain and particle–particle interactions, flow velocity, Brownian diffusion and gravitational sedimentation has been developed (Nabzar and Chauveteau, 1997; Chauveteau et al., 1998; Tufenkji and Elimelech, 2004; Rousseau et al., 2008; Yuan and Shapiro, 2012), while the detachment coefficient is an empirical constant usually determined by tuning from the experimental data. This is a shortcoming of the advective-diffusive attachment–detachment model with kinetics of the particle detachment ((1) and (2)).

Another shortcoming is the asymptotic stabilisation of the retention concentration and permeability when time tends to infinity, while the fines release due to abrupt pressure gradient

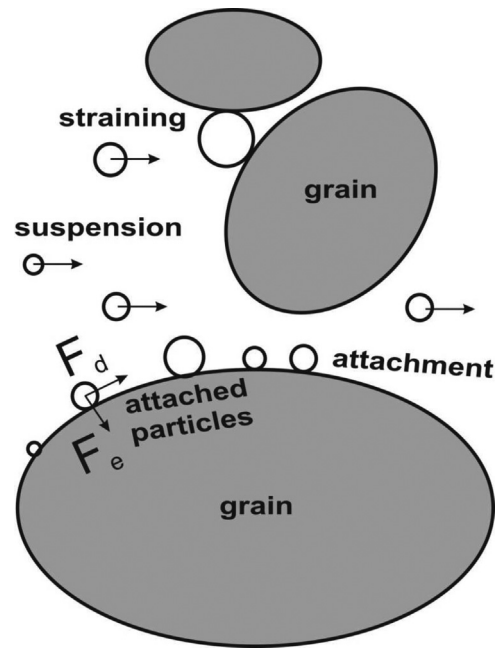


Fig. 1. Fines mobilisation, migration and straining in porous media (F_d : drag force, F_e : electrostatic force).

increase or under salinity alternation happens almost instantly (Miranda and Underdown, 1993; Khilar and Fogler, 1998). The coreflood with sharp rate increase shows an immediate permeability response (Ochi and Vernoux, 1998; Bedrikovetsky et al., 2012; Oliveira et al., 2014).

It has long been recognised that the particle detachment happens if the mechanical equilibrium of a retained particle on the internal filter cake does not take place (Schechter, 1992; Rahman et al., 1994; Civan, 2007). The forces acting on a particle placed on the internal cake are: electrostatic, drag, lifting and gravitational forces. In the majority of the cases, lifting and gravitational forces can be neglected. In particular, the analyses under both ambient and geothermal reservoir conditions show that gravitational and lifting forces are negligible if compared with electrostatic and drag forces (You et al., 2014). Therefore, only drag and electrostatic forces are shown in Fig. 1. Some authors consider a force balance between the drag force acting on the particle from the by-passing fluid, and the friction force with an empirical Coulomb coefficient (Civan, 2007). Another approach includes the momentum balance of forces (Jiao and Sharma, 1994; Freitas and Sharma, 2001):

$$F_d(U, T, r_s)l(r_s) = F_e(\gamma, T, r_s), \quad l = \frac{l_d}{l_e} \quad (3)$$

where F_d and F_e are drag and electrostatic forces, respectively, l_d and l_e are corresponding lever arms, l is the lever arm ratio, U is flow velocity, γ is the ionic strength of the reservoir brine and r_s is the particle radius.

The modified Stokes' formula is derived for a spherical particle located on at the pore wall, and expresses the drag force via velocity and the particle radius (Jiao and Sharma, 1994; Ochi and Vernoux, 1998; Bradford et al., 2013). The drag force expression contains the shape factor that accounts for the particle form, its deformation on the rock surface by attractive electrostatic forces and the rock surface roughness.

Electrostatic force is calculated from the total interaction potential energy. At the micron scale of the reservoir fines, this energy is the sum of London-van-der-Waals, electrical double layer and Born potentials. The explicit expressions of three interaction potential energies are given by the DLVO

(Derjaguin–Landau–Verwey–Overbeek) theory (Derjaguin and Landau, 1941; Verwey and Overbeek, 1948; Israelachvili, 2011). The explicit formulae for the three respective forces versus water ionic strength, velocity, particle and pore radii, as applied for fines migration and used further in this paper, can be found from Khilar and Fogler (1998).

The two approaches are mathematically equivalent. The advective-diffusion equation with kinetic detachment term ((1) and (2)) does not reflect the particle mechanical equilibrium; the detachment term is not affected by the mechanical equilibrium of a single particle.

Drag force in Eq. (3) depends on velocity and particle radius while electrostatic force depends on particle radius, ionic strength and temperature. It allows expressing particle radius r_s from transcendental Eq. (3): $r_{scr} = R(U, \gamma, T)$. For the above mentioned expressions for drag and electrostatic forces, the function R monotonically decreases with U and T , and monotonically increases with γ . It means that r_{scr} is the minimum size of particles mobilised by flow during increase of fluid velocity and temperature, and decrease of salinity, i.e. particles are removed in the order of their radii decrease. Therefore, the total remaining particle concentration is the sum of concentrations for all particles smaller than r_{scr} :

$$\sigma_a = \sigma_{cr}(U, \gamma, T), \quad \sigma_{cr}(U, \gamma, T) = \int_0^{r_{scr}(U, \gamma, T)} \Sigma_a(r_s) dr_s \quad (4)$$

where $\Sigma_a(r_s)$ is the size distribution of attached fine particles. The dependency (4) is called the maximum retention function. It is an empirical function of the properties of porous media and the flowing-through particles.

The modified mathematical model which models the particle release uses the maximum retention concentration as an instant function of velocity, salinity and temperature (Bedrikovetsky et al., 2011, 2012). Change of any of these three parameters at point (x, t) results in either increase or decrease of the maximum retention function, yielding either timely attachment of new particles to the rock or instant detachment. For flow regimes where velocity and temperature monotonically increase and salinity monotonically decreases, the maximum retention function decreases, and the attached particles are mobilised.

So, the maximum retention function is determined by the torque balance on the pore surface of the internal cake, Eq. (3). The phenomenological function (4) substitutes the particle release kinetics in the classical attachment–detachment model (2). The modified model (3) and (4) is free of the above mentioned shortcomings.

The maximum retention function is analogous to adsorption isotherm. The difference is the dependency of the maximum retention function on velocity, which is not a thermodynamic parameter (Bedrikovetsky, 1993). Maximum retention dependency (4) does not correspond to energy minimum, since the drag force in Eq. (3) does not have potential. However, Eq. (4) can be generalised as similar to non-equilibrium sorption.

The works by Bradford et al. (2012, 2013) account for kinetics of the particle release due to salt diffusion from the contact area between the particle and matrix surface, both deformed by the electrostatic “particle-rock” attraction. Their models correspond to the introduction of timely delay into the maximum retention function (4).

The conventional model ((1) and (2)) assumes that the mobilised particle speed is equal to the carrier fluid velocity. This assumption along with that of an instant particle release leads to zero outlet concentration after one pore volume injection, since the particle mobilised at the core entrance arrives at the outlet at the moment of one pore volume injected. Therefore, the pressure drop along the core also stabilises after injection of one pore volume. However, numerous laboratory studies show significant

delay in pressure drop/permeability stabilisation (Lever and Dawe, 1984; Ochi and Vernoux, 1998; You et al., 2014). It is explained by slow particle drift near the grain surfaces (You et al., 2014). Slow movement of released particles have been noticed in several works. Sefrioui et al. (2013) investigated slow particle movement near to pore wall asperities using the Navier–Stokes-based micro-scale modelling. Yuan and Shapiro (2011) and Bradford et al. (2013) observed delayed particle arrival from the breakthrough concentration curves. They proposed the two-speed model that successfully matches the breakthrough concentrations. However, the model contains six empirical kinetics coefficients of mass transfer between attached, slow-near-wall and fast-in-bulk-water particles, which cannot be determined solely from the breakthrough concentration history. Significantly more sophisticated laboratory tests should be performed for complete characterisation of the two-speed model. Besides, mass exchange between fast and slow particle fluxes occurs on the pore scale, so the particle concentrations may be equal on the core scale causing propagation of the overall particle ensemble with the low average speed. Therefore, in the current work we use the single-velocity model with particle speed that is lower than the water velocity.

In the present paper, water flow velocity U in basic equations ((1) and (2)) is substituted by the particle velocity $U_s < U$ that explains long periods for permeability stabilisation by slow surface motion of the mobilised fine particles. Another modification of the governing system ((1) and (2)) is the introduction of the maximum retention function for a monolayer of size-distributed fines, allowing explaining its non-convex form. The exact solution to the obtained system of equations for one-dimensional flow with piecewise constant velocity increase is obtained. The laboratory data on pressure drop along the core during injection have been matched by the analytical model. It is shown that the mobilised particle speed is significantly lower than the carrier water velocity, i.e. $U_s \ll U$. Good agreement between the laboratory and modelling data validates the proposed model for a slow surface motion of released fine particles in porous media. Application of the laboratory-based model to fines migration at higher temperatures in geothermal reservoirs yields significantly higher permeability damage, compared with applications at conventional reservoir temperatures.

The present work uses the laboratory study data obtained in the companion paper by You et al. (2014).

The structure of the text is as follows. Section 2 presents the basic governing equations for one-dimensional suspension-colloidal transport with particle release, migration and straining along with analytical model for injection with piecewise constantly decreasing ionic strength. Tuning of the model coefficients from the laboratory data from the companion paper by You et al. (2014) is shown in Section 3. The discussions of the model validity conclude the paper.

2. Mathematical model for fines migration during coreflooding

In this section we present the model assumptions (Section 2.1), governing system of equations (Section 2.2) and its analytical solution (Section 2.3) for suspension flow with slow migration of detached fines and further straining. The derived analytical model is applied to experimental data treatment in Section 3.

2.1. Assumptions

The assumption that the particle velocity is equal to the carrier fluid velocity in (1) and (2) corresponds to permeability stabilisation at the moment $t=1$ PVI. However, the laboratory data presented in Fig. 2(a) shows that even 25 PVI of the constant fluid ionic strength injection is not enough for the average permeability stabilisation. The delayed stabilisation effect can be explained

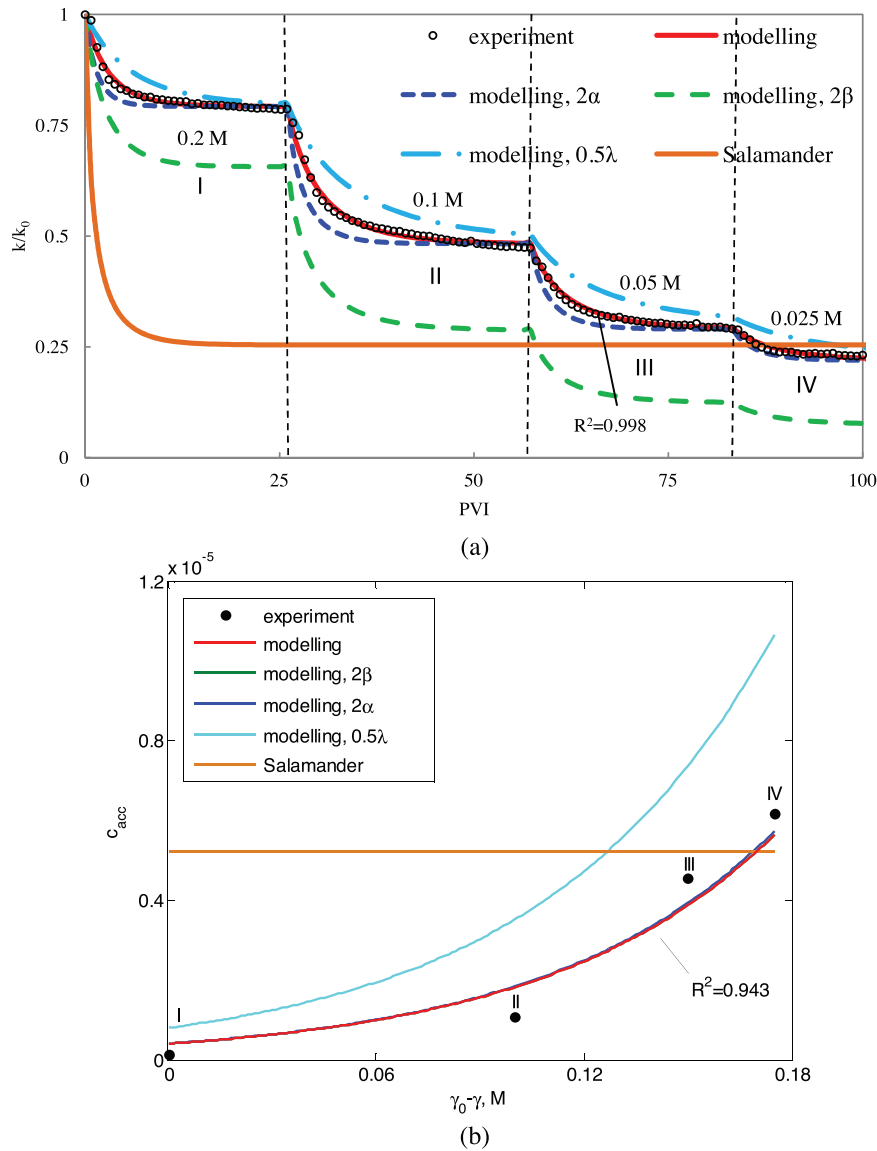


Fig. 2. Tuning the laboratory data from ionic strength alteration test at $T=25^\circ\text{C}$ by the analytical model and prediction for Salamander geothermal field ($T=129^\circ\text{C}$): (a) permeability decline of the core during coreflood with piecewise decreasing ionic strength; (b) cumulative breakthrough concentration (c_{acc}) at different ionic strength values (k : permeability, α : drift delay factor, β : formation damage coefficient, λ : filtration coefficient, γ : ionic strength). (For interpretation of the references to color in text near the figure citation, the reader is referred to the web version of this article.)

by slow drift of mobilised fines along the pore walls and stagnant zones, and also by particle sliding and rolling along the rock surface (Jiao and Sharma, 1994; Sefrioui et al., 2013). Therefore, below it is assumed that the particle transport velocity is equal to αU , where $\alpha < 1$.

The main assumptions of the mathematical model for fines mobilisation, migration and straining are:

- incompressible fluid and particles;
- volume additivity for fluid with suspended, attached and strained particles;
- constant porosity for low attached and strained concentrations;
- particle migration velocity different from the carrier fluid velocity;
- negligible dispersion of fine particles if compared with their advection;
- instant release of attached particles fulfilling the maximum retention condition (3) and (4);
- linear kinetics of the particle straining by porous media with constant filtration and formation damage coefficients;

- no strained particles in rocks before fines mobilisation;
- no detachment of strained particles; and
- negligible permeability increase due to particle detachment if compared with the permeability decrease due to particle straining.

Based on the above assumptions, the next section derives transport equations for colloids and suspensions accounting for particle release, migration and straining.

2.2. Governing equations

The mass balance equation for suspended, attached and strained fines in porous media is:

$$\frac{\partial(\phi c + \sigma_s + \sigma_a)}{\partial t} + \alpha U \frac{\partial c}{\partial x} = 0 \quad (5)$$

where σ_a and σ_s are concentrations of attached and strained fines. The drift delay factor α accounts for slow particle motion.

Particle straining rate is proportional to the suspension flux, delivering particles to pores with the throats smaller than the particles (Herzig et al., 1970):

$$\frac{\partial \sigma_s}{\partial t} = \lambda \alpha U c \quad (6)$$

The proportionality coefficient λ , which is called the filtration coefficient, is equal to the particle capture probability per unit length of the particle trajectory.

Darcy equation accounts for permeability decline due to size exclusion of fine particles:

$$U = -\frac{k(\sigma_s)}{\mu} \frac{\partial p}{\partial x}, \quad k(\sigma_s) = \frac{k_0}{1 + \beta \sigma_s} \quad (7)$$

where k is the permeability as a function of strained particle concentration, β is the formation damage coefficient, k_0 is the initial permeability, μ is the viscosity of suspension and p is the pressure. The above expression for $k(\sigma_s)$ corresponds to the zero and first order Taylor expansion terms.

In the case of clean water injection into the core without initially strained fines, initial and boundary conditions are:

$$c(x, 0) = 0, \quad c(0, t) = 0, \quad \sigma_a(x, 0) = \sigma_{a0}, \quad \sigma_s(x, 0) = 0 \quad (8)$$

The path I → A → B → C in Fig. 3(a) corresponds to initial and boundary conditions (8), i.e. to the transition occurring during the injection of water with ionic strength γ_2 into the core with water ionic strength γ_1 . The diagram illustrates the ionic strength dependency of the attached particle concentration (see Eqs. (3) and (4)). Here, point I(0, σ_{a0}) corresponds to initial attached particle concentration. The attached particle concentration is given by the maximum retention function (3) and (4). The interval I → A corresponds to injection of water with the decreasing ionic strength without particle release. Further transition A → B ends up in release of the first particle with the injection of water with ionic strength γ_2 . Further ionic strength decrease down to γ_3 yields the release of attached particles with the amount $\Delta\sigma$, which is instantly suspended in the flowing water with concentration $\Delta\sigma/\phi$.

Let us consider sequential injections of water with ionic strength $\gamma_i (i = 1, 2, \dots)$. The suspended fines concentration due to particle release with ionic strength alteration from γ_{i-1} (during stage $i - 1$) to γ_i (during stage i) can be calculated from the variation of attached concentration:

$$\Delta c(x, t_i) = \phi^{-1} \{ \sigma_{cr}[\gamma(x, t_{i-1})] - \sigma_{cr}[\gamma(x, t_i)] \} = \phi^{-1} \Delta \sigma_a(\gamma_{i-1}, \gamma_i) \quad (9)$$

i.e. the initial suspended concentration after ionic strength alteration becomes $\Delta\sigma/\phi$. In Eq. (9), t_i corresponds to the moment of ionic strength alteration from γ_{i-1} to γ_i .

The amount of released particles $\Delta\sigma$ in Fig. 3(a) represents the difference between the values of the maximum retention function corresponding to ionic strengths from γ_{i-1} to γ_i . Eq. (9) implies that all mobilised particles are instantly removed into suspension.

Since the attaching electrostatic force depends on water ionic strength, different sized particles are mobilised at different stages, so the values of the drift delay factor $\alpha_i (i = 1, 2, \dots)$ also change from stage to stage. The same relates to filtration and formation damage coefficients.

Introduce the following dimensionless variables into the governing system ((3) and (5)–(8)):

$$S_a = \frac{\sigma_a}{\phi}, \quad S_s = \frac{\sigma_s}{\phi}, \quad \lambda_D = \lambda L, \quad t_D = \frac{1}{\phi L} \int_0^t U(y) dy, \quad x_D = \frac{x}{L}, \quad \alpha = \frac{U_s}{U} \quad (10)$$

where L is the core length and t_D is the injected water volume expressed in core pore volumes.

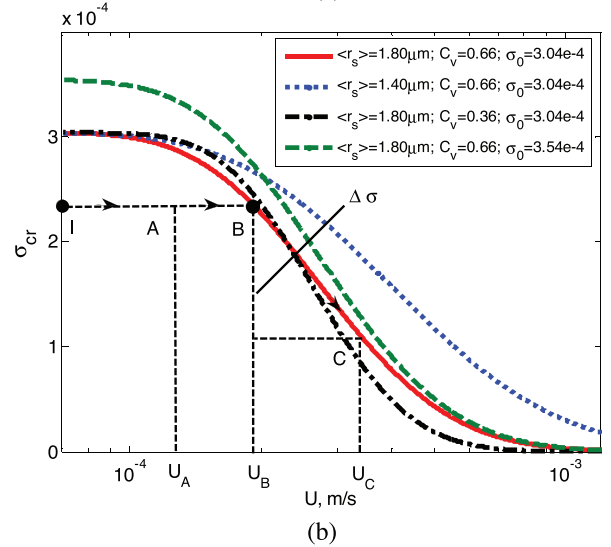
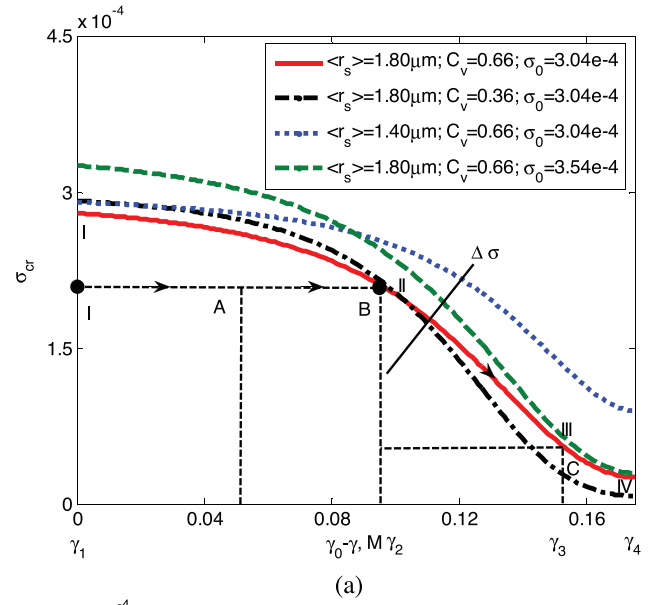


Fig. 3. The maximum retention concentration at different particle size distribution and maximum concentration value with: (a) ionic strength dependency, ionic strength values γ_1 – γ_4 correspond to four conditions applied in the laboratory test, $\gamma_0 = 0.2$ M NaCl; (b) velocity dependency (σ_{cr} : maximum retention concentration, U : velocity, $\langle r_s \rangle$: mean particle size, C_v : variance coefficient, σ_0 : initial concentration of attached particles). (For interpretation of the references to color in this figure citation, the reader is referred to the web version of this article.)

The dimensionless equations for the unknown suspended, strained and attached concentrations c_i , S_{si} and S_{ai} during stage i are obtained by substituting (10) into ((3) and (5)–(8)):

$$\frac{\partial (c_i + S_{si})}{\partial t_D} + \alpha_i \frac{\partial c_i}{\partial x_D} = 0 \quad (11)$$

$$\frac{\partial S_{si}}{\partial t_D} = \alpha_i \lambda_{Di} c_i \quad (12)$$

$$S_{ai}(x_D, t_D) = S_{cr}(\gamma_i) \quad (13)$$

$$c_i(x_D, t_{Di}) = c_{i-1}(x_D, t_{Di}) + \Delta S_a(\gamma_{i-1}, \gamma_i), \quad c_i(0, t_D) = 0, \quad S_{si}(x_D, t_{Di}) = S_{s,i-1}(x_D, t_{Di}) \quad (14)$$

The initial condition for c_i (the first equation in (14)) shows that the amount of particles, released at the moment t_{Di} when the

Table 1
Analytical model for fines mobilisation, migration and suspension.

Term	Notation	Expression
Suspended concentration during stage 1	$c_1(x_D, t_D)$	$\begin{cases} 0, & x_D \leq \alpha_1(t_D - t_{D1}) \\ \Delta S_a(\gamma_0, \gamma_1)e^{-\alpha_1 \lambda_{D1}(t_D - t_{D1})}, & x_D > \alpha_1(t_D - t_{D1}) \end{cases}$
Strained concentration during stage 1	$S_{s1}(x_D, t_D)$	$\begin{cases} \Delta S_a(\gamma_0, \gamma_1)(1 - e^{-\lambda_{D1} x_D}), & x_D \leq \alpha_1(t_D - t_{D1}) \\ \Delta S_a(\gamma_0, \gamma_1)(1 - e^{-\alpha_1 \lambda_{D1}(t_D - t_{D1})}), & x_D > \alpha_1(t_D - t_{D1}) \end{cases}$
Permeability during stage 1	$k_1(t_D)$	$\frac{k_0}{1 + \beta_1 \phi \int_0^1 S_{s1}(x_D, t_D) dx_D}$
Total suspended concentration during stage $i - 1$	$\int_0^1 c_{i-1}(x_D, t_{Di}) dx_D$	$\sum_{j=2}^i \left[(x_{D(i-1),j} - x_{D(i-1),j-1}) \Delta S_a(\gamma_{i-j}, \gamma_{i-j+1}) \prod_{n=i-j+1}^{i-1} Q_n \right]$
Cumulative breakthrough concentration during stage i	$\int_{t_{Di}}^{t_D} \alpha_i c_i(1, t_D) dt_D$	$\frac{1}{\lambda_{Di}} (1 - \exp[-\alpha_i \lambda_{Di}(t_D - t_{Di})]) \times \left\{ \Delta S_a(\gamma_{i-1}, \gamma_i) + \sum_{j=3}^{i+1} \left[\Delta S_a(\gamma_{i-j+1}, \gamma_{i-j+2}) \prod_{n=i-j+2}^{i-1} Q_n \right] \right\}$
Total suspended concentration during stage i	$\int_0^1 c_i(x_D, t_D) dx_D$	$\sum_{j=2}^{i+1} \left[(x_{Di,j} - x_{Di,j-1}) \Delta S_a(\gamma_{i-j+1}, \gamma_{i-j+2}) \prod_{n=i-j+2}^i Q_n \right]$
Total strained concentration during stage i	$\int_0^1 [S_{si}(x_D, t_D) - S_{s,i-1}(x_D, t_{Di})] dx_D$	$\Delta S_a(\gamma_{i-1}, \gamma_i) + \int_0^1 c_{i-1}(x_D, t_{Di}) dx_D - \left[\int_{t_{Di}}^{t_D} \alpha_i c_i(1, t_D) dt_D + \int_0^1 c_i(x_D, t_D) dx_D \right]$
Permeability during stage i	$k_i(t_D)$	$k_0 \left\{ \prod_{n=1}^i \left[1 + \beta_n \phi \int_0^1 (S_{sn}(x_D, t_D) - S_{s,n-1}(x_D, t_{Dn})) dx_D \right] \right\}^{-1}$

salinity switches from γ_{i-1} to γ_i , adds to the suspended concentration profile inherited from the injection of water with salinity γ_{i-1} .

System of four equations (7) and (11)–(13) subject to initial and boundary conditions (14) determines unknown suspended, attached and strained concentrations along with pressure during stage i . The system for concentrations (11)–(13) separates from Eq. (7) for pressure, i.e., the pressure is determined from Eq. (7) after the solution of system (11)–(13).

2.3. Analytical solution

Instant particle release with the following migration and straining is a linear hyperbolic problem allowing for exact solution. The explicit expressions for suspended and strained concentrations along with pressure drop across the core have been presented for the previously discussed case of $\alpha = 1$ (Bedrikovetsky et al., 2011, 2012). The derivations of the analytical model for $\alpha < 1$ are briefly presented in this section.

Suspended fines concentration is determined from Eqs. (11) and (12) using the method of characteristics (Tikhonov and Samarskii, 2013):

$$c_i(x_D, t_D) = \begin{cases} 0, & x_D \leq \alpha_i(t_D - t_{Di}) \\ [c_{i-1}(x_D, t_{Di}) + \Delta S_a(\gamma_{i-1}, \gamma_i)e^{-\alpha_i \lambda_{Di}(t_D - t_{Di})}], & x_D > \alpha_i(t_D - t_{Di}) \end{cases} \quad (15)$$

where $\alpha_i = dx_D/dt_D$ is the speed of the concentration front (Fig. 4(a) shows the first stage). Substituting (15) into straining rate equation (12) and integrating over time result in the formula for strained concentration (the second row in Table 1 shows the strained concentration for the first stage S_{s1}). The suspended concentration is equal to zero behind the front. The moment $1/\alpha_1$ corresponds to the arrival of the “last” released fine particle at the core outlet. Fig. 4(b) shows the three suspended concentration profiles at $t_D = 0$, at the moment t_{Da} before the front arrival at the core outlet and at the moment t_{Db} after the front arrival. The initial suspended concentration is ΔS_{a1} . Before the front arrival, the suspended concentration is equal to zero behind the front and is constant ahead of the front. This constant decreases with time; see (15). The suspended concentration becomes zero after the front arrival, since all particles become either strained or produced at the outlet. Three profiles of

strained concentration at moments 0, t_{Da} and t_{Db} are demonstrated in Fig. 4(c). There are no strained particles in rocks before fines mobilisation. The strained concentration grows with time until the front arrival and remains constant afterwards. The larger is the x_D , the longer is the stabilisation time and the higher is the maximum value of accumulated strained particles, therefore the strained profile grows as x_D increases. The profile is uniform ahead of the front since the particle advective flux is uniform and the particle capture probability is constant.

Suspended fines concentration during stage i is the sum of concentrations of particles inherited from all the previous stages by applying Eq. (15) to each stage:

$$c_{i,j}(x_D, t_D) = \begin{cases} 0, & j = 1 \\ \sum_{j=2}^{i+1} \left(\Delta S_a(\gamma_{i-j+1}, \gamma_{i-j+2}) \prod_{n=i-j+2}^i Q_n \right) & j > 1 \end{cases} \quad (16)$$

in which the function Q_n is defined as

$$Q_n(t_D) = e^{-\alpha_n \lambda_{Dn}(t_D - t_{Dn})} \quad (17)$$

As it follows from the particle population balance equation (11), the total strained concentration in porous media is equal to the initial suspended and strained concentrations at the beginning of stage i minus the total concentration of breakthrough particles and particles suspended in the core. Therefore, the total strained concentration is obtained as:

$$\int_0^1 S_{si}(x_D, t_D) dx_D = \underbrace{\Delta S_a(\gamma_{i-1}, \gamma_i) + \int_0^1 c_{i-1}(x_D, t_{Di}) dx_D + \int_0^1 S_{s,i-1}(x_D, t_{Di}) dx_D}_{\text{initial particles}} - \left[\underbrace{\int_{t_{Di}}^{t_D} \alpha_i c_i(1, t_D) dt_D}_{\text{breakthrough particles}} + \underbrace{\int_0^1 c_i(x_D, t_D) dx_D}_{\text{suspended particles}} \right] \quad (18)$$

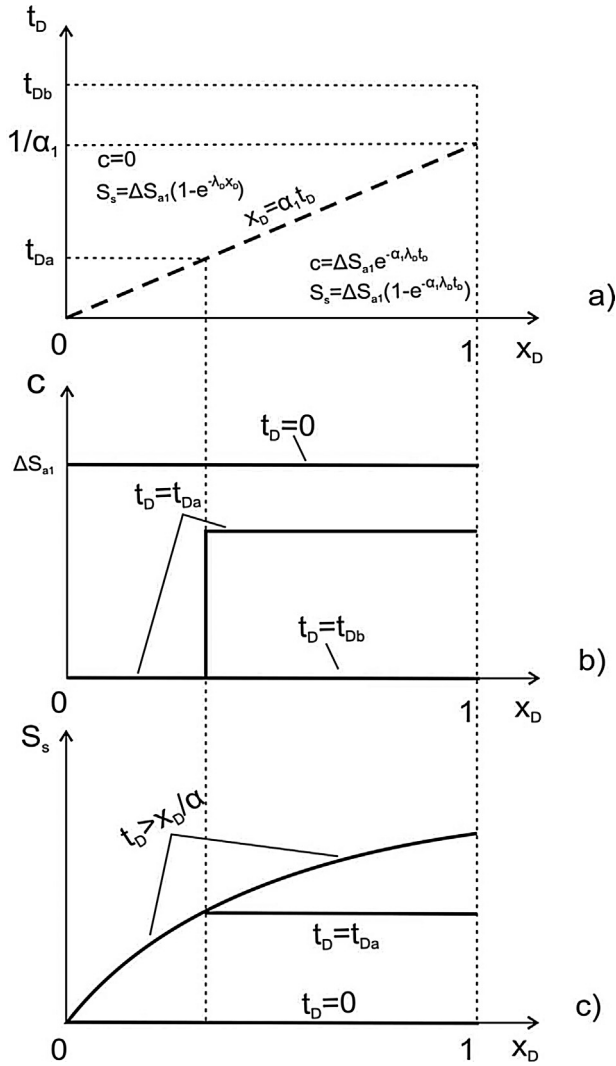


Fig. 4. Solution of fines migration problem under elevated velocity: (a) trajectory of fronts and characteristic lines in (x_D, t_D) plane; (b) suspended concentration profiles in three moments; (c) strained concentration profiles in three moments (c: concentration of suspended particles, S_s : concentration of strained particles, α : drift delay factor, λ : filtration coefficient).

where

$$\int_0^1 c_{i-1}(x_D, t_{Di}) dx_D = \sum_{j=2}^i \left[(x_{D(i-1),j} - x_{D(i-1),j-1}) \Delta S_a(\gamma_{i-j}, \gamma_{i-j+1}) \prod_{n=i-j+1}^{i-1} Q_n \right] \quad (19)$$

represents the total suspended concentration along the core at the end of stage $i-1$. This term together with the mobilised particle concentration at the beginning of stage i provides the total initial suspended concentration for stage i . The cumulative breakthrough concentration during stage i and the total suspended concentration along the core during stage i are obtained by substituting Eq. (16) into the last two terms of (18):

$$\int_{t_{Di}}^{t_D} \alpha_i c_i(1, t_D) dt_D = \frac{1}{\lambda_{Di}} \left\{ 1 - \exp[-\alpha_i \lambda_{Di} (t_D - t_{Di})] \right\} \left\{ \Delta S_a(\gamma_{i-1}, \gamma_i) + \sum_{j=3}^{i+1} \left[\Delta S_a(\gamma_{i-j+1}, \gamma_{i-j+2}) \prod_{n=i-j+2}^{i-1} Q_n \right] \right\} \quad (20)$$

$$\int_0^1 c_i(x_D, t_D) dx_D = \sum_{j=2}^{i+1} \left[(x_{Di,j} - x_{Di,j-1}) \Delta S_a(\gamma_{i-j+1}, \gamma_{i-j+2}) \prod_{n=i-j+2}^i Q_n \right] \quad (21)$$

The permeability as a function of time during stage i is expressed from the second equation of (7), accounting for permeability decline history at each stage:

$$k_i(t_D) = k_{i-1} \left\{ 1 + \beta_i \phi \int_0^1 [S_{si}(x_D, t_D) - S_{s,i-1}(x_D, t_{Di})] dx_D \right\}^{-1} = k_0 \left\{ \prod_{n=1}^i \left[1 + \beta_n \phi \int_0^1 (S_{sn}(x_D, t_D) - S_{s,n-1}(x_D, t_{Dn})) dx_D \right] \right\}^{-1} \quad (22)$$

where $\int_0^1 [S_{si}(x_D, t_D) - S_{s,i-1}(x_D, t_{Di})] dx_D$ is the total strained concentration along the core during stage i , calculated from Eq. (18).

The formulae in the analytical model are summarised in Table 1. The suspended concentration during stage 1 is c_1 , as obtained from Eq. (15) by letting $i = 1$ (see the first row in Table 1). Substituting c_1 into Eq. (12) and integrating over t_D result in strained concentration S_{s1} at stage 1 (see the second row in Table 1). Permeability k_1 during stage 1 is then calculated from (22) and listed in the third row of Table 1. Integrating suspended concentration at the end of the previous stage $i-1$ over the core length $\int_0^1 c_{i-1}(x_D, t_{Di}) dx_D$ delivers the total suspended concentration inherited from stage $i-1$ (the fourth row in Table 1). Cumulative breakthrough concentration during stage i is obtained from Eq. (20) as $\int_{t_{Di}}^{t_D} \alpha_i c_i(1, t_D) dt_D$ (the fifth row in Table 1). The total suspended concentration during stage i is calculated from Eq. (21) as $\int_0^1 c_i(x_D, t_D) dx_D$ (the sixth row in Table 1). The seventh row in Table 1 presents the total strained concentration during stage i , $\int_0^1 [S_{si}(x_D, t_D) - S_{s,i-1}(x_D, t_{Di})] dx_D$, resulting from Eq. (18). Permeability k_i during stage i is calculated from (22) and listed in the last row of Table 1.

3. Treatment of experimental data

The analytical model presented in Section 2.3 is applied to the treatment of experimental data obtained from the coreflood test with piecewise decreasing ionic strength (see the paper by You et al. (2014) for details of the laboratory procedure). The core is taken from Ladbroke Grove formation, which has the rock properties analogous to that in Salamander geothermal field (Badalyan et al., 2014). The following experimental procedures have been applied to the sandstone core with porosity 17.2%, permeability 5.46 mD and length 6.33 cm:

- The core is evacuated down to 1.5 Pa and saturated with 0.6 M NaCl solution;
- The core is placed inside the high-pressure core holder with overburden pressure of 1000 psi;
- 0.6 M NaCl solution is pumped through the core with velocity of 1.4×10^{-4} m/s until the stabilisation of rock permeability, within experimental uncertainty, is reached;
- Effluent samples are collected, particle concentration and size distribution are measured by PAMAS S4031 GO portable particle counter (PAMAS GmbH, Salzuflen, Germany);

Table 2
Values of the model tuning parameters in the coreflood test.

Parameter	Value
r_s (μm)	1.80
C_v	0.66
σ_0	$3.04\text{e}-4$
α_1	$4.10\text{e}-3$
α_2	$2.96\text{e}-3$
α_3	$2.81\text{e}-3$
α_4	$2.74\text{e}-3$
β_1	9793
β_2	7631
β_3	7391
β_4	7158
λ_{D1}	67.14
λ_{D2}	53.79
λ_{D3}	51.11
λ_{D4}	50.13

- Ionic strength is decreased to 0.4 M NaCl and the above procedure is repeated;
- Coreflood tests are performed using water with ionic strengths 0.2, 0.1, 0.05 and 0.025 M NaCl.

The experimental data are presented in Fig. 2. The test started by injection of high salinity water with 0.6 M and 0.4 M NaCl, which is not shown in Fig. 2a. The permeability was observed to remain constant, defined as the initial permeability k_0 . The experimental data of permeability decline history (black circles in Fig. 2(a)) and particle concentration at the outlet (black points in Fig. 2(b)) are used for model tuning. The lognormal form for the particle size distribution is assumed. The method for calculation of the maximum retention function for monolayer of size distributed particles is given by You et al. (2014). The method includes determination of the minimum particle radius r_{scr} mobilised by the injected water with ionic strength γ , from the torque balance equation. So, the particles smaller than r_{scr} remain attached to the rock surface. Therefore, the maximum retention concentration is the total concentration of initially attached particles with radii smaller than $r_{scr}(\gamma)$.

The tuning parameters are: mean particle size $\langle r_s \rangle$, variance coefficient for particle size distribution C_v , drift delay factor α , formation damage coefficient β and filtration coefficient λ . The lower is the injected ionic strength, the smaller particles are mobilised. We assume constant particle radius of mobilised fines at each stage. Therefore, the drift delay factor, formation damage coefficient and filtration coefficient are constant for each stage. Least square goal function of deviation between the model predicted and measured data is used in the model tuning procedure. The Levenberg–Marquardt minimisation algorithm has been applied (Marquardt, 1963). The obtained values of tuning parameters are listed in Table 2. The optimised permeability and outlet concentration curves from modelling are shown as red curves in Fig. 2(a) and (b), respectively. Good agreement is observed between the measured data and model prediction for both permeability and outlet concentration results (the coefficient of determination is $R^2 = 0.998$ for permeability data and $R^2 = 0.943$ for outlet concentration data), which validates the proposed model.

Sensitivity analysis with respect to the three main parameters in the model is presented in Fig. 2(a) and (b). Increase of the drift delay factor α decreases the stabilisation time due to faster movement of particles (see the blue dashed curve in Fig. 2(a)). The smaller filtration coefficient λ corresponds to lower particle capture probability, which leads to longer stabilisation time (light blue dash-dot curve in Fig. 2(a)). The larger formation damage coefficient β causes greater permeability decline over time (green dashed curve in Fig. 2(a)). Fig. 2(b) shows that only the filtration coefficient λ has significant effect on breakthrough particle concentration because

it directly characterises the capture probability of released particles. Decrease of filtration coefficient λ yields higher breakthrough concentration (light blue curve). The effect of the drift delay factor α on breakthrough concentration is negligible, since the concentration of breakthrough particles is much lower than the released particle concentration $\Delta\sigma_i$ from the laboratory test, which means that the breakthrough concentration is insensitive to α (blue curve). Formation damage coefficient β does not affect the breakthrough concentration (green curve).

To address the uniqueness of the fitting parameters, we searched in 20% neighbourhood of the optimal point \mathbf{x}_0 , $\mathbf{x}_0 = (\langle r_s \rangle, C_v, \alpha, \beta, \lambda)$, i.e. “initial guess points” for iterative minimisation were set as $1.1\mathbf{x}_0$ and $0.9\mathbf{x}_0$. So, 10 runs of the optimisation algorithm were performed. All runs converge to the point \mathbf{x}_0 , i.e. the minimum is unique in its 20%-neighbourhood. The coefficient of determination R^2 is lower in all initial guess points than that at the optimal point. To conclude, the obtained optimum is unique in its 20%-neighbourhood. The most sensitive parameters with respect to permeability are the mean particle size $\langle r_s \rangle$ and formation damage coefficient β , while the breakthrough concentration is more sensitive to the filtration coefficient λ .

The orange curve corresponds to the geothermal temperature of the Salamander field; other curves are obtained based on the experimental data (Fig. 2).

The obtained values of filtration and formation damage coefficients (Table 2) are located inside the common intervals of these parameters (Nabzar and Chauveteau, 1997; Pang and Sharma, 1997; Sharma et al., 2000; Civan, 2007).

Fig. 3(a) presents the ionic strength dependency of the maximum retention concentration σ_{cr} calculated from the size distributed monolayer particle model. Red curve corresponds to the tuned values of mean radius and variance coefficient of the attached particle size distribution (Table 2). The maximum retention concentration decreases as ionic strength decreases.

Drag force exerting on fines is proportional to the square of particle size, while the particle-size dependency of electrostatic force is significantly weaker (Khilar and Fogler, 1998; Israelachvili, 2011). Therefore, $r_{scr}(\gamma)$ is a monotonically decreasing function and the particles are mobilised in decreasing order of their sizes with the decrease of ionic strength.

The smaller variance coefficient corresponds to the narrower size distribution of fines. The fraction of large particles is higher for curve with larger variance coefficient. Therefore, the smaller is the variance coefficient, the larger is the maximum retention concentration at high ionic strength (black dash-dot curve in Fig. 3(a)). The maximum retention concentration decreases as the variance coefficient decreases at low ionic strength.

The smaller mean particle size yields higher small particle fraction in the overall particle size distribution, resulting in higher maximum retention concentration (blue dotted curve). The higher σ_0 leads to the higher σ_{cr} at the given ionic strength (green dashed curve).

For the case of monolayer of size distributed attached particles, the size distribution function can be determined from the maximum retention function. Taking derivatives of both sides of Eq. (4) allows expressing the attached concentration distribution $\Sigma_a(r_s)$ via σ_{cr} . However, the resulting formula includes derivative of the experimentally determined function and, therefore, represents an ill-posed solution of the inverse problem (Tikhonov and Samarskii, 2013). Here, we determine a well-posed solution assuming lognormal size distribution for attached particles and define the mean particle size and standard deviation for this distribution by least-square fitting. Size distribution of attached particles obtained from the monolayer particle model is shown in Fig. 5. The fitted curve corresponds to the mean particle size $1.80 \mu\text{m}$ and the variance coefficient 0.66 (Table 2). Axis of abscissa presents the four

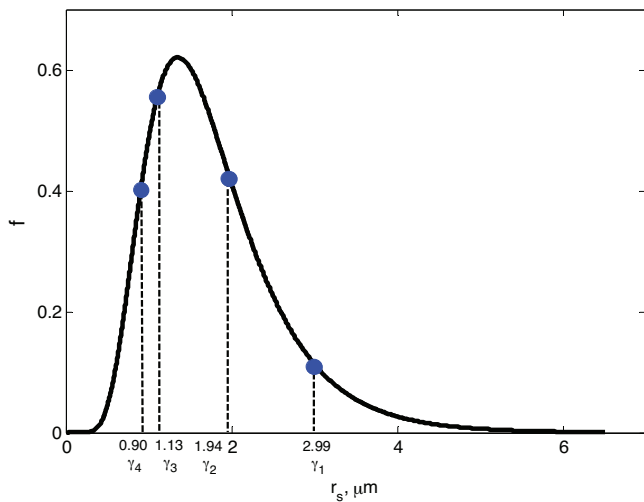


Fig. 5. Size distribution of movable particles obtained from the model (r_s : particle size, f : size distribution function, γ : ionic strength).

critical particle radii corresponding to the four ionic strength values $\gamma_1 \sim \gamma_4$ applied in the coreflood test with piecewise decreasing ionic strength. The critical size of mobilised fines decreases with the reduction of ionic strength from stage 1 to stage 4 (Fig. 5), resulting in the simultaneous decrease of drift delay factor α , formation damage coefficient β and filtration coefficient λ during the test (Table 2).

After calculation of the size distribution $\Sigma_a(r_s)$ for attached particles, we translate the maximum retention concentration as an ionic strength function $\sigma_{cr}(U_0, \gamma)$, into the velocity dependency of the maximum retention concentration $\sigma_{cr}(U_0, \gamma)$. The procedure is described in Section 2.3. The curve $\sigma_{cr}(U_0, \gamma)$ as obtained by the model fitting is shown in Fig. 3(a) in red; the translated curve $\sigma_{cr}(U_0, \gamma)$ is given in Fig. 3(b) in red as well.

The permeability impairment due to fines migration under different temperatures can be estimated by the second equation in (7) using the maximum retention function. Fig. 6 shows dimensionless permeability versus flow velocity (Fig. 6(a)) and ionic strength (Fig. 6(b)) during fines migration at different temperatures. The elevated temperature results in the reduction of electrostatic attaching force (Schembre and Kovscek (2005) have shown it for the conditions of steam-flooding in oilfields; Rosenbrand et al. (2012) reported this effect for kaolinite–quartz interaction in geothermal reservoirs); it also yields decrease of detaching forces due to reduction of fluid viscosity (García et al., 2006; Rosenbrand et al., 2015). Domination of the temperature effect on the electrostatic attaching force reduction leads to the maximum retention concentration as a decreasing function of temperature. Consequently, the higher is the temperature, the larger is the permeability decline during fines migration (Fig. 6(a) and (b)). Weakened electrostatic attaching force at geothermal reservoir temperature $T=129^\circ\text{C}$ of the Salamander field and ionic strength γ below 0.2 M NaCl lead to nearly complete fines detachment (orange curve in Fig. 2(b)). Therefore, the maximum retention concentration approaches zero, causing the permeability reduction to a constant level throughout the range of $\gamma \leq 0.2$ M NaCl (orange curve in Fig. 2(a) and black dashed curve in Fig. 6(b)).

4. Discussions

The mathematical model derived in the present work has some limitations (see the assumptions in Section 2.1). The filtration and formation damage coefficients are considered to be constant, which corresponds to small retention concentration. For the case of high

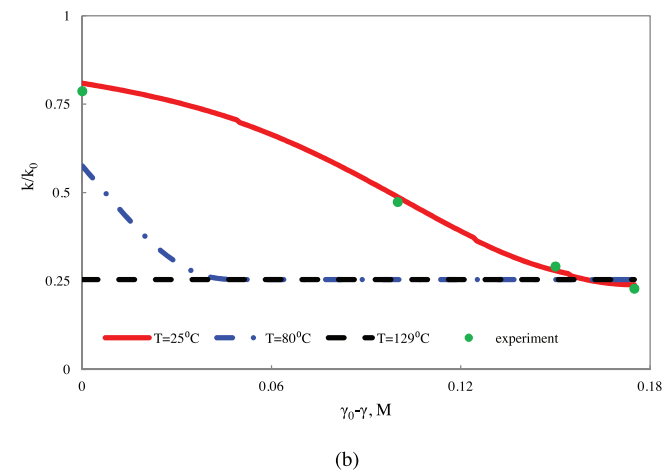
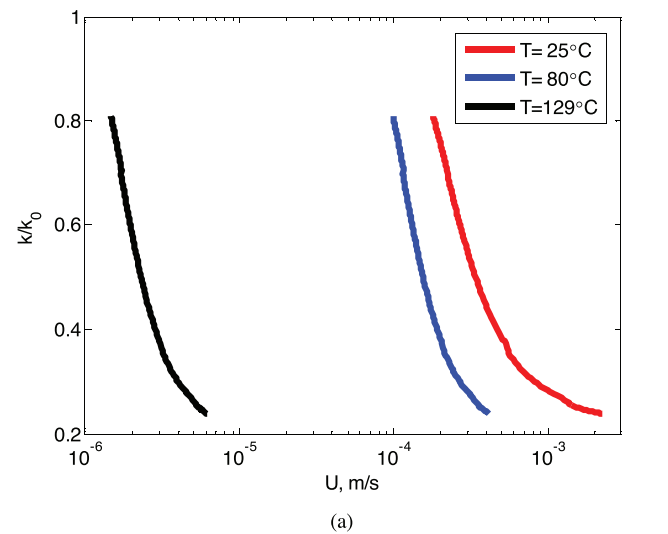


Fig. 6. Temperature effect on rock permeability due to fines migration: (a) velocity dependency; (b) ionic strength dependency (k : permeability, U : velocity, γ : ionic strength, T : temperature).

concentration of retained particles, the retention–concentration-dependent filtration and formation damage functions must be considered.

The laboratory data presented show an instant permeability response to abrupt ionic strength variation. The same phenomenon has been observed in several other studies (Ochi and Vernoux, 1998; Bedrikovetsky et al., 2012). However, some studies report the significant delay between the ionic strength alteration and fines mobilisation. It is explained by slow diffusion of the injected water into the contact area between the matrix surface and the fine particle, where both are deformed by attractive electrostatic force. It is important to understand which physical phenomena are responsible for the difference between two cases.

In the present work, the model for monolayer of size distributed attached fine particles has been considered. The previously derived equation for multilayers of mono sized particles has not been used in the present study, since it exhibits a convex form of the maximum retention function, while the experimental data indicate that the form is not convex (Fig. 3). However, both models are simplified versions of the multilayer of size distributed particles. Derivation of the maximum retention function for the latter case would enrich the mathematical model for fines migration in geothermal fields.

The two-speed model by Yuan and Shapiro (2011) and Bradford et al. (2012) describes particle detachment and transport in more details than the single velocity model, see Eqs. (11)–(13). In

reality, the model (11)–(13) is a particular case of the two-speed model, describing only the particles that drift near to pore walls and assuming zero concentration of the particles suspended in the bulk of carrier water. This case corresponds to low velocity of the carrier fluid, where the detaching force is not sufficient to deliver the mobilised particles into the bulk stream.

The two-speed model contains six kinetics coefficients of mass exchange between the attached particles, the slowly drifting particles near to pore walls and the fast moving particles transported within the bulk of carrier fluid. It is important to find out whether breakthrough concentration curve along with the pressure drop is enough to tune all the model parameters. If not, more sophisticated measurements should be performed: post-mortem measurements of retained profile using chemical analysis, “fast” CT-scanning as applied during the injection where the scanner moves along the core, measurements of pressure drop in the intermediate core points, suspension sampling in the intermediate ports, etc.

The effect of increased temperature on permeability reduction has been reported by several authors and is attributed mostly to fines mobilisation (Khalil and Fogler, 1998; Rosenbrand et al., 2014, 2015). See the detailed analysis of published experimental data in Rosenbrand and Fabricius (2012). These results support the conclusion of the present work that natural reservoirs with elevated temperatures are more susceptible to fines-migration-induced formation damage.

The analytical model shows that the temperature increase yields significant increase in the permeability impairment due to fines mobilisation, migration and subsequent size exclusion. As it follows from this statement, geothermal fields are more susceptible to fines migration with consequent well productivity impairment than conventional aquifers or oilfields. The phenomenon is explained by two competitive effects of temperature increase on fines mobilisation. On the one side, the increase in the reservoir temperature yields decrease of the maximum retention function due to the decrease of electrostatic attaching force. On the other side, the temperature increase also leads to the decrease of fluid viscosity, which results in the reduction of detaching drag and lifting forces, and resultantly, the maximum retention function increase. So, the maximum retention function is determined by these two competitive effects. Implementation of the laboratory-based temperature dependencies of electrostatic constant and water viscosity with corresponding modelling shows that the temperature effect on electrostatic constants dominates over the viscosity effect. Domination of the temperature effect on electrostatic attaching force results in the maximum retention function decrease and permeability reduction increase during the temperature rise. Therefore, the orange curve of permeability decline during fines mobilisation at elevated temperature of the Salamander geothermal field in Fig. 2(a) is located below the other curves, which are obtained at lower temperatures. Finally, the temperature increase from ambient conditions ($T=25^{\circ}\text{C}$) to typical geothermal reservoir conditions ($T=129^{\circ}\text{C}$) yields decrease in maximum retention function nearly to zero and consequent significant permeability decline.

The permeability-damage sensitivity to the physical parameters (r_s), C_v , β , λ and γ presented in Section 3, implies different production well behaviour in geothermal reservoirs with different rock and fluid properties. The rock permeability decline is greater for larger particles and higher formation damage coefficient. The larger is the jamming ratio (between mean particle and pore radii), the higher is the formation damage coefficient. The mean pore radius has the order of magnitude $(k/\phi)^{1/2}$. So, larger values of dimensionless group $r_s(k/\phi)^{-1/2}$ yield higher susceptibility of the reservoir to fines-migration-induced formation damage. The lower is the ionic strength of the reservoir brine, the smaller is the maximum retention concentration, the larger is the amount of mobilised fine

particles and more severe is the formation damage in production wells.

The experimental procedure applied in the present study can be significantly improved. As it is concluded from the history matching of experimental data (Section 3), the rock permeability is sensitive mostly to mean particle size and formation damage coefficient, while the breakthrough concentration is most sensitive to filtration coefficient. The online measurements of particle concentration and size distribution in the effluent fluid enhance the accuracy of mean particle size and filtration coefficient estimation, while the computed tomography (CT) scan of the particle retention profile allows for more accurate determination of the formation damage coefficient (Mays and Hunt, 2005, 2007). However, in this case the population balance model must be used for the parameter tuning (Sharma and Yortsos, 1987a,b; Bedrikovetsky, 2008; Yuan et al., 2013).

5. Conclusions

Modification of the basic equations for fines migration by introducing the drift delay factor and a new form of maximum retention function for size-distributed fine particles, analytical modelling of one-dimensional flows and matching the laboratory coreflood data allow drawing the following conclusions:

- Analytical model for fines mobilisation, migration and straining yields the explicit formulae for suspended and strained concentrations, and permeability along the core;
- Large permeability stabilisation periods during fines migration can be explained by slow motion of released rolling or sliding particles; introduction of the drift delay factor allows for the permeability history matching;
- Good match between the laboratory measured and model predicted permeability has been observed, while the agreement for particle outlet concentration data is just qualitative;
- Size distribution of attached particles can be determined from the maximum retention function;
- Modelling-based predictions for high temperature geothermal conditions show that the maximum retention concentration decreases with temperature, yielding more severe permeability damage if compared with conventional aquifers and petroleum reservoirs.

Acknowledgements

Financial supports from the Australian Research Council (ARC) Discovery Project 1094299, ARC Linkage Projects 100100613 and 110200799, the Australian Renewable Energy Agency (ARENA), and the South Australian Centre for Geothermal Energy Research (SACGER) are gratefully acknowledged. Drs. Ulrike Schacht and Themis Carageorgos (University of Adelaide) are gratefully acknowledged for fruitful co-operation.

References

- Aragón-Aguilar, A., Barragán-Reyes, R.M., Arellano-Gómez, V.M., 2013. Methodologies for analysis of productivity decline: a review and application. *Geothermics* 48, 69–79.
- Badalyan, A., Carageorgos, T., You, Z., Schacht, U., Bedrikovetsky, P., Matthews, C., Hand, M., 2014. A new experimental procedure for formation damage assessment in geothermal wells. In: Proceedings, Thirty-Ninth Workshop on Geothermal Reservoir Engineering. Stanford University, California, USA.
- Baudracco, J., 1990. Variations in permeability and fine particle migrations in unconsolidated sandstones submitted to saline circulations. *Geothermics* 19, 213–221.
- Baudracco, J., Aoubouazza, M., 1995. Permeability variations in Berea and Vosges sandstone submitted to cyclic temperature percolation of saline fluids. *Geothermics* 24, 661–677.
- Bedrikovetsky, P.G., 1993. *Mathematical Theory of Oil & Gas Recovery*. Kluwer Academic Publishers, London/Boston/Dordrecht.

- Bedrikovetsky, P., 2008. Upscaling of stochastic micro model for suspension transport in porous media. *Transp. Porous Media* 75 (3), 335–369.
- Bedrikovetsky, P., Siqueira, F.D., Furtado, C.A., Souza, A.L.S., 2011. Modified particle detachment model for colloidal transport in porous media. *Transp. Porous Media* 86, 353–383.
- Bedrikovetsky, P., Zeinijahromi, A., Siqueira, F.D., Furtado, C.A., de Souza, A.L.S., 2012. Particle detachment under velocity alternation during suspension transport in porous media. *Transp. Porous Media* 91, 173–197.
- Bradford, S.A., Torkzaban, S., Kim, H., Simunek, J., 2012. Modeling colloid and microorganism transport and release with transients in solution ionic strength. *Water Resour. Res.* 48, W09509.
- Bradford, S.A., Torkzaban, S., Shapiro, A.A., 2013. A theoretical analysis of colloid attachment and straining in chemically heterogeneous porous media. *Langmuir* 29, 6944–6952.
- Chauveteau, G., Nabzar, L., Coste, J.P., 1998. Physics and modeling of permeability damage induced by particle deposition. In: *Proceedings – SPE International Symposium on Formation Damage Control*, pp. 409–419.
- Civan, F., 2007. *Reservoir Formation Damage: Fundamentals, Modeling, Assessment, and Mitigation*, 2nd ed. Gulf Publishing Company, Houston, Texas.
- Cortis, A., Harter, T., Hou, L., Atwill, E.R., Packman, A.I., Green, P.G., 2006. Transport of *Cryptosporidium parvum* in porous media: long-term elution experiments and continuous time random walk filtration modeling. *Water Resour. Res.* 42, W12S13.
- Derjaguin, B.V., Landau, L., 1941. Theory of the stability of strongly charged lyophobic sols and of the adhesion of strongly charged particles in solutions of electrolytes. *Acta Phys. Chem. (URSS)* 14, 633–662.
- Freitas, A.M., Sharma, M.M., 2001. Detachment of particles from surfaces: an AFM study. *J. Colloid Interface Sci.* 233, 73–82.
- García-García, S., Jonsson, M., Wold, S., 2006. Temperature effect on the stability of bentonite colloids in water. *J. Colloid Interface Sci.* 298, 694–705.
- Ghassemi, A., Zhou, X., 2011. A three-dimensional thermo-poroelastic model for fracture response to injection/extraction in enhanced geothermal systems. *Geothermics* 40, 39–49.
- Herzig, J.P., Leclerc, D.M., Legoff, P., 1970. Flow of suspensions through porous media – application to deep filtration. *Ind. Eng. Chem.* 62, 8–35.
- Israelachvili, J.N., 2011. *Intermolecular and Surface Forces*, 3rd ed. Elsevier, Amsterdam, The Netherlands.
- Jaya, M.S., Shapiro, S.A., Kristinsdottir, L.H., Bruhn, D., Milsch, H., Spangenberg, E., 2010. Temperature dependence of seismic properties in geothermal rocks at reservoir conditions. *Geothermics* 39, 115–123.
- Jiao, D., Sharma, M.M., 1994. Mechanism of cake buildup in crossflow filtration of colloidal suspensions. *J. Colloid Interface Sci.* 162, 454–462.
- Khiyar, K.C., Fogler, H.S., 1998. *Migrations of Fines in Porous Media*. Kluwer Academic Publishers, Dordrecht, The Netherlands.
- Kristinsdottir, L.H., Flovenz, O.G., Arnason, K., Bruhn, D., Milsch, H., Spangenberg, E., Kulenkampff, J., 2010. Electrical conductivity and P-wave velocity in rock samples from high-temperature Icelandic geothermal fields. *Geothermics* 39, 94–105.
- Lever, A., Dawe, R.A., 1984. Water-sensitivity and migration of fines in the Hopeman Sandstone (Scotland). *J. Pet. Geol.* 7, 97–107.
- Logan, J.D., 2001. *Transport Modeling in Hydrogeochemical Systems*. Springer, New York.
- Marquardt, D., 1963. An algorithm for least-squares estimation of nonlinear parameters. *J. Soc. Ind. Appl. Math.* 11, 431–441.
- Mays, D., Hunt, J., 2005. Hydrodynamic aspects of particle clogging in porous media. *Environ. Sci. Technol.* 39, 577–584.
- Mays, D., Hunt, J., 2007. Hydrodynamic and chemical factors in clogging by montmorillonite in porous media. *Environ. Sci. Technol.* 41, 5666–5671.
- Milsch, H., Kristinsdottir, L.H., Spangenberg, E., Bruhn, D., Flovenz, O.G., 2010. Effect of the water-steam phase transition on the electrical conductivity of porous rocks. *Geothermics* 39, 106–114.
- Miranda, R.M., Underdown, D.R., 1993. Laboratory measurement of critical rate: a novel approach for quantifying fines migration problems. In: *SPE Production Operations Symposium*, 21–23 March. Society of Petroleum Engineers, Oklahoma, OK.
- Nabzar, L., Chauveteau, G., 1997. Permeability damage by deposition of colloidal particles. In: *SPE – European Formation Damage Control Conference*, Proceedings, pp. 161–168.
- Ochi, J., Vernoux, J.F., 1998. Permeability decrease in sandstone reservoirs by fluid injection: hydrodynamic and chemical effects. *J. Hydrol.* 208, 237–248.
- Oliveira, M., Vaz, A., Siqueira, F., Yang, Y., You, Z., Bedrikovetsky, P., 2014. Slow migration of mobilised fines during flow in reservoir rocks: laboratory study. *J. Pet. Sci. Eng.* 122, 534–541.
- Pang, S., Sharma, M.M., 1997. A model for predicting injectivity decline in water-injection wells. *SPE Form. Eval.* 12, 194–201.
- Priisholm, S., Nielsen, B.L., Haslund, O., 1987. Fines migration, blocking, and clay swelling of potential geothermal sandstone reservoirs, Denmark. *SPE Form. Eval.* 2, 168–178.
- Rahman, S.S., Arshad, A., Chen, H., 1994. Prediction of critical condition for fines migration in petroleum reservoirs. In: *SPE Asia Pacific Oil and Gas Conference, Society of Petroleum Engineers, Melbourne, Australia*, 7–10 November.
- Rosenbrand, E., Fabricius, I.L., 2012. Effect of hot water injection on sandstone permeability: an analysis of experimental literature. In: *SPE Europec/EAGE Annual Conference*, Copenhagen, Denmark.
- Rosenbrand, E., Fabricius, I.L., Kets, F., 2013. Kaolinite mobilisation in sandstone: pore plugging vs suspended particles. In: *Proceedings, Thirty-Eighth Workshop on Geothermal Reservoir Engineering*, Stanford University, CA, USA.
- Rosenbrand, E., Fabricius, I.L., Yuan, H., 2012. Thermally induced permeability reduction due to particle migration in sandstones: the effect of temperature on kaolinite mobilisation and aggregation. In: *Proceedings, Thirty-Seventh Workshop on Geothermal Reservoir Engineering*, Stanford University, California, USA.
- Rosenbrand, E., Haugwitz, C., Jacobsen, P.S.M., Kjølner, C., Fabricius, I.L., 2014. The effect of hot water injection on sandstone permeability. *Geothermics* 50, 155–166.
- Rosenbrand, E., Kjølner, C., Riis, J.F., Kets, F., Fabricius, I.L., 2015. Different effects of temperature and salinity on permeability reduction by fines migration in Berea sandstone. *Geothermics* 53, 225–235.
- Rousseau, D., Hadi, L., Nabzar, L., 2008. Injectivity decline from produced-water reinjection: new insights on in-depth particle-deposition mechanisms. *SPE Prod. Oper.* 23, 525–531.
- Schechter, R.S., 1992. *Oil Well Stimulation*. Prentice Hall, Englewood Cliffs, NJ.
- Schembre, J.M., Kovscek, A.R., 2005. Mechanism of formation damage at elevated temperature. *J. Energy Resour. Technol.* ASME 127, 171–180.
- Schijven, J.F., Hassanzadeh, S.M., 2000. Removal of viruses by soil passage: overview of modeling, processes, and parameters. *Crit. Rev. Environ. Sci. Technol.* 30, 49–127.
- Sefrioui, N., Ahmadi, A., Omari, A., Bertin, H., 2013. Numerical simulation of retention and release of colloids in porous media at the pore scale. *Colloids Surf. A: Physicochem. Eng. Asp.* 427, 33–40.
- Shapiro, A.A., 2007. Elliptic equation for random walks. Application to transport in microporous media. *Phys. A: Stat. Mech. Appl.* 375, 81–96.
- Shapiro, A.A., Wesselingh, J.A., 2008. Gas transport in tight porous media. *Gas kinetic approach*. *Chem. Eng. J.* 142, 14–22.
- Shapiro, A.A., Yuan, H., 2013. Application of stochastic approaches to modeling suspension flow in porous media. In: Skogseid, A., Fasano, V. (Eds.), *Statistical Mechanics and Random Walks: Principles, Processes and Applications*. Nova Science Publishers, Inc., New York, USA, pp. 1–38.
- Sharma, M.M., Pang, S., Wennberg, K.E., Morgenthaler, L.N., 2000. Injectivity decline in water-injection wells: an offshore gulf of Mexico case study. *SPE Prod. Facil.* 15, 6–13.
- Sharma, M.M., Yortsos, Y.C., 1987a. Transport of particulate suspensions in porous media: model formulation. *AIChE J.* 33, 1636–1643.
- Sharma, M.M., Yortsos, Y.C., 1987b. Fines migration in porous media. *AIChE J.* 33, 1654–1662.
- Tikhonov, A.N., Samarskii, A.A., 2013. *Equations of Mathematical Physics*. Dover Publications.
- Tufenkji, N., 2007. Colloid and microbe migration in granular environments: a discussion of modelling methods. In: Frimmel, F.H., von der Kammer, F., Flemming, H.-C. (Eds.), *Colloidal Transport in Porous Media*. Springer, Berlin, Germany, pp. 119–142.
- Tufenkji, N., Elimelech, M., 2004. Correlation equation for predicting single-collector efficiency in physicochemical filtration in saturated porous media. *Environ. Sci. Technol.* 38, 529–536.
- Verwey, E.J.W., Overbeek, J.T.G., 1948. *Theory of the Stability of Lyophobic Colloids*. Elsevier, Amsterdam.
- You, Z., Badalyan, A., Bedrikovetsky, P., 2013. Size-exclusion colloidal transport in porous media – stochastic modeling and experimental study. *SPE J.* 18, 620–633.
- You, Z., Badalyan, A., Yang, Y., Bedrikovetsky, P., Hand, M., 2014. Laboratory study of fines migration in geothermal reservoirs. *Geothermics* (submitted for publication).
- Yuan, H., Shapiro, A.A., 2011. A mathematical model for non-monotonic deposition profiles in deep bed filtration systems. *Chem. Eng. J.* 166, 105–115.
- Yuan, H., Shapiro, A.A., 2012. Colloid transport and retention: recent advances in colloids filtration theory. In: Ray, P.C. (Ed.), *Colloids: Classification, Properties and Applications*. Nova Science Publishers, Inc., New York, USA, pp. 201–242.
- Yuan, H., You, Z., Shapiro, A., Bedrikovetsky, P., 2013. Improved population balance model for straining-dominant deep bed filtration using network calculations. *Chem. Eng. J.* 226, 227–237.

5 Laboratory-based mathematical modelling of graded proppant injection in CBM reservoirs

Keshavarz, A., **Yang, Y.**, Badalyan, A., Johnson, R., Bedrikovetsky, P.

International Journal of Coal Geology, 136 (2014) 1-16

Statement of Authorship

Title of Paper	Laboratory-based mathematical modelling of graded proppant injection in CBM reservoirs
Publication Status	<input checked="" type="checkbox"/> Published <input type="checkbox"/> Accepted for Publication <input type="checkbox"/> Submitted for Publication <input type="checkbox"/> Unpublished and Unsubmitted work written in manuscript style
Publication Details	Keshavarz, A., Yang, Y., Badalyan, A., Johnson, R. and Bedrikovetsky, P. (2014). Laboratory-based mathematical modelling of graded proppant injection in CBM reservoirs. International Journal of Coal Geology.136, 1-16.

Author Contributions

By signing the Statement of Authorship, each author certifies that:


- i. the candidate's stated contribution to the publication is accurate (as detailed above);
- ii. permission is granted for the candidate to include the publication in the thesis; and
- iii. the sum of all co-author contributions is equal to 100% less the candidate's stated contribution

Name of Principal Author	Alireza Keshavarz		
Contribution to the Paper	Performed laboratory tests, derived analytical model and performed data treatment		
Signature	<table border="1" style="float: right;"> <tr> <td>Date</td> <td>18.07.2016</td> </tr> </table>	Date	18.07.2016
Date	18.07.2016		

Name of Co-Author (Candidate)	Yulong Yang		
Contribution to the Paper	Derived analytical model and performed data treatment		
Overall percentage (%)	20%		
Signature	<table border="1" style="float: right;"> <tr> <td>Date</td> <td>20.07.2016</td> </tr> </table>	Date	20.07.2016
Date	20.07.2016		

Name of Co-Author	Alex Badalyan		
Contribution to the Paper	Supervised laboratory work, helped in data interpretation		
Signature	<table border="1" style="float: right;"> <tr> <td>Date</td> <td>20.07.2016</td> </tr> </table>	Date	20.07.2016
Date	20.07.2016		

Name of Co-Author	Ray Johnson		
Contribution to the Paper	Supervised development of work, helped in data interpretation and manuscript evaluation		
Signature	<table border="1" style="float: right;"> <tr> <td>Date</td> <td>11/7/2016</td> </tr> </table>	Date	11/7/2016
Date	11/7/2016		

Name of Co-Author	Pavel Bedrikovetsky
Contribution to the Paper	Supervised development of work, helped in data interpretation and manuscript evaluation
Signature	 21/07/2016



Laboratory-based mathematical modelling of graded proppant injection in CBM reservoirs



Alireza Keshavarz, Yulong Yang, Alexander Badalyan, Ray Johnson, Pavel Bedrikovetsky*

Australian School of Petroleum, The University of Adelaide, Adelaide, 5005, Australia

ARTICLE INFO

Article history:

Received 26 August 2014

Received in revised form 18 October 2014

Accepted 18 October 2014

Available online 24 October 2014

Keywords:

Proppant injection

Coal bed methane

Analytical model

Laboratory study

DLVO

Fine migration

ABSTRACT

The graded proppant injection into a connected cleat system of coal bed methane (CBM) reservoir allows deeper particle penetration and straining in the remote open cleats yielding higher well productivity index. The analytical model for axisymmetric flow has been derived for exponential stress–permeability relationship and accounting for permeability variation outside the stimulated zone. Laboratory proppant injections into coal cores have been performed for different proppant sizes and water salinities. It is shown that the proppant suspension based on low salinity water prevents the particle–particle and particle–coal attraction with the consequent core inlet plugging and external cake formation. However, low salinity of the injected water may cause mobilisation, migration and straining of the natural reservoir fines resulting in high formation damage. The interval where salinity is low enough for the rock inlet not to be plugged by the injected proppant, and is high enough for large formation damage due to fine migration not to occur, is proposed for the cores under investigation. The analytical model is tuned from the laboratory data and used for well index prediction. Ignoring the model matching by the laboratory results causes the overestimation of the incremental productivity index, as achieved by the graded proppant injection into coal beds below the fracturing pressure.

© 2014 Elsevier B.V. All rights reserved.

1. Introduction

Low productivity index in CBM wells have been widely reported in the literature. It places the CBM production on the margin of economic efficiency (Clarkson, 2013). Therefore, well stimulation in coal seam gas fields has the primary importance for gas production. The hydraulic fracturing is the most widely used CBM well stimulation method (Economides and Martin, 2007; Ghalambor et al., 2009; Guo and Ghalambor, 2012; Guo et al., 2011; Johnson et al., 2002). However, the hydraulic fracturing is often restricted by the environmental regulations. Besides, the available injection power may not be sufficient to fracture the well. The way around this problem is stimulation of a natural cleat system keeping the reservoir pressure below the fracturing pressure (Rahman et al., 2002). The traditional acidizing is also used for well stimulation below the fracturing pressure.

The method of natural cleat system stimulation by graded proppant injection has been proposed recently (Bedrikovetsky et al., 2012; Keshavarz et al., 2013; Khanna et al., 2013).

Fig. 1a shows the coal cleat network that provides the coal conductivity. Zoom around the fracture shows the cleat opening that widens under the pore pressure increase and narrows down during the pressure blow down (Fig. 1b). The cleat aperture variation along the fracture

is denoted by color green in the figure. The purpose of the proppant injection into a natural cleat is keeping it open during the production, where the pore pressure declines with time. Pressure decreases along each tortuous flow path from well inside the reservoir. So, the fracture aperture also decreases with radius (Fig. 2). Therefore, first the small particles are injected in order to be strained in remote areas and to plug the thin cleats, keeping them open during the production. Then, the intermediate size proppant particles are injected in order to fill in the cleats in the bulk of the drainage area. Finally, the larger proppant particles are injected to strain the cleats near the well. Fig. 2 shows how the particle sizes increase with radius tending to the wellbore radius r_w . The treated zone size is determined by the minimum particle size; therefore, the graded injection provides with a larger stimulation area than the injection of mono-sized suspension.

Let us discuss the efficiency of graded proppant injection in porous and fractured rocks. The low circle in Fig. 3 is a cross section of the porous core; here blue balls correspond to grains and red balls show the strained proppant particles. The upper circle in Fig. 3 is a cross section of the fractured rock; large red balls strain the face cleats while the butt cleats are strained by smaller proppant particles. Fig. 3 shows that proppant injection into rocks where the conductivity is provided by pores yields pore straining and permeability impairment. The proppant injection into fractured rocks keeps the cleats open during the pressure depletion with stress enhancement. The above is illustrated by the permeability change during the loading–unloading cycles. The black curve corresponds to pressure increase during the particle-free water

* Corresponding author at: Australian School of Petroleum, The University of Adelaide, Adelaide, Australia, 5005. Tel: + 61883133082.

E-mail address: pavel@asp.adelaide.edu.au (P. Bedrikovetsky).

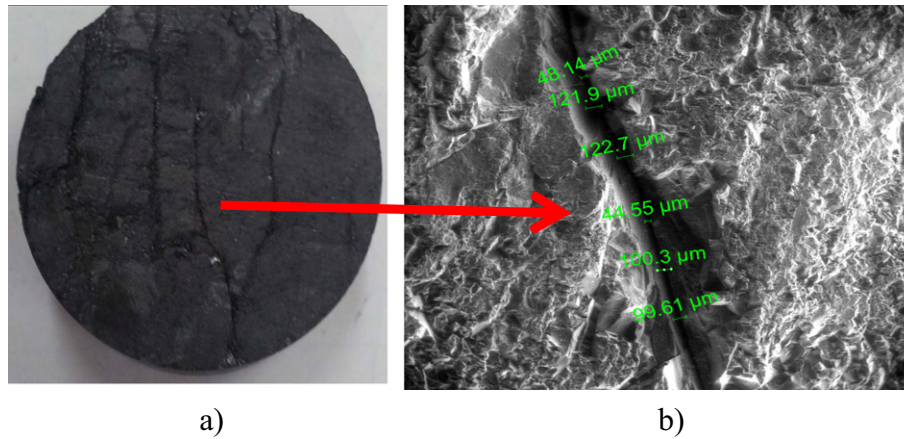


Fig. 1. Photo of inlet cross section of the coal plug: a) inlet cross section image; b) image under SEM showing the open cleat.

injection and the proppant particle injection at the highest pressure. Green arrow shows how the permeability declines during proppant injection. The blue curve corresponds to pore plugging by the injected particles in the rock with predominantly pore conductivity; further permeability decrease occurs after the proppant pumping during the pressure blow-down production. The resulting permeability after the rock loading is below the initial permeability – the black point at the maximum effective stress is above the blue point. In this case, the particle injection spoils well productivity. On the contrary, proppant injection into a cleat system increases well productivity, since it maintains the cleats open during the production. Pressure depletion in the fractured system corresponds to the red curve in Fig. 3. The red curve crosses the black curve and remains above it under higher values of effective stress (under low pore pressures). The final red point is located above the initial black point, indicating the permeability enhancement due to the proppant injection in the case of fracture-dominant rock conductivity.

Khanna et al. (2013) proposed a mathematical model to predict well index increase due to the graded proppant injection under the cubic relationship between the permeability and pore pressure. However, the model has not been validated by either laboratory or field studies. The current paper presents the results of the laboratory proppant injection with the mathematical model matched from the laboratory data in order to perform the reliable laboratory-based well index predictions.

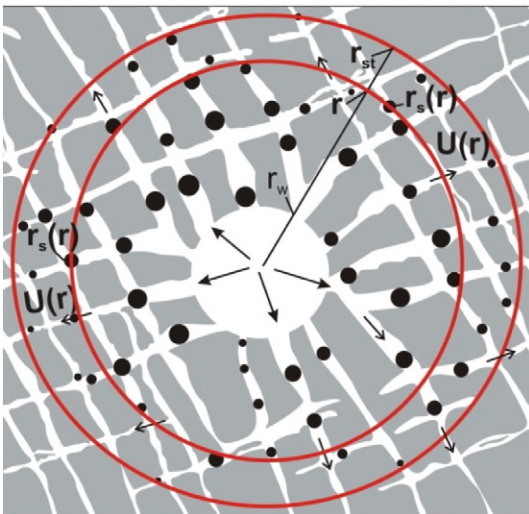


Fig. 2. Graded particle injection into naturally fractured rock: the geometric schema for the proppant straining.

Numerous works concentrate on studies of coal bed deformations and related permeability alterations (Connell, 2009; Pan and Connell, 2012; Pan et al., 2010; Shi and Durucan, 2005; Wang et al., 2007; Wang et al., 2009; Wang et al., 2010). Exponential and cubic relationships for the permeability stress dependency have been proposed (Connell et al., 2010; Palmer and Mansoori, 1998; Pan and Connell, 2012; Seidle et al., 1992; Shi and Durucan, 2005). The permeability stress dependencies are used in geo-mechanic models for flow and deformations in coal beds (Seidle, 2011). The presented laboratory measurements indicate the exponential relationship, which is used in the mathematical modelling.

In the present paper, the axisymmetric flow of suspended particles in fractured system of coal cleats is discussed. Derivations of the model include exponential form of the pressure–permeability dependence and accounts for permeability variation in the non-treated zone. The explicit formulae are derived for the injection schedule and well productivity index. Tuning the mathematical model from the coreflood data allows for reliable experiment-based behaviour prediction for the wells submitted to graded proppant particle injection.

The structure of the text is as follows. The mathematical model for graded proppant injection including explicit formulae for injection schedule and well productivity is presented in Section 2. Section 3 describes the laboratory materials, procedures and the experimental results. Tuning of the mathematical model from the laboratory data and the well behaviour predictions caused by the injection of graded particles are presented in Section 4. The discussions of the model validity and the graded proppant injection applicability (Sections 5 and 6) conclude the paper.

2. Mathematical model for well productivity with graded proppant injection

The section derives an analytical model for horizontal graded proppant injection into a CBM layer including steady state permeability and cleat opening profiles during the particle-free injection (Section 2.1), alternated pressure and permeability profiles after the graded proppant injection (Section 2.2), formulae for injection schedule providing maximum permeability for each distance to the well inside the stimulated area (Section 2.3) and the productivity index expression (Section 2.4).

The assumptions of the model include incompressibility of water and proppant particles, volume additivity with suspension of the particles in water, exponential stress dependence of permeability, proportionality of permeability to cube of the fracture aperture, axisymmetric flow from the well towards the reservoir, Darcy's law for flow of injected suspension, the particle and water velocities are equal, steady state pressure

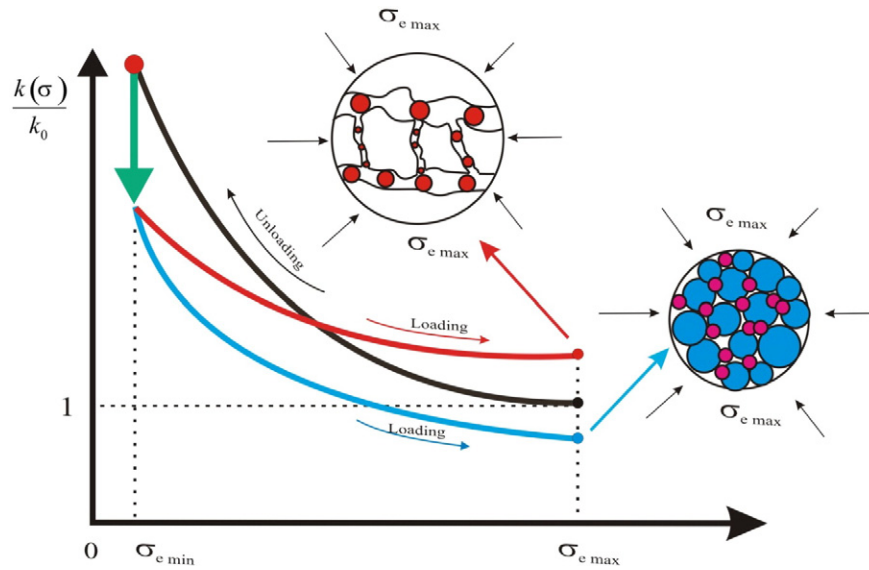


Fig. 3. The proppant particles plug the porous media, while the particles keep the cleats open in the fractured rocks.

distribution during the proppant suspension flow, constant values of suspension viscosity, proppant straining in the cleat with opening equal to the particle diameter, particle path tortuosity is neglected, the fracture permeability decrease due to straining and rock deformation is the same as that for the ideal fracture with parallel walls.

2.1. Axisymmetric flow in fractured rocks

Let us discuss the injection of incompressible fluid without particles into a fractured reservoir. The permeability is pressure-dependent or effective stress-dependent (Pan et al., 2010)

$$k(p) = k_0 \exp\{3C_f \alpha((p-p_0))\} \quad (1)$$

where permeability k_0 corresponds to reservoir pressure p_0 , C_f is the fracture compressibility, and the Biot's constant α is a pressure multiplier in the Terzhagy formula (Biot, 1941):

$$\sigma_e = \sigma - \alpha p \quad (2)$$

where σ_e is the effective stress and σ is the overburden stress. Assuming constant overburden σ , pressure becomes a function of effective stress and vice versa. It allows changing an independent variable from pressure to effective stress and vice versa in the formulae for permeability (Eq. (1)) further in the text.

The expression for rate with the axisymmetric flow and accounting for Darcy's law with stress-dependent permeability is

$$q = -\frac{2\pi r k(p) dp}{\mu dr} \quad (3)$$

Another assumption of the model is incompressibility of the injected fluid with particles, resulting in a constant rate q .

Substituting the permeability expression (Eq. (1)) into Eq. (3), separating variables and integrating accounting for the reservoir pressure at the drainage zone boundary yields the pressure distribution during either injection or production

$$p(r, q) = p_0 + \frac{1}{3\alpha C_f} \ln \left[1 - \frac{3\alpha C_f \mu q}{2\pi k_0} \ln \frac{r}{r_e} \right] \quad (4)$$

Here we keep rate q as an independent variable in order to distinguish between the pressure distributions during injection at $q > 0$ and production for $q < 0$.

Combining Eqs. (1) and (4) results in the areal permeability distribution during the injection

$$k(r, q) = k_0 \left[1 - \frac{3\alpha C_f \mu q}{2\pi k_0} \ln \frac{r}{r_e} \right] \quad (5)$$

The fractured system permeability is proportional to the cube of the fracture aperture (Civan, 2007; Reiss, 1980; van Golf-Racht, 1982):

$$\frac{k}{k_0} = \left(\frac{h}{h_0} \right)^3 \quad (6)$$

Considering whatever geometry of the fractured system that is a realisation of probabilistic distribution of fractures over size, areal position and opening (Fig. 1), an estimation of rock permeability k can be performed using percolation theory, effective medium theory or their combination (Bedrikovetsky, 1993). Each model results in Eq. (6), which means that the expansion of the opening of every individual fracture a times results in permeability increase a^3 times.

Substituting Eq. (5) into Eq. (6) yields the areal distribution of the fracture opening:

$$h(r) = h_0 \left(\frac{k(r)}{k_0} \right)^{\frac{1}{3}} = h_0 \left(1 - \frac{3\alpha C_f \mu q}{2\pi k_0} \ln \frac{r}{r_e} \right)^{\frac{1}{3}}, \quad h_0 = h(r_e) \quad (7)$$

Now let us discuss the injection of a proppant suspension in water. It is assumed that the particle is trapped in fracture when its aperture reaches the value of particle diameter, $h = 2r_s$. As it follows from Eq. (7), the particle with radius r_s is trapped at the distance $r = r(r_s)$:

$$r(r_s) = r_e \exp \left\{ \frac{2\pi k_0 \left[1 - \left(\frac{2r_s}{h_0} \right)^3 \right]}{3\alpha C_f \mu q} \right\} \quad (8)$$

Radius of the treated (stimulated) zone r_{st} corresponds to the minimum size particles (Fig. 2):

$$r_{st} = r(r_{smin}) = r_e \exp \left\{ \frac{2\pi k_0 \left[1 - \left(\frac{2r_{smin}}{h_0} \right)^3 \right]}{3\alpha C_f \mu q} \right\} \quad (9)$$

allowing the calculation of the stimulated zone radius.

2.2. Axisymmetric flow with strained particles

The permeability–straining diagram allows the determination of the permeability alteration after particle injection and its variation versus effective stress or pressure (Fig. 4). The curves correspond to variation of normalised permeability $f = k(\sigma) / k_0$ versus proppant aspect ratio $\beta = 2r_s / l$, where l is the distance between the strained particles in the fracture under constant effective stress. For a given geometry of particle straining in a fracture, the aspect ratio β can be expressed via the concentration of strained particles. The values of dimensionless effective stress

$$\varepsilon_{\sigma} = \frac{\sigma_e (1 - \nu^2)}{E} \quad (10)$$

are shown in Fig. 4 above each curve.

According to Eq. (1), the higher is the effective stress the lower is the permeability; consequently, the lower is the curve location in the diagram. The dependency (Eq. (1)) is monotonic, so the curves do not intersect. The upper envelope curve corresponds to zero effective stress. The curves have been obtained by solving system of equation for flow of incompressible viscous liquid in the fracture with strained proppant particles accounting for elastic matrix and proppant deformation with pressure decrease during the depletion stage (Khanna et al., 2012, 2013). The computation fluid dynamics package ANSYS calculates pressure drop across the fracture, allowing calculation of the permeability correction factor f (Stolarski et al., 2006). The larger is the inter-particle distance l the lower is the fracture aperture due to deformation of fracture walls; so the fracture can be closed at some large l . Therefore, f becomes equal to zero at some small β -value, corresponding to crossing the abscissa axes by the curve. The smaller is the inter-particle distance the lower is the permeability due to hydraulic resistivity of packed particles in the fracture. So, the curves tend to negligibly small f -value as β tends to one. Therefore, each curve has maximum β^* corresponding to the optimal particle placement: $k(\beta^*(\sigma_e), \sigma_e) > k(\beta, \sigma_e)$. The

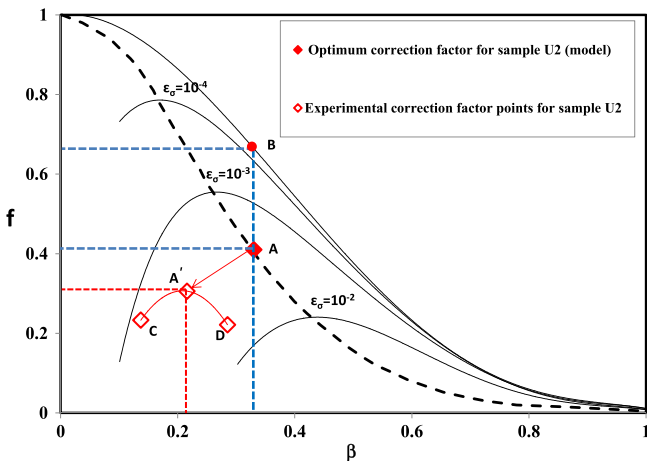


Fig. 4. The diagram for f -normalised permeability vs. proppant aspect ratio for constant values of dimensionless effective stress.

traced normalised permeability curve corresponds to the points of maximum permeability at each effective stress value: $f = f(\beta^*(\sigma_e), \sigma_e)$.

Let us calculate pressure distribution after injection of water with particles, plugging and further production. The “initial” permeability profile before plugging is determined by Eq. (5), where $q > 0$ is the injection rate. The proppant injection is carried out with increasing particle size and decreasing concentration in time, in order to achieve maximum permeability with the normalised permeability value $f(r) = f(\beta^*(\sigma_e(r)), \sigma_e(r))$ in each point of the reservoir. The production stage is described by Eq. (3) with the following areal permeability distribution

$$k(r) = \begin{cases} f(\beta^*(p), p) \cdot k(r, q_j) & r \leq r_{st} \\ k(r, q_p) & r > r_{st} \end{cases} \quad (11)$$

Eq. (4) determines pressure in the non-treated zone $r > r_{st}$, including pressure at the stimulated zone boundary $p_{st} = p(r_{st}, q_p)$. The effect of permeability variation in un-stimulated zone has not been accounted for by Khanna et al. (2013).

Substituting the expression for permeability in stimulated zone (Eq. (11)) into Eq. (3), separating variables and integrating in r from the point $r < r_{st}$ up to the stimulated zone boundary yields the implicit formula for pressure distribution in the treated area

$$\int_p^{p_{st}} f(\beta^*(p), p) dp = \frac{q_p \mu}{2\pi k_0} \int_r^{r_{st}} \frac{dr}{r \left[1 - \varepsilon_q \ln \left(\frac{r}{r_e} \right) \right]}, \quad \varepsilon_q = \frac{3\alpha C_f \mu q_j}{2\pi k_0} \quad (12)$$

where q_p and q_j are production and injection rates, respectively.

2.3. Optimal injection schedule

Let us calculate the travelling time of the particle before its capture by straining in the cleats. The particle speed in the cleat at a distance r from the well for incompressible fluid flow with non-deformable particles is

$$\frac{dr(t)}{dt} = \frac{q}{n(r)h(r)} \quad (13)$$

where q is the injection rate per unit thickness of the reservoir, $n(r)$ is the number of cleats through which the fluid flows and $h(r)$ is the aperture of the cleats. Let us calculate the number of cleats $n(r)$ encountered by the injected fluid. Assuming two perpendicular sets of evenly spaced vertical cleats in thin horizontal reservoir (the matchstick model), the number of cleats crossing a circle with radius r is:

$$n(r) = 8r/a \quad (14)$$

where a is the cleat spacing. The number of cleats that crosses a circle with radius r increases with increasing distance from the wellbore. Substituting Eqs. (14) and (7) into formula (13), separating the variables and integrating both sides of the equation results in an expression for time taken by a particle to travel along the distance r

$$\frac{qL}{8h_0} t = \int_{r_w}^r r \left(1 - \varepsilon_{qj} \ln \frac{r}{r_e} \right)^{1/3} dr. \quad (15)$$

Here r is the dummy integration variable. The above expression assumes that the particle velocity is the same as the velocity of the carrier fluid. In terms of the dimensionless radial coordinate $r_D = r/r_e$, the travelling time is given by:

$$\frac{qL}{8h_0} t = r_e^2 \int_{r_{wD}}^{r_D} r \left(1 - \varepsilon_{qj} \ln r \right)^{1/3} dr. \quad (16)$$

Substituting the expression for plugging distance given by Eq. (8) into Eq. (16) yields the settling time t_s or the time it takes for the particle of size r_{Ds} to strain in the thinning cleat,

$$t_s(r_{Ds}) = \frac{8hr_e^2}{qL} \int_{r_{wd}}^{r_D(r_{Ds})} r(1-\varepsilon_{qj} \ln r)^{\frac{1}{2}} dr, \quad r_{Ds} = r_s/h_0. \quad (17)$$

Eq. (17) is used to calculate the total injection time that is the travelling time for the smallest particle $t_s(r_{smin})$. A higher injection rate results in a smaller settling time, corresponding to faster arrival of an r_{smin} particle to its plugging site. Eq. (17) shows that the total injection time decreases with the injection rate increase.

Now we calculate the required particle concentration based on the optimal proppant placement. It is assumed that the proppant particles fill the cleats in the form of a partial coverage monolayer. The concentration of particles can be expressed in terms of the inter particle distance $l(r_{Ds})$ along the cleat. The volume of a cleat section that contains a single particle is given by

$$V(r_{Ds}) = l(r_{Ds}) \int_{r_D(r_{Ds})}^{r_D(r_{Ds})+l(r_{Ds})} h(r) dr \quad (18)$$

The packing aspect ratio β^* corresponds to maximum permeability in permeability-straining diagram (Fig. 4)

$$\beta^*(r_{Ds}) = \frac{2r_{Ds}}{l(r_{Ds})}. \quad (19)$$

Free variable in Eq. (19) could be radius r due to Eq. (8) or pressure p due to Eq. (4). Zero packing aspect implies that there are no proppant particles in the cleats. Packing aspect ratio that is equal to one implies that the proppant particles form a full monolayer in the cleat system. The concentration of particles of a given size is obtained from Eqs. (7), (18) and (19) as

$$c(r_{Ds}) = \frac{1}{V(r_{Ds})} = \left[h_0 \frac{2r_{Ds}}{\beta^*(r_{Ds})} \int_{r_D(r_{Ds})}^{r_D(r_{Ds})+\frac{2r_{Ds}}{\beta^*(r_{Ds})}} \left(1-\varepsilon_q \ln \frac{r}{r_e}\right)^{\frac{1}{2}} dr \right]^{-1}. \quad (20)$$

The moment when the particle with size r_{Ds} is injected is equal to

$$t(r_{Ds}) = t_s(r_{smin}) - t_s(r_{Ds}). \quad (21)$$

Finally, Eq. (20) presents the injected particle concentration at the moment t ; Eq. (21) shows the particle radius injected at the same moment. Two Eqs. (20) and (21) present the optimal injection schedule. Well index calculations, where the optimal injection schedule is followed during well stimulation, are presented in the next section.

2.4. Well index derivation

Let us derive the formulae for productivity index before the particle injection. Substituting Eq. (5) into Eq. (3) and integrating pressure gradient from r_w to r_e yields

$$PI_0 = \frac{q_p}{p_0 - p_w} = \frac{-3\alpha C_f q}{\ln \left[1 - \frac{3\alpha C_f q \mu}{2\pi k_0} \ln \frac{r_w}{r_e} \right]}. \quad (22)$$

Well productivity index after the proppant injection is

$$PI = \frac{q_p}{(p_0 - p_{st}) + (p_{st} - p_w)}. \quad (23)$$

Here wellbore pressure p_w is determined from Eq. (12) by substituting $r = r_w$ and $p = p_w$.

The first term in Eq. (23) is the pressure drop between the drainage and treated zone contours; it is defined explicitly by Eq. (4). The second term is the pressure drop across the treated zone; it is determined implicitly by Eq. (12).

3. Laboratory study

This section presents laboratory materials, methods and the results of the experimental study. Core samples and proppant material along with the experimental set-up are presented in Section 3.1. Section 3.2 shows measurements and calculations of cleat system porosity, permeability, fracture spacing and aperture. Measurements in Section 3.3 allow establishing the stress–permeability relationship. The methodology of the sequential coal unload–load intercalated by proppant injection is given in Section 3.4. The favourable salinity and pH conditions for those tests are found in Section 3.5, followed by the test results in Section 3.6. The additional conditions preventing fine migration are found in Section 3.7.

3.1. Cores, proppant and set-up

Two blocks of bituminous coal samples were obtained from two different mines. The first one (Coal block A) is taken from Dawson Mine Central, Queensland, Australia. The second block (Coal block U) is taken from Affinity coal mine, West Virginia, US. Four core samples drilled from Coal block-A are referred to further in the text as A_1, \dots, A_4 . Those drilled from Coal block U are called U_1, \dots, U_5 . After drilling and cutting of the core surfaces, the core lengths and radii are measured by a digital calliper; the results are presented in Tables 1 and 2.

Core samples A_1, A_2, U_1 and U_2 are used in the particle placement tests. The geo-mechanical property measurements in uniaxial stress tests are performed for core samples A_3, A_4, U_3 and U_4 . Core sample U_5 is used in the fines migration test.

Helium gas expansion porosimetry and the imbibition method are used for core porosity measurements (Amyx et al., 1960; Keshavarz et al., 2014). The Helium and water porosity values for coal samples A_1, A_2, U_1, U_2 and U_5 are presented in Table 1. Coal cores A_3, A_4, U_3 and U_4 are tested in a uniaxial stress test apparatus. The Young's modulus and Poisson's ratio values are calculated from the experimental axial load, axial strain and radial strain data (Table 2). The average values of Young's modulus and Poisson's ratio as obtained for samples A_3 and A_4 are assumed for samples A_1 and A_2 ; they are denoted in Table 3 as $\langle A \rangle$. The average values of Young's modulus and Poisson's ratio as calculated for samples U_3 and U_4 and denoted in Table 3 as $\langle U \rangle$ are assumed for samples U_1 and U_2 .

Prior to the start of the particle placement tests, core samples are tightly wrapped with a Teflon tape to prevent water leakage between the core outer surface and rubber sleeve, holding the cores inside a high-pressure core holder. All tests are conducted at constant ambient temperature of 25 °C.

The particles chosen for injection are the spherical ultra-light and high-strength hollow borosilicate glass microspheres SPHERICEL 110P8 and SPHERICEL 60P18 (Potters Industries LLC, South Yorkshire, UK). The particle sizes $r_s = 5 \mu\text{m}$ and $r_s = 9.5 \mu\text{m}$ are used in the tests.

Fig. 5 shows the photo of the laboratory set-up. Fig. 6 is the schematic of the set-up. Here 1 is the coal core; 2 is the rubber sleeve; 3 is the high-pressure core holder; 4 is the manual overburden pressure generator; 5 is the 15 PA 33X gauge pressure transmitters; 6 is the suspension with glass particles; 7 is the high-pressure separator; 8 is the piston; 9 is the MilliQ water; 10 is the HPLC pump; 11–13 and 20–23 are manual valves; 14 is the back-pressure regulator; 16–19 are Validyne differential pressure transducers; 24 is the ADAM-4019 + analogue data acquisition module; 25 is the ADAM-5060 RS-232/RS-485 signal converter; 26 is the personal computer; 27 is the ADAM-4024 analogue output module; 28 are beakers; and 29 is the PAMAS S4031 GO portable particle counter. More details about the equipment can be found from Keshavarz et al. (2014).

Table 1
Properties of core plugs.

Coal	D , cm	L , cm	ϕ_{wv} %	ϕ_H %	ϕ_{c0}^a %	C_f , psi^{-1}	α	k_0^a , md	h_0^a , μm	a^a , mm	$h(\sigma_{e-\text{min}})$	j_1	j_2
A ₁	3.88	2.45	3.1	5.26	0.61	0.00095	0.82	5.41	45.79	15.01	41.26	0.24	0.46
A ₂	3.88	2.96	3.53	6.27	0.52	0.0012	0.90	6.22	53.22	20.47	49.72	0.20	0.38
U ₁	3.86	3.17	3.58	5.74	0.48	0.00088	0.88	4.94	49.17	20.49	49.73	0.20	0.38
U ₂	3.86	3.44	3.25	5.53	0.54	0.0011	0.91	5.80	50.44	18.68	48.23	0.21	0.39
U ₅	3.86	2.70	3.82	6.35	0.72	–	–	4.13	36.73	10.20	–	–	–

^a ($P_{ob} - P_{inlet} = 100$ psi).

3.2. Cleat property measurements

The coal cores A₁, A₂, U₁, U₂ and U₅ are installed in the core holder and submitted to flow under four loading cycles before carrying out experiments, to make sure that the results are repeatable.

The initial natural fracture and cleat porosity and permeability of each coal core plug are measured according to the Gash's method (Gash, 1991) in the following sequence. First, the coal sample is saturated with water. Then, an overburden pressure is increased up to 150 psi, and flow of water is established through the sample at a constant inlet pressure of 50 psi until a steady-state flow condition is achieved. Finally, the initial permeability of the core plug is measured. After achieving the initial permeability value, water is displaced by helium. The displaced water mass is converted into the sample's initial cleat porosity ϕ_{c0} . The initial cleat permeability and porosity values are presented in Table 1.

The assumption of vertical matchstick geometry of matrix blocks intercalated by vertical fractures is used for definition of coal permeability and porosity (Seidle, 2011):

$$\phi_{c0} = \frac{h_0}{500a} \quad (24)$$

$$k_0 = 1.0555 \times 10^5 (\phi_{c0}^3 a^2) \quad (25)$$

where a is the cleat spacing; h_0 is the initial cleat opening; k_0 and ϕ_{c0} are initial cleat permeability and porosity, respectively. The initial cleat opening and cleat spacing for each sample as calculated by formulae (24) and (25) are presented in Table 1.

According to filtration theory in porous media, the particle jamming ratio $j = \left(\frac{r_s}{h}\right)$ should not exceed 1/3 of the average pore size in order to provide the particle penetration into the rock without being trapped at the inlet face (Bedrikovetsky, 2008; Van Oort et al., 1993). The particle jamming ratio should exceed 1/7th of the average pore size in order to avoid the capture-free particle motion in the rock; in this case some particles remain in the cleats and do not allow the cleat closure during the pore pressure depletion. To the best of our knowledge, the above thresholds for fractured media are not available in the literature (Noam, 2012; Rodrigues and Dickson, 2014).

The permeability at the minimum effective stress is determined for each sample. The permeability of the fractured media is proportional to the cube of the aperture (Eq. (6)) allowing the calculation of the fracture aperture at minimum effective stress for each sample (Table 1). For two particle sizes $r_s = 5 \mu\text{m}$ and $r_s = 9.5 \mu\text{m}$, the jamming ratios j_1 and j_2 are calculated for core samples A₁, A₂, U₁ and U₂. All jamming ratios

Table 2
Geo-mechanical properties of core plugs.

Coal	D , cm	L , cm	ν	E , GPa
A ₃	3.88	3.87	0.29	1.025
A ₄	3.89	4.12	0.27	0.91
<A>			0.28	0.97
U ₃	3.86	4.73	0.3	1.13
U ₄	3.87	4.3	0.31	1.25
<U>			0.305	1.19

exceed 1/7th of the average cleat aperture. However, j -values for cores A₂, U₁ and U₂ slightly exceed 1/3rd of the average cleat opening. It reaches the higher value $j = 0.46$ for core A₁. As it is shown further in the text, the injected $r_s = 5 \mu\text{m}$ and $r_s = 9.5 \mu\text{m}$ particles perform deep bed filtration and are strained in the cleats.

3.3. Stress sensitivity for permeability

The goal of the section is determination of the pressure/stress-dependency of permeability, including the calculations of α - and C_f -coefficients. The core A₁ has been submitted to flow under different overburden stresses and pore pressures in the coreflood rig (Figs. 5, 6). The exponential permeability–pressure dependency (Eq. (1)) in semi-log coordinates becomes straight line. Three straight lines are shown in Fig. 7a for three different overburden values. Fig. 7b shows straight lines corresponding to different permeabilities as obtained from Fig. 7a. Three point triples are located on straight lines. Indeed, permeability is determined by the effective stress; overburden is a linear function of pressure for a constant effective stress, see Eq. (2). Slope of straight lines in Fig. 7b is Biot's coefficient. For the case discussed, $\alpha = 0.82$. Since permeability is fully determined by effective stress, three sets of points, as recalculated from Fig. 7a into permeability–effective stress dependency, are located on the same curve (Fig. 7c). This curve becomes straight line in semi-log coordinates, the slope is equal to $-3C_f$. Finally, the cleat compressibility coefficient for the case considered $C_f = 0.00095 \text{ psi}^{-1}$. The coefficient of determination R^2 for the graphs shown in Fig. 7d is equal to 0.94, allowing considering the stress dependency of log-permeability to be a linear function (Eq. (1)) with high accuracy.

The agreement between the laboratory data for core A₁ and cubic permeability–stress formula (Palmer and Mansoori, 1998; Pan and Connell, 2012) is 0.9 for core A₁, which is lower than the agreement coefficient $R^2 = 0.94$ for exponential permeability expression (Eq. (1)). Therefore, the exponential permeability–pressure dependency is chosen for modelling in the current paper.

The same tests have been carried out for cores A₂, U₁ and U₂. The results are presented in Table 1.

3.4. Particle placement tests

The schema for particle injection tests is shown in Figs. 3 and 4. The injection of particle-free water is carried out under piece-wise constant pore pressure in the increasing mode until the maximum pore pressure is reached (black curve in Fig. 3). This motion corresponds to movement along the f -normalised permeability envelope from point (0,1) to point B in Fig. 4. The proppant particles are injected at higher pore pressure in order to provide the maximum cleat opening; the corresponding permeability decline is shown by the green arrow; it corresponds to interval BA in Fig. 4. Then the injection of particle-free water continues under piece-wise constant pore pressure in the decreasing mode until the initial pore pressure is reached (red and blue curves in Fig. 3).

The sequence of floods corresponds to the proppant injection into the reservoir under the elevated pressures followed by water production during the reservoir dewatering.

Table 3

Zeta potential values for particle and coal suspensions under different IS and pH of the carrier water.

IS (M)	pH		pH		pH		pH		pH	
	0	ζ (mV)	0.1	ζ (mV)	0.2	ζ (mV)	0.4	ζ (mV)	0.6	ζ (mV)
Particle	3.05	−32.53	3.02	−14.93	2.93	−10.80	3.04	−7.68	2.86	−5.32
	6.07	−40.84	4.73	−29.44	4.69	−25.24	6.28	−17.74	5.19	−13.10
	9.66	−51.23	9.51	−38.30	9.24	−31.04	9.36	−19.04	9.35	−14.41
	11.26	−60.10	11.52	−37.71	11.32	−30.55	10.15	−20.64	11.28	−13.87
	11.89	−59.93	11.97	−37.24	12.07	−29.71	11.65	−20.33	11.87	−14.34
Coal	2.84	−14.42	2.86	−10.07	2.71	−7.09	2.73	−6.22	2.71	−6.56
	3.71	−19.94	3.98	−14.26	3.98	−13.35	4.08	−8.07	4.14	−11.23
	6.54	−42.55	6.82	−30.84	7.67	−27.19	7.98	−19.40	7.96	−18.51
	9.68	−50.18	9.48	−33.34	9.52	−30.64	9.79	−21.19	9.51	−19.97
	11.30	−62.57	11.35	−36.94	11.34	−33.30	11.23	−20.55	11.06	−21.50

3.5. Electrostatic coal–proppant interaction

The unsuccessful proppant injection with high salinity brine in coals has been reported in our previous paper (Keshavarz et al., 2014). The permeabilities of cores A₁ and U₁ after particle injection and stress loading are the same and even less than the initial permeability. It is attributed to particle–particle attachment yielding the particle agglomeration with consequent straining at the core inlet. Another reason for enhanced hydraulic resistance at high salinity is the attachment between proppant and coal at high salinity, resulting in plugging of the near-entrance core area and formation of external filter cake. Therefore, in the current section we study the electrostatic particle–rock interaction to find the conditions providing the mutual proppant–coal and particle–particle repulsion and avoiding the core entrance clogging.

The Derjaguin–Landau–Verwey–Overbeek (DLVO) theory is used to evaluate the extent of particle–particle and particle–coal interaction at various ionic strengths and pH of suspensions (see Appendix A for details). As it is shown in Table 3, surfaces of proppant particles and coal are negatively charged in the entire studied range of ionic strengths and pH of suspensions. The higher values of pH and the lower values of the ionic strengths of suspensions correspond to higher absolute values of zeta potentials for both particles and coal. The conditions of high pH and low salinity translate to a greater particle–particle and particle–coal repulsion due to increased thickness of electrical double layer. The proppant particle agglomeration and particle–coal attachment occur where the electrical double layer is compressed at the elevated ionic strength of the proppant suspension.

Fig. 8 shows the particle–particle interaction in the suspension of 0.6, 0.1 and 0.05 M NaCl for 9.5 μm (solid lines) and 5 μm (dashed lines) proppant particles.

The depth of the minimum potential energy increases with increase in ionic strength from 0.05 to 0.6 M. The values of highest depth of minima potential energy that occurs at 0.6 M are −520 and −280 k_BT

for 9.5 μm and 5 μm particles respectively. High negative values of primary minima in the total potential energy curves for both particle sizes indicate the compressed electrical double layer. The interaction energy of particle–coal surface is presented in Fig. 9. Similar to the case of particle–particle system (Fig. 8), the higher values of the ionic strength correspond to the higher values of the depth of the minimum energy. The values of the minima potential energy of particle–coal surface system at 0.6 M, for $r_s = 9.5 \mu\text{m}$ and $r_s = 5 \mu\text{m}$ particles are about −11,800 and −6000 k_BT respectively. The very low minimum potential energy corresponds to significantly compressed electrical double layer and attraction of proppant particles to the coal surface.

Decrease of ionic strength from 0.6 to 0.05 M NaCl makes particle–particle and particle–coal interactions less attractive since the depth of the primary minimum decreases significantly for both particle sizes.

As it follows from Figs. 8 and 9, the shallow minima depths on DLVO potential curves at lower ionic strength of 0.05 and 0.1 M NaCl may not lead to agglomeration of proppant particles and particle attachment on the coal surface due to Brownian force and heat fluctuations.

Fig. 10 shows the suspension solution under the optical microscope for both high and low salinities. Significant particle agglomeration is observed for 0.6 M suspension (Fig. 10a) while almost no agglomeration occurs at lower ionic strength of 0.05 M (Fig. 10b).

So, at salinities below 0.1 M, both particle–particle and particle–coal repulse. Therefore, injection of proppant particles into coal bed has been performed under 0.1 M salinity; the results are presented in the next section.

3.6. Proppant injection with low salinity water

The laboratory procedure repeats the sequence, which is supposed to be performed in CBM well; the injection of water with proppant particles with further production under the pressure blow-down (Fig. 3). The tests are planned in order to provide the optimal return permeability. Point A at Fig. 4 is the maximum permeability point located at the curve for high effective stress, which corresponds to initial low pore pressure. This point is a target after the proppant injection at high pressure and return to the low pressure. Particle injection with permeability decline under high pore pressure (low effective stress) corresponds to the state point movement from the point (0,1) down along the envelope curve. Consider point B on the envelope curve that has the same abscissa as point A, so the states A and B have the same concentrations of the retained particles. Injection of the proppant until point B, i.e. until the normalised permeability decreases from one to f_B , provides the permeability decrease until f_A after decreasing the pore pressure up to the initial value. So, the test with the proppant injection until the permeability decreases up to f_B results in maximum permeability that is achievable at low pressure.

First, the core is submitted to flood with piecewise constant increasing pore pressure (blue dashed curve in Fig. 11). Then 5 μm proppant particles are injected at the maximum pressure, resulting in permeability decline (green vertical arrow). Then the proppant-free water is injected

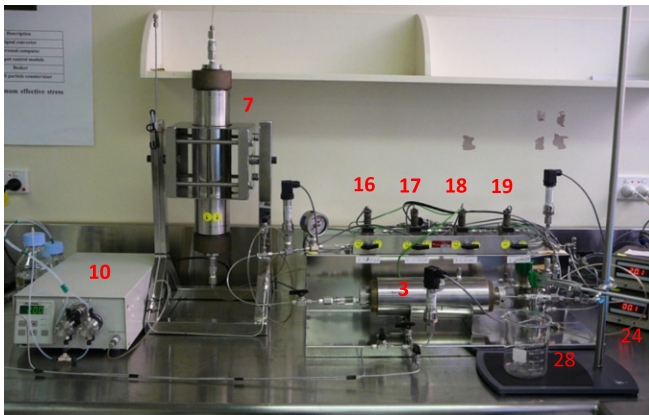


Fig. 5. Photo of set-up.

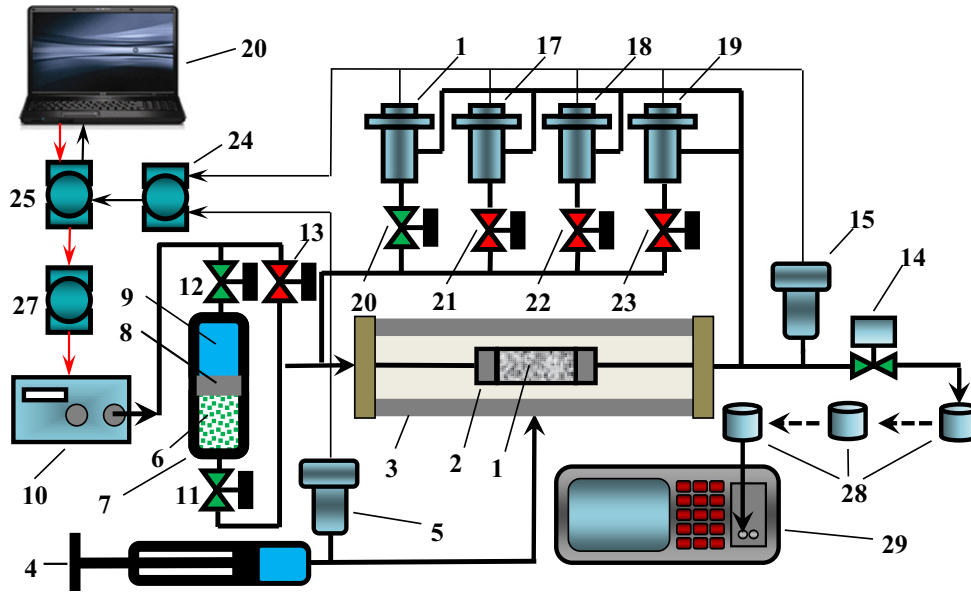


Fig. 6. Schematic for laboratory set-up.

under piecewise constant decreasing pore pressure, which corresponds to the red continuous curve. Further increase of pore pressure in the same internal follows the red curve up, i.e. the process is reversible. Afterwards 9.5 μm proppant particles are injected at the maximum

pressure; the resulting permeability decrease is shown by another green vertical arrow. Waterflood under the pressure decrease is shown by black continuous curve. The proppant-free flood with pressure increase also shows no hysteresis; the corresponding state point moves

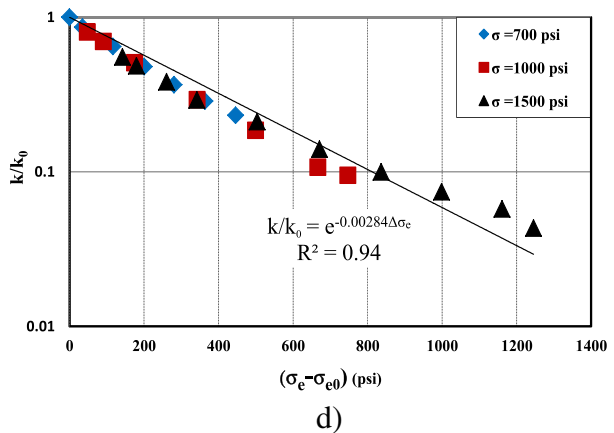
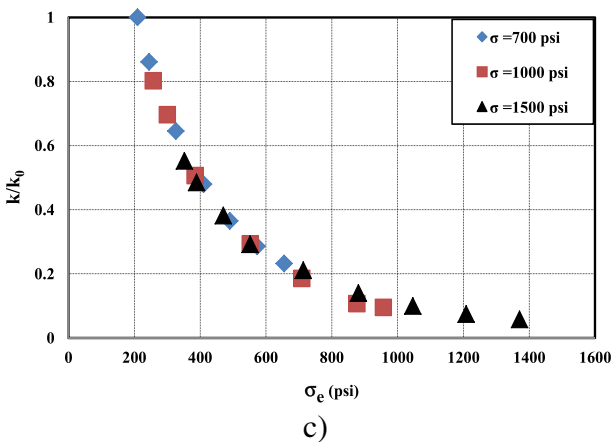
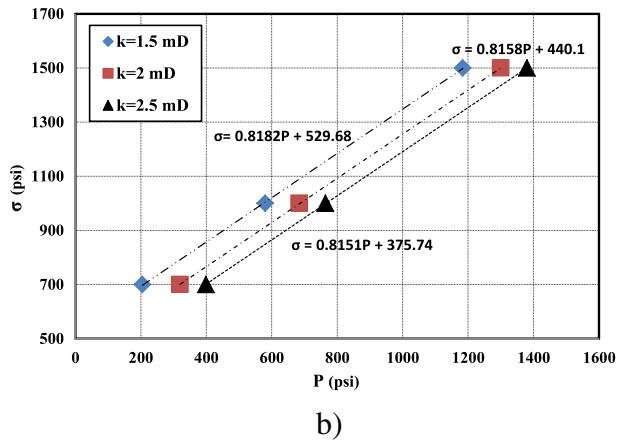
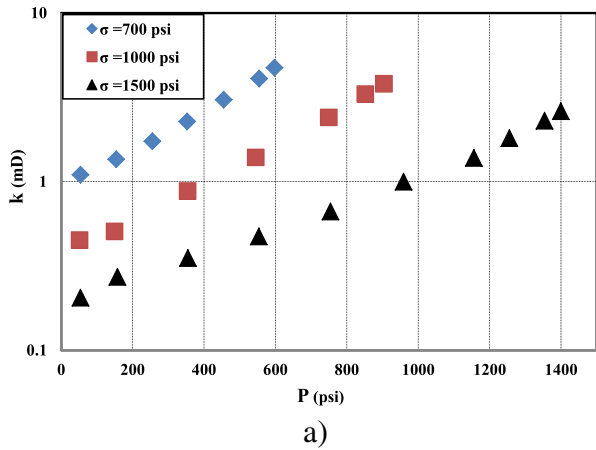


Fig. 7. Permeability versus stress for deformable coal: a) permeability vs pore pressure for different overburden stresses; b) graphical determination of the effective stress coefficient α ; c) dimensionless permeability vs effective stress; d) the cleat compressibility coefficient C_{1s} is found from the exponential effective stress dependency.

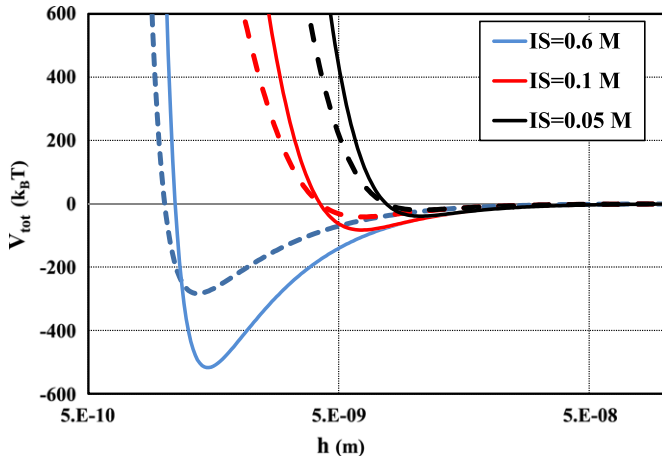


Fig. 8. DLVO interaction potential in proppant particle-particle system. Dashed lines correspond to small particles ($r_s = 5 \mu\text{m}$) and solid lines correspond to larger particles ($r_s = 9.5 \mu\text{m}$).

up reversibly along the black curve. Further proppant injection at high pressure yields further permeability decrease. Pressure decrease flood follows the continuous green curve.

Fig. 11 shows the results of tests for core U_2 , which are carried out for salinity 0.05 M and pH = 9. The initial permeability at low pressure $p = 50$ psi is equal to 0.37 md. Blue line injection increases permeability up to 3.88 md at $p = 900$ psi. Injection of $5 \mu\text{m}$ proppant particles yields the permeability decreases up to 2.53 md. The return red curve exhibits the permeabilities lower than that of the blue curve at pressure above 600 psi. Two curves cross at this pressure; the return permeabilities at red curve are above those at blue curves, showing the permeability enhancement due to particle injection at high pressure and keeping the cleats open at lower pressures. The red curve ends up at permeability of 0.9 md, exhibiting the enhancement against the initial core permeability of 0.37 md.

Further injection of $9.5 \mu\text{m}$ proppant particles at highest pressure causes further decrease of permeability from 2.53 md to 2.14 md. The pressure decrease return is shown by black curve. Further permeability increase from 0.9 md to 1.19 md occurs at the initial pressure.

However, secondary injection of $9.5 \mu\text{m}$ proppant (green curve) decreases the effect of remaining cleat aperture by strained proppant – the green curve comes back at almost the same permeability as the red curve does.

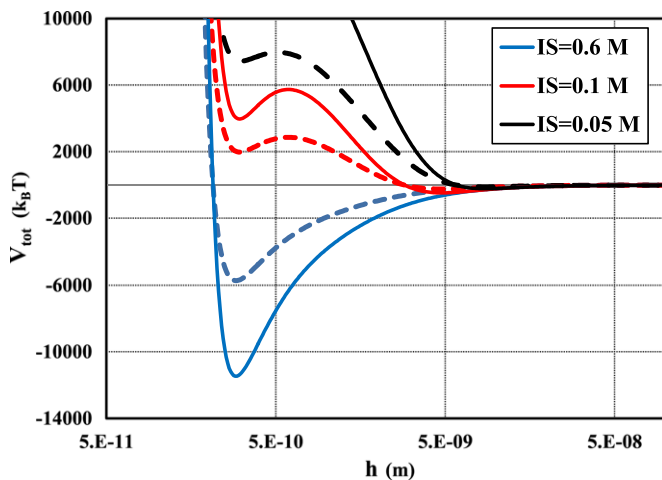


Fig. 9. DLVO interaction potential in particle-coal system. Dashed lines correspond to small particles ($r_s = 5 \mu\text{m}$) and solid lines correspond to large particles ($r_s = 9.5 \mu\text{m}$).

Injection of $5 \mu\text{m}$ proppant particles keeps cleat open during pressure depletion and causes permeability increase. Injection of larger particles ($9.5 \mu\text{m}$) at high pressure results in further enhancement of the cleat aperture and in the further permeability increase. Secondary large particle injection yields the increase of strained particle density in the cleats that leads to the increased hydraulic resistivity with consequent permeability decline. Therefore, there does exist an optimal concentration of size excluded particles placed in cleats that yields the maximum return permeability.

The accumulated breakthrough particle concentrations are measured after each of three injections. Since the injected proppant concentration is known, it allows the determination of the retained strained concentration and, consequently, the aspect ratio coefficient β . Fig. 4 shows point C after injection of $5 \mu\text{m}$ particles, point A' after first injection of $9.5 \mu\text{m}$ particles and point D after second injection of $9.5 \mu\text{m}$ particles. Abscissas of those points are calculated from the retained concentrations. The point ordinates correspond to return permeabilities.

Fig. 12a shows the optical microscope image of the core inlet after the test for sample U_2 . The inlet cleats are not plugged by particles, there is no external cake. Higher resolution photo of the cleat shows some size exclusion in situ, which does not impair the flow paths. So, the particle-particle and particle-coal electrostatic repulsion provide the particle transport throughout the core with the uniform particle placement in cleats.

Similar results are obtained from the tests with core A_2 , which are carried out for salinity 0.1 M and pH = 9. Initial permeability at low pressure $k = 0.45$ md is increased up to 0.95 md after injection of $5 \mu\text{m}$ proppant particles and return to the initial pressure. Further injection of $9.5 \mu\text{m}$ proppant causes permeability enhancement up to 1.33 md. Secondary flush by $9.5 \mu\text{m}$ proppant particles yields some decrease of the return permeability up to 1.13 md.

So, the proppant particle injection under low water salinity results in particle-coal repulsion, providing particle transport inside the core and particle straining throughout the core. The lower is the solution ionic strength, the higher is the repulsion. The above results suggest that low salinity promotes the repulsion between the proppant and coal, so the proppant particles must be injected at low ionic strength. However, flow of low salinity water causes lifting of reservoir fines, their migration and plugging the rock with consequent permeability and productivity decline. In order to determine the salinity value that do not cause drastic permeability damage due to fines migration, in the next section we carry out the laboratory and mathematical modelling of fines migration in coals.

3.7. Fine migration in coals

The traditional test on coreflood with piece wise constant decreasing salinity is carried out (Civan, 2010; Khilar and Fogler, 1987; Lever and Dawe, 1984). Core U_5 was used in set-up presented in Figs. 4 and 5. Eight values of salinity decreasing from 0.6 M up to 0.025 M have been applied. Fig. 13 shows drastic permeability decrease during the lowest salinity injection of 0.025 M, while the salinity decrease from 0.6 M to 0.050 M yields the moderate rock permeability decrease.

The experimental points in Fig. 13 are denoted by blue circles. The red curve corresponds to tuning of the model coefficients from the pressure drop data. The tuning results are presented in Table 4. The filtration coefficient λ_s and the drift delay factor α^* are assumed to be constant. As it follows from Eq. (B-6), the value $\beta_d \Delta \sigma_a^*$ is the increase of dimensionless pressure after straining of the amount of $\Delta \sigma_a^*$ of the fine particles. This value is tuned for each injection period.

Generally, the coefficient of determination R^2 is close to one, so the agreement between the experimental data and the modelling results is good. The experimental points lay on the red curves for salinities 0.6–0.05 M. However, there is some deviation during the injection of water with lowest salinity 0.025 M. It is explained by significant permeability decline that corresponds to mobilisation of the largest

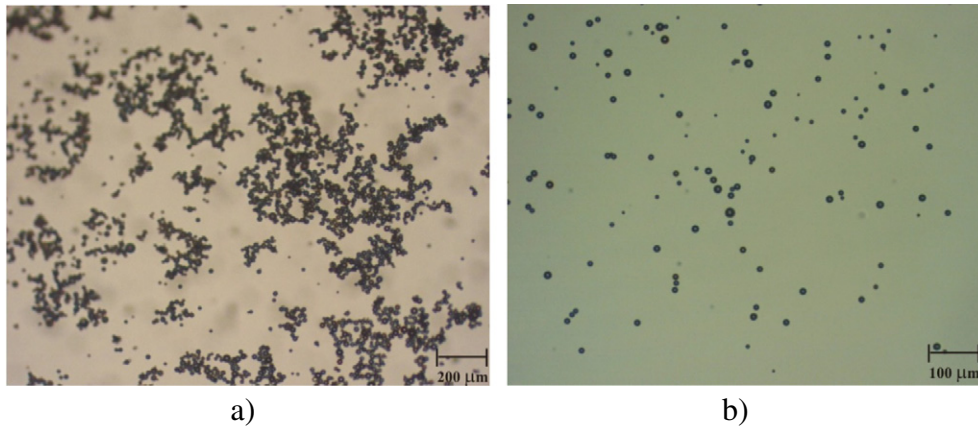


Fig. 10. Particle suspended in injected fluid: a) high salinity suspension; b) low salinity suspension.

fine amount if compared with other injections with higher salinity; the highly concentrated suspension might cause a multi particle bridging rather than a single particle plugging, so deep bed filtration system (B-5) must be modified.

The curve-fitting tool box of the software package MatLab-2013a based on the optimisation algorithm for the least-square method has been used (MATLAB, 2013).

Fig. 13 presents the results of sensitivity analysis of the tuned laboratory data with respect to drift delay factor that was increased two times, to filtration coefficient that was decreased two times and to products $\beta_d \Delta \sigma_{ai}^*$, $i = 1, 2, \dots, 8$ that were decreased two times. The corresponding permeability curves are shown in green, black and grey, respectively. Small perturbation of tuned parameters results in small perturbation of the measured data, suggesting that the inverse problem of the parameter tuning is well posed.

The obtained values of tuned parameters are located in common intervals that validate the explanation of the permeability decline in coal core during injection of low salinity water by fines migration.

The above assumptions of constant filtration coefficient λ^* and drift delay factor α^* correspond to low concentration of strained particles. However, those depend on the pore space geometry. Alteration of the geometry of the porous space by fines straining in thin cleat zones yields the strained-concentration-dependent filtration coefficient and drift delay factor. The problem of deep bed filtration with the filtration coefficient and drift delay factor as functions of the strained concentration allows for exact solution (Bedrikovetsky, 2008; Vjazmina et al., 2007). It yields well-posed inverse problem (see Alvarez et al., 2006,

2007). However, more information from the fine-migration test is required for unique determination of the functions $\lambda^* = \lambda(\sigma_s^*)$ and $\alpha^* = \alpha(\sigma_s^*)$. One of the ways around the problem is to measure pressure in the middle point of the core besides the inlet and outlet pressures (Bedrikovetsky et al., 2001).

Fig. 13 suggests that injection of water with ionic strength above 0.05 M results in moderate permeability decline, while injection of water with 0.025 M salinity causes strong decline in permeability. The results of Section 3.7 show that low salinity water should be used for graded particle injection. The current section's results suggest that the salinity should exceed 0.05 M in order to prevent the fine-migration-induced permeability damage.

4. Laboratory-based well behaviour prediction

4.1. Tuning of the permeability–straining diagram

In this section, the permeability–straining diagram is tuned from the laboratory tests presented in Section 3.6.

The results of the proppant injection tests are shown in Figs. 4 and 11. Points C, A' and D correspond to coal sample permeability at lowest (initial) pore pressure after injection of 5 µm proppant, first injection of 9.5 µm and second injection of 9.5 µm, respectively. Since the lowest pressure is the same for three injection cycles, the effective stress is also the same, so three points lay on the same curve with $\varepsilon_\sigma = \text{const}$. Points 1, 2, ..., 6 above the points C, A' and D correspond to permeabilities at lower pressures (higher stresses) after the proppant injection. All points 1 lay on the envelope due to zero effective stress at the injection pressure. Seventh points coincide with the points C, A' and D. Points with the same number are located on the same curves $\varepsilon_\sigma = \text{const}$. In particular, points C, A' and D lay on the curve $\varepsilon_\sigma = 4.9 \times 10^{-3}$.

So, there are 21 points to tune the permeability–straining diagram. The iso-effective-stress curves are interpolated by six order polynomials. The curve-fitting tool box of the software package MatLab-2013a has been used (MATLAB, 2013). The fitting results are shown in Fig. 14. Points 2', ..., 7' correspond to maximum permeabilities at a given effective stress; those are the target points. The target point that corresponds to points 1 has coordinates (0,1) in the plain (β, f) . Fig. 15 presents the target points for initial permeability–straining diagram (in black) and for tuned diagram (in blue). Six points 2', ..., 7' correspond to dimensionless effective stress values from the highest initial value up to the lowest value during the proppant injection. The points lay on a straight line with a good accuracy. It allows using this straight line for pressure dependency of permeability (Eq. (12)) inside the stimulated zone for calculation of the productivity index. The results of calculations are presented in the next section.

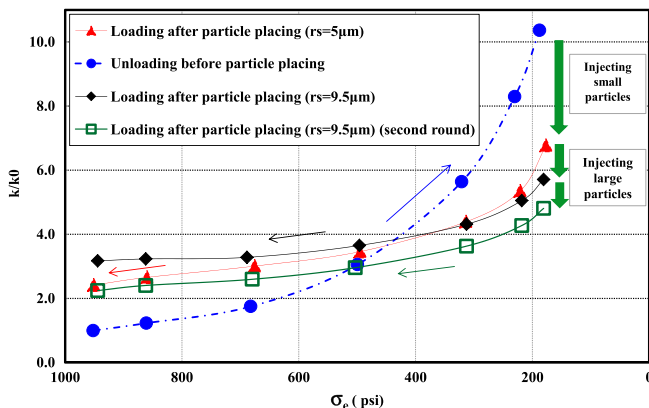


Fig. 11. Normalised permeability vs effective stress in low salinity water.

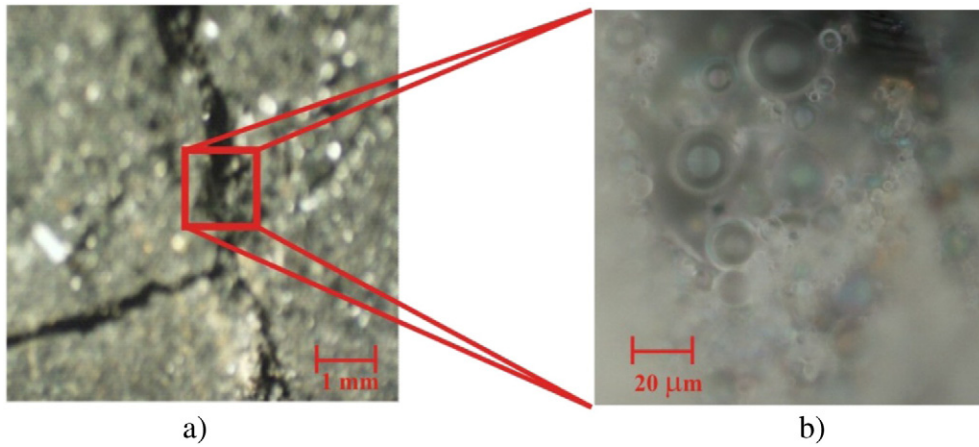


Fig. 12. Optical microscope images of the coal core inlet after low salinity suspension injection: a) fractured rock scale; b) deep inside fracture.

4.2. Calculation of productivity index

The permeability profile during the production after stimulation is shown in Fig. 16. The continuous blue curve corresponds to permeability profile during the depletion without stimulation. It was calculated using Eq. (5). The lower is the pore pressure, the lower is the permeability, see Eq. (1).

The purple, red and green curves correspond to permeabilities in stimulated zone under wellbore pressures during proppant injection that are $0.9P_{fr}$, $0.8P_{fr}$ and $0.7P_{fr}$. All injection pressures are maintained below the fracturing pressure in order to avoid the hydraulic fracturing. The higher is the injection pressure the wider are the cleats and the larger are the particles injected at the end of the schedule period that keep cleats open near the wellbore. Consequently, the higher is the injection pressure under the optimal injection schedule, the larger is the permeability. The profiles corresponding to theoretical permeability–straining diagram are marked by continuous curves; the dashed curves correspond to the matched diagram. The permeability profiles as calculated by the initial diagram are above those predicted from the diagram matched to the laboratory data.

Fig. 17 presents the pressure profiles during the production stage. The black curve corresponds to pressure profile without stimulation. Blue, green and red curves correspond to the stimulated areas with radii $0.03r_e$, $0.05r_e$ and $0.1r_e$. Pressure profiles inside the stimulated zones are located above that without stimulation. Therefore, the proppant injection allows achieving the same rate at the lower pressure drawdown, yielding the productivity index increase.

Fig. 18 shows the normalised productivity index versus stimulated radius for different injection pressures. The initial data for well behaviour prediction are adopted from the field case of Crowsnest coalfield (Fernie Basin, South-East British Columbia, Canada) (Gentzis, 2009). The larger is the stimulated area the higher is the productivity index after the stimulation. The higher is the injection pressure the higher is the productivity index.

The continuous curves correspond to initial permeability–straining diagram while the dashed curves have been calculated from the laboratory-data-matched diagram. The laboratory-based modelling produces almost the same results as the calculations based on the initial diagram in the case of small stimulation zone. However, the deviation becomes significant at large stimulation zone. The lower is the injection pressure the higher is the deviation (Fig. 18). The relative productivity index increases 2.5–5 times due to the graded injection of proppant particles.

The results of sensitivity analysis of the productivity index after stimulation with respect to fracture compressibility C_f is shown in Fig. 19. The higher is the fracture compressibility the larger proppant particles are injected and the higher is the final well productivity index. The deviation between the initial and laboratory-based modelling increase as C_f increases. PI increases as the injection pressure increases.

5. Discussions

The mathematical model for graded particle injection into naturally fractured porous media has numerous limitations; the corresponding assumptions are presented in Section 2. More advanced model for fractured media permeability versus stress and strained particle concentration may enhance the reliability of the well index prediction. For example, the presented model assumes the constant aperture and the network structure of the initial cleat system. The improved models for particle flow and capture into natural fractured systems should account for stochastic probabilistic distributions of fractures by their

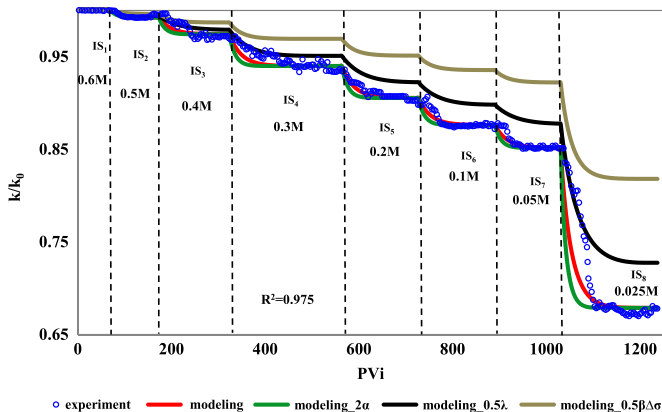


Fig. 13. Fines migration in coal beds during the salinity decrease.

Table 4
Tuned parameters of fines mobilisation straining.

Stage i	$(\beta_d \Delta \sigma_a^*)_i$	α_i^*	λ_{si}
2	0.0095	0.0055	5.669
3	0.0223	0.0055	5.669
4	0.0443	0.0055	5.669
5	0.0463	0.0055	5.669
6	0.0404	0.0055	5.669
7	0.0353	0.0055	5.669
8	0.3088	0.0055	5.669

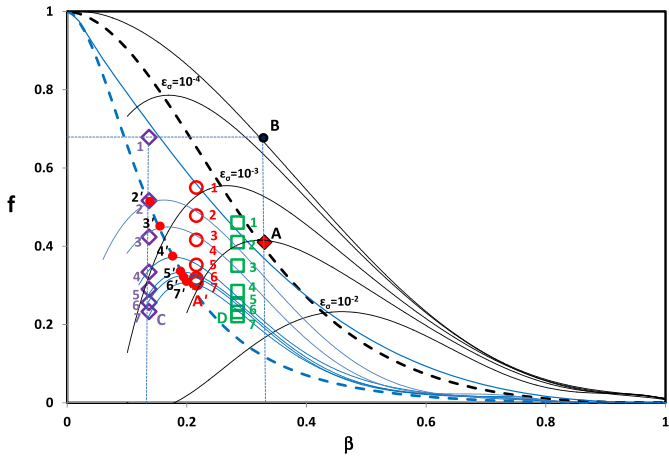


Fig. 14. Experimentally tuned f -normalised permeability vs proppant aspect ratio for various values of dimensionless effective stress.

opening, size and direction. The stochastic population balance models can be extended for fractured media and used for design and planning of the proposed technology under specific field conditions; percolation and effective medium theories can be used for transport properties prediction in the population balance models (Bedrikovetsky, 1993, 2008).

The common threshold values for the proppant jamming ratios in porous media are used in Section 3.2 to determine the proppant size that provides the proppant placement in the cleats. The above mentioned stochastic model for suspension transport would provide the threshold values for fractured systems, which can differ significantly from those in porous networks.

The present paper discusses well productivity enhancement during CBM dewatering due to graded proppant injection. However, the method can enhance the productivity during gas production too. Pressure depletion with the consequent effective stress increase results in micro fracturing of coal near to contact proppant–coal points. It causes the increase of the coal matrix surface and acceleration of methane desorption from the coal, finally resulting in well productivity enhancement. Besides, the proppant particles strained in the cleats capture the migrating fines and decrease their production, causing a positive environmental impact.

High potential energy barriers calculated via DLVO theory indicate the mutual particle–particle and particle–coal repulsion which prevents particles from agglomeration and attachment to coal matrix leading to permeability enhancement at low salinity injection. Increase of brine salinity results in the external cake formation, attachment neat to core inlet and decrease in the overall coal core permeability.

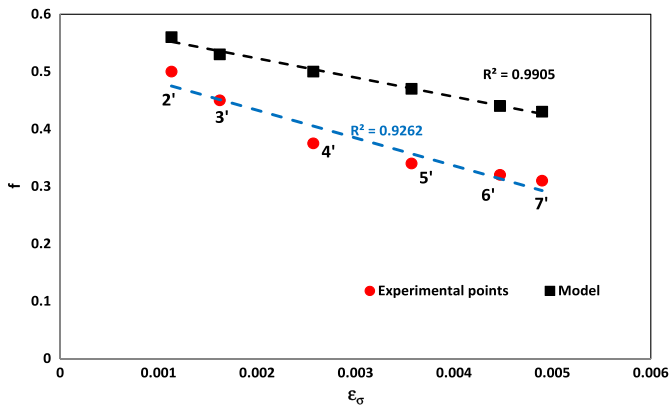


Fig. 15. The permeability correction factor f as a function of dimensionless effective stress for theoretical prediction and from experimental data.

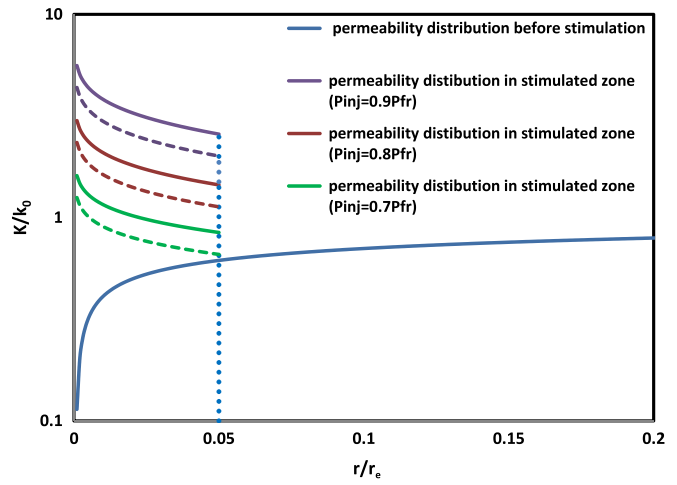


Fig. 16. Permeability distribution profile for stimulation zone radius $r_{st} / r_e = 0.05$. Here solid lines represent permeability distributions calculated theoretically. Dash lines represent the permeability distributions calculated using the experimentally tuned model.

According to the mathematical model, higher injection pressure results in a greater increase of well productivity index due to graded proppant injection. The higher is the cleat compressibility the higher is the well productivity index. The lower is the stimulation zone, the less is the difference between the pure theoretical model and the experimentally tuned model. The above speculations are helpful for optimal design and planning of the graded particle injection into CBM reservoirs for well stimulation without hydraulic fracturing.

Wider spectrum of coal properties must be investigated in laboratory for more general formulations of the favourable conditions for the proposed technology applications.

We discuss the effect of graded proppant injection on dewatering of CBM reservoirs. The effects on gas production accounting for micro fracturing and incremental gas desorption are subject of a separate forthcoming work.

Further developments of the graded proppant injection include periodical injections alternated by the gas production periods, where the coal bed shrinks during pressure depletion and desorption, resulting in deeper proppant penetration after each injection cycle due to continuous pore pressure decrease with matrix shrinkage and the permeability enhancement.

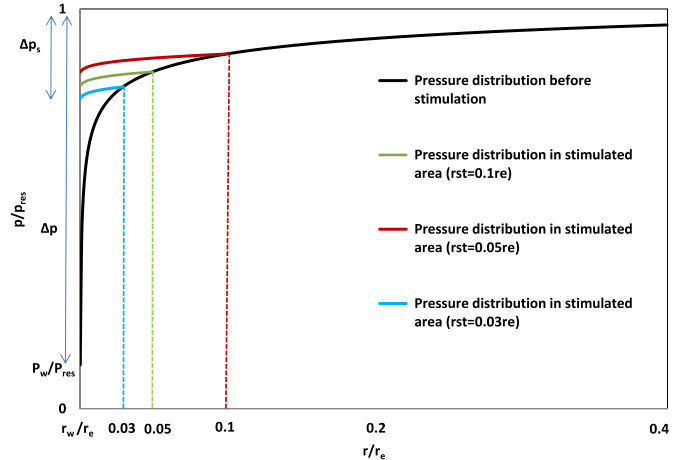


Fig. 17. Pressure distribution profiles during production.

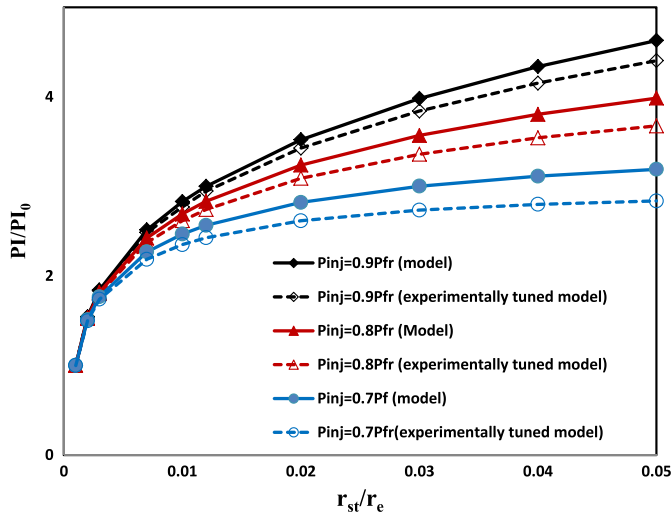


Fig. 18. Normalised productivity index vs stimulation radius.

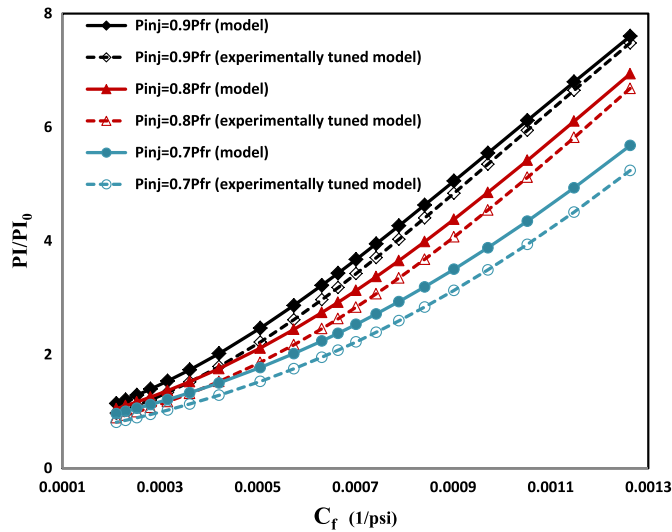


Fig. 19. Normalised productivity index versus fracture compressibility for $r_{st} / r_e = 0.05$.

Another application is an additional well stimulation during the hydraulic fracturing. Graded proppant injection during hydraulic fracturing can transport fine particles into cleats during the leak-off. The effect of dewatering acceleration by keeping the cleats open during the production is the main advantage of the proposed technology.

6. Conclusions

The analytical modelling of the graded proppant injection into CBM reservoirs based on the laboratory corefloods allows drawing the following conclusions:

- The analytical model for graded proppant injection into fractured media, accounting for exponential permeability dependency of stress and rock deformation in untreated zone, allows for explicit formulae for areal pressure and permeability distributions and well index during injection and production.
- DLVO-theory-based calculations provide the ionic strength and pH conditions for the proppant–coal and proppant–proppant attachment and repulsion.

- Using the low salinity water prevents proppant–coal attraction, providing deep bed filtration of the proppant and its placement in the cleats. However, it facilitates fine migration, resulting in cleat plugging and permeability damage.
- The salinity interval favourable for the coal–proppant repulsion and low fines migration for the coal samples investigated in the presented study is 0.1–0.05 M.
- If compared with modelling based on the permeability–straining diagram for a single rectangular fracture, tuning of the mathematical model from the laboratory experiments results in 10% decrease of the productivity index, for the case where the stimulated zone is 5% of the drainage area.
- The ultra-fine glass proppant injection results in 3.0–3.2 times permeability enhancement for the coal samples investigated. For injection pressures $0.9P_{fr}$, $0.8P_{fr}$ and $0.7P_{fr}$, it yields 3–5 times enhancement of well productivity index.
- The sensitivity analysis of well index shows that the most influential parameters are the stimulated zone size, injection pressure and the cleat system compressibility.

Nomenclature

A_{123}	Hamaker constant, $M L^2 T^{-2}$
a	Cleat spacing, L
c	Concentration of suspension fluid, L^{-3}
C_f	Cleat compressibility, $M^{-1} L T^2$
D	Core diameter, L
d_p	Particle diameter, L
E	Young's modulus of elasticity, $M L^{-1} T^{-2}$
e	Elementary electric charge, IT
F	Axial load, $M L T^{-2}$
F_e	Electrostatic force, $M L T^{-2}$
F_d	Drag force, $M L T^{-2}$
f	Permeability correction factor
h	Cleat aperture, L
h^*	Separation distance, L
IS	Ionic strength
j	Jamming ratio
k	Permeability of reservoir, L^2
k_B	Boltzmann constant, $M L^2 T^{-2} K^{-1}$
l	Distance between adjacent proppant particles, L
l^*	Lever arm ratio
l_n	Lever arm for normal forces, L
L	Core length, L
n	Number of cleats
n_∞	Bulk number density of ions, L^{-3}
p	Fluid pressure, $M L^{-1} T^{-2}$
p_f	Fracturing pressure, $M L^{-1} T^{-2}$
p_0	Reservoir fluid pressure, $M L^{-1} T^{-2}$
p_w	Fluid pressure at wellbore, $M L^{-1} T^{-2}$
p_{inlet}	Inlet pressure, $M L^{-1} T^{-2}$
p_{ob}	Overburden pressure, $M L^{-1} T^{-2}$
PI_0	Well productivity index of non-stimulated reservoir, $M^{-1} L^3 T$
PI	Well productivity index of stimulated reservoir, $M^{-1} L^2 T^3$
q	Injection/production rate per unit reservoir thickness, $L^2 T^{-1}$
r	Distance from wellbore, L
r_D	Dimensionless radius
r_{Ds}	Dimensionless particle size
r_e	Drainage radius, L
r_s	Particle radius, L
r_{smin}	Minimum particle radius, L
r_{st}	Stimulation radius, L
r_{scr}	The minimum particle size mobilised by the flow with salinity, L
r_w	Wellbore radius, L

r_{wD}	Dimensionless wellbore radius
s	Salinity
t_s	Settling time, T
T	Absolute temperature, K
u_t	Tangential cross flow velocity of fluid in the centre of the particle
U_E	Electrophoretic mobility of particle, M T ² I
Z	Valence of a symmetrical electrolyte solution
V	Total potential of interaction, M L ² T ⁻²

Greek Letters

α	Biot effective stress coefficient
α^*	Drift delay factor
β	Dimensionless packing aspect ratio
β^*	Optimum dimensionless packing aspect ratio
β_d	Formation damage coefficient
γ_1	Reduced surface potential for particles
γ_2	Reduced surface potential for coals
ε	Dielectric permittivity of MilliQ water
ε_q	Dimensionless rate
ε_{cr}	Dimensionless stress
ζ	Zeta potential M L ² T ⁻³ I ⁻¹
κ	Debye–Hückel reciprocal length, L ⁻¹
λ	Characteristic wavelength of the interaction L
λ_s	Filtration coefficient for straining L ⁻¹
μ	Dynamic viscosity of fluid, M L ⁻¹ T ⁻¹
ν	Poisson's ratio
σ	Stress, M L ⁻¹ T ⁻²
σ_c	Collision diameter, L
σ_{cr}^*	Maximum retention concentration
σ_e	Effective stress, M L ⁻¹ T ⁻²
σ_{hi}	Minimum horizontal stress, M L ⁻¹ T ⁻²
σ_{H}^*	Maximum horizontal stress, M L ⁻¹ T ⁻²
σ_s^*	Retention concentration of fines,
$\Delta\sigma_a^*$	Mobilised concentration of attached particles
Σ_a	Particle size distribution on the surface
ϕ_c	Cleat porosity
ϕ_H	Helium porosity
ϕ_w	Water porosity
ω	Drag factor

Subscript

o	Initial value of a parameter
P	Production
J	Injection
cr	Critical
$part$	Particle
$coal$	Coal

Superscript

exp	Experiment
$model$	Model

Abbreviations

CBM	Coal bed methane
DLVO	Derjaguin–Landau–Verwey–Overbeek
EDL	Electrical double layer

Acknowledgements

The authors are grateful to Dr. T. Carageorgos (Australian School of Petroleum) for fruitful discussions. Prof. S. Golding (University of Queensland) was helpful in providing the coal samples.

The work was generously sponsored by Australian Research Council (Linkage Project 110200799).

Appendix A. Electrostatic interactions in the particle–coal systems

The total interaction potential energy between the injected particles and coal matrix is a sum of interaction potential energies arising from the long-range London–van der Waals forces, the short-range attractive/repulsive electrical double layer and Born's repulsion forces as follows (Gregory, 1981; Israelachvili, 2011; Landau and Lifshitz, 1980; Verwey et al., 1999):

$$V = -\frac{A_{123}r_s}{6h^*} \left[1 - \frac{5.32h^*}{\lambda} \ln \left(1 + \frac{\lambda}{5.32h^*} \right) \right] + \frac{128\pi r_s n_\infty k_B T}{\kappa^2} \gamma_1 \gamma_2 e^{-\kappa h^*} + \frac{A_{123}\sigma_c^6}{7560} \left[\frac{8r_s + h^*}{(2r_s + h^*)^7} + \frac{6r_s - h^*}{h^{*7}} \right]. \tag{A-1}$$

Here A_{123} is the Hamaker constant; $\lambda = 100$ nm is the characteristic wavelength of the interaction adopted from; h^* is particle–surface (sphere–plate) separation distance, n_∞ is bulk number density of ions; $k_B = 1.381 \times 10^{23}$ J/K is the Boltzmann constant; $T = 298.15$ K is absolute temperature of the system; $\gamma_1 = \tanh\left(\frac{ze\zeta_p}{4k_B T}\right)$ and $\gamma_2 = \tanh\left(\frac{ze\zeta_c}{4k_B T}\right)$ are reduced surface potentials for particles and coals; ζ_p and ζ_c are zeta potentials for injected particles and coal, respectively; z is valence of a symmetrical electrolyte solution, $z = 1$ for NaCl; $e = 1.602 \times 10^{-19}$ C is the elementary electric charge. Hamaker constant is calculated for a system glass–water–coal for 0.6 M NaCl suspension according to the formula proposed in Israelachvili (2011). The calculations for ionic strength varying from 0.05 to 0.6 M show that Hamaker constant varies by 0.3% only. Thus, the effect of ionic strength on Hamaker constant is neglected. The calculated value $A_{123} = 1.270 \times 10^{-20}$ J excellently agree with that reported for coals by Chaturvedi et al. (2009). The typical value for the collision diameter $\sigma_c = 0.5$ nm is adopted from Elimelech et al. (1995).

The choice of the appropriate expressions for electrostatic double layer (EDL) interaction potential energies depends on the Debye–Hückel parameter, κ , and the particle radius, r_s . The inverse to κ is equal to the EDL thickness. The Debye–Hückel constant is a function of the ionic solution strength (Elimelech et al., 1995). The EDL thickness, $\frac{1}{\kappa}$, varies from 3.92×10^{-4} to 1.36×10^{-3} μm for the studied ionic strengths in the range from 0.6 to 0.05 M NaCl, respectively. The EDL thickness is significantly smaller than the particle sizes. For this case, the formulae for the double electric layer energy for sphere–plate interactions corresponds to the second additive in Eq. (A-1) (Elimelech et al., 1995).

The third additive in Eq. (A-1) corresponds to Born's potential energy (Ruckenstein and Prieve, 1976).

The total interaction potential energy between the injected particles is also a sum of interaction potential energies arising from the long-range London–van der Waals forces, the short-range attractive/repulsive electrical double layer and Born's repulsion forces as follows:

$$V = -\frac{A_{123}r_s}{12h^*} \left[1 - \frac{5.32h^*}{\lambda} \ln \left(1 + \frac{\lambda}{5.32h^*} \right) \right] + \frac{64\pi r_s n_\infty k_B T}{\kappa^2} \gamma_1 \gamma_2 e^{-\kappa h^*} + \frac{A_{123}\sigma_c^6}{7560} \left[\frac{8r_s + h^*}{(2r_s + h^*)^7} + \frac{6r_s - h^*}{h^{*7}} \right]. \tag{A-2}$$

Appendix B. Mathematical model for fines migration

Following the work by Bedrikovetsky et al. (2011), in this Appendix we briefly derive maximum retention concentration as a function of ionic strength, which is the model for fines detachment with following straining of the coal cleats.

The fine particle on the pore wall is subject to drag and electrostatic forces. Gravity and lifting forces are negligibly smaller than drag and electrostatic forces. Mechanical equilibrium of the fine particle on the

cleat surface is described by torque balance of drag and electrostatic forces

$$F_e l^* = F_d, \quad F_e = \max\left(-\frac{\partial V}{\partial h^*}\right). \quad (\text{B-1})$$

Here l^* is the lever arm ratio that is equal to the ratio between the normal and tangential levers; the electrostatic force is determined by the total DLVO energy potential, see Eq. (A-1). Since the fine detachment occurs if the drag torque exceeds the torque of the electrostatic force F_e , maximum value of F_e is the particle detachment condition in Eq. (B-1).

The expression for drag force exerting the particle on the plane surface is obtained from asymptotic solution of the Navier–Stokes equations (O'Neill, 1968):

$$F_d = \omega \pi \mu r_s u_t \Big|_{\frac{h}{2}-r_s} \quad (\text{B-2})$$

where μ is the viscosity, r_s is the particle radius, h is the width of the channel, u_t is the tangential cross flow velocity of fluid in the centre of the particle that is calculated from Hele–Shaw flow and the drag factor ω is equal to $6\pi \times 1.7$. The case of $\omega = 6$ corresponds to the Stokes formula for a particle in the uniform boundary-free flux.

The Hertz's theory presents with the explicit formula for radius of the contact area which is equal to the normal lever l_n . It was originally derived by Derjaguin et al. (1975) for the case of particle deformed by electrostatic force:

$$l^* = \left(\frac{3F_e(1-\nu^2)}{r_s^2 E}\right)^{1/3}. \quad (\text{B-3})$$

Here, ν is the Poisson's ratio and E is Young's elasticity modulus of the particle and of the rock.

Let us consider the concentration distribution of attached particles with different sizes $\Sigma_a(r_s)$ retained in a monolayer. Both forces in Eq. (A-1) for mechanical equilibrium are particle-size dependent while electrostatic force is ionic-strength dependent. So, Eq. (A-1) is a transcendental equation for implicit dependency for the critical radius of the particle mobilised by the flow with ionic strength (IS): $r_s = r_{scr}(IS)$. The critical size of released particle $r_{scr}(IS)$ is a monotonically decreasing function and the particles are mobilised in decreasing order of their sizes with the decrease of ionic strength. Therefore, the maximum retention concentration for a given velocity U includes all the particles with radii smaller than $r_{scr}(IS)$:

$$\sigma_{cr}^*(U) = \int_p^{r_{scr}(IS)} \Sigma_a(r_s) dr_s. \quad (\text{B-4})$$

The salinity change from 1 to 2 results in release of particles with sizes between r_{scr1} and r_{scr2} . The migration of the released particles causes their straining in thin pores and consequent permeability decline. Mass balance of suspended and strained fines in porous media is (Civan, 2007, 2010):

$$\frac{\partial \phi c}{\partial t} + \alpha^* U \frac{\partial c}{\partial x} = -\lambda_s c \alpha^* U \quad (\text{B-5})$$

where c and c_s^* are concentrations of suspended and strained fines; λ_s is the filtration coefficient for straining. The drift delay factor α^* accounts for slow particle motion.

Darcy equation accounts for permeability decline due to size exclusion of fine particles:

$$U = -\frac{k(\sigma_s^*)}{\mu} \frac{\partial p}{\partial x}, \quad k(\sigma_s^*) = \frac{k_0}{1 + \beta_d \sigma_s^* (\Delta \sigma_a^*)} \quad (\text{B-6})$$

where k is the permeability as a function of strained particle concentration, β_d is the formation damage coefficient, $\Delta \sigma_a^*$ is the mobilised concentration of attached particles, k_0 is the initial permeability, μ is the viscosity of suspension and p is the pressure.

The exact solution of the problem (B-5) is presented in Bedrikovetsky et al. (2011) and is used for tuning of the experimental data on fines migration in coals in Section 3.7.

References

- Alvarez, A.C., Bedrikovetsky, P., Hime, G., Marchesin, D., Rodríguez, J.R., 2006. A fast inverse solver for the filtration function for flow of water with particles in porous media. *J. Inverse Prob.* 22, 69–88.
- Alvarez, A.C., Hime, G., Marchesin, D., Bedrikovetsky, P., 2007. The inverse problem of determining the filtration function and permeability reduction in flow of water with particles in porous media. *Transp. Porous Media* 70, 43–62.
- Amyx, J.W., Bass, D.M., Whiting, R.L., 1960. *Petroleum Reservoir Engineering: Physical Properties*. McGraw-Hill College.
- Bedrikovetsky, P., 1993. *Mathematical Theory of Oil and Gas Recovery: With Applications to Ex-USSR Oil and Gas Fields*. Springer.
- Bedrikovetsky, P., 2008. Upscaling of stochastic micro model for suspension transport in porous media. *Transp. Porous Media* 75, 335–369.
- Bedrikovetsky, P.G., Marchesin, D., Checaira, F., Serra, A.L., Resende, E., 2001. Characterization of deep bed filtration system from laboratory pressure drop measurements. *J. Pet. Sci. Eng.* 64 (3), 167–177.
- Bedrikovetsky, P., Siqueira, F.D., Furtado, C.A., Souza, A.L.S., 2011. Modified particle detachment model for colloidal transport in porous media. *Transp. Porous Media* 86, 353–383.
- Bedrikovetsky, P.G., Keshavarz, A., Khanna, A., McKenzie, K.M., Kotousov, A., 2012. Stimulation of natural cleats for gas production from coal beds by graded proppant injection. *SPE Asia Pacific Oil and Gas Conference and Exhibition, Perth, Australia*. SPE-158761.
- Biot, M.A., 1941. General theory of three-dimensional consolidation. *J. Appl. Phys.* 12, 155–164.
- Chaturvedi, T., Schembre, J., Kovscek, A., 2009. Spontaneous imbibition and wettability characteristics of Powder River Basin coal. *Int. J. Coal Geol.* 77, 34–42.
- Civan, F., 2007. *Reservoir Formation Damage (Fundamentals, Modeling, Assessment, and Mitigation)*, 2nd ed. Gulf Professional Publishing.
- Civan, F., 2010. Non-isothermal permeability impairment by fines migration and deposition in porous media including dispersive transport. *Transp. Porous Media* 85, 233–258.
- Clarkson, C.R., 2013. Production data analysis of unconventional gas wells: review of theory and best practices. *Int. J. Coal Geol.* 109, 101–146.
- Connell, L.D., 2009. Coupled flow and geomechanical processes during gas production from coal seams. *Int. J. Coal Geol.* 79, 18–28.
- Connell, L.D., Lu, M., Pan, Z., 2010. An analytical coal permeability model for tri-axial strain and stress conditions. *Int. J. Coal Geol.* 84, 103–114.
- Derjaguin, B., Muller, V., Toporov, Y.P., 1975. Effect of contact deformations on the adhesion of particles. *J. Colloid Interface Sci.* 53, 314–326.
- Economides, M.J., Martin, T., 2007. *Modern Fracturing: Enhancing Natural Gas Production*. ET Publishing Houston, Texas.
- Elimelech, M., Gregory, J., Jia, X., Williams, R., 1995. *Particle Deposition and Aggregation: Measurement, Modelling, and Simulation*. Butterworth-Heinemann, New-York, USA.
- Gash, B.W., 1991. Measurement of “rock properties” in coal for coalbed methane production. *SPE Annual Technical Conference and Exhibition, Inc., Dallas, Texas*. SPE-22909-MS.
- Gentzis, T., 2009. Stability analysis of a horizontal coalbed methane well in the Rocky Mountain Front Ranges of southeast British Columbia, Canada. *Int. J. Coal Geol.* 77, 328–337.
- Ghalambor, A., Ali, S.A., Norman, W.D., 2009. *Frac Packing Handbook*. Society of Petroleum Engineers.
- Gregory, J., 1981. Approximate expressions for retarded van der Waals interaction. *J. Colloid Interface Sci.* 83, 138–145.
- Guo, B., Ghalambor, A., 2012. *Natural Gas Engineering Handbook*, 2nd Ed. Gulf Professional Publishing.
- Guo, B., Lyons, W.C., Ghalambor, A., 2011. *Petroleum Production Engineering, a Computer-assisted Approach*. Gulf Professional Publishing.
- Israelachvili, J.N., 2011. *Intermolecular and Surface Forces*, Revised third edition. Academic Press.
- Johnson Jr., R.L., Flottman, T., Campagna, D.J., 2002. Improving results of coalbed methane development strategies by integrating geomechanics and hydraulic fracturing technologies. *SPE Asia Pacific Oil and Gas Conference and Exhibition*. SPE-77824-MS.
- Keshavarz, A., Mobbs, K., Khanna, A., Bedrikovetsky, P., 2013. Stress-based mathematical model for graded proppant injection in coal bed methane reservoirs. *APPEA J.* 337–346.
- Keshavarz, A., Badalyan, A., Carageorgos, T., Bedrikovetsky, P., Johnson, R., 2014. Enhancement of CBM well fracturing through stimulation of cleat permeability by ultra-fine particle injection. *APPEA J.* 155–166.
- Khanna, A., Kotousov, A., Sobey, J., Weller, P., 2012. Conductivity of narrow fractures filled with a proppant monolayer. *J. Pet. Sci. Eng.* 100, 9–13.
- Khanna, A., Keshavarz, A., Mobbs, K., Davis, M., Bedrikovetsky, P., 2013. Stimulation of the natural fracture system by graded proppant injection. *J. Pet. Sci. Eng.* 111, 71–77.

- Khilar, K.C., Fogler, H.S., 1987. Colloidally induced fines migration in porous media. *Rev. Chem. Eng.* 4, 41–108.
- Landau, L., Lifshitz, E., 1980. *Course of Theoretical Physics: Statistical Physics Part 1*. Robert Maxwell, MC.
- Lever, A., Dawe, R.A., 1984. Water-sensitivity and migration of fines in the hopeman sandstone. *J. Pet. Geol.* 7, 97–107.
- MATLAB R2013a, The MathWorks, Inc., Natick, Massachusetts, United States.
- Noam, W., 2012. A review of colloid transport in fractured rocks. *J. Mt. Sci.* 6, 006.
- O'Neill, M., 1968. A sphere in contact with a plane wall in a slow linear shear flow. *Chem. Eng. Sci.* 23, 1293–1298.
- Palmer, I., Mansoori, J., 1998. How permeability depends on stress and pore pressure in coalbeds: a new model. *SPE Reserv. Eval. Eng.* 6, 539–544 (SPE-52607-PA).
- Pan, Z., Connell, L.D., 2012. Modelling permeability for coal reservoirs: a review of analytical models and testing data. *Int. J. Coal Geol.* 92, 1–44.
- Pan, Z., Connell, L.D., Camilleri, M., 2010. Laboratory characterisation of coal reservoir permeability for primary and enhanced coalbed methane recovery. *Int. J. Coal Geol.* 82, 252–261.
- Rahman, M., Hossain, M.M., Rahman, S., 2002. A shear-dilation-based model for evaluation of hydraulically stimulated naturally fractured reservoirs. *Int. J. Numer. Anal. Methods Geomech.* 26, 469–497.
- Reiss, L.H., 1980. *The Reservoir Engineering Aspects of Fractured Formations*. Editions Technip.
- Rodrigues, S., Dickson, S., 2014. A phenomenological model for particle retention in single, saturated fractures. *Groundwater* 52, 277–283.
- Ruckenstein, E., Prieve, D.C., 1976. Adsorption and desorption of particles and their chromatographic separation. *AIChE J.* 22, 276–283.
- Seidle, J., 2011. *Fundamentals of Coalbed Methane Reservoir Engineering*. PennWell Books.
- Seidle, J., Jeansonne, M., Erickson, D., 1992. Application of matchstick geometry to stress dependent permeability in coals. *SPE Rocky Mountain Regional Meeting*. SPE-24361.
- Shi, J.-Q., Durucan, S., 2005. A model for changes in coalbed permeability during primary and enhanced methane recovery. *SPE Reserv. Eval. Eng.* 8, 291–299 (SPE-87230-PA).
- Stolarski, T., Nakasone, Y., Yoshimoto, S., 2006. *Engineering Analysis with ANSYS Software*. Elsevier.
- Van Golf-Racht, T.D., 1982. *Fundamentals of Fractured Reservoir Engineering*. Elsevier.
- van Oort, E., van Velsen, J.F.G., Leerlooijer, K., 1993. Impairment by suspended solid invasion: testing and prediction. *J. SPE Prod. Facil.* 8, 178–184 SPE-23822-PA.
- Verwey, E.J.W., Overbeek, J.T.G., Overbeek, J.T.G., 1999. *Theory of the Stability of Lyophobic Colloids*. Courier Dover Publications.
- Vjazmina, E., Bedrikovetsky, P., Polyanin, A.D., 2007. Exact solutions of non-linear equations for flow in porous media and for convective mass transfer. *J. Theor. Fundam. Chem. Eng.* 41 (5), 580–588.
- Wang, G., Wang, Z., Rudolph, V., Massarotto, P., Finley, R., 2007. An analytical model of the mechanical properties of bulk coal under confined stress. *Fuel* 86, 1873–1884.
- Wang, G., Massarotto, P., Rudolph, V., 2009. An improved permeability model of coal for coalbed methane recovery and CO₂ geosequestration. *Int. J. Coal Geol.* 77, 127–136.
- Wang, G., Wei, X., Wang, K., Massarotto, P., Rudolph, V., 2010. Sorption-induced swelling/shrinkage and permeability of coal under stressed adsorption/desorption conditions. *Int. J. Coal Geol.* 83, 46–54.

6 Deep bed and cake filtration of two-size particle suspension in porous media

Sacramento, R.N., **Yang, Y.**, You, Z., Waldmann, A., Martins, A.L., Vaz, A.S., Zitha, P.L., Bedrikovetsky, P.

Journal of Petroleum Science and Engineering, 126 (2014) 201-210

Statement of Authorship

Title of Paper	Deep bed and cake filtration of two-size particle suspension in porous media
Publication Status	<input checked="" type="checkbox"/> Published <input type="checkbox"/> Accepted for Publication <input type="checkbox"/> Submitted for Publication <input type="checkbox"/> Unpublished and Unsubmitted work written in manuscript style
Publication Details	Sacramento, R.N., Yang, Y., You, Z., Waldmann, A., Martins, A.L., Vaz, A.S., Zitha, P.L. and Bedrikovetsky, P., 2015. Deep bed and cake filtration of two-size particle suspension in porous media. Journal of Petroleum Science and Engineering, 126, pp.201-210.

Author Contributions

By signing the Statement of Authorship, each author certifies that:

- i. the candidate's stated contribution to the publication is accurate (as detailed above);
- ii. permission is granted for the candidate to include the publication in the thesis; and
- iii. the sum of all co-author contributions is equal to 100% less the candidate's stated contribution

Name of Principal Author	Sacramento, R.N.		
Contribution to the Paper	Performed laboratory tests, derived analytical model and performed data treatment		
Signature		Date	

Name of Co-Author (Candidate)	Yulong Yang		
Contribution to the Paper	Derived analytical model, performed data treatment and manuscript preparation		
Overall percentage (%)	50%		
Signature		Date	20/07/2016

Name of Co-Author	Zhenjiang You		
Contribution to the Paper	Helped in data interpretation and manuscript preparation		
Signature		Date	20/7/16

Name of Co-Author	Alex Waldmann		
Contribution to the Paper	Supervised development of work and manuscript evaluation		
Signature		Date	

Name of Co-Author	André L. Martins		
Contribution to the Paper	Supervised development of work and manuscript evaluation		
Signature		Date	

Name of Co-Author	Alexandre Vaz		
Contribution to the Paper	Supervised development of work, helped in data interpretation		
Signature		Date	11/JUL/2016

Name of Co-Author	Pacelli L.J. Zitha		
Contribution to the Paper	Consulted on formulation of the work and manuscript evaluation		
Signature		Date	

Name of Co-Author	Pavel Bedrikovetsky		
Contribution to the Paper	Supervised development of work, helped in data interpretation and manuscript evaluation		
Signature		Date	21/07/2016



ELSEVIER

Contents lists available at ScienceDirect

Journal of Petroleum Science and Engineering

journal homepage: www.elsevier.com/locate/petrol

Deep bed and cake filtration of two-size particle suspension in porous media

Rebeca N. Sacramento^a, Yulong Yang^b, Zhenjiang You^{b,*}, Alex Waldmann^c, André L. Martins^c, Alexandre S.L. Vaz^a, Pacelli L.J. Zitha^d, Pavel Bedrikovetsky^b^a Laboratory of Exploration and Production Engineering LENEPE, North Fluminense State University UENF, Macaé, RJ, Brazil^b Australian School of Petroleum, The University of Adelaide, SA 5005, Australia^c Research and Development Centre CENPES, Petrobras, Rio de Janeiro, RJ, Brazil^d Department of Geotechnical, Delft University of Technology, Delft, The Netherlands

ARTICLE INFO

Article history:

Received 11 September 2013

Accepted 4 December 2014

Available online 13 December 2014

Keywords:

External cake

Deep bed filtration

Cake formation

Transition time

Porous media

Analytical solution

ABSTRACT

Formation of low permeable external filter cake during drilling and water injection has been widely reported in the literature. It may cause significant decrease in well index. The process is very sensitive to size distribution of injected particles. We propose a new mathematical model for cake formation with deep bed filtration for two-particle-size injection. The basic equations account for three stages: formation of cake from large particles with simultaneous deep bed filtration of small particles; small particle capture in the cake with formation of the internal cake inside the external cake; build-up of the uniform cake from the mixture of two-size particles. The analytical model is derived for three stages. Two regimes of the cake formation are identified, which correspond to the high and low concentrations of injected small particles. The laboratory coreflood with two-particle-size suspension injection with monitoring the rate and pressure drop along the core is performed. The matched mathematical model shows good agreement with the laboratory data.

© 2014 Elsevier B.V. All rights reserved.

1. Introduction

Deep bed filtration and external filter cake formation are common phenomena encountered in the petroleum industry, which may lead to severe permeability decline and formation damage (Ghalambor and Economides, 2002; Ding et al., 2004; Ding and Renard, 2005; Ding et al., 2006; Wagner et al., 2006; Civan, 2007; Dalmazzone et al., 2007; Quintero et al., 2007; Ding et al., 2008; Salimi et al., 2009; Lohne et al., 2010; Karimi et al., 2011). During drilling, completion or produced water reinjection, fluids carrying suspended particles enter the wellbore. Due to the pressure difference between the wellbore and the reservoir formation (the pressure in the well is higher than that of the formation during the overbalanced drilling), the fluid penetrates into the formation. Particles suspended in the fluid with sizes larger than the pore throats in the formation may accumulate on the wellbore surface, forming a cake. This process is known as the external cake formation (Ruth, 1935; Ochi et al., 1999; Parn-anurak and Engler, 2005; Ochi et al., 2007; Windarto et al., 2011; Ytrehus

et al., 2013). However, those fine particles smaller than the pore throats of external cake may pass through the cake and penetrate into the formation. During the filtration, the solid particles suspended in the carrier fluid may be separated from the liquid phase due to several different mechanisms, such as gravity, Brownian motion, size exclusion, etc. (Ochi and Vernoux, 1999; Shapiro et al., 2007; Yuan and Shapiro, 2011; You et al., 2013; Yuan et al., 2013). The process of suspension transport in porous media accompanied by particle capture in the pores is called deep bed filtration (Payatakes et al., 1974; Pang and Sharma, 1997; Khilar and Fogler, 1998; Bedrikovetsky, 2008; You et al., 2014).

The classical deep bed filtration (DBF) model developed by Herzig et al. (1970) consists of two equations—one for particle population balance and the other for particle capture kinetics. The macro scale functions including suspended and retained particle concentrations and the filtration coefficient as a function of retained concentration are introduced into the model. Analytical solutions to the direct problems for model prediction (Herzig et al., 1970) and to the inverse problems for parameter determination (Wennberg and Sharma, 1997; Bedrikovetsky et al., 2001) have been obtained. This model has shown a good agreement with experimental data and has been used to predict the well injectivity decline based on the experimental core flood data.

* Corresponding author. Fax: +61 8 8303 4345.

E-mail address: zyou@asp.adelaide.edu.au (Z. You).

Nomenclature			
L	core length, m	T_3	catching-up time of the internal cake front
r_s	small particle radius, m	X	dimensionless coordinate
r_1	large particle radius, m	x	coordinate, m
c_1^0	initial total particle concentration, ppm	z	internal cake thickness, m
c_2^0	initial large particle concentration, ppm		
c_3^0	initial small particle concentration, ppm	<i>Greek letters</i>	
D_p	particle diameter, m	α	critical coefficient
D_3	speed of mixture cake growth	β	formation damage coefficient
J	impedance	λ	filtration coefficient
$k_m(0)$	initial core permeability, m^2	μ	viscosity of suspension, Pa s
k_{ec12}	permeability of external cake filled by internal cake of small particles, m^2	τ	tortuosity
R	ratio of external cake porosity and core porosity	ϕ_1	core porosity
ΔP_{ec1}	pressure drop between the fronts of external and internal cake, Pa	ϕ_2	porosity of internal cake
ΔP_{ec2}	pressure drop between the front of internal cake and the core inlet, Pa	ϕ_3	porosity of external cake
ΔP_m	pressure drop of the core, Pa	ϕ_4	porosity of the mixture cake
S	dimensionless retention concentration	σ	retained particle concentration, m^{-3}
U	Darcy velocity, m/s	<i>Subscripts</i>	
T	dimensionless time	m	medium
t	time, s	c	cake
T_{tr}	transition time	ec	external cake
		ecmix	mixture cake

Analytical models for deep bed filtration with constant and varying rates for linear and axisymmetric flows have been derived by Civan and Rasmussen (2005). Numerous laboratory tests have been treated by the analytical model with the observation of good agreement between the analytical and experimental modelling. More complex model for deep bed filtration is proposed by Civan and Nguyen (2005). All pathways are divided into two parts—those plugging and non-plugging. The analytical models as well as their tuning by laboratory tests have been performed.

During particle deep bed filtration through porous media, there exists a critical moment when the retention concentration of particles at the core inlet reaches its critical value (Khatib, 1994). After the moment, few particles can penetrate into the core. Instead, the new-coming particles form external cake only. This critical moment is termed as the transition time. The existence of transition time has been observed and its evaluation has been studied intensively (Ochi et al., 1999; Zitha et al., 2013). The phenomenon of particle deep bed filtration followed by the formation of external filter cake is not described in the above classical DBF models (Tien, 2012).

Moreover, the oversimplified DBF model using the overall particle concentrations does not account for the effect of pore and particle size distributions on permeability decline in field cases (Veerapen et al., 2001; Massei et al., 2002; Windarto et al., 2012). Glenn and Slusser (1957) reported that certain distribution of particle sizes may reduce the permeability impairment for a given pore size distribution, i.e., the particle size distribution must be accounted for in the cake formation model. Corapcioglu and Abboud (1990) developed a model for cake filtration process accounting for different size particle penetration at the cake surface and migration in the cake. Furthermore, the compressibility effect of the external cake is taken into account with the modelling of the cake growth dynamics considering cake filtration (Sherwood and Meeten, 1997; Tien et al., 1997; Lohne et al., 2010). Civan (1998a, 1998b) investigated cake formation and stabilisation for cross flow filtration. The kinetics model accounts for erosion rate, which is proportional to the difference between the critical and current values of the shear stress. Non-Newtonian fluid properties are taken into account. The analytical models have been derived. Good

agreement between the modelling and experimental data has been observed for both linear and radial flows.

The traditional model presents a linear growth of pressure drop over time along the core and its abrupt increase during the external filter cake formation. It results in the delay of external cake formation if compared to particle penetration into the rock. The growth of internal cake formed by the fine particles inside the external cake after the transition time is not accounted for in the models for either drilling fluid invasion or water injectivity (Pang and Sharma, 1997; Wennberg and Sharma, 1997; Suri and Sharma, 2004; Bedrikovetsky et al., 2005). So, the above models assume DBF occurring before the transition time and build-up of external cake afterwards. Yet, in practice, a significant fraction of particles in drilling fluid exceeds pore sizes, so the formation of external cake starts at the beginning of injection, simultaneously with fine particle DBF (Abrams, 1977; Hands et al., 1998; Massei et al., 2002; Tien, 2012).

To the best of our knowledge, the mathematical model for cake filtration that accounts for co-occurring deep bed filtration and cake formation as well as internal cake formed by small particles inside the external cake by large particles is not available in the literature.

The present work aims to partly fill the gap considering injection of bi-sized suspension in the rock. The large particles start building the cake at the beginning of injection; while the small particles simultaneously filtrate through the built-up cake and penetrate into the porous media. After the transition time, the small particles filtrate in the external cake only. The aim of the present work is to develop a mathematical model for cake filtration (i.e. cake formation and deep bed filtration), including the external cake formation by large particles, DBF of small particles, internal cake growth inside external cake after the transition time, and possible formation of mixture cake after the catching-up time. Besides, the laboratory experiments on the injection of bi-sized suspension into a reservoir core have been performed. The results obtained from the proposed model match the laboratory data with high accuracy, which validates the model proposed.

The structure of the paper is as follows. First, the traditional deep bed filtration and cake formation model for mono-size particles is

briefly reviewed. It is followed by the development of advanced two-size particle model for external cake formation. Afterwards, the obtained results applying the proposed model are analysed. Finally, the treatment of data from laboratory tests validates the present model.

2. Traditional deep bed filtration and cake formation model for mono-size particles

In this section, the traditional model describing external cake formation and deep bed filtration of mono-size particles in porous media is reviewed. The assumptions of the model include cake formed by compact particle packing, constant porosity of the core and the cake due to low retention of particles, and incompressibility of particle suspension and cake.

Traditional theory considers mono-modal narrow particle size distribution and focused mostly on two extremes: (a) particles larger than pores and (b) particles much smaller than pores.

Let us start from the simplest case, in which the injected particle size is larger than all the pore sizes in the media. Therefore, particles accumulate outside the core inlet and form the external cake. There is no deep bed filtration in this case. Darcy's equation

$$\frac{\partial P}{\partial x} = -\frac{\mu U}{k} \quad (1)$$

is integrated in terms of the distance x to calculate the pressure drop in the core

$$\Delta P_m = \frac{\mu U L}{k_m} \quad (2)$$

and the pressure drop in the cake

$$\Delta P_{ec} = \frac{\mu U L_c(t)}{k_{ec}} \quad (3)$$

The total pressure drop is the sum of these two parts

$$\Delta P = \Delta P_m + \Delta P_{ec} = \mu U \left[\frac{L}{k_m} + \frac{L_c(t)}{k_{ec}} \right] \quad (4)$$

where k_m and k_{ec} are the permeability of the core and cake, respectively; L and $L_c(t)$ stand for the length of the core and thickness of external cake, respectively. μ is the viscosity of injected suspension and U is the Darcy velocity. The total pressure drop ΔP is a linear function of time.

In the case of injected particle size smaller than the pore size of the media, particles first filtrate into porous media, then followed by the formation of external cake after a certain moment (transition time). The model describing this process consists of the following two equations:

Population balance of total suspended and retained particles

$$\frac{\partial}{\partial t}(\phi c + \sigma) + U \frac{\partial c}{\partial x} = 0 \quad (5)$$

Kinetics equation of particle retention

$$\frac{\partial \sigma}{\partial t} = \lambda c U \quad (6)$$

as well as the initial and boundary conditions $t=0: c(x, 0) = \sigma(x, 0) = 0; x=0: c(0, t) = c^0$. The filtration coefficient is denoted as λ .

The retained particle concentration $\sigma(x, t)$ is solved from Eqs. (5) and (6) and applied to the formula for pressure drop along the core

$$\Delta P_m = \mu U \int_0^L \frac{1 + \beta \sigma(x, t)}{k_m(0)} dx \quad (7)$$

in which β is the formation damage coefficient. The pressure drop in the external cake is calculated using Eq. (3). The sum of these two parts gives the total pressure drop

$$\Delta P = \Delta P_m + \Delta P_{ec} = \mu U \left[\int_0^L \frac{1 + \beta \sigma(x, t)}{k_m(0)} dx + \frac{L_c(t)}{k_{ec}} \right] \quad (8)$$

3. Deep bed and external filtration of two-size particles

In this section, the model of external cake formation with injection of two-size particle is derived.

The size of injected small particles r_s is smaller than pore size r_p , while the size of injected large particles r_l is larger than r_p (Fig. 1). The process of small particle deep bed filtration in the core and simultaneous external cake formation described by the present model can be divided into three stages as follows (Fig. 2):

In Stage 1 (Fig. 2a,b), large particles cannot enter the porous medium and only form the external cake from the beginning of injection, since $r_l > r_p$. Small particles filtrate through the cake and into the core ($r_s < r_p$). Suspended particle concentration in the core decreases, while the retention concentration increases. At the transition moment, the retained particle concentration reaches its critical value at the core inlet. No particles can enter the core after the transition moment. This is the end of Stage 1.

The total pressure drop $\Delta P = \Delta P_{ec} + \Delta P_m$, where ΔP_{ec} and ΔP_m represent the pressure drops in the external cake and in the porous medium, respectively:

$$\Delta P_{ec} = \frac{\mu U L}{k_{ec}(0)} [D_1 + \beta \phi_3 c_3^0 (D_1 + 1)] T + \frac{\mu U L}{k_{ec}(0)} \beta \phi_3 c_3^0 \frac{(D_1 + 1)^2}{D_1 \lambda_c} \left[\exp\left(-\lambda_c \frac{D_1 T}{(D_1 + 1)}\right) - 1 \right] \quad (9)$$

$$\Delta P_m = \frac{\mu U L}{k_m(0)} \left\{ 1 + \beta \phi_1 C_3^0 \lambda \frac{D_1 + 1}{\lambda_c D_1} \left[\frac{1}{\lambda} (1 - \exp(-\lambda)) - \frac{R(D_1 + 1)}{\lambda_c D_1 - R \lambda (D_1 + 1)} \left(\exp\left(\frac{\lambda_c D_1 - R \lambda (D_1 + 1)}{R(D_1 + 1)} - \frac{\lambda_c D_1 T}{D_1 + 1}\right) - \exp\left(-\frac{\lambda_c D_1 T}{D_1 + 1}\right) \right) \right] \right\} \quad (10)$$

The derivation of pressure drops (9) and (10) is provided in the Appendix B.

In Stage 2 (Fig. 2c), the external cake formed by large particles keeps growing. Small particles start to accumulate outside the core inlet and form the internal cake inside the external cake of large particles. The retained particle concentration in the core is unchanged, since no more particles can penetrate into the medium.

The total pressure drop $\Delta P = \Delta P_m + \Delta P_{ec1} + \Delta P_{ec2}$, in which the three components ΔP_m , ΔP_{ec1} and ΔP_{ec2} are the pressure drop in the medium, between the fronts of external and internal cakes,

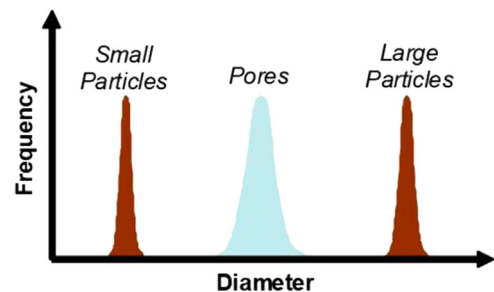


Fig. 1. Large particles do not penetrate into the media and start forming the cake at once while small particles perform deep bed filtration in the media.

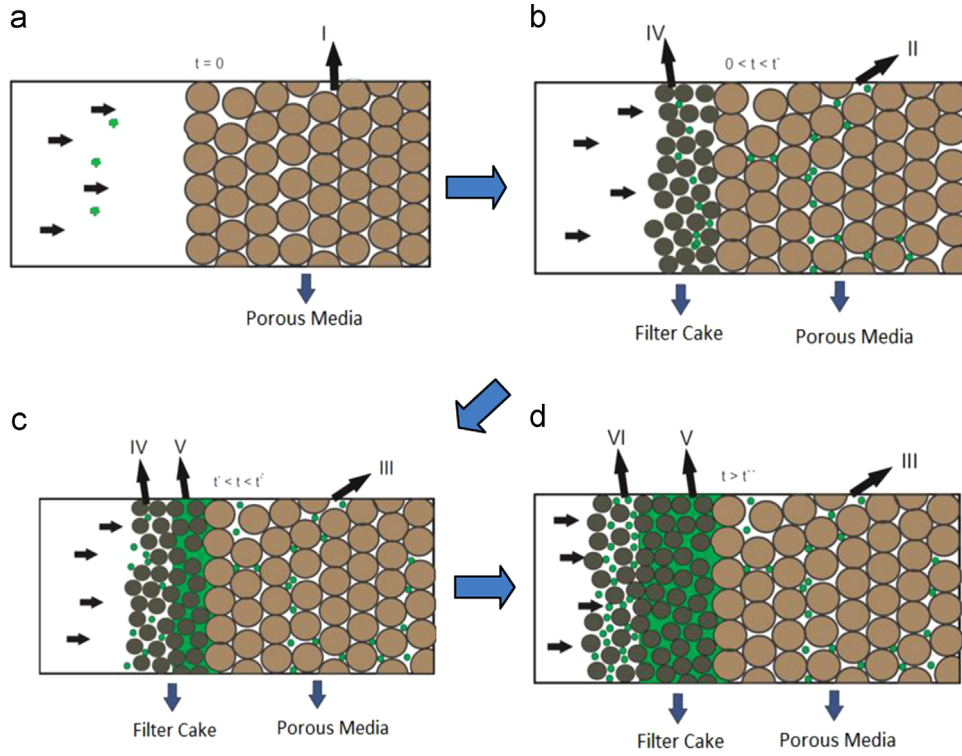


Fig. 2. Two scenarios for two-size particle cake formation: (a) beginning of two-size particle suspension injection; (b) deep bed filtration of small particles with simultaneous formation of cake by large particles; (c) small particles start filling pore space of the cake after the transition time; (d) development of the mixed-particle cake after small particle cake front catching up with the large particle cake front. Zone I: clean core at $t=0$; Zone II: DBF of small particles in the core; Zone III: unchanged retention concentration profile in the core; Zone IV: small particles filtration in external cake; Zone V: internal cake growth inside external cake; Zone VI: new cake formed by mixed two-size particles.

and between the front of internal cake and core inlet, respectively:

$$\Delta P_m = \frac{\mu UL}{k_m(0)} \left\{ 1 + \beta \phi_1 C_3^0 \lambda \frac{D_1 + 1}{\lambda_c D_1} \left[\frac{1}{\lambda} (1 - \exp(-\lambda)) - \frac{R(D_1 + 1)}{\lambda_c D_1 - R\lambda(D_1 + 1)} \left(\exp\left(\frac{\lambda_c D_1 - R\lambda(D_1 + 1)}{R(D_1 + 1)} - \frac{\lambda_c D_1 T_{tr}}{D_1 + 1}\right) - \exp\left(-\frac{\lambda_c D_1 T_{tr}}{D_1 + 1}\right) \right) \right] \right\} \quad (11)$$

$$\Delta P_{ec1} = \frac{\mu UL}{k_{ec}(0)} \left[1 + \beta \phi_3 C_3^0 \frac{(D_1 + 1)}{D_1} \right] (D_1 T + z(T)) + \frac{\mu UL}{k_{ec}(0)} \beta \phi_3 C_3^0 \frac{(D_1 + 1)^2}{D_1 \lambda_c} \left[\exp\left(-\lambda_c \frac{D_1 T + z(T)}{(D_1 + 1)}\right) - 1 \right] \quad (12)$$

$$\Delta P_{ec2} = \frac{\mu UL}{k_{ec12}} (-z(T)) \quad (13)$$

in which the thickness of internal cake $z(T)$ is calculated from

$$z(T) = \frac{D_1 + 1}{\lambda_c} \ln \left[\left(1 - \frac{C_3^0 \exp(-((\lambda_c D_1)/(D_1 + 1)) T_{tr})}{(1 - \phi_2) D_1} \right) \exp\left(\frac{\lambda_c D_1}{D_1 + 1} T\right) + \frac{C_3^0}{(1 - \phi_2) D_1} \right] - D_1 T \quad (14)$$

Derivations of Eqs. (11)–(14) are given in the Appendix C.

The front moving speed of the external cake formed by large particles may differ from that of the internal cake formed by small particles. It depends on the concentration ratio of small and large particles in the injected suspension as well as the porosities of the core and the cake. If the internal cake front moves slower than the front of the external cake, Stage 2 continues. Otherwise, if the front of internal cake moves faster than that of the external cake, the internal cake

front catches up with the external cake front. Stage 2 transits to Stage 3 at the catching-up time.

In Stage 3 (Fig. 2d), a new cake formed by the mixture of two-size particles begins to grow. The total pressure drop in this stage $\Delta P = \Delta P_m + \Delta P_{ec} + \Delta P_{ecmix}$, where the three components ΔP_m , ΔP_{ec} and ΔP_{ecmix} are the pressure drop in the medium, from the intersection of the two cake fronts to the core inlet, and in the mixture cake, respectively:

$$\Delta P_{ec} = -\frac{\mu UL}{k_{ec12}} D_1 T_3 \quad (15)$$

$$\Delta P_{ecmix} = \frac{\mu UL}{k_{ecmix}} D_3 (T - T_3) \quad (16)$$

and ΔP_m is calculated by Eq. (11). The catching-up time T_3 is obtained from

$$T_3 = \frac{D_1 + 1}{\lambda_c D_1} \ln \left[\frac{1 - C_3^0 / ((1 - \phi_2) D_1)}{1 - C_3^0 \exp(-((\lambda_c D_1)/(D_1 + 1)) T_{tr}) / ((1 - \phi_2) D_1)} \right] \quad (17)$$

Eqs. (15)–(17) are derived in the Appendix D.

For constant injection rate, the impedance caused by cake formation is the ratio of total pressure drop at time T and the initial pressure drop

$$J = \frac{\Delta P(T)}{\Delta P(0)} \quad (18)$$

The complete set of formulae for impedance profile in all stages is summarised in Table 1.

Table 1
Formulae for impedance profile at each stage.

Time interval	Impedance (J)
$T < T_{tr}$	$J_{ec} = \frac{1}{\Delta p_0} \left\{ \frac{\mu UL}{k_{ec}(0)} [D_1 + \beta \phi_3 c_3^0 (D_1 + 1)] T + \frac{\mu UL}{k_{ec}(0)} \beta \phi_3 c_3^0 \frac{(D_1 + 1)^2}{D_1 \lambda_c} \left[\exp\left(-\lambda_c \frac{D_1 T}{D_1 + 1}\right) - 1 \right] \right\}$ $J_m = \frac{1}{\Delta p_0} \left\{ \frac{\mu UL}{k_m(0)} \left\{ 1 + \beta \phi_1 c_3^0 \lambda_c \frac{D_1 + 1}{\lambda} \left[\frac{1}{\lambda} (1 - \exp(-\lambda)) - \frac{R(D_1 + 1)}{\lambda_c D_1 - R\lambda(D_1 + 1)} \left(\exp\left(\frac{\lambda_c D_1 - R\lambda(D_1 + 1)}{R(D_1 + 1)} - \frac{\lambda_c D_1 T}{D_1 + 1}\right) - \left(\exp\left(-\frac{\lambda_c D_1 T}{D_1 + 1}\right) \right) \right] \right\} \right\}$ $J = J_{ec} + J_m$
$T_{tr} < T < T_3$	$J_{ec1} = \frac{1}{\Delta p_0} \left\{ \frac{\mu UL}{k_{ec}(0)} \left[1 + \beta \phi_3 c_3^0 \frac{(D_1 + 1)}{D_1} \right] (D_1 T + z(T)) + \frac{\mu UL}{k_{ec}(0)} \beta \phi_3 c_3^0 \frac{(D_1 + 1)^2}{D_1 \lambda_c} \left[\exp\left(-\lambda_c \frac{D_1 T + z(T)}{D_1 + 1}\right) - 1 \right] \right\}$ $J_{ec2} = \frac{1}{\Delta p_0} \frac{\mu UL}{k_{ec12}} (-z(T))$ <p>where $z(T) = \frac{D_1 + 1}{\lambda_c} \ln \left[\left(1 - \frac{c_3^0 \exp(-\frac{\lambda_c D_1 T}{D_1 + 1})}{(1 - \phi_2) D_1} \right) \exp\left(\frac{\lambda_c D_1 T}{D_1 + 1}\right) + \frac{c_3^0}{(1 - \phi_2) D_1} \right] - D_1 T$</p> $J_m(T_{tr}) = \frac{1}{\Delta p_0} \frac{\mu UL}{k_m(0)} \left\{ 1 + \beta \phi_1 c_3^0 \lambda_c \frac{D_1 + 1}{\lambda} \left[\frac{1}{\lambda} (1 - \exp(-\lambda)) - \frac{R(D_1 + 1)}{\lambda_c D_1 - R\lambda(D_1 + 1)} \left(\exp\left(\frac{\lambda_c D_1 - R\lambda(D_1 + 1)}{R(D_1 + 1)} - \frac{\lambda_c D_1 T_{tr}}{D_1 + 1}\right) - \exp\left(-\frac{\lambda_c D_1 T_{tr}}{D_1 + 1}\right) \right) \right] \right\}$ $J = J_{ec1} + J_{ec2} + J_m(T_{tr})$
$T < T_3$	$J_{ec} = -\frac{1}{\Delta p_0} \frac{\mu UL}{k_{ec12}} D_1 T_3$ $J_{ecmix} = \frac{1}{\Delta p_0} \frac{\mu UL}{k_{ecmix}} D_3 (T - T_3)$ $J_m(T_{tr}) = \frac{1}{\Delta p_0} \frac{\mu UL}{k_m(0)} \left\{ 1 + \beta \phi_1 c_3^0 \lambda_c \frac{D_1 + 1}{\lambda} \left[\frac{1}{\lambda} (1 - \exp(-\lambda)) - \frac{R(D_1 + 1)}{\lambda_c D_1 - R\lambda(D_1 + 1)} \left(\exp\left(\frac{\lambda_c D_1 - R\lambda(D_1 + 1)}{R(D_1 + 1)} - \frac{\lambda_c D_1 T_{tr}}{D_1 + 1}\right) - \exp\left(-\frac{\lambda_c D_1 T_{tr}}{D_1 + 1}\right) \right) \right] \right\}$ $J = J_m + J_{ec} + J_{ecmix}$

4. Analysis of modelling results

The results of impedance are calculated from the model developed above for all the three stages. Effects of different parameters on the impedance profile are analysed in this section.

The impedance as a function of time with different injected small particle concentration c_3^0 is shown in Fig. 3. Here the dimensionless time $PVI = Ut / (\phi_1 L)$. The larger is c_3^0 , the more is the captured particles per unit time, and the earlier is the transition time T_{tr} . The larger is the small particle concentration c_3^0 , the faster is the impedance growth at each stage. This is due to the smaller porosity and lower permeability caused by the larger proportion of small particles at each stage. Moreover, the higher fraction of small particles corresponds to the earlier catching-up of the internal cake front.

The impedance curves calculated using different values of internal cake porosity are compared in Fig. 4. If the external cake porosity is fixed, the impedance grows more slowly as the internal cake porosity increases at Stage 2. The value of internal cake porosity does not affect the impedance at other stages. With the constant internal cake porosity in Fig. 5, it is shown that the decrease of external cake porosity leads to faster impedance growth at Stages 1 and 2.

Fig. 6 shows the obtained impedance curves with different values of formation damage coefficient β . A larger formation damage coefficient results in a faster impedance growth at Stage 1. The other two stages are not affected by the value of damage coefficient β in the core.

The impedance as a function of time with different values of medium filtration coefficient λ_m is shown in Fig. 7. Higher value of

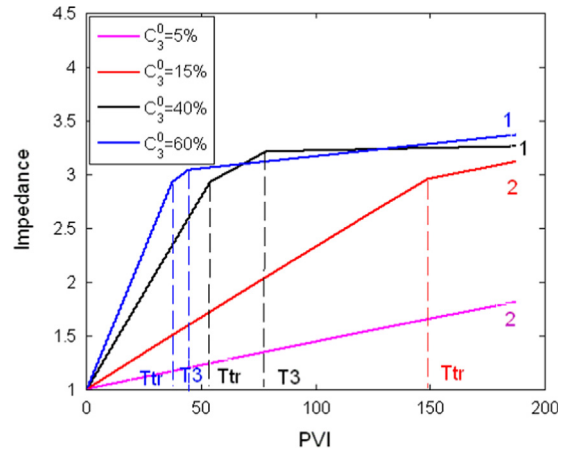


Fig. 3. Impedance curves with different small particle concentrations for two-size model ($c_3^0 = 5\%, 15\%, 40\%, 60\%$). Scenario 1: internal cake front can catch up with the external cake front; Scenario 2: internal cake front cannot catch up with the external cake front. T_{tr} is the transition time. T_3 is the catching-up time in the first scenario.

λ_m indicates a larger number captured particles per unit time, which leads to an earlier transition time. However, the effect of the cake filtration coefficient λ_c on the transition time is negligible (Fig. 8). This is due to the small thickness of the external cake, which results in relatively small number of captured particles in the external cake compared to the injected suspension concentration.

Fig. 9 delivers the impedance curves obtained using different value of the critical coefficient $\alpha = \sigma(0, T_{tr}) / \phi$. The smaller is the

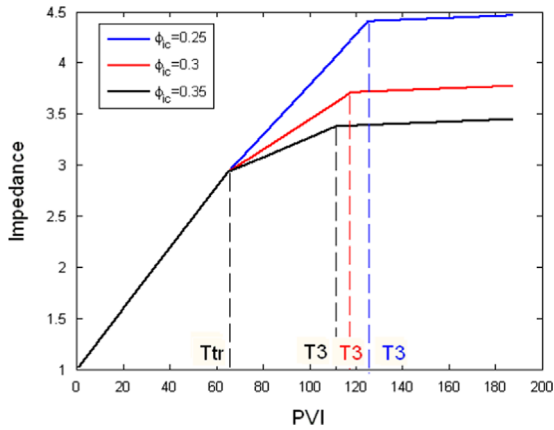


Fig. 4. Impedance curves with different internal cake porosity ϕ_{ic} .

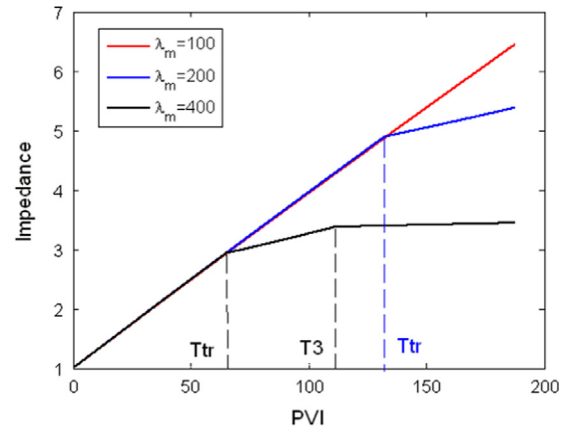


Fig. 7. Impedance curves for different formation filtration coefficients λ_m .

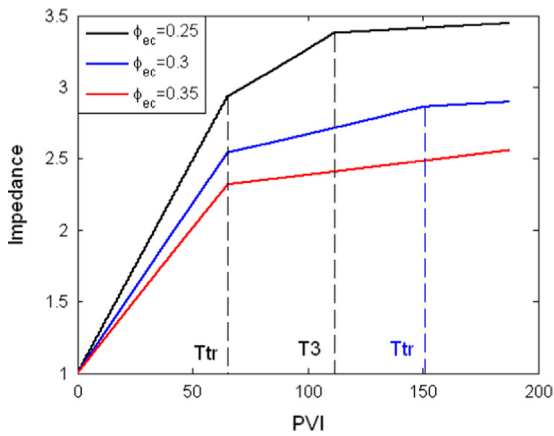


Fig. 5. Impedance curves with different external cake porosity ϕ_{ec} .

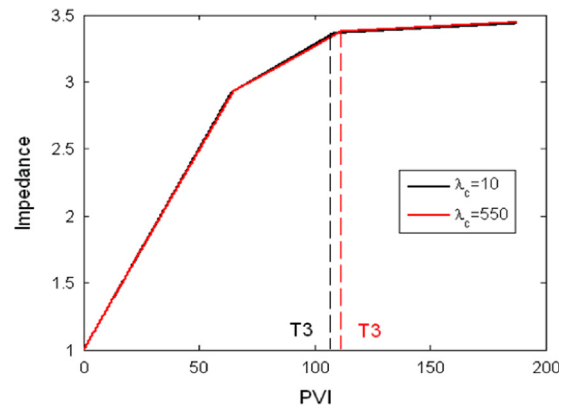


Fig. 8. Impedance curve behaviour for different cake filtration coefficients λ_c .

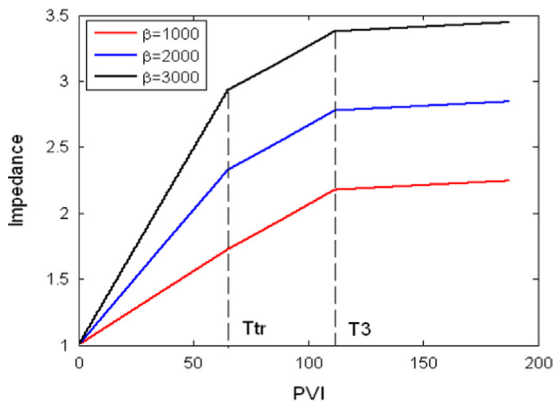


Fig. 6. Impedance versus time for different values of formation damage coefficient β .

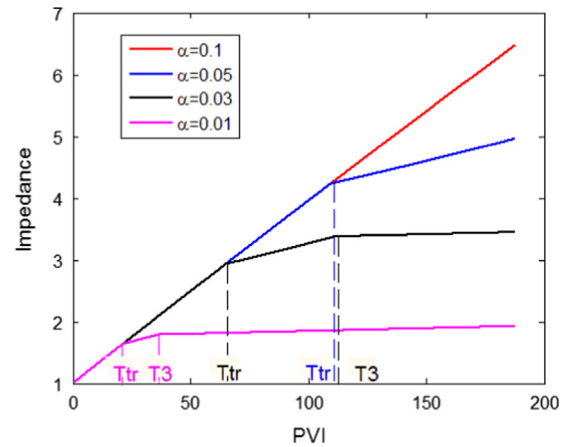


Fig. 9. Impedance curves for different critical porosity coefficients α .

critical coefficient, the earlier is the transition time. Furthermore, the catching-up time of the internal cake front T_3 reduces with α due to the smaller thickness of external cake at the transition time.

5. Experimental validation

Laboratory test on the process of particle deep bed filtration and external cake formation has been performed using the Berea Sandstone core. In the experiment, the injected large and small particle concentrations are 50 and 25 ppm, respectively. The diameters of large and small particles are 100 and 1 μ m,

respectively. The core length is 4.7 cm, core permeability is 317 md and porosity is 0.2. The diameter of the core cross-section is 3.8 cm.

The impedance profile calculated from the measured data is treated by the two-size model accounting for two scenarios (Fig. 10). The tuning parameters for Scenario 1 are as follows: the critical coefficient $\alpha=0.03$, formation damage coefficient $\beta=3200$, external cake porosity $\phi_1=0.24$, porosity of internal cake $\phi_2=0.35$. The tuning parameters for Scenario 2 are: $\alpha=0.03$, formation damage coefficient $\beta=4500$, external cake porosity $\phi_1=0.38$, porosity of internal cake $\phi_2=0.20$. The permeabilities of external and internal cakes are calculated from the Kozeny-Carman formula (A-8).

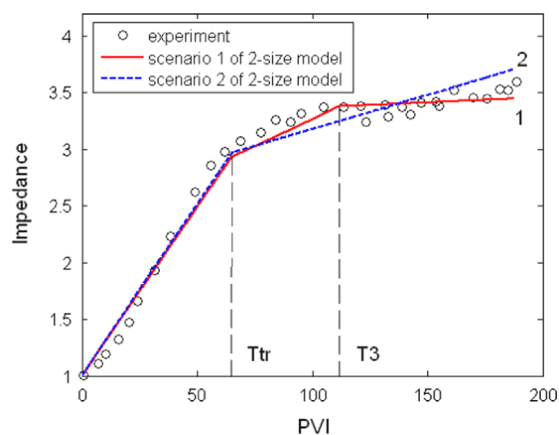


Fig. 10. Impedance profile prediction accounting for different scenarios of the two-size model. Scenario 1: internal cake front can catch up with the external cake front; Scenario 2: internal cake front cannot catch up with the external cake front. T_{tr} is the transition time. T_3 is the catching-up time in the first scenario. (For interpretation of the references to colour in this figure, the reader is referred to the web version of this article.)

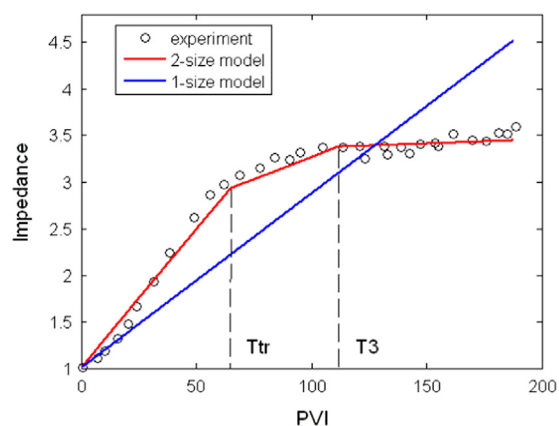


Fig. 11. Comparison of impedance profile using the present two-size model and the traditional mono-size model. T_{tr} is the transition time. T_3 is the catching-up time in the two-size model.

In Scenario 1, the internal cake front can catch up with the external cake front. Therefore, all the three stages exist (see the red curve in Fig. 10). Scenario 2 corresponds to the case that internal cake front cannot catch up with the external cake front. Only Stages 1 and 2 appear in this scenario (the blue dashed curve in Fig. 10). It is clear that the first scenario results in a better agreement between the experimental data and the model prediction than the second scenario.

Comparison of the impedance prediction between the proposed two-size model and the traditional mono-size model is presented in Fig. 11. It is worth noting that the averaged particle size applied in the mono-size model is larger than the pore sizes, therefore all the particles accumulate to form the external cake and no DBF happens in the core. There is no transition time in the mono-size model, which causes the predicted curve using the traditional model deviates from the measured impedance profile (the coefficient of determination $R^2=0.620$). The present two-size model predicts the transition time and the catching-up time successfully and agree well with the impedance profile from lab data ($R^2=0.985$).

So, the mathematical model for deep bed filtration and external cake formation during the injection of bi-sized suspension exhibit more complex behaviour than the mono-sized model. Moreover, the mono-sized model cannot match the laboratory data on

bi-sized suspension injection, while the bi-sized suspension injection model matches the laboratory data with high accuracy. It allows expecting that the developed bi-sized suspension injection model can match well with the data on injection of water with particles or invasion of drilling fluids and, therefore, can be used in the design and planning of these processes. However, additional studies are required to support this claim.

6. Conclusions

Mathematical modelling and laboratory experiments on the injection of two-size particle suspension in porous media allow drawing the following conclusions:

The external filter cake formation during injection of two-size particle suspension in porous media can be described by the analytical model. Pressure drop along the core and cake, as well as the suspended and retained particle concentrations can be expressed by explicit formulae.

Two different regimes of cake formation have been distinguished in the model and in laboratory experiments: (1) slow growth of the external large-particle cake with fast moving of the small-particle cake front inside the large-particle cake followed by further cake build-up from the mixture of injected particles; (2) fast growth of the external large-particle cake with slow development of the internal small-particle cake filled in the large-particle cake.

The first regime is typical for high concentration of small particles in the injected suspension, which exhibits piecewise impedance curve with three segments; while the second regime takes place for low concentration of small particles, presenting two-segment piecewise impedance curve.

Treatment of the laboratory test data by the analytical model shows that the first regime of the external cake formation has been occurring in the experiment.

The experimental data on two-size particle injection with deep bed filtration and external cake formation can be matched by the analytical model with high accuracy. Good agreement between the laboratory and modelling data validates the proposed two-size model, which delivers better prediction of the impedance profile than the traditional mono-size particle cake model.

Mathematical modelling using the analytical solution shows that the larger is the injected concentration of small particle, the faster is the impedance growth at each stage. It is explained by smaller porosity and permeability resulting from small particles.

Acknowledgements

Financial support from the Australian Research Council (ARC) Discovery Project 1094299, Linkage Projects 100100613 and 110200799 is gratefully acknowledged.

Appendix A. Governing equations and analytical solution for particle deep bed filtration

Consider injection of suspension with two-size particles. Particles with the larger size are larger than all the pore throats. Hence, they cannot enter the porous medium; instead, they form the external filter cake from the beginning of injection. Small particles injected first filtrate through the external cake formed by large particles and then penetrate in the porous rock.

System of equations for particle deep bed filtration consists of the population balance equation for all the small particles

$$\frac{\partial}{\partial t}(\phi c + \sigma) + U \frac{\partial c}{\partial x} = 0 \quad (\text{A-1})$$

and the kinetics equation of particle capture

$$\frac{\partial \sigma}{\partial t} = \lambda c U \quad (\text{A-2})$$

Darcy's law is applied to calculate the pressure drop along the distance

$$U = -\frac{k}{\mu(1+\beta\sigma)} \frac{\partial p}{\partial x} \quad (\text{A-3})$$

Introduction of dimensionless variables and parameters

$$X \rightarrow \frac{x}{L}, \quad T \rightarrow \frac{Ut}{\phi L}, \quad C = \frac{c}{c_3^0}, \quad S = \frac{\sigma}{\phi c_3^0}, \quad \lambda = \lambda_0 L, \quad P = \frac{k}{U\mu L} P \quad (\text{A-4})$$

into Eqs. (A-1)–(A-3) yields the following dimensionless system of governing equations

$$\frac{\partial(C+S)}{\partial T} + \frac{\partial C}{\partial X} = 0 \quad (\text{A-5})$$

$$\frac{\partial S}{\partial T} = \lambda C \quad (\text{A-6})$$

$$1 = -\frac{1}{1+\phi c_3^0 \beta S(X,T)} \frac{\partial P}{\partial X} \quad (\text{A-7})$$

Here μ is the viscosity of suspension, U is the Darcy velocity, β is the formation damage coefficient, λ is the dimensionless filtration coefficient, which is denoted as λ_c for the filter cake and λ_m for the porous medium. c_3^0 is the injected small particle concentration, and C is the dimensionless particle concentration. σ is the retained particle concentration, and S is the dimensionless retained particle concentration. L is the core length, ϕ is the porosity. For convenience, ϕ_1 and ϕ_3 are introduced in the model for porous media porosity and external cake porosity, respectively. $k(0)$ is the initial permeability, $k_m(0)$ and $k_{ec}(0)$ stand for the initial permeability of the porous medium and that of the external cake, respectively.

The initial permeability is calculated using the Kozney–Carman equation (Civan, 2007)

$$k(0) = \frac{1}{72\tau} \frac{\phi^3 D_p^2}{(1-\phi)^2} \quad (\text{A-8})$$

here τ is the tortuosity and D_p is the particle diameter.

The analytical model presented below is based on the solution of the initial-boundary problem for constant concentration suspension injection into a clean bed. The initial and boundary conditions are

$$t = 0 : C = S = 0$$

$$x = 0 : C = 1 \quad (\text{A-9})$$

The solution to the equation system (A-5)–(A-7) with conditions (A-9) is obtained as

$$C(X, T) = \begin{cases} e^{-\lambda X}, & X < T \\ 0, & X > T \end{cases} \quad (\text{A-10})$$

$$S(X, T) = \begin{cases} \lambda(T-X)e^{-\lambda X}, & X < T \\ 0, & X > T \end{cases} \quad (\text{A-11})$$

Appendix B. Pressure drop in the first stage of cake formation (before transition time): $0 < T < T_{tr}$

The characteristic curve passing through a point (X, T) crosses the external cake front at the point $(-D_1 T_2, T_2)$, so

$$D_1 T_2 + X = T - T_2, \quad T_2 = \frac{T-X}{D_1+1} \quad (\text{B-1})$$

where D_1 corresponds to the speed of external filter cake built of the large particles. It is obtained from the mass conservation of injected large particles: $D_1 = \phi_3 c_2^0 / (1 - \phi_3)$.

Substituting Eq. (B-1) into (A-10) results in the suspended particle concentration in external cake

$$C(X, T) = \exp[-\lambda_c(D_1 T_2 + X)] = \exp\left[-\lambda_c \frac{D_1 T + X}{D_1 + 1}\right] \quad (\text{B-2})$$

Retained concentration of particles $S(X, T)$ is derived by integration of (B-2) in terms of T from $-X/D_1$ to T

$$S(X, T) = \frac{D_1 + 1}{D_1} \left\{ 1 - \exp\left[-\lambda_c \frac{D_1 T + X}{D_1 + 1}\right] \right\} \quad (\text{B-3})$$

Finally, the pressure drop over the external cake is obtained by using the Darcy's law

$$\Delta p_{ec} = \frac{\mu U L}{k_{ec}(0)} \int_{-D_1 T}^0 (1 + \beta \phi_3 c_3^0 S(X, T)) dX \quad (\text{B-4})$$

which is expressed as

$$\Delta p_{ec} = \frac{\mu U L}{k_{ec}(0)} [D_1 + \beta \phi_3 c_3^0 (D_1 + 1)] T + \frac{\mu U L}{k_{ec}(0)} \beta \phi_3 c_3^0 \frac{(D_1 + 1)^2}{D_1 \lambda_c} \left[\exp\left(-\lambda_c \frac{D_1 T}{D_1 + 1}\right) - 1 \right] \quad (\text{B-5})$$

At the core inlet, the suspended concentration, as it follows from (B-2), is

$$X = 0 : C(0, T) = \exp\left[-\lambda_c \frac{D_1 T}{D_1 + 1}\right] \quad (\text{B-6})$$

The propagation velocities are different in the cake and in the core. The coefficient $R = \phi_3 / \phi_1$ is used to normalise the propagation velocity in the core based on that in the external cake

$$\frac{dX}{dT} = R = \frac{\phi_3}{\phi_1} \quad (\text{B-7})$$

The characteristic curve crossing the point (X, T) intersects the core inlet at the moment T' . Integrating the above Eq. (B-7) leads to

$$\int_0^X dX = R \int_{T'}^T dT \quad (\text{B-8})$$

Thus, we have

$$T' = T - \frac{1}{R} X \quad (\text{B-9})$$

The characteristic curve covers the distance $D_1 T_1$ inside the external cake and distance x in the core. We can calculate the particle concentration by the new boundary condition $x = 0 : C = C(0, T)$

$$C(X, T) = \exp(-\lambda_c D_1 T_1) \exp(-\lambda X) = \exp\left(-\lambda_c D_1 \frac{T'}{D_1 + 1}\right) \exp(-\lambda X) = \exp\left(-\lambda_c D_1 \frac{T - X/R}{D_1 + 1}\right) \exp(-\lambda X) \quad (\text{B-10})$$

Retained concentration $S(X, T)$ is found by integrating the above equation in terms of t from X/R to T

$$S(X, T) = \lambda \exp(-\lambda X) \frac{D_1 + 1}{\lambda_c D_1} \left[1 - \exp\left(-\lambda_c D_1 \frac{T - X/R}{D_1 + 1}\right) \right] \quad (\text{B-11})$$

From (B-11), we have

$$S(0, T) = \lambda \frac{D_1 + 1}{\lambda_c D_1} \left[1 - \exp\left(-\lambda_c D_1 \frac{T}{D_1 + 1}\right) \right] \quad (\text{B-12})$$

It allows calculating the transient time T_{tr}

$$\frac{\phi_1 \alpha}{c_3^0 \phi_3} = \lambda \frac{D_1 + 1}{\lambda_c D_1} \left\{ 1 - \exp\left[-\lambda_c \frac{D_1 T_{tr}}{D_1 + 1}\right] \right\} \quad (\text{B-13})$$

which results in

$$T_{tr} = -\frac{D_1 + 1}{\lambda_c D_1} \ln \left(1 - \frac{(\phi_1 / \phi_3) \alpha \lambda_c D_1}{c_3^0 (D_1 + 1) \lambda} \right) \quad (\text{B-14})$$

The pressure drop in porous medium is obtained by using the Darcy's law

$$\Delta p_m = \frac{\mu UL}{k_m(0)} \int_0^1 (1 + \beta \phi_1 c_3^0 S(X, T)) dX \quad (\text{B-15})$$

Substituting Eq. (B-11) into the above Eq. (B-15), we have Δp_m as

$$\Delta p_m = \frac{\mu UL}{k_m(0)} \left\{ 1 + \beta \phi_1 c_3^0 \lambda \frac{D_1 + 1}{\lambda_c D_1} \left[\frac{1}{\lambda} (1 - \exp(-\lambda)) - \frac{R(D_1 + 1)}{\lambda_c D_1 - R\lambda(D_1 + 1)} \left(\exp\left(\frac{\lambda_c D_1 - R\lambda(D_1 + 1)}{R(D_1 + 1)} - \frac{\lambda_c D_1 T}{D_1 + 1}\right) - \exp\left(-\frac{\lambda_c D_1 T}{D_1 + 1}\right) \right) \right] \right\} \quad (\text{B-16})$$

Thus, the total pressure drop is obtained by the sum of the pressure drop over the external cake and that in the porous medium.

Appendix C. Pressure drop in the second stage of cake formation (interval between transition time and cake front catching-up time): $T_{tr} < T < T_3$

After the transition time T_{tr} , small particles cannot penetrate into the core anymore. Therefore, suspension concentration at the core inlet is zero, and retained particle concentration remains constant.

At the moment T_{tr} , the internal cake formed by injected small particles starts to accumulate inside the external cake of large particles; simultaneously, injected small particles still filtrate in the external cake and can be captured before reaching the front of the internal cake.

Suspension concentration at the front of internal cake, which propagates inside the external cake $X=z(T)$, as it follows from (B-2), is given by

$$C(z(T), T) = \exp\left[-\lambda_c \frac{D_1 T + z(T)}{D_1 + 1}\right] \quad (\text{C-1})$$

The moving speed of the internal cake front is obtained from the mass balance of injected small particles:

$$\frac{dz}{dT} = \frac{C(z, T) c_3^0}{1 - \phi_2} \quad (\text{C-2})$$

where ϕ_2 is the porosity of the internal cake formed by the small particles. Combining Eqs. (C-1) and (C-2) results in the ordinary differential equation for the internal cake front location $z(T)$

$$\frac{dz}{dT} = \frac{1}{1 - \phi_2} \exp\left[-\lambda_c \frac{D_1 T + z}{D_1 + 1}\right] \quad (\text{C-3})$$

By solving the above equation, we obtain the front location of internal cake $z(T)$ as a function of time T

$$z(T) = \frac{D_1 + 1}{\lambda_c} \ln \left[\left(1 - \frac{c_3^0 \exp(-((\lambda_c D_1)/(D_1 + 1))T_{tr})}{(1 - \phi_2) D_1} \right) \exp\left(\frac{\lambda_c D_1}{D_1 + 1} T\right) \right]$$

$$+ \frac{c_3^0}{(1 - \phi_2) D_1} \Big] - D_1 T \quad (\text{C-4})$$

The moment when the internal cake front catches up with the front of the external cake T_3 is calculated from the intersection of front trajectories:

$$z(T_3) = -D_1 T_3 \quad (\text{C-5})$$

which leads to the formula for the catching-up time T_3

$$T_3 = \frac{D_1 + 1}{\lambda_c D_1} \ln \left[\frac{1 - c_3^0 / ((1 - \phi_2) D_1)}{1 - c_3^0 \exp(-((\lambda_c D_1)/(D_1 + 1))T_{tr} / ((1 - \phi_2) D_1))} \right] \quad (\text{C-6})$$

From Eq. (A-7), the pressure drop of the external cake between the fronts of external and internal cake can be derived by integrating in terms of x from $-D_1 T$ to $z(T)$

$$\Delta p_{ec1} = \frac{\mu UL}{k_{ec}(0)} \int_{-D_1 T}^{z(T)} (1 + \beta \phi_3 c_3^0 S(X, T)) dX \quad (\text{C-7})$$

The pressure drop between the front of internal cake and the core inlet can be calculated by the Darcy's law directly

$$\Delta p_{ec2} = -\frac{\mu UL}{k_{ec12}} z(T) \quad (\text{C-8})$$

where k_{ec12} is the permeability of external cake filled by internal cake of small particles.

Thus, the total pressure drop is the sum of the pressure drop in the porous medium (B-16) at $T=T_{tr}$, that in the external cake between the two cake fronts (C7) and that between the internal cake front and core inlet (C-8), as follows

$$\Delta p = \Delta p_m + \Delta p_{ec1} + \Delta p_{ec2} \quad (\text{C-9})$$

Appendix D. Pressure drop in the third stage of cake formation (after the cake front catching-up time): $T > T_3$

After the intersection of the fronts of external and internal cakes at point (X_3, T_3) , a new cake is formed by the mixture of two size particles (overall injected suspension). The front speed D_3 is obtained from the mass balance of injected large and small particles: $D_3 = \phi_3 (c_1^0 + c_2^0) / (1 - \phi_4)$. Here, ϕ_4 is the porosity of the cake formed by two size particles (overall injected suspension). There is no deep bed filtration the third stage.

The pressure drop of the mixture cake formed by two size particles can be obtained from

$$\Delta p_{ecmix} = \frac{\mu UL}{k_{ecmix}} D_3 (T - T_3) \quad (\text{D-1})$$

where k_{ecmix} is the permeability of the mixture cake formed by two size particles.

The pressure drop of the external cake from the intersection of the two cake fronts to the core inlet can be calculated as

$$\Delta p_{ec} = -\frac{\mu UL}{k_{ec12}} D_1 T_3 \quad (\text{D-2})$$

Finally, the total pressure drop can be calculated by

$$\Delta p = \Delta p_m + \Delta p_{ec} + \Delta p_{ecmix} \quad (\text{D-3})$$

The impedance caused by cake formation for constant injection rate is defined as

$$J = \frac{\Delta p(T)}{\Delta p(0)} \quad (\text{D-4})$$

References

- Abrams, A., 1977. Mud design to minimize rock impairment due to particle invasion. *J. Pet. Technol.* 29, 586–592.
- Bedrikovetsky, P., 2008. Upscaling of stochastic micro model for suspension transport in porous media. *Transp. Porous Media* 75, 335–369.
- Bedrikovetsky, P., et al., 2001. Characterisation of deep bed filtration system from laboratory pressure drop measurements. *J. Pet. Sci. Eng.* 32 (2–4), 167–177.
- Bedrikovetsky, P.G., et al., 2005. Well-history-based prediction of injectivity decline during seawater flooding. SPE European Formation Damage Conference. Society of Petroleum Engineers, Scheveningen, The Netherlands.
- Civan, F., 1998a. Incompressible cake filtration: mechanism, parameters, and modeling. *AIChE J.* 44 (11), 2379–2387.
- Civan, F., 1998b. Practical model for compressive cake filtration including fine particle invasion. *AIChE J.* 44 (11), 2388–2398.
- Civan, F., 2007. Reservoir Formation Damage: Fundamentals, Modeling, Assessment, and Mitigation. Gulf Publishing Company, Houston, Texas.
- Civan, F., Nguyen, V., 2005. Modeling particle migration and deposition in porous media by parallel pathways with exchange. In: Vafai, K. (Ed.), *Handbook of Porous Media*, 2nd ed. CRC Press, Boca Raton, FL, pp. 457–484.
- Civan, F., Rasmussen, M.L., 2005. Analytical models for porous media impairment by particles in rectilinear and radial flows. In: Vafai, K. (Ed.), *Handbook of Porous Media*, 2nd ed. CRC Press, Boca Raton, FL, pp. 485–542.
- Corapcioglu, M.Y., Abboud, N.M., 1990. Cake filtration with particle penetration at the cake surface. *SPE Reserv. Eng.* 5 (3), 317–326.
- Dalmazzone, C.S., Follot, A.L., Audibert-Hayet, A., Twynam, A.J., Poitrenaud, H.M., 2007. Development of an Optimized Formulation for Cleaning Water Injection Wells Drilled With Oil-Based Systems, European Formation Damage Conference. Society of Petroleum Engineers, Scheveningen, The Netherlands.
- Ding, Y., Herzhaft, B., Renard, G., 2006. Near-wellbore formation damage effects on well performance: a comparison between underbalanced and overbalanced drilling. *SPE Prod. Oper.* 21 (1), 51–57.
- Ding, Y., Longeron, D., Renard, G., Audibert, A., 2004. Modeling of both near-wellbore damage and natural cleanup of horizontal wells drilled with water-based drilling fluids. *SPE J.* 9 (3), 252–264.
- Ding, Y., Renard, G., 2005. Evaluation of horizontal well performance after drilling-induced formation damage. *J. Energy Resour. Technol., Trans. ASME* 127 (3), 257–263.
- Ding, Y., Renard, G., Herzhaft, B., 2008. Quantification of uncertainties for drilling-induced formation damage. *SPE Prod. Oper.* 23 (2), 221–231.
- Ghalambor, A., Economides, M.J., 2002. Formation damage abatement: a quarter-century perspective. *SPE J.* 7 (1), 4–13.
- Glenn, E.E., Slusser, M.L., 1957. Factors affecting well productivity II. Drilling fluid particle invasion into porous media. *Pet. Trans. AIME* 210, 132–139.
- Hands, N., Kowbel, K., Maikranz, S., Nouris, R., 1998. Drill-in fluid reduces formation damage, increases production rates. *Oil Gas J.* 96 (28), 65–69.
- Herzig, J.P., Leclerc, D.M., Legoff, P., 1970. Flow of suspensions through porous media – application to deep filtration. *Ind. Eng. Chem.* 62 (5), 8–35.
- Karimi, M., Ghalambor, A., Montgomery, M., Moellendick, T.E., 2011. Formation Damage and Fluid Loss Reduction due to Plastering Effect of Casing Drilling, SPE European Formation Damage Conference. Society of Petroleum Engineers, Noordwijk, The Netherlands.
- Khatib, Z.I., 1994. Prediction of formation damage due to suspended solids: modeling approach of filter cake buildup in injectors, SPE Annual Technical Conference and Exhibition. Society of Petroleum Engineers, New Orleans, Louisiana.
- Khilar, K.C., Fogler, H.S., 1998. Migrations of Fines in Porous Media. Theory and Applications of Transport in Porous Media. Kluwer Academic Publishers, Dordrecht, The Netherlands.
- Lohne, A., et al., 2010. Formation-damage and well-productivity simulation. *SPE J.* 15 (3), 751–769.
- Massei, N., Lacroix, M., Wang, H.Q., Dupont, J.P., 2002. Transport of particulate material and dissolved tracer in a highly permeable porous medium: Comparison of the transfer parameters. *J. Contam. Hydrol.* 57 (1–2), 21–39.
- Ochi, J., Detienne, J.-L., Rivet, P., 2007. Internal formation damage properties and oil-deposition profile within reservoirs during PWRI operations, European Formation Damage Conference. Society of Petroleum Engineers, Scheveningen, The Netherlands.
- Ochi, J., Detienne, J.-L., Rivet, P., Lacourie, Y., 1999. External filter cake properties during injection of produced waters, SPE European Formation Damage Conference. Society of Petroleum Engineers, The Hague, Netherlands.
- Ochi, J., Vernoux, J.F., 1999. A two-dimensional network model to simulate permeability decrease under hydrodynamic effect of particle release and capture. *Transp. Porous Media* 37 (3), 303–325.
- Pang, S., Sharma, M.M., 1997. A model for predicting injectivity decline in water-injection wells. *SPE Form. Eval.* 12 (3), 194–201.
- Parn-anurak, S., Engler, T.W., 2005. Modeling of fluid filtration and near-wellbore damage along a horizontal well. *J. Pet. Sci. Eng.* 46 (3), 149–160.
- Payatakes, A.C., Rajagopalan, R., Tien, C., 1974. Application of porous media models to the study of deep bed filtration. *Can. J. Chem. Eng.* 52, 722–731.
- Quintero, L., Jones, T.A., Clark, D., Twynam, A.J., 2007. NAF Filter Cake Removal Using Microemulsion Technology, European Formation Damage Conference. Society of Petroleum Engineers, Scheveningen, The Netherlands.
- Ruth, B.F., 1935. Studies in Filtration III. Derivation of General Filtration Equations. *Ind. Eng. Chem.* 27 (6), 708–723.
- Salimi, S., Khansari, A.N., Ghalambor, A., Tronvoll, J., 2009. Application of UBD Technology To Maximize Recovery From Horizontal Wells in the Naturally Fractured Carbonate Reservoirs, IADC/SPE Managed Pressure Drilling and Underbalanced Operations Conference & Exhibition. In: Proceedings of the 2009 IADC/SPE Managed Pressure Drilling and Underbalanced Operations Conference and Exhibition, San Antonio, Texas.
- Shapiro, A.A., Bedrikovetsky, P.G., Santos, A., Medvedev, O.O., 2007. A stochastic model for filtration of particulate suspensions with incomplete pore plugging. *Transp. Porous Media* 67 (1), 135–164.
- Sherwood, J.D., Meeten, G.H., 1997. The filtration properties of compressible mud filtercakes. *J. Pet. Sci. Eng.* 18 (1–2), 73–81.
- Suri, A., Sharma, M.M., 2004. Strategies for sizing particles in drilling and completion fluids. *SPE J.* 9 (1), 13–23.
- Tien, C., 2012. Principles of Filtration. Elsevier Science, Boston.
- Tien, C., Bai, R., Ramarao, B.V., 1997. Analysis of cake growth in cake filtration: effect of fine particle retention. *AIChE J.* 43 (1), 33–44.
- Veerapen, J.P., Nicot, B., Chauveteau, G.A., 2001. In-depth permeability damage by particle deposition at high flow rates (Copyright 2001). SPE European Formation Damage Conference. Society of Petroleum Engineers Inc., The Hague, Netherlands.
- Wagner, M.R., et al., 2006. Horizontal drilling and openhole gravel packing with oil-based fluids – an industry milestone. *SPE Drill. Complet.* 21 (1), 32–43.
- Wennberg, K.E., Sharma, M.M., 1997. Determination of the filtration coefficient and the transition time for water injection wells (Copyright 1997). SPE European Formation Damage Conference. Society of Petroleum Engineers, Inc., The Hague, Netherlands.
- Windarto, W., Gunawan, A.Y., Sukarno, P., Soewono, E., 2011. Modeling of mud filtrate invasion and damage zone formation. *J. Pet. Sci. Eng.* 77 (3–4), 359–364.
- Windarto, Gunawan, A.Y., Sukarno, P., Soewono, E., 2012. Modelling of formation damage due to mud filtrate invasion in a radial flow system. *J. Pet. Sci. Eng.* 100, 99–105.
- You, Z., Badalyan, A., Bedrikovetsky, P., 2013. Size-exclusion colloidal transport in porous media—stochastic modeling and experimental study. *SPE J.* 18 (4), 620–633.
- You, Z., Osipov, Y., Bedrikovetsky, P., Kuzmina, L., 2014. Asymptotic model for deep bed filtration. *Chem. Eng. J.* 258, 374–385.
- Ytrehus, J.D., Cerasi, P., Opedal, N., 2013. Dynamic Fluid Erosion on Filter Cakes, Proceedings of the 10th SPE International Conference and Exhibition on European Formation Damage. Society of Petroleum Engineers, Noordwijk, The Netherlands.
- Yuan, H., Shapiro, A.A., 2011. Induced migration of fines during waterflooding in communicating layer-cake reservoirs. *J. Pet. Sci. Eng.* 78 (3–4), 618–626.
- Yuan, H., You, Z., Shapiro, A.A., Bedrikovetsky, P., 2013. Improved population balance model for straining-dominant deep bed filtration using network calculations. *Chem. Eng. J.* 226, 227–237.
- Zitha, P., Frequin, D., Bedrikovetsky, P., 2013. CT Scan Study of the Leak-Off of Oil-Based Drilling Fluids into Saturated Media, Proceedings of the 10th SPE International Conference and Exhibition on European Formation Damage. Society of Petroleum Engineers, Noordwijk, The Netherlands.

7 Conclusions

The analytical modelling and laboratory study of fines migration due to velocity/salinity/temperature/pH variations during coreflooding, and of simultaneous deep bed filtration and cake formation during injection of two-sized particles, allow drawing the following conclusions:

1. Low-velocity fines drift along rock surface (rolling and sliding) explains the long permeability-stabilisation periods. The stabilisation time significantly exceeds one pore volume injected, indicating that the particles migrate with a velocity much (two-three orders of magnitude) lower than the carrier water velocity.
2. Another explanation for long permeability-stabilisation periods is the delay in particle release due to slow diffusion of salt from the grain-particle contact area into the bulk of the fluid.
3. One-dimensional problem of slow fines migration with delayed particle release after varying velocity/salinity/pH, allows for exact solution. The analytical model consists of explicit formulae for breakthrough and retained concentrations, and pressure drop history.
4. Matching the measured permeability and accumulative outlet particle concentration by the analytical model, accounting for both slow fines migration and delayed release, shows excellent agreement between measured data and modelling results.
5. Slow-particle model matches the experimental data with higher accuracy than the delay-release model. The straining-concentration and salinity dependencies of model parameters, obtained from tuning by the slow-particle model, have typical forms as

that observed in other studies; whereas those obtained using the delay-release model reveal an untypical form of the maximum retention function.

6. Fine particles are mobilised during velocity, temperature, and pH increase, or salinity decrease in the order of particle size reduction.

7. The maximum retention function for size-distributed particles, attached to rock surface in a mono-layer, is expressed by an explicit formula that includes the size distribution of attached particles and the critical detached size curve. This function is equal to accumulated concentration of particles smaller than that mobilised by the flux with given flow velocity.

8. Size distribution of the attached movable particles can be obtained from the maximum retention function and the critical detached size curve.

9. The laboratory “velocity-ionic strength” and “temperature-ionic strength” translation procedures, along with the torque balance equation for particles, allows to determine velocity- and temperature-dependencies of the maximum retention concentration from experiments with varying ionic strength.

10. The effect of electrostatic attraction weakening with temperature increase on the maximum retention function, dominates over that of the water viscosity decrease with temperature increase in this study. This leads to a maximum retention concentration decrease with temperature. Therefore, geothermal fields are more susceptible to fines migration than conventional petroleum reservoirs and aquifers.

11. Two different scenarios of cake formation are distinguished during injection of two-sized particle suspension in porous media. The first scenario is the slow growth of the external large-particle cake with fast moving of the small-particle cake front

inside the large-particle cake followed by further cake build-up from the mixture of injected particles. It is typical for high concentration of small particles in the injected suspension, which exhibits piecewise impedance curve with three segments.

12. The second scenario of cake formation is the fast growth of the external large-particle cake with slow development of the internal small-particle cake filled in the large-particle cake. This scenario occurs for low concentration of small particles, presenting two-segment piecewise impedance curve.